

DISSERTATION

SCOUR CAUSED BY RECTANGULAR IMPINGING JETS
IN COHESIONLESS BEDS

Submitted by

Julio Martin Kuroiwa

Department of Civil Engineering

In partial fulfillment of the requirements
for the Degree of Doctor of Philosophy

Colorado State University

Fort Collins, Colorado

Spring 1999

COLORADO STATE UNIVERSITY

October 23, 1998

WE HEREBY RECOMMEND THAT THE DISSERTATION PREPARED UNDER OUR SUPERVISION BY JULIO MARTIN KUROIWA ENTITLED SCOUR CAUSED BY RECTANGULAR IMPINGING JETS IN COHESIONLESS BEDS BE ACCEPTED AS FULFILLING IN PART REQUIREMENTS FOR THE DEGREE OF DOCTOR OF PHILOSOPHY.

Committee on Graduate Work

Ellen E. Wohl

Richard J. Witter

Wayne S. Charlie

Pierre Julien

Adviser

James F. Ruff

Department Head

N. I. I. I. I.

ABSTRACT OF DISSERTATION

SCOUR CAUSED BY RECTANGULAR IMPINGING JETS
IN COHESIONLESS BEDS

An experimental investigation was conducted to obtain a better predictor of the depth of scour caused by impinging jets on cohesionless beds. The variables of importance considered in this study were the unit discharge, q , the velocity of impingement, V_i , the thickness of the jet at impingement, b_i , the tailwater depth TW , the angle of impingement, δ , the particle size diameter, d_n , the submerged specific density of the particle, $(G - 1)$, and the gravity acceleration, g . Dimensional analysis indicated that the dimensionless depth of scour, $Y/(q_2/g)^{1/3}$ was related to the Froude number to the jet at impingement, $V_i/(g b_i)^{0.5}$, the dimensionless tailwater depth, $TW/(b_i \cos \delta)$, and the dimensionless fall velocity $w/(g b_i)^{0.5}$. The fall velocity of the particle, w , is approximately equal to $(g (G - 1) d_n)^{0.5}$, for particles whose $d_n > 0.1$ mm.

A large facility was built at Colorado State University to conduct the tests. The Dam Foundation Erosion (DFE) Facility consists of a tailbox whose dimensions are 16.76 m by 9.14 m, conveyance structures and a diffuser that contains a nozzle. The diffuser was mounted on a supporting structure above the tailbox. The cross section of the nozzle is 3.05 m by 0.087 m and the angle of issuance can be changed in 5 degrees increments. Water was conveyed from Horsetooth Reservoir by pipelines to the testing site and water was released as a jet.

The experimental phase of this study was divided in two parts. In the first part, the bed material was 19.05 mm roadbase. A constant discharge of $2.735 \text{ m}^3/\text{s}$ was released by a diffuser impinging the tailwater at four different water depths for each angle of issuance. The angles of issuance with respect to the vertical were 15, 25 and 35 degrees. An increase in the tailwater depth always caused a decrease in the depth of scour when the angle of issuance remained constant. Furthermore, the scour hole was shallower as the angle of issuance departed from vertical. The geometric characteristics of the scour hole were documented and a strong correlation between the downstream slope and the angle of impingement was found.

A second test series was conducted to study the erodibility of fractured rock. Fractured rock was simulated using concrete blocks. They were fluted on one side, flat on the other side and were 0.39 m long, 0.20 m wide, and 0.064 m thick. The specific gravity of the blocks was 1.65. Three thousand six hundred blocks were placed in two layers at a 45 degree angle pointing into the flow. Scour tests were conducted under minimum tailwater conditions. The upper layer was dislodged at a unit discharge of $0.372 \text{ m}^2/\text{s}$. The bottom layer was dislodged at a unit discharge of $0.650 \text{ m}^2/\text{s}$.

In both test series, the degree of aeration of the jet was high. Instrument measurement of air concentration yielded values between 90% and 98% when the unit discharge was $2.735 \text{ m}^3/\text{s}$. This was confirmed visually, because the jet expanded as it fell. The thickness of the jet at issuance was 0.087 m, and the thickness of the jet at impingement varied between 1.80 m and 2.00 m.

Additional data was obtained from the studies conducted by Thomas (1953), Hallmark (1955) and Lencastre (1961) to complement the database obtained during the

experimental phase of this study. The jets were formed at an overfall and photographic records indicate that the amounts of air entrained was not appreciable.

During the data analysis, it was necessary to separate the expression developed for compact jets and it was determined that the scour caused by highly aerated jets can not be predicted using the expression obtained for compact jets. It was shown that air entrainment affects the scouring capacity of the jet. The expression obtained using dimensionless analysis was validated for compact jets first. A second expression was obtained for highly aerated jets. The effects of power dissipation of the jets after they impinge the tailwater surface are more pronounced in highly aerated jets.

Fractured rock can be treated as a collection of large cohesionless materials, provided that there is no cementing material between the blocks. The spherical equivalent diameter of the blocks is used to obtain a characteristic particle size, d_n . The dislodgement of the blocks is controlled by the depth of the rock layers.

The unit discharge, tailwater depth, angles of impingement, particle size, and the degree of aeration of jets, proved to be major factors in the prediction of the ultimate depths of scour holes.

Julio Martin Kuroiwa
Department of Civil Engineering
Colorado State University
Fort Collins, CO 80523
Spring 1999

ACKNOWLEDGMENTS

I would like to thank Dr. James Ruff for all his support and encouragement during my graduate studies. Working for him has been a great experience. Not only I learned from him in the laboratory and in the classroom, but I also enjoyed the talks we had about aspects of life other than academic.

I am also thankful to Dr. Rodney Wittler, leader of the Dam Foundation Erosion Studies Team, for the ideas and the assistance provided and also for serving as a committee member.

I would also like to thank the committee members who supervised my graduate work: Dr. Pierre Julien, Dr. Wayne Charlie and Dr. Ellen Wohl. Their ideas and suggestions have been included in this study.

This study would not have been completed without the participation of my office mates who participated in the tests conducted at the Dam Foundation Erosion Facility for almost three years. Tom Gill and Jason Ward performed the calibration of the Pitot tubes and the air concentration and velocity measurements. Jason also drew the DFE plans. Bill Strand conducted part of the particle size distribution analysis. Subhendu Mishra, along with my other office mates, participated gathering data in various tests. My deepest recognition to all of them.

This study required the skills of the members of the Engineering Research Center Shop led by Mr. Jerry Davis. Messrs. Robert Brennan and Halley Pringle built the diffuser and the supporting structures. Mr. Horacio Garza Jr. promptly fixed any electrical problem

that we had during our tests. Mr. Bart Rust built various devices used in the experimental part of this study. Mr. Herman Vasquez was in charge of the Tool Crib during the completion of this study. Without them, the projects conducted by the investigators and their assistants at the ERC would not be possible.

The final copy of this document was edited and formatted by Ms. Gloria Garza, whose dedication is gratefully acknowledged.

I would like to also thank my family for the support I received all these years. I thank my parents, Julio and Gloria, and my brother Héctor.

This study was funded through Cooperative Agreement 1425-5-FC-81-20350 between the U.S. Bureau of Reclamation and Colorado State University to study the characteristics of scour produced by rectangular jets downstream of dams.

DEDICATION

This dissertation is dedicated to my parents, Julio and Gloria, and my brother Héctor.

TABLE OF CONTENTS

	<u>Page</u>
ABSTRACT	iii
ACKNOWLEDGEMENTS	vi
DEDICATION	viii
LIST OF TABLES	xii
LIST OF FIGURES	xviii
LIST OF SYMBOLS	xxviii
1 INTRODUCTION	1
1.1 Organization of This Investigation	4
2 LITERATURE REVIEW	6
2.1 General	6
2.2 Jet Diffusion	7
2.3 Pressure Fluctuations	22
2.4 Scour Caused by Impinging Jets in Cohesionless Materials	26
2.4.1 General concepts related to scour	26
2.4.1.1 Flow over smooth surfaces	26
2.4.1.2 Flow over rough surfaces	27
2.4.1.3 Drag coefficient	28
2.4.1.4 Incipient particle motion	30
2.4.2 Experimental studies on scour holes produced in cohesionless materials	32
2.5 Scour Caused by Impinging Jets in Rock Strata	48
2.5.1 Rock description	48
2.5.2 Scour studies in rock strata	49
3 THEORETICAL CONSIDERATIONS	52
3.1 Introduction	52
3.2 Initial Boundary Conditions	54
3.3 Scour Hole "Final" Boundary Conditions	55
3.4 Scour Process	56
3.5 Influence of Air Entrainment in the Available Power of the Jet at Impingement	59
3.6 Kinematics of Jet Travel	61

3.7	Geometry of a Compact Falling Jet	66
3.8	Total Dynamic Available Heat at the Tailwater Surface and Trajectory Length	68
3.9	Phase Two Pressure Head Dissipation of an Impinging Jet	69
3.10	Pressure Distribution at the Bottom of a Plunge Pool	70
3.11	Condition of Incipient Motion at the Bottom of a Scour Hole Using a Moment Model	71
3.12	Equation to Calculate the Depth of Scour Caused by a Rectangular Jet in a Cohesionless Bed	73
4	RESEARCH FACILITIES, EQUIPMENT AND PROCEDURES	79
4.1	Dam Foundation Erosion Facility	79
4.2	Test Procedures and Data Acquisition Equipment	82
4.3	Velocity and Air Concentration Tests	87
4.4	Fissured Rock Tests	88
5	DATA COLLECTION	93
5.1	General	93
5.2	Appearance of the Jet	95
5.3	Variation of Tailwater Depths in the Vicinity of the Zone of Impingement	96
5.4	Velocity Measurements Across the Nozzle	97
5.5	Effect of Time on Scour Hole Development	98
5.6	Formation and Armoring of the Scour Hole and the Mound	100
5.7	Geometry of the Scour Hole	103
5.8	Location of Deepest Points of the Scour Hole and Highest Points of the Mound	105
5.9	Slopes of Scour Holes	105
5.10	Dimensionless Longitudinal Profiles of Scour Holes	106
5.11	Air Concentration and Velocities at the Section of Impingement and Below the Tailwater Surface	108
5.12	Simulated Fractured Rock Tests	111
5.12.1	General	111
5.12.2	Block failure at 1.13 m ³ /s (40 cfs)	112
5.12.3	Block failure at 1.27 m ³ /s (45 cfs)	112
5.12.4	Block failure at 1.42 m ³ /s (50 cfs)	116
5.12.5	Block failure at 1.98 m ³ /s (70 cfs)	118
6	DATA ANALYSIS AND DISCUSSION	122
6.1	Introduction	122
6.2	Angle of Downstream Slope Versus Angle of Impingement	123
6.3	Position of the Deepest Point of the Scour Hole	127
6.4	Drawdown Depth	128
6.5	Representative Particle Size	129

6.6	Time Dependency of Depth of Scour	131
6.7	Predictors of Scour Depth	132
6.7.1	Compact jets	132
6.7.2	Highly aerated (diverging jets)	137
6.8	Comparison Between Maximum Depth of Scour Using Mason's Formulae and the Actual Depth of Scour	147
6.9	Alternative Methods to Calculate the Depth of Scour Produced by Impinging Jets	153
6.9.1	Power per unit area versus erodibility	154
6.9.2	Calculation of maximum depth of scour using equation of Bohrer et al. and Annandale's approach	155
6.9.3	Simulated fractured rock test	160
6.9.4	Comparison between the calculated velocity of the jet, V_L , and the velocity of the particle at the downstream slope calculated using Equation (3.23)	161
6.9.5	Depth of scour versus calculated velocity at the initial bed surface	163
7	CONCLUSIONS AND RECOMMENDATIONS	165
7.1	Summary	165
7.2	Conclusions	169
7.3	Recommendations for Future Research	171
	REFERENCES	173
APPENDIX A	Influence of TW/b_1 on Pressure Dissipation	178
APPENDIX B	Dam Foundation Erosion Facility & Nozzle and Diffuser Diagrams	183
APPENDIX C	Data Used in This Study/Calculations	189
APPENDIX D	Manometer Readings at DFE Diffuser and Nozzle	231
APPENDIX E	Depth of Scour Versus Time at Various Locations -- DFE Studies	241
APPENDIX F	Particle Size Distribution of Before and After the Tests & Particle Size Distribution in Hallmark and Thomas Test	254
APPENDIX G	Scour Hole Geometry	264
APPENDIX H	Air Concentration and Velocity Readings	327
APPENDIX I	Forces at the Bottom of a Block, $Q = 1.13 \text{ m}^3/\text{s}$ (40 cfs), $Q = 1.27 \text{ m}^3/\text{s}$ (45 cfs), and $Q = 1.42 \text{ m}^3/\text{s}$ (50 cfs)	333
APPENDIX J	Calculations of Interlocking Factor	341
APPENDIX K	Prediction of Drawdown Depths Using Zahoor's Equation	356
APPENDIX L	Prediction of Depths of Scour Using Hoffman, Machado, and Mirtskhulava et al. Equations	360

LIST OF TABLES

	<u>Page</u>
Table 5.1 Summary of tests	94
Table 5.2 Median size of particles found across the scour hole and the mound .	103
Table 5.3 Longitudinal slopes	106
Table 6.1 Summary of data used in this study	123
Table 6.2 Angle of downstream slopes versus angles of impingement	124
Table 6.3 Drawdown depths versus calculated angles of impingement	128
Table 6.4 Median diameter of material found in different sections of the scour hole with respect to initial bed particle size distribution	131
Table 6.5 Parameters of compact jets in Equation (6.3)	133
Table 6.6 Parameters for highly aerated jets (diverging jets) in Equation (6.3)	139
Table 6.7 Parameters for highly aerated (diverging) jets discarding the Froude number of the jet at impingement	142
Table 6.8 Ratios of approximate length of jet to disintegration length using Horeni's equation	147
Table 6.9 Erodibility of the granular material used in the Dam Foundation Erosion Studies (d_{50})	159
Table 6.10 Erodibility of the granular material used in the Dam Foundation Erosion Studies (d_{85})	159
Table 6.11 Velocities V_L calculated at a distance $L = (TW+Y)/\cos \delta$ from the tailwater surface using Bohrer's equation	159

Table 6.12	Comparison between estimated scour threshold velocities at the bottom of scour holes and calculated velocities at a distance $(TW + Y)/\cos \delta$	160
Table 6.13	Erodibility of the blocks used in the Dam Foundation Erosion Studies	161
Table 6.14	Hydraulic conditions at the threshold of erosion. Simulated fissured rock tests	161
Table 6.15	Comparison between the calculated velocity at the bottom of the scour hole from Equation (3.23) and the threshold velocity, V_p	163
Table 6.16	Lengths of scour $Y/\cos \delta$ versus estimated velocities at original bed surface V_L	164
Table A.1	Relative pressure heads at a plate for different relative water depths. Data is taken from Lencastre (1961)	179
Table C.1.1	Compact jet data used in this study	191
Table C.1.2	Dimensionless parameters in Equation (6.3) — compact jet data	194
Table C.1.3	Measured values of Y/y_c and summary of predicted values of Y/y_c using Equation (6.4) for each data set — compact jet data	197
Table C.1.4	Predicted values of Y/y_c using Equation (6.4) and measured values of Y/y_c used to calculate the regression coefficient — compact jet data	200
Table C.1.5	Summary of measured values of scour using Equation (6.4) and predicted values of scour for each data set — compact jet data	203
Table C.1.6	Predicted values of Y using Equation (6.4) and measured values of Y used to calculate the regression coefficient — compact jet data	206
Table C.1.7	Number of predictions falling within 25% of measured values and within 35% of measured values — compact jet data	209
Table C.2.1	Highly aerated jet data used in this study	211
Table C.2.2	Dimensionless parameters in Equation (6.3) — highly aerated jet data	212
Table C.2.3	Measured values of Y/y_c and summary of predicted values of Y/y_c using Equation (6.5) by data set — highly aerated jet data	213

Table C.2.4	Predicted values of Y/y_c using Equation (6.5) and measured values of Y/y_c used to calculate the regression coefficient — highly aerated jet data	214
Table C.2.5	Summary of measured values of scour and predicted values of scour using Equation (6.5) for each data set — highly aerated jet data	215
Table C.2.6	Predicted values of Y using Equation (6.5) and measured values of Y used to calculate the regression coefficient — highly aerated jet data	216
Table C.2.7	Number of predictions falling within 25% of measured values and within 35% of measured values — highly aerated jet data	217
Table C.3.1	Highly aerated jet data used in this study	218
Table C.3.2	Dimensionless parameters used to develop Equation (6.6)	219
Table C.3.3	Measured values of Y/y_c and summary of predicted values of Y/y_c using Equation (6.6) for each data set — highly aerated jet data	220
Table C.3.4	Predicted values of Y/y_c using Equation (6.6) and measured values of Y/y_c used to calculate the regression coefficient — highly aerated jet data	221
Table C.3.5	Summary of measured values of scour and predicted values of scour using Equation (6.6) for each data set — highly aerated jet data	222
Table C.3.6	Predicted values of Y using Equation (6.6) and measured values of Y used to calculate the regression coefficient — highly aerated jet data	223
Table C.3.7	Computation of predicted values falling within 25% of measured values and within 35% of measured values — highly aerated jet data	224
Table C.4.1	Prediction of depth of scour using compact jet formula Equation (6.4) -- compact jet data and highly aerated jet data	225
Table C.5.1	Prediction of depth of scour using compact jet formula Equation (6.5) -- compact jet data and highly aerated jet data	228
Table D.1	DFE nozzle Pitot tube calibration	233
Table D.2	Manometer readings at DFE diffuser and nozzle	236

Table E.1	Dam Foundation Erosion Studies — depth of scour hole with respect to time (SI units), 09/09/96, 09/23/96, 09/30/96, 07/16/97 . . .	243
Table E.2	Dam Foundation Erosion Studies — depth of scour hole with respect to time (SI units), summary of 07/16/97	244
Table E.3	Dam Foundation Erosion Studies — depth of scour hole with respect to time (SI units), 07/23/97	245
Table E.4	Dam Foundation Erosion Studies — depth of scour hole with respect to time (SI units), summary of 07/23/97	246
Table E.5	Dam Foundation Erosion Studies — depth of scour hole with respect to time (SI units), 09/02/97	247
Table E.6	Dam Foundation Erosion Studies — depth of scour hole with respect to time (SI units), summary of 09/02/97	248
Table E.7	Dam Foundation Erosion Studies — depth of scour hole with respect to time (SI units), 09/11/97	249
Table E.8	Dam Foundation Erosion Studies — depth of scour hole with respect to time (SI units), summary of 09/11/97	250
Table F.1	Particle size distribution data from DFE Studies	256
Table F.2	Particle size distribution of particles found in scour hole — 07/16/97	257
Table F.3	Particle size distribution of particles found in scour hole — 07/24/97	258
Table F.4	Particle size distribution of particles found in scour hole — 09/02/97	259
Table F.5	Particle size distribution of particles found in scour hole — 09/11/97	260
Table G.1	Volumes of scour and deposition	266
Table G.2.1	Dam Foundation Erosion Studies — angle of downstream slope, θ , versus angle of impingement, δ	268
Table G.2.2	Dam Foundation Erosion Studies — DFE data	269
Table G.2.3	Dam Foundation Erosion Studies — Doehring data	270

Table G.3	Dam Foundation Erosion Studies — statistical properties of angle of downstream slope versus angle of impingement	271
Table G.4	DFE Studies 1996/97 — L2 versus Y (distance from the DFE Studies)	322
Table G.5	Calculated distance of impact at bottom of scour hole, X_t , versus actual distance of impact, X_{max} (measured from north wall)	325
Table G.6	Side slopes	326
Table H.1	Dam Foundation Erosion Studies — air concentration and velocity readings (SI units)	329
Table I.1	Dam Foundation Erosion Studies — “fractured rock” test 1997, location of piezometer taps in bricks	334
Table I.2	Manometer readings	335
Table I.3	Summary of piezometer data — USC units	336
Table I.4	Summary of piezometer data — metric	337
Table I.5	Heads in excess of static head close to the region of impingement . .	340
Table J.1	Values of the function $(\sin \theta + (K_1 a / K_2 c) \cos \theta) / (1 + K_3 (K_1 a / K_2 c))$ -- $K_3 = 0.1$	343
Table J.2	Values of the function $(\sin \theta + (K_1 a / K_2 c) \cos \theta) / (1 + K_3 (K_1 a / K_2 c))$ -- $K_3 = 0.2$	346
Table J.3	Values of the function $(\sin \theta + (K_1 a / K_2 c) \cos \theta) / (1 + K_3 (K_1 a / K_2 c))$ -- $K_3 = 0.3$	349
Table J.4	Values of the function $(\sin \theta + (K_1 a / K_2 c) \cos \theta) / (1 + K_3 (K_1 a / K_2 c))$ -- $K_3 = 0.4$	352
Table J.5	Summary of average values of interlocking factor	355
Table K.1	Calculation of drawdown depth using Zahoor’s equation	358
Table K.2	Summary	359
Table L.1	Hoffman’s equation (1998)	362
Table L.2	Predicted depths of scour using Machado’s formula	363

Table L.3	Predicted depths of scour using Machado's general equation (Equation (2.59))	364
Table L.4	Mirtskhulava et al. Equation (1967)	365

LIST OF FIGURES

	<u>Page</u>
Figure 1.1	Potential problem induced by dam foundation erosion 2
Figure 2.1	Zones of flow establishment and zone of established flow (Albertson et al., 1950) 8
Figure 2.2	Jet velocity and shear stress distribution near a wall (Beltaos and Rajaratnam, 1974) 12
Figure 2.3	Mechanisms of jet impingement (McKeogh and Elsayy, 1980) . 14
Figure 2.4	Conditions of flow downstream of a weir (Leutheusser and Birk, 1990) 16
Figure 2.5	Pressure distribution across a plate being impinged by a jet 23
Figure 2.6	Pressure dissipation with increase in tailwater depth (Lancastre, 1961) 23
Figure 2.7	Definitions of zones in an impinging jet (Ervine et al., 1997) . . . 25
Figure 2.8	Pressure coefficients versus pool depth/impact diameter ratio . . . 26
Figure 2.9	Drag coefficient of natural sands and gravel 30
Figure 2.10	Dimensionless critical shear stress versus dimensionless particle diameter (Julien, 1995) 32
Figure 2.11	Definition of variables for an impinging jet (Stein and Julien, 1994) 44
Figure 2.12	Rate of energy dissipation (kW/m ²) versus erodibility index (Annandale, 1995) 45
Figure 3.1	Phases of a scouring impinging jet 56
Figure 3.2	Sketch of air entrainment in a section of a jet 59

Figure 3.3	Variables of interest in this study	64
Figure 3.4	Geometry of a compact impinging jet	67
Figure 3.5	Variables of interest defining the depth of a scour hole	71
Figure 3.6	Moments acting on a particle located on the downstream slope of the scour hole	72
Figure 3.7(a),(b)	Similarity between the pressure distribution of two jets	76
Figure 4.1	Dam Foundation Erosion Facility	80
Figure 4.2	Dam Foundation Erosion Facility — plan, side elevation and front elevation	81
Figure 4.3	Gradation of bed material in Dam Foundation Erosion Studies . .	83
Figure 4.4	Photograph of the DFE Facility from the west side	84
Figure 4.5	Surveying of the bed after a test	86
Figure 4.6	Block used in a fissured rock test with tubes installed	90
Figure 4.7	Simulated fractured rock testing surface	90
Figure 4.8	Piezometers setup prior to block installation	91
Figure 5.1	Depth of scour hole (Y) versus tailwater depth (TW)	94
Figure 5.2	Front view of the jet. Some lateral expansion is observed	96
Figure 5.3	Typical velocity distribution across the nozzle. Test was conducted on August 26, 1996	98
Figure 5.4	Typical scour development with time for points located along the centerline of the scour hole	99
Figure 5.5(a)	Typical particle size distribution of material in space after test	101
Figure 5.5(b)	Appearance of material gathered at different locations. From the upper left dish in clockwise rotation the location in which they were collected follows: downstream slope, upstream slope, original bed material, mound, and bottom of scour hole	102

Figure 5.6	Three dimensional view of scour hole after test carried out on September 9, 1996. Dimensions are in feet	104
Figure 5.7	Photograph of a scour hole	104
Figure 5.8	Dimensionless profiles of scour holes for an angle of issuance of 15 degrees	108
Figure 5.9	Depth of water above the Pitot tube versus air concentrations recorded on test conducted July 29, 1997. Unit discharge is $0.897 \text{ m}^2/\text{s}$	110
Figure 5.10	Measured velocities of the jet at different depths below the tailwater surface	110
Figure 5.11	Mechanism of failure of fissured rocks under the action of the jet	113
Figure 5.12	Mat after failure at $1.13 \text{ m}^3/\text{s}$ (40 cfs)	113
Figure 5.13	Piezometer readings in the north-south direction of the block setup across the centerline. $Q = 1.13 \text{ m}^3/\text{s}$ (40 cfs)	114
Figure 5.14	Piezometer readings at $1.27 \text{ m}^3/\text{s}$ (45 cfs) in the north-south direction of the testing surface along the centerline of the jet . . .	114
Figure 5.15	Mat after failure at $1.27 \text{ m}^3/\text{s}$ (45 cfs)	116
Figure 5.16	Mat after failure at $1.42 \text{ m}^3/\text{s}$ (50 cfs)	117
Figure 5.17	Piezometer readings at $1.42 \text{ m}^3/\text{s}$ (50 cfs) in the north-south direction of the testing surface along the centerline of the jet . . .	117
Figure 5.18	Photograph of the scour hole after test conducted at $1.98 \text{ m}^3/\text{s}$ (70 cfs)	120
Figure 5.19	Detail showing the blocks protruding above their initial position	120
Figure 5.20	Photograph of the scour hole after test conducted at $2.78 \text{ m}^3/\text{s}$ (98 cfs)	121
Figure 6.1	Angle of downstream slope (θ) versus angle of impingement (δ)	125

Figure 6.2	Interlocking factor as a function of the moment arm ratio, $(K_1 a/(K_2 c))$, and the lift coefficient to drag coefficient ratio, K_3	127
Figure 6.3	Drawdown depths versus angles of impingement for DFE studies	130
Figure 6.4	Ratios of depths of scour at certain times to the final depth of scour (Y_t/Y) versus ratios of time to the total time of tests (t/T_f)	132
Figure 6.5	Predicted values of Y/y_c versus measured values of Y/y_c for compact jets	134
Figure 6.6	Predicted values of depth of scour versus measured values of depth of scour using Equation (6.4). The upper line (broken) corresponds to the values overestimated by 25% and the lower line (dotted) corresponds to the values underestimated by 25%	134
Figure 6.7	Predicted relative depth of scour versus measured relative depth of scour for highly aerated jets using Equation (6.5)	140
Figure 6.8	Predicted depths of scour using Equation (6.5) versus measured depths of scour. The upper broken line indicates an overestimation of 25% and the lower dotted line indicates an underestimation of 25%	141
Figure 6.9	Predicted values of the relative depths of scour versus the measured values of the depths of scour using Equation (6.6)	143
Figure 6.10	Predicted depths of scour using Equation (6.6). The upper broken line represents an overestimation of 25%. The lower dotted line represents an underestimation of 25% of the measured values	143
Figure 6.11	Predicted values of depths of scour using Equation (6.4). The depths of scour of highly aerated jets tends to be overestimated	145
Figure 6.12	Predicted values of depths of scour using Equation (6.5). The depths of scour of compact jets tend to be underestimated	145
Figure 6.13	Predicted values of scour using Mason and Arumugan's model equation versus predicted measured values of scour. Negative values of Y indicate that the estimated value of depth below the tailwater surface was lower than the tailwater depth	149

Figure 6.14	Predicted values of scour using Mason and Arumugan's prototype equation versus measured values of scour. Negative values of Y indicate that the estimated value of depth below the tailwater surface was lower than the tailwater depth	149
Figure 6.15	Predicted depths of scour using Equation (2.53) (Hoffman, 1998)	151
Figure 6.16	Predicted depths of scour using Equation (2.44) (Machado, 1980)	152
Figure 6.17	Predicted depths of scour using Equation (2.59) (Machado, 1980)	152
Figure 6.18	Predicted depths of scour using Equation (2.42) (Mirtskhulava et al., (1980)	153
Figure 6.19	Diagram showing the calculated velocity, V_L , and the velocity of the particle, V_p	156
Figure 6.20	Depths of scour along the centerline of the jet versus estimated velocities V_L at a distance $TW/\cos \delta$ from the point of impingement	165
Figure A.1	Excess dimensionless mean pressure heads of a jet impinging on a plate with a dimensionless tailwater depth TW/b_i	180
Figure B.1	Dam Foundation Erosion Facility	184
Figure B.2	Dam Foundation Erosion Facility diffuser	185
Figure B.3	Dam Foundation Erosion Facility nozzle	186
Figure B.4	Mounting of Pitot tubes	187
Figure B.5	Position of manometers and Pitot tubes	188
Figure D.1	DFE nozzle Pitot tube calibration	235
Figure E.1	Dam Foundation Erosion Studies — discharge, TW depth, and scour depth versus time for 09/09/96	251
Figure E.2	Dam Foundation Erosion Studies — discharge, scour depth, and rate versus time for 09/23/96	251
Figure E.3	Dam Foundation Erosion Studies — discharge, TW depth, and scour depth versus time for 07/16/97	252

Figure E.4	Dam Foundation Erosion Studies — discharge, TW depth, and scour depth versus time for 07/24/97	252
Figure E.5	Dam Foundation Erosion Studies — discharge, TW depth, and scour depth versus time for 09/02/97	253
Figure E.6	Dam Foundation Erosion Studies — discharge, TW depth, and scour depth versus time for 09/11/97	253
Figure F.1	Dam Foundation Erosion Studies — Western Mobile 3/4 in. roadbase particle size distribution	256
Figure F.2	Dam Foundation Erosion Studies — particle size distribution, 07/16/97	257
Figure F.3	Dam Foundation Erosion Studies — particle size distribution, 07/24/97	258
Figure F.4	Dam Foundation Erosion Studies — particle size distribution, 09/02/97	259
Figure F.5	Dam Foundation Erosion Studies — particle size distribution, 09/11/97	260
Figure F.6	Hallmark Series A Tests — particle size distribution	261
Figure F.7	Hallmark Series B Tests — particle size distribution	262
Figure G.1	Width of scour hole versus tailwater depth	267
Figure G.2	Dam Foundation Erosion Studies — angle of downstream slope versus angle of impingement plot	272
Figure G.3	Dam Foundation Erosion Studies — dimensionless scour profiles, $\alpha = 15^\circ$	272
Figure G.4	Dam Foundation Erosion Studies — dimensionless scour profiles, $\alpha = 25^\circ$	273
Figure G.5	Dam Foundation Erosion Studies — dimensionless scour profiles, $\alpha = 35^\circ$	273
Figure G.6	Dam Foundation Erosion Studies — contour map of scour hole for test conducted on August 26, 1996	274
Figure G.7	Dam Foundation Erosion Studies — contour map of scour hole for test conducted on September 3, 1996	275

Figure G.8	Dam Foundation Erosion Studies — contour map of scour hole for test conducted on September 9, 1996	276
Figure G.9	Dam Foundation Erosion Studies — contour map of scour hole for test conducted on September 23, 1996	277
Figure G.10	Dam Foundation Erosion Studies — contour map of scour hole for test conducted on September 30, 1996	278
Figure G.11	Dam Foundation Erosion Studies — contour map of scour hole for test conducted on October 3, 1996	279
Figure G.12	Dam Foundation Erosion Studies — contour map of scour hole for test conducted on October 9, 1996	280
Figure G.13	Dam Foundation Erosion Studies — contour map of scour hole for test conducted on October 18, 1996	281
Figure G.14	Dam Foundation Erosion Studies — contour map of scour hole for test conducted on July 16, 1997	282
Figure G.15	Dam Foundation Erosion Studies — contour map of scour hole for test conducted on July 23, 1997	283
Figure G.16	Dam Foundation Erosion Studies — contour map of scour hole for test conducted on September 2, 1997	284
Figure G.17	Dam Foundation Erosion Studies — contour map of scour hole for test conducted on September 11, 1997	285
Figure G.18	Dam Foundation Erosion Studies — longitudinal profile of scour hole for test conducted on August 26, 1996	286
Figure G.19	Dam Foundation Erosion Studies — longitudinal profile of scour hole for test conducted on September 3, 1996	287
Figure G.20	Dam Foundation Erosion Studies — longitudinal profile of scour hole for test conducted on September 9, 1996	288
Figure G.21	Dam Foundation Erosion Studies — longitudinal profile of scour hole for test conducted on September 23, 1996	289
Figure G.22	Dam Foundation Erosion Studies — longitudinal profile of scour hole for test conducted on September 30, 1996	290
Figure G.23	Dam Foundation Erosion Studies — longitudinal profile of scour hole for test conducted on October 3, 1996	291

Figure G.24	Dam Foundation Erosion Studies — longitudinal profile of scour hole for test conducted on October 9, 1996	292
Figure G.25	Dam Foundation Erosion Studies — longitudinal profile of scour hole for test conducted on October 18, 1996	293
Figure G.26	Dam Foundation Erosion Studies — longitudinal profile of scour hole for test conducted on July 16, 1997	294
Figure G.27	Dam Foundation Erosion Studies — longitudinal profile of scour hole for test conducted on July 23, 1997	295
Figure G.28	Dam Foundation Erosion Studies — longitudinal profile of scour hole for test conducted on September 2, 1997	296
Figure G.29	Dam Foundation Erosion Studies — longitudinal profile of scour hole for test conducted on September 11, 1997	297
Figure G.30	Dam Foundation Erosion Studies — lateral profile of scour hole for test conducted on August 26, 1996	298
Figure G.31	Dam Foundation Erosion Studies — lateral profile of scour hole for test conducted on September 3, 1996	299
Figure G.32	Dam Foundation Erosion Studies — lateral profile of scour hole for test conducted on September 9, 1996	300
Figure G.33	Dam Foundation Erosion Studies — lateral profile of scour hole for test conducted on September 23, 1996	301
Figure G.34	Dam Foundation Erosion Studies — lateral profile of scour hole for test conducted on September 30, 1996	302
Figure G.35	Dam Foundation Erosion Studies — lateral profile of scour hole for test conducted on October 3, 1996	303
Figure G.36	Dam Foundation Erosion Studies — lateral profile of scour hole for test conducted on October 9, 1996	304
Figure G.37	Dam Foundation Erosion Studies — lateral profile of scour hole for test conducted on October 18, 1996	305
Figure G.38	Dam Foundation Erosion Studies — lateral profile of scour hole for test conducted on July 16, 1997	306
Figure G.39	Dam Foundation Erosion Studies — lateral profile of scour hole for test conducted on July 23, 1997	307

Figure G.40	Dam Foundation Erosion Studies — lateral profile of scour hole for test conducted on September 2, 1997	308
Figure G.41	Dam Foundation Erosion Studies — lateral profile of scour hole for test conducted on September 11, 1997	309
Figure G.42	Dam Foundation Erosion Studies — three dimensional view of scour hole for test conducted on August 26, 1996	310
Figure G.43	Dam Foundation Erosion Studies — three dimensional view of scour hole for test conducted on September 3, 1996	311
Figure G.44	Dam Foundation Erosion Studies — three dimensional view of scour hole for test conducted on September 9, 1996	312
Figure G.45	Dam Foundation Erosion Studies — three dimensional view of scour hole for test conducted on September 23, 1996	313
Figure G.46	Dam Foundation Erosion Studies — three dimensional view of scour hole for test conducted on September 30, 1996	314
Figure G.47	Dam Foundation Erosion Studies — three dimensional view of scour hole for test conducted on October 3, 1996	315
Figure G.48	Dam Foundation Erosion Studies — three dimensional view of scour hole for test conducted on October 9, 1996	316
Figure G.49	Dam Foundation Erosion Studies — three dimensional view of scour hole for test conducted on October 18, 1996	317
Figure G.50	Dam Foundation Erosion Studies — three dimensional view of scour hole for test conducted on July 16, 1997	318
Figure G.51	Dam Foundation Erosion Studies — three dimensional view of scour hole for test conducted on July 23, 1997	319
Figure G.52	Dam Foundation Erosion Studies — three dimensional view of scour hole for test conducted on September 2, 1997	320
Figure G.53	Dam Foundation Erosion Studies — three dimensional view of scour hole for test conducted on September 11, 1997	321
Figure G.54	Dam Foundation Erosion Studies — width of scour hole versus tailwater depth, 96/97	323
Figure G.55	L2 versus DFE Studies	324

Figure H.1	Dam Foundation Erosion Studies — air concentration versus depth, 07/29/97	330
Figure H.2	Dam Foundation Erosion Studies — velocities versus depth, 07/09/97	330
Figure H.3	Dam Foundation Erosion Studies — air concentration versus depth, 09/04/97	331
Figure H.4	Dam Foundation Erosion Studies — velocities versus depth, 09/04/97	331
Figure I.1	Dam Foundation Erosion Studies — piezometer readings, $Q = 1.13 \text{ m}^3/\text{s}$	338
Figure I.2	Dam Foundation Erosion Studies — piezometer readings, $Q = 1.27 \text{ m}^3/\text{s}$	338
Figure I.3	Dam Foundation Erosion Studies — piezometer readings, $Q = 1.42 \text{ m}^3/\text{s}$	339
Figure K.1	Predicted values of drawdown depth using Zahoor's equation versus measured values of drawdown depth	359

LIST OF SYMBOLS

A	area of a particle [L^2]
A_1	dimension of a parallelepiped in the direction of the flow [L]
a	a constant
B	volumetric air/water ratio in Ervine's formula
B_1	dimension of a parallelepiped perpendicular to the direction of the flow [L]
b	a constant
b'	a constant
b_1	an exponent
b_o	thickness of the jet at the section of issuance [L]
b_{gs}	virtual thickness of the jet at the ground surface [L]
b_i	thickness of the jet at the plane of impingement [L]
C	vertical dimension of a parallelepiped [L]
C_2	a constant
C_d	drag coefficient of a particle
C_l	lift coefficient of a particle
C_{diff}	coefficient of diffusion of a jet
C_{2v}	a coefficient representing the resistance of the particle in Hoffman's equation for 2 dimensional jets (2D jets)
c	a constant
D	depth of the scour hole as measured from the tailwater elevation in meters in Mason's formula [L]

D_{\max}	maximum depth of scour [L]
D_p	the diameter of the jet at impingement [L]
D_i	is the diameter of the jet at issuance [L]
$D.I.$	discharge intensity = $Q/(gD^5)^{0.5}$
d	diameter of a spherical particle having the same volume as the particle being represented [L]
d_n	nominal diameter of a particle, n indicates the percentage finer by weight [L]
d_s	depth of the scour cavity below the elevation of the initial ground level [L]
d_{sm}	maximum scour depth in Mendoza's equation for a scour hole caused by culverts [L]
d_{10}	nominal diameter for which 10% is finer by weight [L]
d_{50}	nominal diameter for which 50% is finer by weight [L]
d_{85}	nominal diameter for which 85% is finer by weight [L]
d_{90}	nominal diameter for which 90% is finer by weight [L]
d^*	dimensionless particle diameter
E	initial energy flux of a jet [ML^2T^{-2}]
E_m	energy flux of a jet at a section [ML^2T^{-2}]
e	a constant equal to 2.71828
Fr	Froude number
G	specific gravity of a particle
H	distance from nozzle to the bed [L]
ΔH	an incremental drop height or a difference in elevation between two horizontal planes [L]
H_{act}	actual (or measured) available head at the surface of impingement [L]
H_d	vertical distance from the outlet to the pool [L]

H_e	the height of fall required to achieve minimum entrainment [L]
H_{gs}	head at the centerline of the jet near the initial ground surface [L]
H_o	theoretical available head at the surface of impingement [L]
h	tailwater depth in Mason's formula [L]
h_c	upstream tailwater depth in Zahoor's formula [L]
h_o	drawdown (difference in elevation between the tailwater surface upstream of the point of impingement and the tailwater surface downstream of the point of impingement) [L]
g	gravity acceleration [LT^{-2}]
J_s	orientation factor in Annandale's approach
k_s	grain roughness height [L]
K_b	a function of particle size in Annandale's approach
K_d	interlocking factor in Annandale's approach
K_h	erodibility index
K_1	fraction of the longest axis of a particle
K_2	fraction of the shortest axis of a particle
K_3	lift coefficient to drag coefficient ratio = C_L/C_d
L_d	the disintegration length (meters) in Ervine's et al. formula [L]
M_s	mass strength number
P	power per unit area [MT^{-3}]
q	unit discharge (flow of volume per unit time per unit length) [$L^2 T^{-1}$]
Q	discharge (flow of volume per unit time) [$L^3 T^{-1}$]
R_h	hydraulic radius [L]
R_p	Reynolds number of a particle
R^2	regression coefficient

S_o	the slope of a channel
S_w	the standard deviation of fall velocity [$L T^{-1}$]
t	time [T]
T	temperature [C]
T_f	total time of a test [T]
TW	tailwater depth [L]
U	approach velocity [$L T^{-1}$]
U_a	velocity of the ascending stream [LT^{-1}]
U'	fluctuating component of the velocity at the nozzle [LT^{-1}]
u_*	shear velocity [$L T^{-1}$]
u_n	velocity of the jet at the nozzle [LT^{-1}]
V	velocity of the jet [$L T^{-1}$]
V_a T^{-1}]	velocity of the ascending stream in Mirtskhulava et al.'s equation (1967) [L
V_c	minimum velocity to entrain air [LT^{-1}]
V_i	the velocity of the jet at the tailwater surface [LT^{-1}]
V_j	the velocity at the end of the jth incremental length [LT^{-1}]
V_{j-1}	the velocity at the beginning of the jth incremental length [LT^{-1}]
V_m	the centerline velocity in the free jet region [$L T^{-1}$]
V_{mi}	maximum velocity in the impingement region [$L T^{-1}$]
V_{max}	the centerline velocity of the jet [$L T^{-1}$]
V_o	the initial velocity of the jet [$L T^{-1}$]
V_{vol}, V'	constants (in units of volume) [L^3]
V_p	velocity of a particle [$L T^{-1}$]

V_t	volume of air at the impingement section [L^3]
Vol	volume of a particle whose diameter is d_n
w	fall velocity of a particle [$L T^{-1}$]
W_m	is the geometric mean fall velocity of the bed material scoured [$L T^{-1}$]
W_n	the width of the nozzle [L]
W	the width of the basin [L]
x	the distance of the section under study from the section of issuance [L]
x_1	distance from the point of impingement to the initial ground surface [L]
x_2	distance from the point of impingement to the bottom of the scour hole [L]
X_{tb}	horizontal distance measured from the north wall of the DFE tailbox [L]
Y_{tb}	distance measured from the east wall of the DFE tailbox [L]
Z_{tb}	relative elevation measured from the reference level of the DFE tailbox [L]
Y	depth of the scour hole, measured from the initial bed level [L]
Y_t	depth of the scour hole, at a time t [L]
y_b	depth of a channel at a brink
y_c	critical depth or $(q^2/g)^{1/3}$ [L]
z [L]	difference in elevation from the section of issuance to the tailwater surface [L]
z_d	length of the ascending stream [L]

Greek symbols

α	angle of the nozzle with respect to the vertical (deg.)
β	angle of impingement with respect to the horizontal (deg.)
χ	the angle at which the centerline of a jet impinges the bed in Stein and Julien's equation
δ	angle of impingement measured from the vertical ($90 - \beta$) (deg.)

ϵ	turbulence level of the jet at issuance
ϕ	angle of repose of bed material
γ	the specific weight [$M L^{-2} T^{-2}$]
γ_s	the specific weight of a solid particle [$M L^{-2} T^{-2}$]
γ_w	the specific weight of water [$M L^{-2} T^{-2}$]
η	is a constant greater than 1 in Mirtskhulava et al. equation
μ_a	dynamic viscosity of the air [$M L^{-1} T^{-1}$]
μ_w	dynamic viscosity of water [$M L^{-1} T^{-1}$]
ν	kinematic viscosity [$L^2 T^{-1}$]
θ	downstream slope of the scour hole
ρ	density [$M L^{-3}$]
ρ_a	density of air
ρ_w	density of water
τ_o	bed shear stress [$M L^{-1} T^{-2}$]
τ_m 2]	is the maximum shear stress developed in the impingement region [$M L^{-1} T^{-2}$]
τ_*	dimensionless shear stress
τ_{*c}	critical dimensionless shear stress

CHAPTER 1

INTRODUCTION

Dams are used for creating impoundments to store large amounts of water for agricultural use, municipal consumption, recreational purposes, flood control, and power generation. In general, dams can be classified as earth dams and concrete dams. In order to design safe dams, spillways are built to convey the excess volumes of water during large floods. Spillways are large chutes (steep canals) built in various forms. They allow the safe passage of flood waters from the reservoir to a point located downstream of the dam. Hydrological data have been gathered systematically near dam sites. Recent studies indicate that large flood events might have been underestimated. Larger floods than expected might occur at the dam sites. The capacity of the spillways and auxiliary outlet structures could be exceeded and dams might be overtopped. If a concrete dam is overtopped, a jet is formed that could cause excessive scour downstream of the dam as seen in Figure 1.1. The stability of the dam foundation might also be compromised due to erosion occurring at its base. Undermining of the bed could lead to the collapse of the dam.

When a dam collapses, the sudden release of large volumes of water usually produces severe damage downstream of the dam, destroying the infrastructure of the area and occasionally causing the loss of human lives. Given the rapid nature of the event people usually are not given adequate warning of the flood induced by the collapse of the

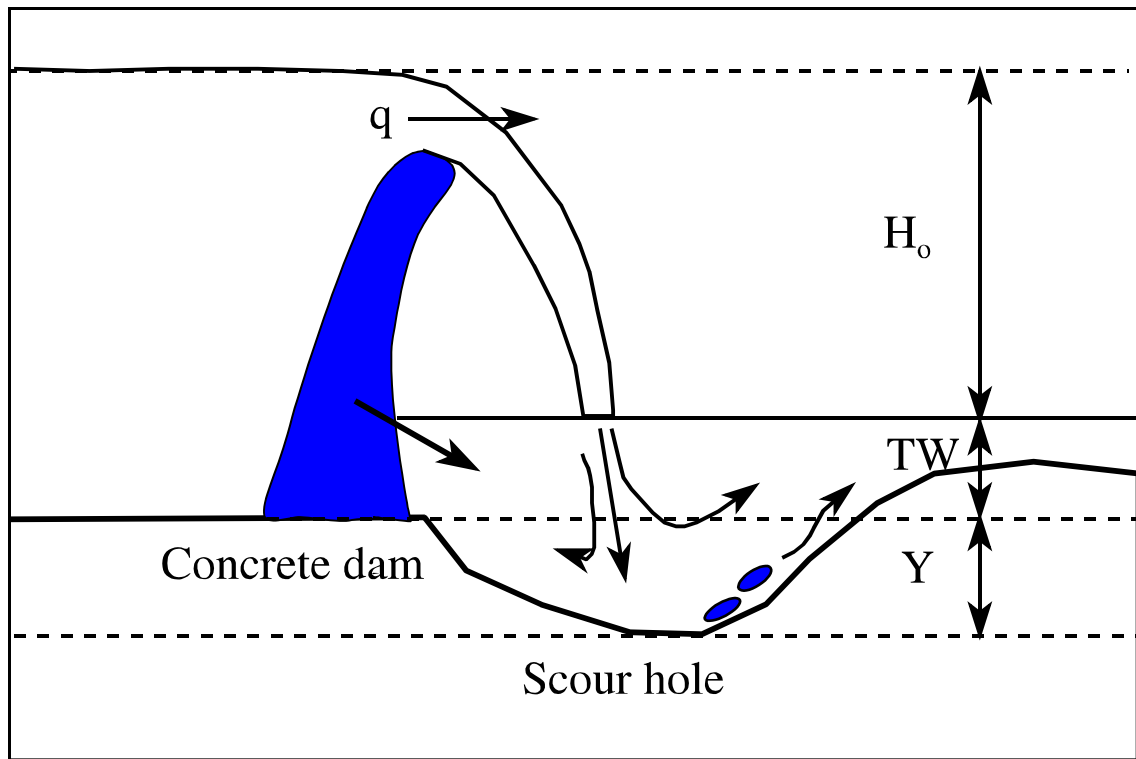


Figure 1.1. Potential problem induced by dam foundation erosion.

dam. Modification of the physical characteristics of the environment could also permanently destroy the habitat of regional species. Excessive erosion downstream of the dam could permanently alter the characteristics of the channel, and destroy structures that are beneficial to the people living downstream of the dam site. Overtopping can potentially be avoided by upgrading the spillway capacity or by removing the dam. The first option can be very costly, and the second option is undesirable because economic activities downstream of reservoirs already depend on their operation. A third option is to allow overtopping of dams during large floods. Due to the possible hazards cited earlier, dam safety regulations require reasonable evidence that overtopping will not result in destabilization of the dam due to erosion in the foundation and abutment areas.

Consequently, it is necessary to predict, with reasonable accuracy, the maximum depth of scour at the foundation produced by dam at the foundation.

Research has been conducted systematically during the last sixty years to investigate the velocity field of the jets, pressures and shear stresses developed along a surface being impinged by a jet, and the mechanics of jet erosion. Different types of jets have been studied and include submerged jets and impinging jets, as well as circular jets and rectangular jets. In most cases, small-scale models were used to observe the velocity distribution within the jet; to measure pressures and shear stresses in the vicinity of a non-eroding surface such as a flat plate; or to find a relation between the maximum depth of the scour hole, tailwater depth, bed material, unit discharge, and available head. One limitation of small-scale models is the fact that geometric characteristics of the resulting scour hole and the resulting mound cannot be observed in detail. Also, constraints related to the width of the canal downstream of the zone of impingement might significantly affect the results, because a narrow canal would force the streamlines of the resulting flow to be straightened.

Differences in bed material behavior during the scour process have been assessed by several researchers. Forces resisting removal are mostly gravitational in cohesionless soils, whereas electrochemical forces are expected to play a major role in cohesive soils. This study is limited to the study of cohesionless materials. Also, fundamental differences exist between scour produced by freely-falling impinging jets, semi-submerged jets and submerged jets. Free falling is defined as jets whose section of issuance is located above the tailwater surface. Submerged jets are issued below the water surface. The section of issuance of semi-submerged jets is partially obstructed by the tailwater.

The focus of this dissertation is to investigate scour produced by freely-falling jets on cohesionless beds and simulated fractured rocks. The experimental phase of this study was conducted in a large facility, to allow visualization of flow patterns and the geometric characteristics of the scour hole. Also, attempts were made to measure velocities and air concentration in the zone of impingement.

This dissertation is limited to the study of scour produced by free falling jets. The objectives of this study are:

- To develop a method to predict the dimensions of the scour hole produced by jet downstream of dams in a form that can be used by practicing engineers and to address the limitations of this method.
- To study the influence of the angle of issuance of the jet and the tailwater depth on the maximum dimensions of the scour hole.
- To observe other processes that influence the formation of the scour hole and to address their importance in the development of the scour hole.

1.1 Organization of This Investigation

A comprehensive literature review was conducted. This study is limited to investigating the scour produced by impinging jets in cohesionless materials and pertinent investigations are included in Chapter 2. Investigations associated with general scour concepts are included as well. Studies related to pressures produced at the bottom of a plunge pool and concepts of jet diffusion are also summarized in Chapter 2.

The development of equations to calculate the maximum depth of scour produced by impinging rectangular jets is described in Chapter 3. Jets are assumed to be compact.

If sufficient data are available, correction factors will be used if major differences exist between compact jets and highly aerated jets.

The facilities, equipment, materials and procedures used in this study are described in Chapter 4. Chapter 5 summarizes the observations made during the experimental phase of this study.

Data collected in this study are analyzed in Chapter 6, and the results of this investigation are compared with data from other authors. Data availability and the range of the variables of interest were taken into account to generate a more diverse database. In many cases, data were incomplete. The variables of interest in this study were not gathered by researchers who conducted experiments performed with the same conditions under which this study was conducted. Therefore, data from many experiments were not included in the analysis.

Chapter 7 summarizes the observations and the results of data analysis. Recommendations have also been given for conducting future tests that are believed to provide better understanding of the phenomenon of jet scour. Other pertinent information is also included in the Appendices.

CHAPTER 2

LITERATURE REVIEW

2.1 General

A comprehensive literature review was conducted. Papers including information related to jet diffusion, jet development, pressure fluctuations due to impinging jets, and scour holes produced by impinging jets in cohesionless materials were reviewed in this study. Past research efforts to predict the velocities of the jet, to describe the process of disintegration of the jet, and to predict air entrainment are summarized in Section 2.2. Tailwater has cushioning effects because the dynamic pressure at the bottom of a pool being impinged by a jet decreases as the tailwater increases. The velocity of the centerline of the jet is expected to decrease as energy is transferred to the surrounding fluid by shear stresses. If the velocity of the jet decreases, less energy is available to move material from the bottom of the scour hole. Section 2.3 describes the studies conducted to predict impact pressures in a flat plate with or without a water cushion. The main goal of this project is to predict the depth of the scour hole in an erodible bed. However, the studies reviewed in Section 2.3 can provide information about the forces that act on the bottom of a scour hole. The first part of Section 2.4 includes general concepts related to scour and the second part summarizes studies directly related to scour holes produced by impinging jets in loose

cohesionless materials. Information about scour produced in rock strata by impinging jets has been compiled in Section 2.5.

2.2 Jet Diffusion

Tollmien (Rajaratnam, 1976) used the integral momentum equation, the integral energy equation, and Prandtl's mixing length formula for deriving a formula that describes the velocity distribution of a plane turbulent jet. A non-linear second-order ordinary differential equation was obtained and solved numerically for velocities. Results were presented in graphical form. Using the Pi-theorem and conservation of moment principle along the jet, the following equation was proposed:

$$\frac{V_m}{V_o} = \frac{C_1}{\sqrt{\frac{x}{b_o}}} \quad (2.1)$$

where: V_m = the velocity of the centerline of the jet;

V_o = the average velocity at the issuance point;

C_1 = a constant;

x = the distance from the issuance point; and

b_o = the width of the jet at issuance.

Data taken by Fortier (Rajaratnam, 1976) confirmed that such a relationship could be used for describing the velocity of the centerline of the jet.

Albertson et al. (1950) studied the behavior of submerged jets in both air and water. Tests were conducted using circular and rectangular nozzles. They found that two distinct zones exist downstream of the section of issuance. As the jet exits the nozzle, the

momentum is transferred to the surrounding fluid, inducing movement. The velocity is essentially the same across the issuance section. The jet retains the centerline velocity in the zone of flow establishment, and velocity diminishes along the edges of the jet until it reaches the centerline. The flow is established where the centerline velocity starts diminishing. This section separated the zones of flow establishment from the zone of established flow (Figure 2.1).

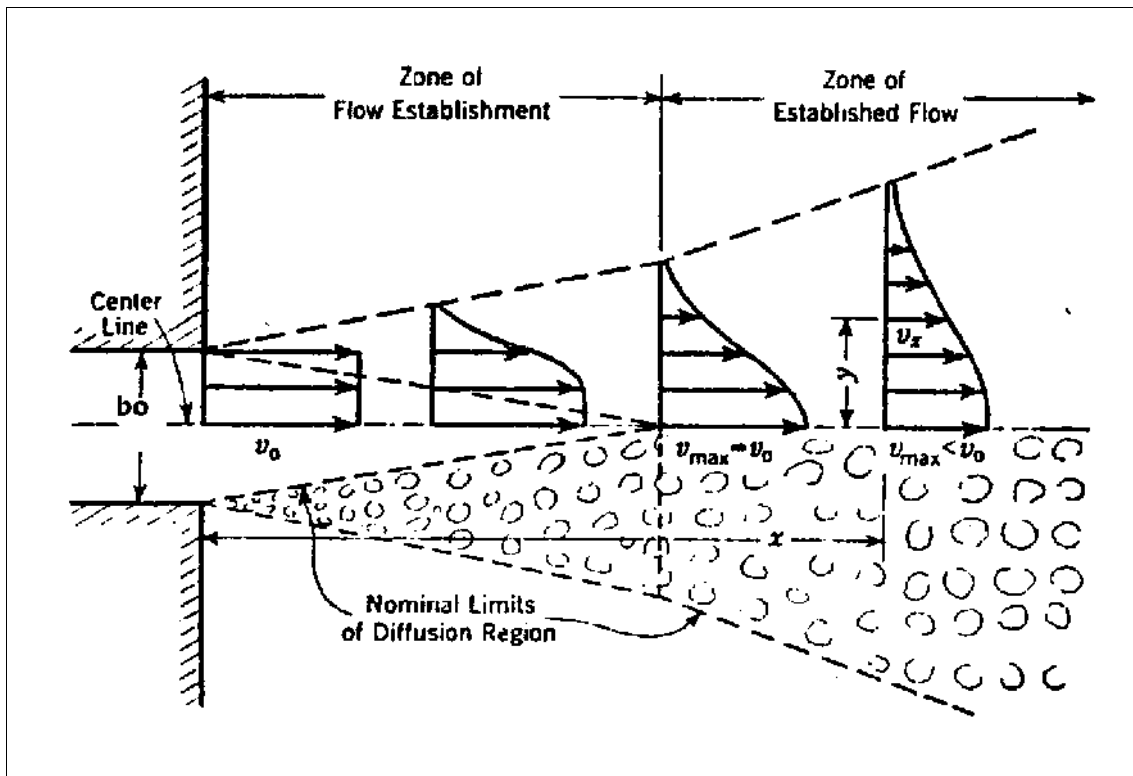


Figure 2.1. Zones of flow establishment and zone of established flow (Albertson et al., 1950).

Characteristics of the flow through the zone of influence of the impinging jet were described by means of mathematical equations. Velocity, discharge, and energy flux were expressed as a function of the distance x from the nozzle, and the characteristic length of

the nozzle, D. For the zone of established flow, the following equations were formulated for “circular” jets:

$$\frac{V_m}{V_o} = C_{diff} \frac{D_i}{x} \quad (2.2)$$

$$\frac{Q_m}{Q} = 0.32 \frac{x}{D_i} \quad (2.3)$$

$$\frac{E_m}{E} = 4.10 \frac{D_i}{x} \quad (2.4)$$

where: V_o = the exit velocity;

V_m = the centerline jet velocity at any section in the downstream direction;

C_{diff} = the jet diffusion coefficient equal to 6.2;

D_i = the pipe diameter;

x = the coordinate in the direction of the flow;

Q = the initial flow rate;

Q_m = the flow rate at any section;

E = the initial energy flux; and

E_m = the energy flux at any section.

Jet flow from slots was also studied. The following expressions were proposed:

$$\frac{V_{max}}{V_o} \sqrt{\frac{x}{b_o}} = 2.28 \quad (2.5)$$

where: V_{max} = the centerline velocity of the jet;

V_o = the initial velocity of the jet;

b_o = the width of the slot; and

x = the distance of the section under study from the section of issuance.

Hom-ma (1953) found that there are not distinct zones, such as the ones observed in submerged jets, for jets issued from a point located above the water surface. Once the jet enters the water, the centerline velocity is reduced exponentially in contrast to linearly for a submerged jet. Reynolds numbers were calculated using the velocity at the nozzle, and the characteristic length is the diameter of the pipe. Kinematic viscosity was calculated using the temperature of the water at which the tests were conducted. The following relationships were developed for a circular falling jet to predict the centerline velocity, V_m , at a distance x from the centerline of the nozzle exit section:

$$\frac{V_m}{V_p} = 1.24e^{-0.109(x/D_p)} \quad (2.6)$$

for $Re < 25,000$ and

$$\frac{V_m}{V_p} = 1.24e^{-0.137(x/D_p)} \quad (2.7)$$

for $Re > 30,000$

where: V_p = the penetration velocity, the jet velocity as it enters the water; and

D_p = the penetration diameter.

For a jet penetrating the water cushion at a 60° inclination the following relationship was developed:

$$\frac{V_m}{V_p} = 1.24 e^{-0.024(x/D_p)} \quad (2.8)$$

Hom-ma did not explain the cause of the difference in the velocity distribution due to a difference in Reynolds numbers. A general equation for describing the velocity field for different Reynolds numbers was not provided.

Beltaos and Rajaratnam (1974) studied air jets impinging on a wall. They found that three regions exist for jets impinging against a solid surface. One region, in which the jet behaves as if the solid boundary does not exist. A second region is the impingement region where the jet undergoes considerable deflection. They found that the impingement region in the vicinity of a wall began where $x/H > 0.86$, where H is the distance from the nozzle to the wall and x is the distance measured from the nozzle along the centerline of the jet (Figure 2.2). The jet is parallel to the wall in the third region. The following relationships were proposed for a circular impinging jet:

$$\frac{V_{mi}}{V_m} = 3.1 \frac{x}{H} (1 - x/H)^{1/2} \quad (2.9)$$

$$\tau_m = 0.166 \frac{\rho V_o^2}{(H/D_i)^2} \quad (2.10)$$

where: V_m = the centerline velocity in the free jet region;

V_{mi} = the maximum velocity in the impingement region;

D_i = the jet diameter at the section of issuance;

H = the distance from nozzle to the bed;

τ_m = the maximum shear stress developed in the impingement region; and

V_o = the velocity of the jet at the nozzle.

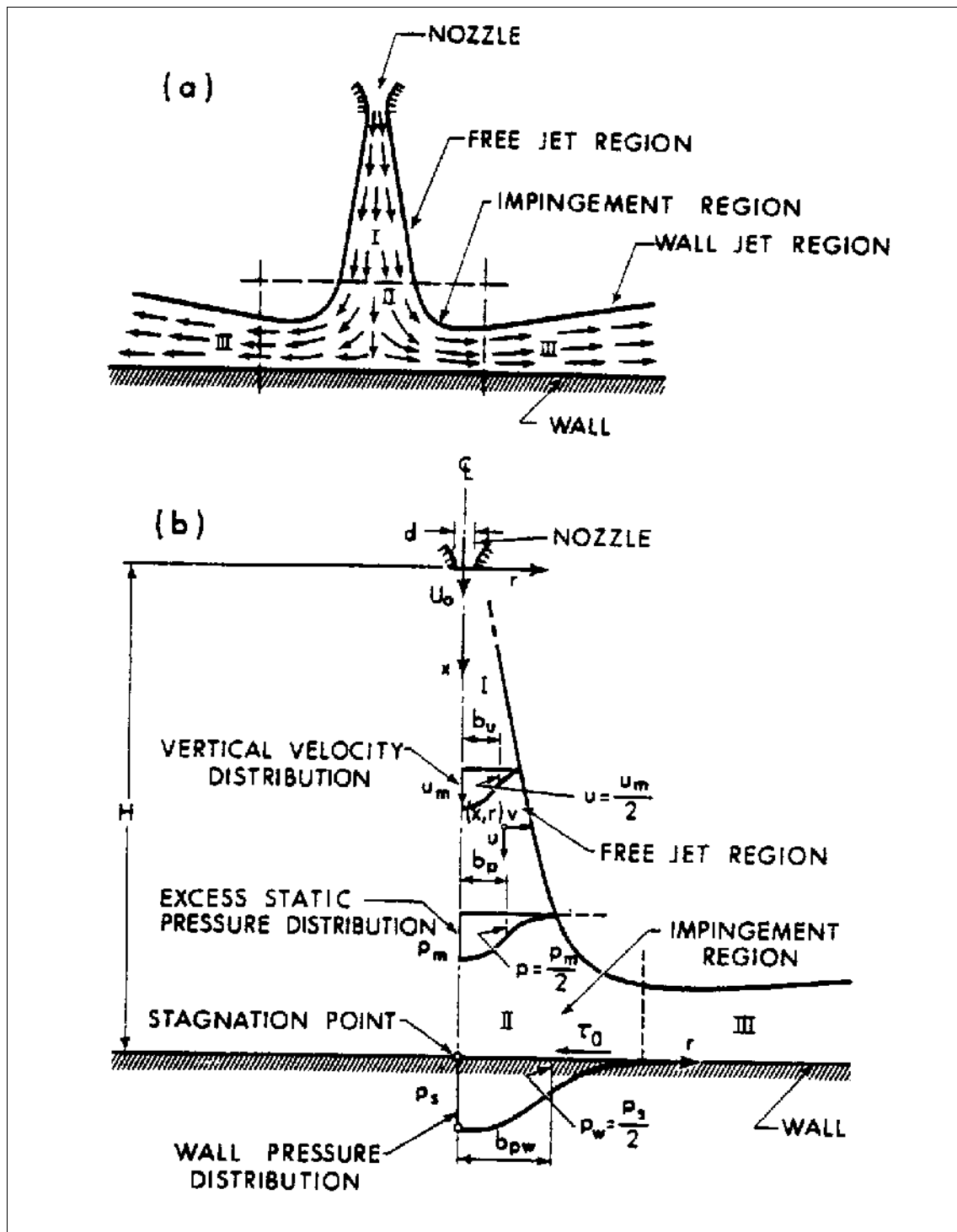


Figure 2.2. Jet velocity and shear stress distribution near a wall (Beltaos and Rajaratnam, 1974).

Beltaos (1976) studied the shear stress distribution of plates being impinged by jets. He found that the maximum shear stress was not a function of the angle of impingement. However, the position where the maximum shear stress was recorded was a function of the angle of impingement of the jet.

Kawakami (Novak, 1984) presented results of field investigations of jet trajectories for ski-jump spillways and introduced a coefficient of air resistance for the trajectory equations. The effect of air resistance was small when the initial velocity of the jet was less than 20 m/s. Factors such as the thickness and the shape of the jet seemed to be of primary importance, because the jet is broken into droplets by entrained air.

McKeogh and Elsayy (1980) studied circular jets and defined four mechanisms of aeration (Figure 2.3):

- a. Annular oscillations: in which the jet is laminar and causes a depression of the meniscus.
- b. Intermittent vortex - transition between laminar and turbulent. Inward flow in the vicinity of the interface.
- c. Turbulent occlusion: in which the indentation of the surface becomes highly irregular.
- d. Droplet entrainment: in this case, the jet disintegrates in the area of impingement and discrete drops entrain air upon impact in the pool.

They also found that the velocity at which the impinging jet causes air entrainment depends on the turbulence level of the jet, ϵ , and obtained expressions for calculating the amount of air retained in pools by plunging water jets:

$$\epsilon = \sqrt{u'/u_n} \times 100\% \quad (2.11)$$

where: u_n = the velocity at the nozzle; and

u' = the fluctuating velocity component.

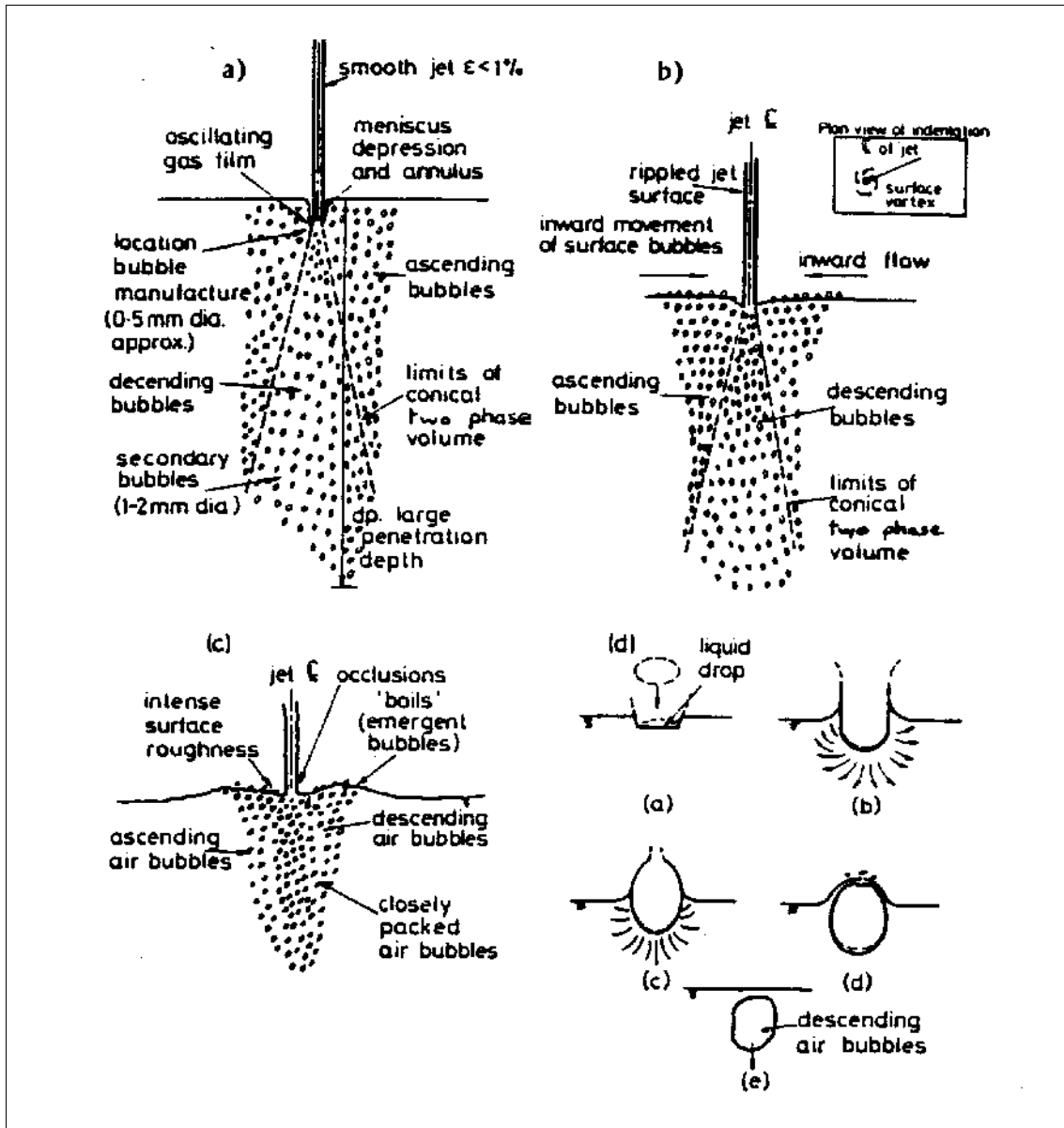


Figure 2.3. Mechanisms of jet impingement (McKeogh and Elsaywy, 1980).

The turbulent intensity at the point of issuance was measured using a transducer probe.

McKeogh and Elsaywy also defined a “disintegration length,” which is a length at which the jet becomes discrete particles. Disintegration length was a function of the water discharge and the turbulence intensity. Air content was measured at different depths within the aerated region, and a photographic method was used for recording data. The turbulence level of the jet was found to play a major role in the degree of air entrainment. It was shown that the volume of air V_t was:

$$V_t = 0.88V' \left(\frac{z}{L_d} \right)^{0.85} + V_{vol} \quad (2.12)$$

for turbulence levels, ϵ , (or $\epsilon = 5\%$) and

$$V_t = 0.9V' \left(\frac{z - H_e}{L_d} \right)^{0.87} + V_{vol} \quad (2.13)$$

for turbulence levels, ϵ , (or $\epsilon = 1\%$)

where: z = the height of falls (meters);

H_e = the height of fall required to achieve minimum entrainment;

L_d = the disintegration length (meters); and

V_{vol}, V' = are constants (in units of volume).

Leutheusser and Birk (1990) pointed out that four situations could occur near the zone of impingement of a jet being released by a weir as seen in Figure 2.4. When the tailwater depth is very low, the hydraulic jump is formed at a considerable distance

downstream of the point of impact. With increasing tailwater depth, the swept-out hydraulic jump is pushed upstream until it reaches its optimum location, immediately downstream of the point of impact. Further increase in tailwater depth pushes the jump against the weir and the nappe plunges. The jump becomes submerged and a strong rotating current is formed below the surface, downstream of the nappe. When the weir becomes immersed, the nappe stays at the surface and the jump is wiped out. Standing waves are formed downstream of the weir.

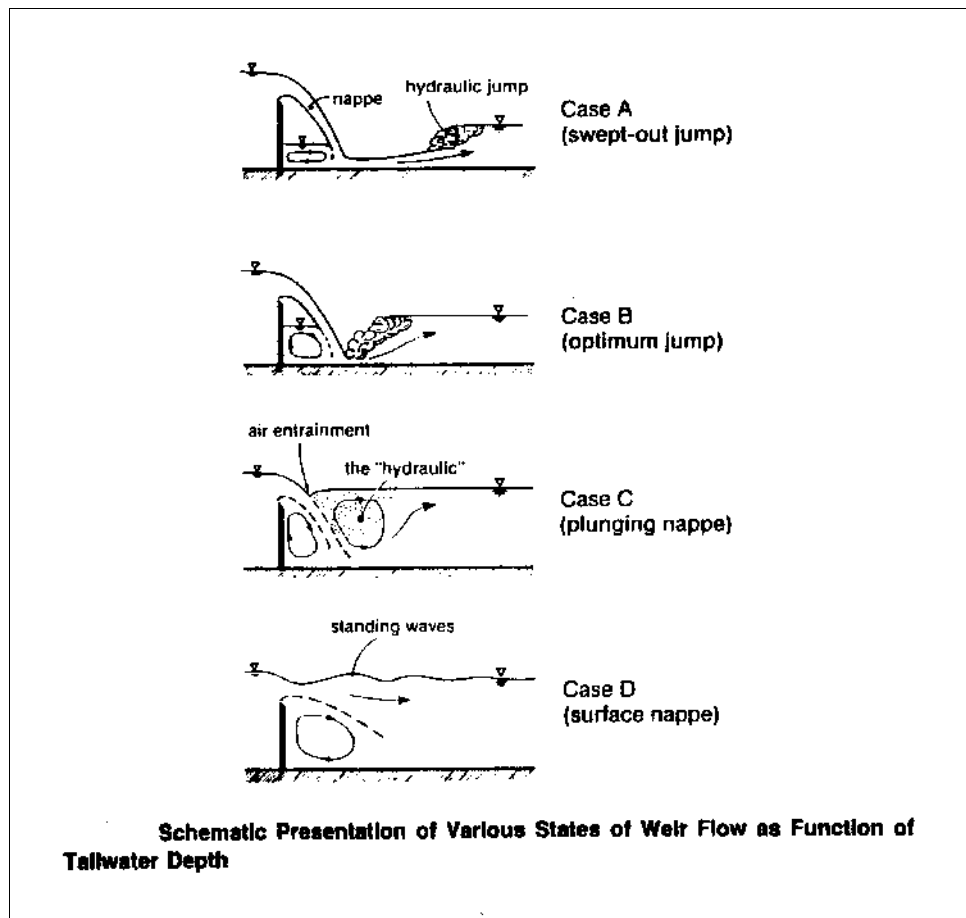


Figure 2.4. Conditions of flow downstream of a weir (Leutheusser and Birk, 1990).

Zahoor (1992) studied energy dissipation within a flip bucket stilling basin. A model of a flip bucket stilling basin was constructed in a laboratory flume. The experimental setup consisted of a spillway chute, a circular toe curve from chute to flip bucket, a flip bucket, a plunge pool basin, and an exit channel. The principles of energy conservation and momentum conservation were used to develop an expression to calculate the drawdown upstream of the zone of impact. Experimental data were used to validate the expression. The performance of different energy dissipation basins was evaluated for different conditions. Design criteria for optimal performance were presented in graphical form and as equations.

Lewis (1996) developed an equation to predict the impact velocity of a free-falling developed jet. A model test facility consisted of a sidewall orifice assembly. The angle of issuance with respect to the vertical, α , was varied from 0 to 30 degrees in 15-degree increments. He found that aerodynamic drag was a significant decelerating force on the developed jet in the atmosphere due to the absence of a solid core. The developed jet was assumed to be comprised of discrete, uniform water droplets. The following expression was proposed:

$$V_i = \sqrt{V_o^2 + 2gH_d \sec(\alpha)} - \sqrt{3C_d \left(\frac{\rho_a}{\rho_w} \right) \left(\frac{H_d \sec(\alpha)}{d} \right) V_o^2} \quad (2.14)$$

where: V_i = the impact velocity of the jet;

V_o = the initial velocity of the jet;

g = the gravity acceleration;

H_d = the vertical distance from the outlet to the surface of the pool;

α = the angle of issuance of the jet with respect to the vertical;

C_d = the drag coefficient of the drop;

ρ_a = the air density;

ρ_w = the water density; and

d = the diameter of a sphere having the same volume as a water drop.

Using sprinkler irrigation theory, the size of the drop is 6 mm. Also, Lewis recommended use of $C_d = 0.49$ and $\rho_a/\rho_w = 0.00112$.

Bohrer and Abt (1996) developed the following expression for impact velocity based on dimensional analysis and additional tests conducted in the same facility used by Lewis:

$$V_i = \sqrt{V_o^2 + 2gH} - 3C_d \left(\frac{\rho_a}{\rho_w} \right) \left(\frac{H}{d} \right) V_o \quad (2.15)$$

An iterative procedure was proposed, based on the fact that drag effects change as the developed jet velocity changes. The proposed iterative technique was expressed as:

$$V_j = \sqrt{V_{j-1}^2 + 2g \Delta H} - 3 C_d \left(\frac{\rho_a}{\rho_w} \right) \left(\frac{\Delta H}{d} \right) V_{avg_j} \quad (2.16)$$

$$V_{avg_j} = \frac{(V_{j-1} + \sqrt{V_{j-1}^2 + 2g\Delta H})}{2} \quad \text{for } j = 1, 2, \dots, \frac{H}{\Delta H} \quad (2.17)$$

$$V_i = V_{\frac{H}{\Delta H}} - C_i \quad (2.18)$$

where: ΔH = the incremental length of the drop height;

V_j = the velocity at the end of the j th incremental length;

V_{j-1} = the velocity at the beginning of the j th incremental length;

V_{ave_j} = the estimated average velocity using the beginning and end velocities of the j th incremental length;

$V_{H/\Delta H}$ = the velocity at the end of the $H/\Delta H$ th incremental length; and

C_i = the impact velocity constant = 0.5 m/s.

The iterative technique was validated for drop heights of 0.94 m to 1.88 m and issuance velocities of 2.63 m/s to 5.25 m/s. The angle of issuance remained constant at 18 degrees departure from vertical.

Bohrer and Abt (1996) also studied velocity decay in the plunge pool. They considered three types of rectangular jets: a highly turbulent, fully air entrained, highly dispersed jet (fully developed jet); a highly turbulent, fully air entrained, refined jet (developed jet); and a highly turbulent, non-air entrained jet (undeveloped jet). Drop heights were varied between 0.94 m and 1.78 m and jet issuance velocities ranged from 3.04 m/s to 5.55 m/s. Velocity at a certain depth L below the water surface was found to be a function of the average density of an air entrained jet at impact with the water surface, ρ_i . The following expression was proposed for a fully developed jet:

$$-\ln\left(\frac{V}{V_i}\right) = -0.5812 \ln\left[\left(\frac{\rho_i}{\rho_w}\right) \left(\frac{V_i^2}{gL}\right)\right] + 2.107 \quad (2.19)$$

The above expression is valid for values of $\ln[(\rho_i/\rho_w)(V_i^2/(gL))]$ ranging from -0.29 to 2.6.

A similar expression was presented for developed jets:

$$-\ln\left(\frac{V}{V_i}\right) = -0.6381 \ln\left[\left(\frac{\rho_i}{\rho_w}\right) \left(\frac{V_i^2}{gL}\right)\right] + 1.848 \quad (2.20)$$

The above expression is valid for the range $-0.42 < \ln[(\rho_i/\rho_w)(V_i^2/(gL))] < 2.05$.

A third expression was given for an undeveloped jet:

$$\left(\frac{V}{V_i}\right) = 0.0675 \left[\left(\frac{\rho_i}{\rho_w}\right) \left(\frac{V_i^2}{gL}\right)\right] + 0.1903 \quad (2.21)$$

This expression was found to be valid for values of $[(\rho_i/\rho_w)(V_i^2/(gL))]$ ranging from 0.51 to 5.76. Both in Lewis' thesis and in Bohrer and Abt's report it was recommended to improve the accuracy of velocity measuring devices, because the variability of the velocity measurements was relatively high. Bohrer and Abt also developed a method to predict the air concentration at impact for an impinging jet. If the turbulence intensity is relatively constant, the air concentration can be described as a function of the following parameter, which is a modified Froude number:

$$\text{Parameter} = \frac{V_o^2}{g \left[\frac{A}{H}\right]} \quad (2.22)$$

where: V_o = the issuance velocity of the jet;

g = the gravity acceleration;

A = the area of the jet; and

H = the height of the fall.

The impact air concentration for the fully developed jet was:

$$\text{Impact Air Concentration} = 12.286 \ln \left[\frac{V_o^2 H}{g A} \right] + 17.535 \quad (2.23)$$

and, for the developed jet, the following expression was presented:

$$\text{Impact Air Concentration} = 9.4679 \ln \left[\frac{V_o^2 H}{g A} \right] + 39.278 \quad (2.24)$$

Hamilton and Abt (1997) conducted a series of experiments to determine circulation patterns in a plunge pool, measuring velocities with an acoustic doppler velocimeter. The flow pattern produced by the developed free-falling jet indicated that flow circulates upstream of the jet impact region on the surface, vertically down into the plunge pool at the back wall, downstream along the floor, and out of the basin. Also, when the basin width was reduced, an increase in the velocity vectors was noticed. Velocities were a function of the width of the basin, water depth in the roller region, adjusted air concentration, and impact velocity.

Rajaratnam and Albers (1998) studied the spatial distribution of water in high velocity water jets. They tested jets with diameters of 2, 2.5, and 3 mm. Velocities ranged from 85 to 155 m/s and they diffused like submerged jets. They found that three regions exist in free-falling jets. An inner region carries most of the flow. Water drops are visible in an intermediate region. Water is carried as a fine mist in the outer region. The relative momentum flux carried by the water phase of the jet decreased as it traveled away from the nozzle.

2.3 Pressure Fluctuations

Lencastre (1961) studied pressure fluctuations produced by impinging jets on fixed flat bottoms. The water jet was released through a slot. The jet impinged against a smooth, flat plate. At first, the tailwater depth was zero, and pressure heads at the plate were recorded. The tailwater depth was increased and pressure heads were measured at various points along the centerline of the tailbox. The unit discharge was held constant for each data set. A comparison was made between the excess heads obtained with no tailwater depth and the excess head with various tailwater depths. Results were presented in graphical form as seen in Figure 2.5 and Figure 2.6. The ratio of excess head at the plate to the initial excess head at the tailwater surface (H_{gs}/H_{act}), was plotted against the ratio tailwater depth to thickness of jet at impingement (TW/b_i). Pressure decreased rapidly from the center of the jet at impact toward the sides for low values of tailwater depth. The pressure gradient from the centerline to the sides was much less pronounced for deeper tailwater depths. Also, pressure fluctuations were much more pronounced (between zero and 2.8 times the mean pressure) when the tailwater depths were shallow. Deep water cushions attenuated the fluctuations in pressure. In addition, attempts to measure the influence of the air in the dissipation of the energy of the jet were made. Velocities were measured along the centerline of vertical jets at different positions using Pitot tubes. The square of the average velocity of the jet at a distance z , V_z^2 , was compared to the square of the theoretical average velocity, $V_o^2 + 2gz$ for every position in which measurements were taken. The distance traveled by the jet was expressed as the ratio of the fall height, z , to the thickness of the jet b_o . The lowest measured value of $V_z^2/(V_o^2 + 2gz)$ was approximately 0.5 when the ratio z/b_o was near 15.2.

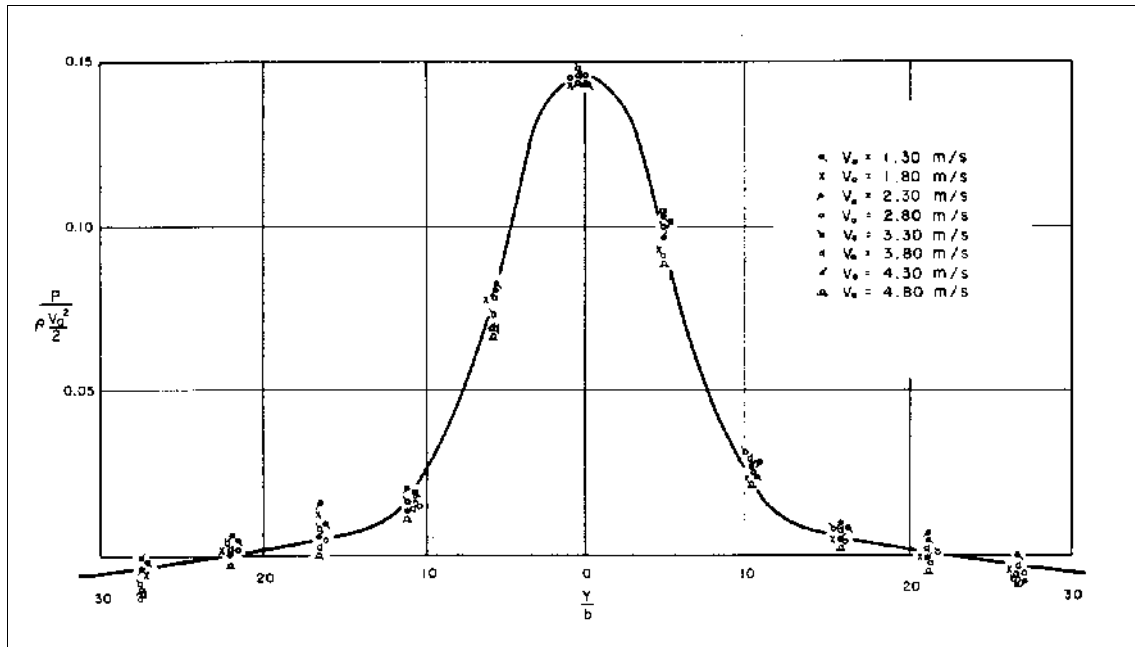


Figure 2.5. Pressure distribution across a plate being impinged by a jet.

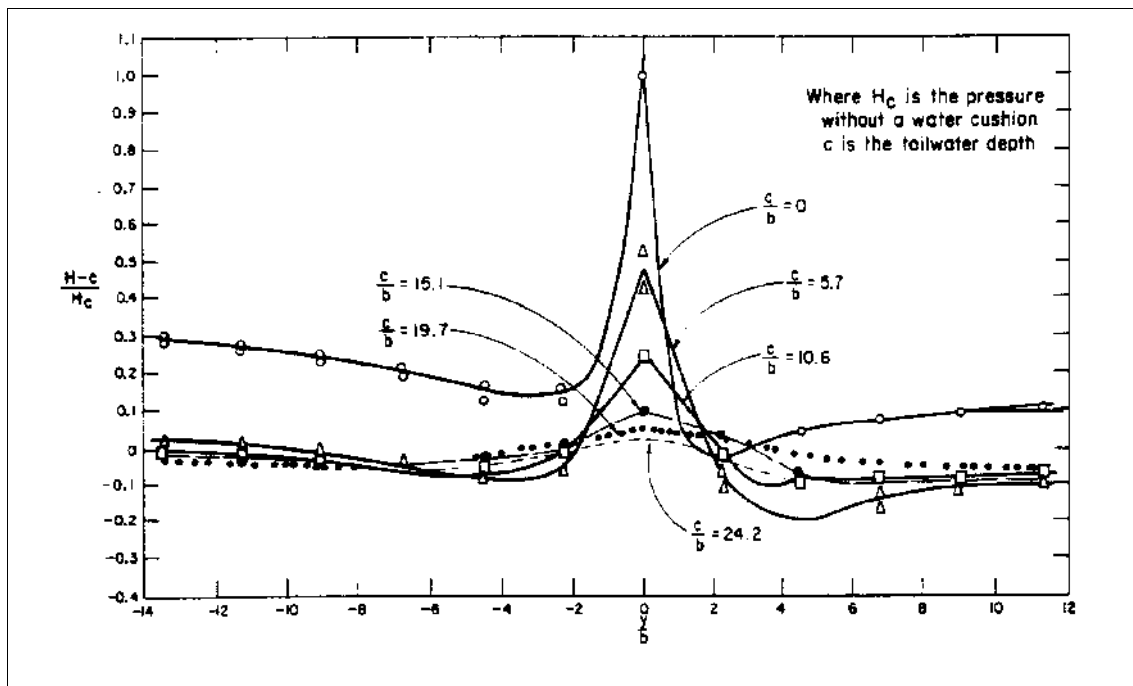


Figure 2.6. Pressure dissipation with increase in tailwater depth (Lencastre, 1961) .

George (1980) summarized eight reports on pressures caused by impinging jets on flat plates and condensed the information available at the time the report was written. Several factors pertaining to the pressure in the solid bottom of a plunge pool were addressed. For water depths lower than eight times the tailwater depth, the maximum pressure at the bottom was the same as without the water cushion.

Ervine et al. (1997) accounted for the process of jet disintegration for calculating pressure fluctuations in the floor of a plunge pool. They reported that three different zones had been identified in a jet as seen in Figure 2.7. In the upstream section three sub-zones are defined. In Zone A, near the section of issuance, the jet is "glossy," showing minor disturbances. Formation of waves takes place downstream of the glass-like sub-zone and regularly spaced waves appear. In the next sub-zone, surface waves become circumferential vortex elements. In Zone B, the circumferential vortices break. Within the jet, a "solid core" where air entrainment has not taken place is defined. Disturbances grow in the downstream direction randomly, penetrating the jet, so that the solid core section is reduced until the jet becomes discrete droplets. The distance between the section of issuance and the section where the jet does not have a solid core is defined as the breakup length. Downstream of the breakup length a third zone is defined as Zone C in Figure 2.7.

The mean dynamic pressure coefficient on the floor of the pool was a function of the ratio of pool depth to minimum depth thickness and the ratio length of the jet at impingement to the breakup length. Results were presented both in graphical form and as mathematical equations. Disintegration of jets also affects pressures caused by rectangular jets at the bottom of plunge pools, as can be seen in Figure 2.8.

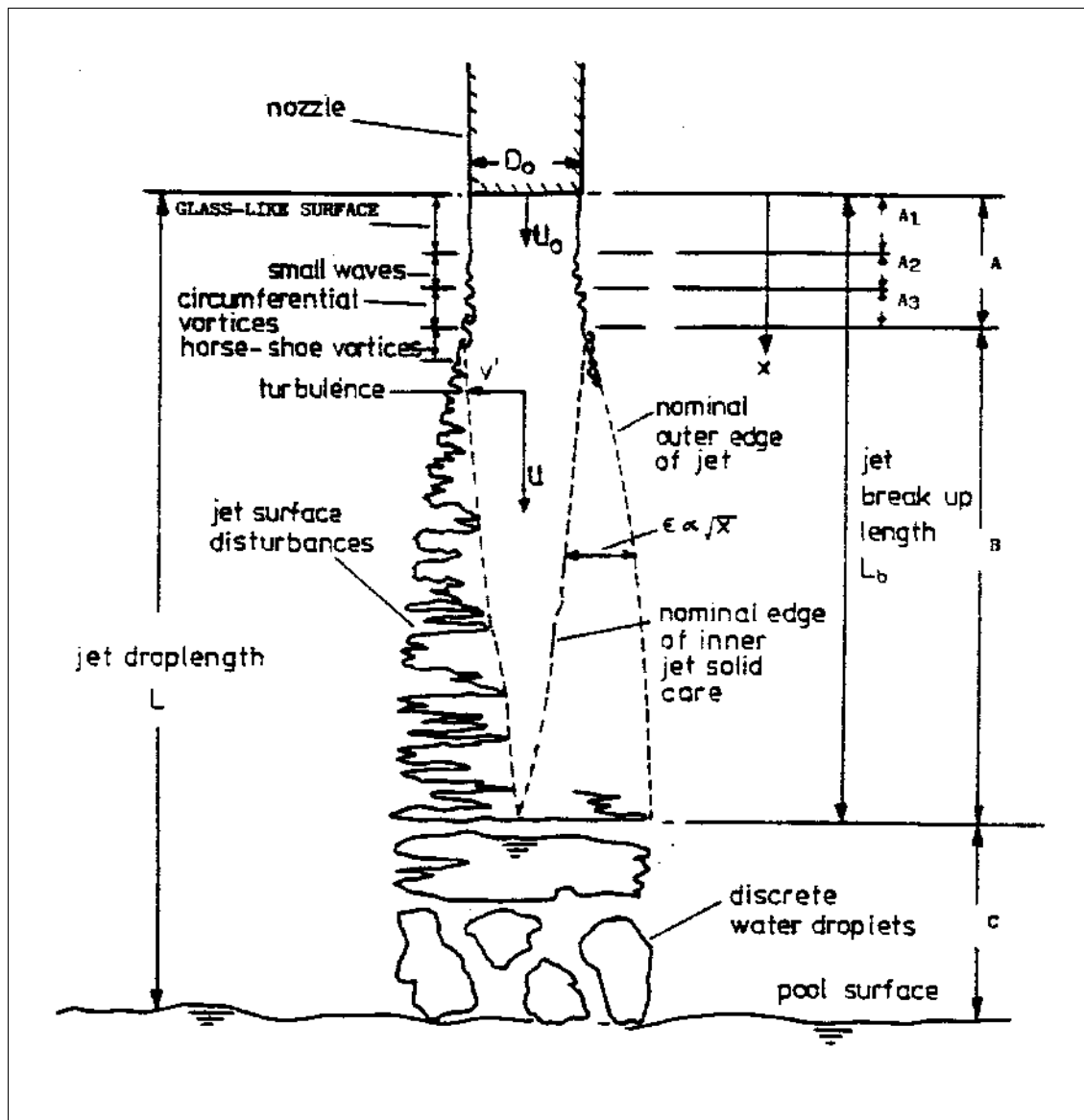


Figure 2.7. Definitions of zones in an impinging jet (Ervin et al., 1997).

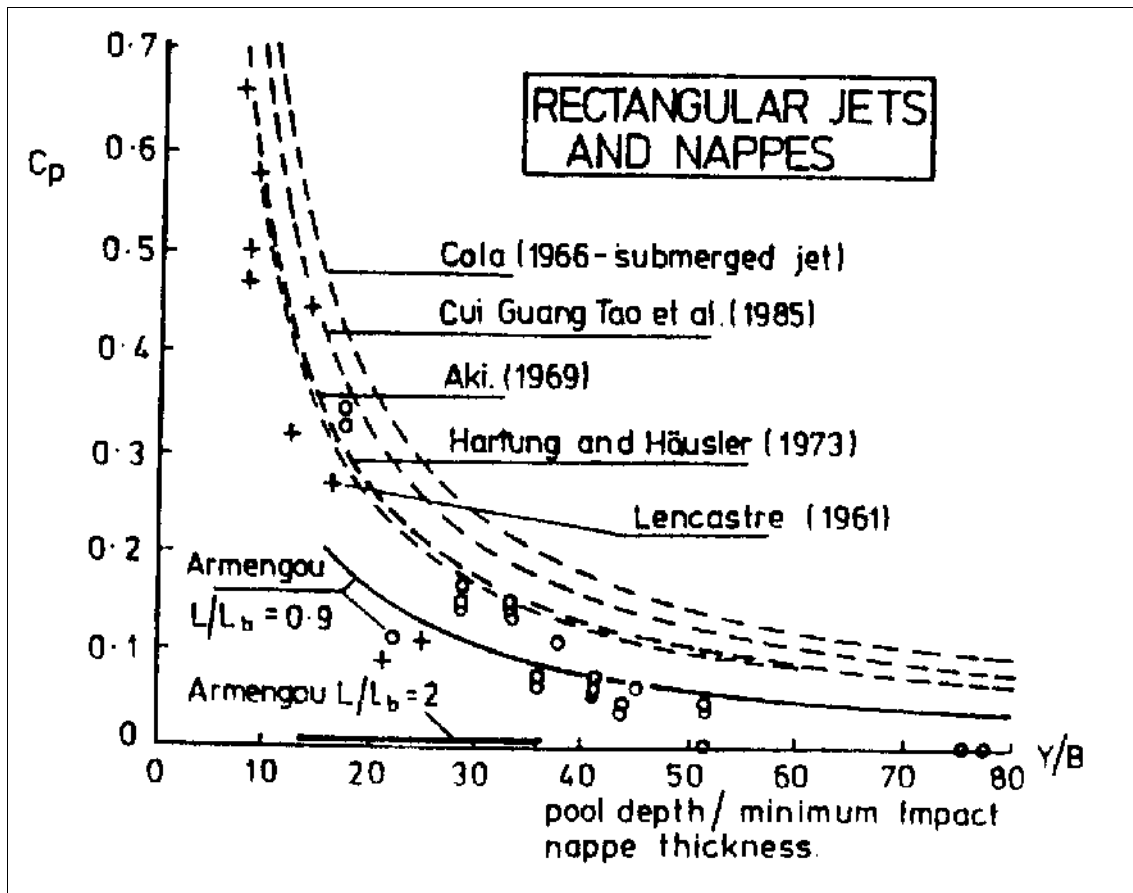


Figure 2.8. Pressure coefficients versus pool depth/impact diameter ratio.

2.4 Scour Caused by Impinging Jets in Cohesionless Materials

2.4.1 General concepts related to scour

2.4.1.1 Flow over smooth surfaces

Considering the non-slip condition at a solid boundary, the velocity of a fluid in the vicinity of a bed decreases and the viscous acceleration terms are greater than the viscous acceleration terms. A thin viscous sublayer is formed if its thickness is several times greater than the grain thickness.

2.4.1.2 Flow over rough surfaces

Consider a wide canal flowing with depth h_c . The characteristic particle size is d_n . The relative submergence (h_c/d_n) of a canal has a substantial effect on its velocity distribution (Julien, 1995). The roughness of the bed can be expressed as:

$$k_s = 3 d_{90} \quad (2.25)$$

Therefore, the Chezy coefficient is expressed as follows:

$$C' = \sqrt{\frac{8g}{f'}} = \frac{2.3}{\kappa} \sqrt{g} \log\left(\frac{12.2 R_h}{3 d_{90}}\right) = 5.75\sqrt{g} \log\left(\frac{4h_c}{d_{90}}\right) \quad (2.26)$$

The logarithmic formulation can be transformed into an equivalent power function, if:

$$\sqrt{\frac{8}{f}} = a \left(\frac{h}{d_s}\right)^{b_1} = \hat{a} \ln\left[\frac{b'h}{d_s}\right] \quad (2.27)$$

The transformation results in:

$$b_1 = \frac{1}{\ln\left(\frac{b'h_c}{d_s}\right)} \quad (2.28)$$

where: $b' =$ a constant equal to 12.2.

Davis et al. (1998) conducted an experimental investigation using a rectangular flume to study free overfalls. They investigated the effect of channel-bed roughness and slope on the relationship between the upstream critical depth and the brink depth.

Roughness was found to have a greater effect on steeper slopes. If both the slope of the channel, and the Mannings coefficient, n , are known, y_b/y_c can be found from Equation (2.29):

$$\frac{y_b}{y_c} = 0.846 - 0.219 \sqrt{\frac{S_o}{n}} \quad (2.29)$$

where: y_b = the depth at the brink;

y_c = the critical depth;

S_o = the slope of the flume; and

n = the average Manning's coefficient.

When the Manning's coefficient is unknown, the following expression can be used:

$$\frac{y_b}{y_c} = 134.84S_o^2 - 12.66S_o + 0.778 \quad (2.30)$$

2.4.1.3 Drag coefficient

Drag and lift are defined as the force components exerted on a body by the moving fluid parallel and normal, respectively, to the relative approach velocity. Both pressures and viscous stresses act on an immersed body and either or both contribute to the resultant forces (Streeter and Wylie, 1985). Conceptually, the lift and drag forces can be computed directly from the pressure and viscous stresses. If a differential surface area, dA , is at an angle, θ , with respect to the horizontal the differential drag is:

$$d(\text{Drag}) = p \, dA \sin \theta + \tau_o \, dA \cos \theta \quad (2.31)$$

Then the total drag force is:

$$\mathbf{Drag} = \int (\mathbf{p} \sin \theta + \tau_o \cos \theta) dA \quad (2.32)$$

Similarly, the total lift force is:

$$\mathbf{Lift} = \int (\mathbf{p} \cos \theta - \tau_o \sin \theta) dA \quad (2.33)$$

Due to the complexity of flow around a body, the drag is often expressed as:

$$\mathbf{Drag} = C_d \rho A \frac{U^2}{2} \quad (2.34)$$

where: A = the projected area of the object of study perpendicular to the direction of the flow;

U = the approach velocity;

ρ = the density of the fluid; and

C_d = the drag coefficient, obtained empirically from experimentation.

A similar expression is used for the lift.

The drag coefficient has been found for regular shaped objects such as spheres and plates. Experiments have also been conducted for finding the drag coefficient of natural sediments such as sands and gravels. The following relationship of the drag coefficient seems best suited to natural sands and gravels (Julien, 1995):

$$C_d = \frac{24}{Re_p} + 1.5 \quad (2.35)$$

where: Re_p = the Reynolds number of the particle.

The fall velocity is used as the reference velocity. The drag coefficient can be considered equal to 1.5 for large particles, such as gravels, cobbles and boulders. Figure 2.9 shows the relation between the drag coefficient and the Reynolds number of the particle.

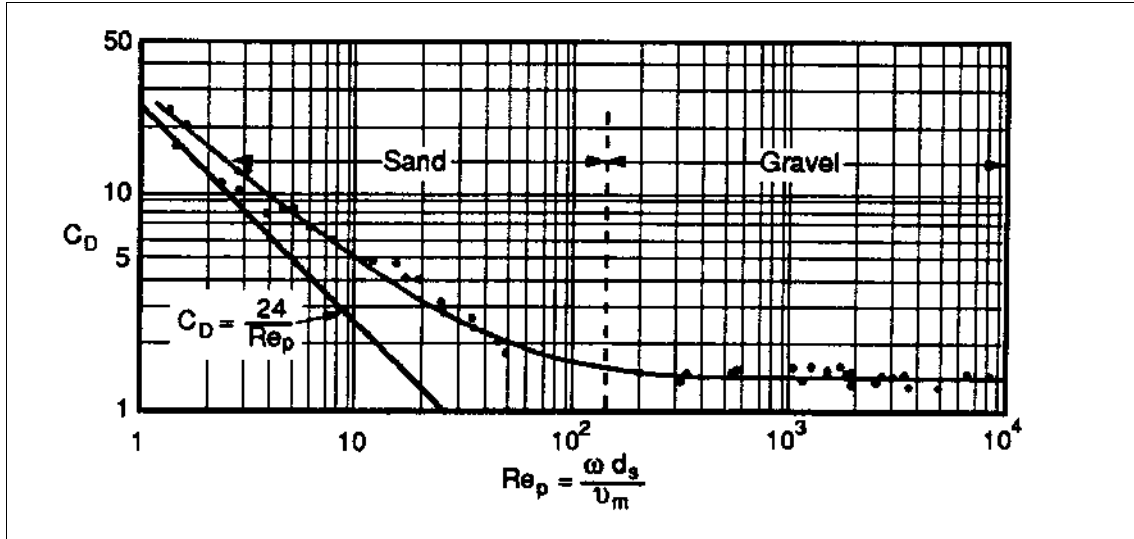


Figure 2.9. Drag coefficient of natural sands and gravel.

2.4.1.4 Incipient particle motion

A flow in an open channel is considered in which the slope of the bed is close to horizontal. If flow is passing by a particle, the hydrodynamic forces, lift and drag are proportional to the density of the fluid, the approach velocity, and the square of the characteristic length. The resisting forces essentially correspond to the submerged weight of the particle, which is proportional to the specific weight of the particle and its volume, which is, in turn, proportional to the cube of the characteristic dimension of the particle. The ratio of the hydrodynamic forces to the submerged weight is called the Shields parameter or the dimensionless shear stress τ_* :

$$\tau_* = \frac{\tau_o}{d_h (\gamma_s - \gamma_m)} = \frac{\rho_m u_*^2}{(\gamma_s - \gamma_m) d_h} \quad (2.36)$$

where: τ_o = the bed shear stress;

γ_s = the specific weight of a particle;

γ_m = the specific weight of the flowing fluid;

d_n = the characteristic dimension of a particle; and

u_* = the shear velocity.

Shields developed a diagram in which he plotted the critical dimensionless shear stress versus the grain shear Reynolds number ($u_* d_s/\nu$) for the condition of incipient motion. A similar plot can be created eliminating the characteristic dimension of the particle and plotting τ_{*c} versus the dimensionless particle diameter d_* (which is equal to $d_{50} [(G - 1)g/\nu^2]^{1/3}$). The critical values of the Shields parameter are a function of the dimensionless particle diameters and the angle of repose when the dimensionless particle diameter is less than fifty. When the dimensionless particle diameter is greater than fifty, the critical shear stress is a function of the angle of repose (Julien, 1995) (Figure 2.10).

Stevens and Simons (1971) developed a method for analyzing the stability of coarse materials on slopes. A particle is considered stable if the sum of the moments acting to displace the particle are less than the components of the submerged moment that provide the resisting moment. The ratio of acting moments to resisting moments is the safety factor.

A more practical approach to predict scour in an open channel was proposed by Scobey and Fortier (Chang, 1988). Erosion does not occur in an aging channel if a

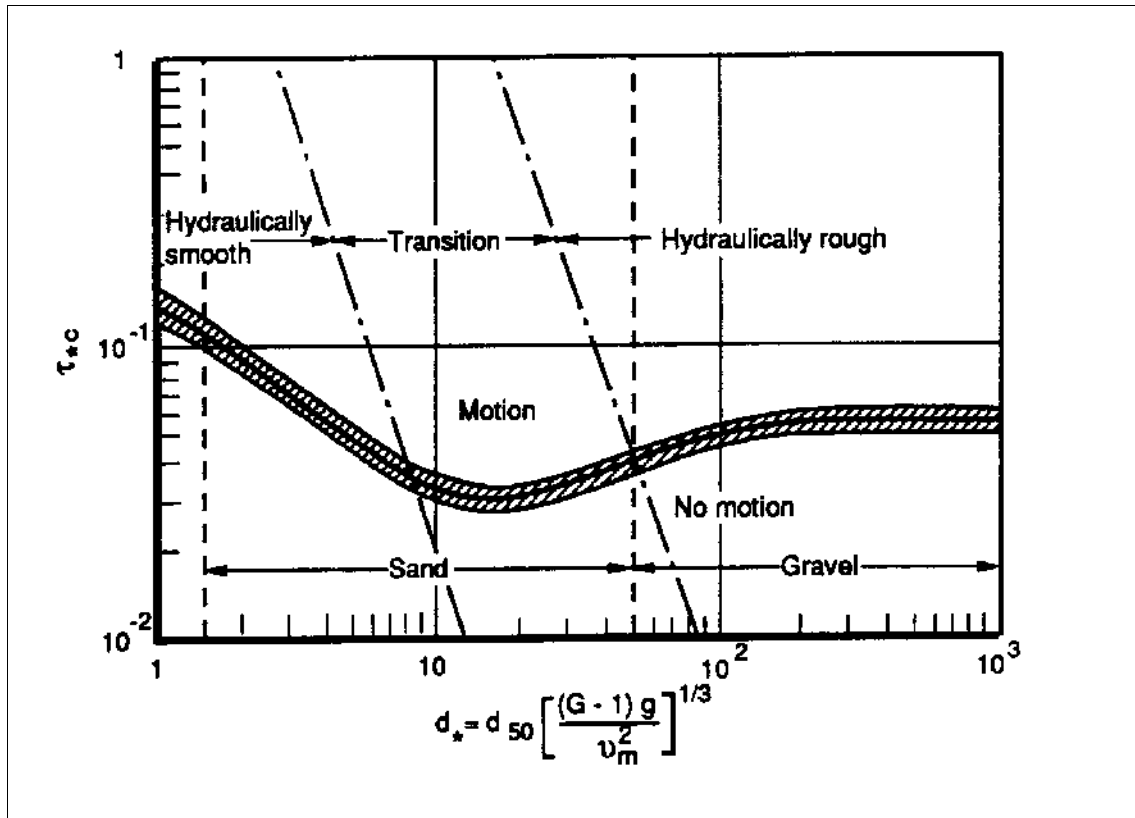


Figure 2.10. Dimensionless critical shear stress versus dimensionless particle diameter (Julien, 1995).

maximum permissible velocity is not exceeded. The maximum permissible velocity is a function of the particle size, water turbidity, and cohesion of the bed material.

2.4.2 Experimental studies on scour holes produced in cohesionless materials

Scimemi (Vanoni, 1975) studied the effect of grain size on the maximum depth of the scour hole produced by an impinging jet in 1947. He tested noncohesive material that was made successively finer in consecutive tests, in the course of the model study of a spillway for a debris barrier. A maximum depth of scour was obtained for each test. The limiting scour depth increased as the size of the sediment decreased.

Doddiah (1949) compared the scour caused by hollow circular jets and solid circular jets. He used four different nozzles at the end of the pipes he used in the tests. Comparison was made between jets of similar impinging areas and no significant difference in scour depth was found.

Laursen (1952) stated the basic principles of scour valid for scour caused by jets:

- The rate of scour will equal the difference between the capacity for transport out of the scoured area and the rate of supply to that area.
- The rate of scour will decrease as the flow section is enlarged.
- There will be a limiting extent to the scour.
- The maximum scour depth will be approached asymptotically.

Thomas (1953) studied a free-falling jet of water and its resulting scour on a uniform gravel bed material. For this study, a free overfall was constructed with a sudden drop in elevation from one horizontal bed to a lower horizontal bed. The tailwater depth was varied for different tests. The geometric mean of the particle size was held constant, but the standard deviation of the particle size was varied. The following relationship was obtained:

$$\frac{Y}{TW} = f \left(\frac{H}{TW}, \frac{Hw_m}{q}, \frac{qT}{H^2}, s_w \right) \quad (2.37)$$

where: Y = the depth of scour (from the original bed level to the bottom of the scour hole);

TW = the tailwater depth (from the original bed level to the top of the water surface);

H = the height of fall from the bed level upstream to the bed level downstream;

q = the discharge per unit width of crest;

T = the time of test run;

w_m = the geometric mean fall velocity of the bed material scoured; and

S_w = the standard deviation of fall velocity.

The following conclusions were reached:

- The depth of scour continues to increase with a geometric progression of time.
- An increase in discharge causes a greater increase of depth of scour.
- A critical tailwater depth is reached at which either an increase or decrease in tailwater causes a decrease in the scour depth.

Hallmark (1955) studied the influence of particle size gradation at the base of a free overfall. Basically, his research focused on armor plate design for avoiding excessive scour. A tailbox with a width approximately equal to the width of the jet at issuance was used to contain the bed material. Gravel of two different sizes was used and armorplating was found to significantly reduce the depth of the scour hole. A critical tailwater depth at which either an increase or decrease in tailwater depth caused a decrease in scour depth was reported. He observed that a 50% decrease in the standard deviation of the size distribution resulted in a 50% increase in depth of scour when $qt/H^2 = 3 * 10^5$. Other important conclusions were:

- Only a relatively small amount of armorplating material is necessary for a relatively large decrease in the rate of scour.

- The rate of scour decreases with a decrease in the size of the armorplate material while the armorplate material remains larger than the largest particle size of the bed material.
- The rate of scour decreases with an increase in the amount of armorplate placed in the scour hole.
- Graded armor plate material decreases the rate of scour more effectively than uniform material.

Lencastre (1961) carried out tests and compared the effect of the configuration of the water releasing structure on the final dimensions of the scour hole. Scour holes produced by adhering sheet jets and free impinging jets were compared for the same upstream head and tailwater depth. Depths of the scour holes for free impinging jets were greater than for adhering sheet jets when the upstream head was held constant. Evidently, a fraction of the available energy is converted into friction in an adhering sheet jet situation, so that less energy is available for eroding the bed. Also, the angle of entrainment of the jet is horizontal in the case of adhering sheet jets. Lencastre also pointed out that a critical tailwater depth exists for which the depth of scour is a maximum. For deeper or shallower tailwater depths, depth of scour decreases.

Mirtskhulava et al. (1967) stated that the scour process ceases when the maximum velocity of the ascending stream at the hole water table is equal to the fall velocity of those particles which compose the bottom of the scour hole at a given moment of the scouring process. Velocities of the jet were modeled based on observations and the fluctuating nature of the velocities was also taken into account in this model, as well as the impinging

angle of the jet. The following relations were proposed for describing the significant velocities:

$$V_m = \frac{V_i}{0.9 + 0.09 \frac{x_1}{b_i} + 0.12 \frac{x_2}{b_i}} \quad (2.38)$$

$$U_a = \frac{V_m}{0.9 + 0.4 \left(\frac{z_d}{b_i} \right)^2} \quad (2.39)$$

where: U_a = the velocity of the ascending stream;

V_i, V_m = the velocity in the entrance section and the maximum velocity in the section located at a distance x from the entrance section, respectively;

b_i = the stream width at the entrance point. For natural conditions, often $b_i = 0.8q/V_i$, q = unit discharge;

x_1, x_2 = the distance of the stream along the axis from the stream entrance section to the downstream base and to the hole bottom, respectively;
and

z_d = the distance of the ascending stream along the axis from the contact point of the falling stream with the bottom.

Due to the fluctuating nature of the velocities, and the fact that scour ceases when the acting velocity equals the fall velocity of the particle the following equation applies:

$$\eta U_a = w \quad (2.40)$$

where: η = a constant whose range is 1.5 - 2.0, $\eta = 1.5$ for laboratory experiments, and

$\eta = 2.0$ for field conditions; and

w = the fall velocity of the particles.

The fall velocity can be obtained from:

$$w = \sqrt{\frac{2 g (\gamma_s - \gamma_{aw}) d_{90}}{1.75 \gamma_{aw}}} \quad (2.41)$$

where: g = the gravity acceleration;

γ_s = the specific weight of the particles;

γ_{aw} = the specific weight of the jet fluid; and

d_{90} = the nominal diameter particle for which 90% of the material is finer.

The influence of the angle of impingement was taken into account for developing the following relation that predicts the maximum depth of the scour hole:

$$Y = \left(\frac{3\eta V_i b_i}{w} - 7.5b_i \right) \frac{\sin \beta}{1 - 0.175 \cot \beta} + 0.25TW \quad (2.42)$$

where: β = the angle of impingement of the jet with respect to the horizontal; and

TW = the tailwater depth downstream of the zone of impingement.

It was also found that it is necessary to multiply the first term of the equation by a correction factor for particles measuring less than 2 mm.

Machado (1980) proposed a formula for calculating the maximum depth of the scour hole from the tailwater surface, using a shear stress formula, proposed by Shields and a modeled velocity distribution of a rectangular jet:

$$D_{max} = 1.35 C_v^{0.5} \frac{q^{0.5} \Delta H^{0.3145}}{d_{90}^{0.0645}} \quad (2.44)$$

where: C_v = the velocity coefficient of the outlet structure;

D_{\max} = the maximum depth of scour measured from the tailwater surface in meters;

q = the unit discharge in m^2/s ;

ΔH = the difference in elevation between the upstream reservoir surface and the downstream tailwater surface in meters; and

d_{90} = the diameter of the bed material for which 90% of the material is finer by weight in meters.

Mendoza (1980) studied the influence of headwalls on the scour downstream of culverts. He used an exponential decreasing type law for describing variation of depth as a function of time:

$$\frac{d_s}{d_{sm}} = 1 - e^{-at} \quad (2.45)$$

where: d_s = the depth of the scour cavity below the elevation of the initial ground level;

d_{sm} = the maximum scour depth;

a = the constant; and

t = the time from initiation of scour.

This type of equation describes the initial and final conditions of the scour hole, because at $t = 0$; $d_s/d_{sm} = 0$; and at $t = \infty$; $d_s/d_{sm} = 1$. The maximum depth of scour d_{sm} has to be known.

$$\left(\frac{d_{sm}}{D_1} \right)_{NH} = 2.14 (D.L.)^{0.35}$$

$$\left(\frac{d_{\text{mm}}}{D} \right)_H = 2.09 (D.I.)^{0.35}$$

where: D_i = culvert diameter;

$D.I.$ = $Q/(\text{sqrt}(gD^5))$;

Q = discharge;

g = gravity acceleration;

H = headwall condition; and

NH = not headwall condition.

Rajaratnam (1981a) studied the influence of the angle of impingement on erosion of a polystyrene bed by a circular air jet. Correlations were found for the characteristic lengths developed for the asymptotic state.

Mason and Arumugan (1985) proposed formulae for predicting the maximum depth of the scour hole caused by rectangular impinging jets. Model and prototype data were used and different expressions were given for each case. The following formula was proposed for calculating total depth in models:

$$D = 3.27 \frac{q^{0.60} H_o^{0.05} h^{0.15}}{g^{0.30} d^{0.10}} \quad (2.46)$$

where: q = the unit discharge in m^3/s ;

H_o = the available head in meters;

h = the tailwater depth in meters;

g = the acceleration of gravity ($9.81 \text{ m}^2/\text{s}$);

- d = the representative size of the particle which is d_{50} in this case (in m); and
- D = the depth of the scour hole as measured from the tailwater elevation in meters.

A second formula for prototypes was proposed based on reports written by different authors:

$$D = K \frac{q^x H_o^y h^w}{g^z d^z} \quad (2.47)$$

in which $K = (6.42 - 3.10 H_o^{0.10})$; $v = 0.30$; $w = 0.15$; $x = (0.60 - H_o/300)$; $y = (0.15 - H_o/200)$; and $z = 0.10$ (with an assumed constant value of d of 0.25 m for prototypes). Mason's formula was derived for vertical jets and, therefore, does not allow any correction for different angles of impingement. In the prototype formula, the available head has an increasing importance as it becomes larger.

Doehring (1987) studied the effect of drop height on the ultimate dimensions of the scour produced by circular jets. Four discharge intensities were tested and drop height was varied between zero and four times the diameter of the pipe. The width of the tailbox was 60 times the pipe diameter. He concluded that the maximum depth of scour produced by a pipe located at a height above the bed is always greater than that produced with zero drop height. Also, the length of the scour hole decreased for increasing heights of the pipe. The angle of impingement approached vertical as the height was increased for the same discharge. Changes in geometry were attributed to a change in the angle of impingement. Horizontal velocities were taken within the scour hole, and it was found that the point of maximum velocity occurs lower in the scour hole as the drop height increases.

Mason (1989) included the concept of jet aeration in the development of a new formula for predicting the maximum depth of the scour hole. He studied the effects of air entrainment on plunge pool scour. Tests were carried out by him using a hydraulic model in which the unit flow, q , the head drop, H_o , and the air/water ratio, B , in the plunge pool could each be varied separately. Scour depths were found to be only dependent on q and B . Variations of B with H_o could explain this phenomenon. Air was supplied by a high-volume, low pressure fan. It was found that in the absence of entrained air, the scour depth was dependent solely on q and independent of H_o . With the addition of air in proportions calculated to be equivalent to what a free-falling jet would entrain naturally, the effect of q on the scour process appeared to be modified and the scour also appeared to vary with H_o . According to Mason, the degree of aeration may have affected the formulas obtained by different authors, leading to discrepancies in proposed values for x and y in:

$$D = K \frac{q^x H_o^y}{d^z} \quad (2.48)$$

where: D = the scour depth; and

d = the characteristic bed particle size.

The volumetric air/water ratio, B , can be calculated using Ervine's formula:

$$B = 0.13 (1 - V_e/V_i) (z/b_i)^{0.446} \quad (2.49)$$

where: V_i = the jet impact velocity;

V_e = the minimum jet velocity to entrain air (taken as 1.1 m/s);

b_i = the jet thickness at impact; and

z = the falling height.

The plunge-pool scour depth can be calculated from the equation:

$$D = 3.39 \frac{q^{0.60}(1 + B)^{0.30}h^{0.16}}{g^{0.30}d^{0.06}} \quad (2.50)$$

The previous equation can be approximated by the expression proposed by Mason and Arumugan (1985):

$$D = 3.27 \frac{q^{0.60}H_o^{0.05}h^{0.15}}{g^{0.30}d^{0.10}} \quad (2.51)$$

In which the factor $H_o^{0.05}$ is, in fact, an approximation to the effect of air entrainment in the plunge pool. This equation introduced tailwater depth, h , above an unscoured river bed level, as a further factor to improve accuracy. The gravitational constant, g , was introduced to allow dimensional balance.

Shafai-Bajestan (1989) used a half jet to find criterion for defining incipient motion and incipient failure in gravels. Velocities and jet diameters were varied throughout the tests. For a given velocity, tailwater was lowered until movement was observed and recorded.

Bormann and Julien (1991) derived an equilibrium scour equation based on the concepts of jet diffusion and particle stability in scour holes produced downstream of hydraulic structures:

$$D = \left(\frac{\gamma \sin \phi}{\sin (\phi + a)\beta(\gamma_s - \gamma)g} \right)^{0.8} \frac{C_{diff}^2 b_i^{0.6} V_i^{1.6} \sin \beta'}{d_{90}^{0.4}} - D_p \quad (2.52)$$

where: d_{90} = the nominal diameter for which 90% is finer by weight;

g = the gravitational acceleration;

β = the coefficient of friction relationship;

C_{diff} = the jet diffusion coefficient;

- D_p = the drop height of structure;
 D = the equilibrium scour depth;
 V_i = the jet velocity entering tailwater;
 b_i = the jet thickness entering tailwater;
 g = the specific weight of the water;
 γ_s = the specific weight of sediment;
 a = the embankment angle;
 β' = the jet angle near bed; and
 ϕ = the submerged angle of repose of the granular material.

Stein and Julien (1994) derived an equation for calculating the maximum depth of a scour hole produced by an impinging jet downstream of a free overfall (Figure 2.11). Based on the approach by Albertson et al. (1950) and Beltaos and Rajaratnam (1974), a jet is assumed to have a zone of establishment. Dimensionless relationships between scour volume, sediment concentration, maximum scour depth, and time were obtained. The scour volume per unit width was found to be twice the square of the maximum scour depth at any time. The depth of scour below the tailwater surface, D , is calculated from Equation (2.53).

$$D = \frac{C_d^2 C_f V_i^2 b_i \sin \chi}{\tau_c} \quad (2.53)$$

- where: C_d = the diffusion coefficient;
 C_f = the friction coefficient = $0.22/8 (q/v)^{-0.25}$;
 V_i = the velocity of the jet at the tailwater surface;

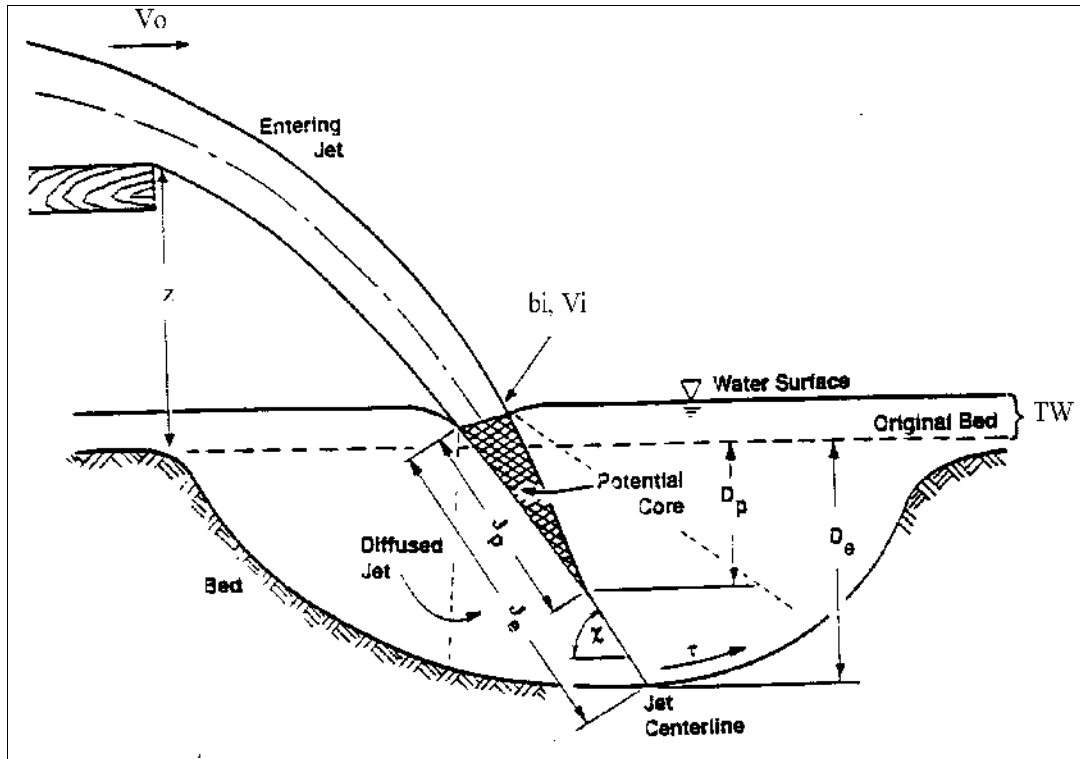


Figure 2.11. Definition of variables for an impinging jet (Stein and Julien, 1994).

b_i = the thickness of the jet at the tailwater surface;

q = unit discharge;

ν = kinematic viscosity;

χ = the angle of impingement of the jet with respect to the horizontal; and

τ_c = the critical shear stress to entrain a characteristic particle.

Abt et al. (1995) conducted scale model tests to simulate scour occurring at the base of an existing dam at 22% of the Probable Maximum Flood (PMF). Veronese's equation was found to overestimate the scour depth, whereas Mason's equation was found to underestimate it.

Annandale (1995) correlated the rate of hydraulic energy dissipation per unit area with the erodibility of different kinds of earth materials, K_h . The rate of energy dissipation is related to the maximum pressure fluctuations. Several cases in which dissipation of hydraulic energy occurs such as headcuts, canal flow, hydraulic jumps, and changes in slope were addressed. Using laboratory and field data, the rate of energy dissipation per unit area was plotted versus the erodibility of earth materials ranging from very fine cohesionless materials to massive rock. A log-log plot showed that the threshold to initiate erosion of a material can be predicted for any given set of hydraulic conditions as shown in Figure 2.12. The parameters that define erodibility for different materials can be found using low cost field tests that do not require the use of specialized tools or equipment.

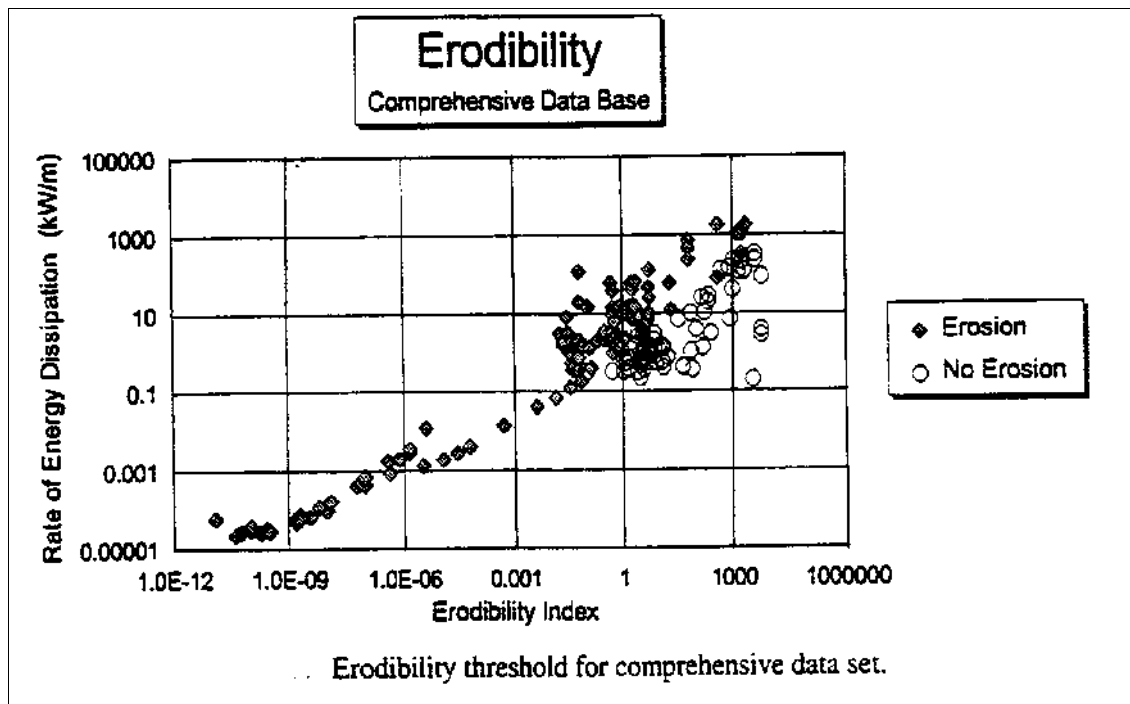


Figure 2.12. Rate of energy dissipation (kW/m^2) versus erodibility index (Annandale, 1995).

In general, the erodibility index, K_h , is obtained by multiplying four factors: the mass strength number, M_s , which represents the strength of the material to external forces; K_b , which is a function of the block or particle size; K_d , which depends on the interlocking of the particles and J_s , which depends upon the particle shape and the orientation of the particles relative to the flow.

In a cohesionless material, M_s depends upon the compactness and the specific gravity of the soil. The second factor, K_b , depends upon the median particle size in a cohesionless soil and is equal to $1000 d_{50}^3$. The third factor, K_d , is a function of the interlocking of the particles and is approximated by the tangent of the residual friction angle. Erodibility also depends upon the orientation of the particles and the ratio of fracture joint spacing in the directions perpendicular to the flow. Both are included in the factor J_s . J_s is equal to one in granular materials. The erodibility index, K_h , is given below:

$$\mathbf{K_h = M_s K_b K_d J_s} \quad (2.54)$$

Erosion occurs when the power per unit area, P , exceeds the critical power per unit area necessary to produce removal of the particles whose erodibility index is K_h . The extent of erosion can not be directly predicted from the chart. However, a larger departure from the threshold would indicate a greater potential of erosion.

If the bed material is rock, the Mass Strength number, M_s , is given by its resistance to jacking (i.e., necessary numbers of hits to produce dislodgement using a geological pick), and its specific weight. The resistance of the bed material to erosion, which is given by the factor K_b , also depends upon the number of joints per unit length in the three directions. The interlocking of the particles and the presence of a cementing material also affects rock erosion. These effects are accounted for in the factor K_d . If no cementing

material is present, a sliding test is used to obtain the friction angle. In that case, the tangent of the friction angle becomes K_d . Finally, the orientation of the blocks of rock with respect to the direction of the flow, and the ratio of joint spacing in the two axis perpendicular to the flow is given in the factor J_s . The erodibility index is calculated using Equation (2.54).

Recently, Hoffman (1998) presented an equation that relates the total depth of scour, $Y + TW$, to the unit discharge, q , the velocity of impingement, V_i , the angle of impingement, and a factor that depends upon the characteristic sediment size, d_{90} . Newton's second law of motion was applied to a fluid mass to derive relations for the maximum scour depth in the equilibrium phase.

$$Y + TW = C_{2v} \sqrt{\frac{q V_i \sin (90 - \delta)}{g}} \quad (2.55)$$

where C_{2v} was found to be:

$$C_{2v} = \frac{20}{(d_{90}^*)^{1/3}} \quad (2.56)$$

if $d_{90} < 0.0125$ m and:

$$C_{2v} = 2.9 \quad (2.57)$$

if $d_{90} > 0.0125$ m. The dimensionless sediment diameter is $d_{90}^* = d_{90} ((G - 1)g/v)^{1/3}$.

2.5 Scour Caused by Impinging Jets in Rock Strata

Few researchers have studied the scour caused by impinging jets in rock strata. Some introductory concepts are given below, because they are related to this study and to tests conducted by other researchers.

2.5.1 Rock description

Geological aspects: rocks are classified according to their origin as igneous rocks, sedimentary rocks, and metamorphic rocks. Igneous rocks are formed when hot molten material called magma solidifies. Most sedimentary rocks are formed from the breakdown products of pre-existing rocks by consolidation (mainly by weight of the overburden and dewatering) and cementation. Metamorphic rocks are formed from pre-existing rocks and have structurally changed mainly due to changes in the physical and chemical environment.

Joints in a rock mass reduce its effective shear strength at least in a direction parallel with the discontinuities. Joints offer no resistance to tension whereas they offer high resistance to compression (Bell, 1992).

Using triaxial tests and Mohr's theory of principal planes of failure, researchers have found that a linear relation exists between shear stresses and compressions at failure. The slope of the curve is the tangent of the angle of friction of the material and the intercept with the Y axis is the apparent cohesion for a given rock mass. This approach is similar to failure theory used in soil mechanics. The main difference is that rocks are highly anisotropic, because they have surfaces of failure. The friction angle can be increased due to asperities in rock joints, so that roughness accounts for an increase of resistance to shear. Barton (Bell, 1992) provided a graph showing the scale of the

roughness corresponding to a factor called Joint Roughness Coefficient (JRC). Therefore, the nature of the opposing joint surfaces influences rock mass behavior, as the smoother they are, the easier movement can take place along them. Also, if the separation between joints is large (greater than 10 mm), then shear strength depends upon the strength of the filling material.

The difficulty of studying scour caused by impinging jets in rock strata, due not only to the complex nature of jet diffusion, but to the complexity of this type of material, forced researchers to use different approaches, such as placing regular shaped objects to simulate fissured rock.

2.5.2 Scour studies in rock strata

Part of the studies conducted by Lencastre (1961) included a comparison of the depth of scour produced in loose material and scour produced in cubes placed in horizontal rows. The cubic blocks measured 5 cm per side and were placed by hand in horizontal rows. Rocks had a median diameter of approximately 4.8 cm. The maximum depths of the scour holes for rocks and blocks were comparable when tests were run for similar conditions. Unit discharges tested were in the range of 0.023 m²/s to 0.134 m²/s.

Mirtskhulava et al. (1967) proposed a model for rocky beds being impinged by a jet. He divided rock erosion into two cases. In the first case, there is no cohesion between rocks. In the second case, aggregates filling the gaps act as a cementing material. Rocks were modeled as parallelepipeds in which C is the vertical dimension, and A_1 and B_1 are the dimensions along and across the stream, respectively. The depth of the scour hole, Y , is given below:

$$Y = \left(\frac{8.3 V_i b_i}{\sqrt{\frac{2gmB_1^2 [R_f + C (\gamma_p - \gamma_o)]}{\gamma_o n \sin \beta (0.60B_1^2 + 0.20C^2)}}} - 7.5b_i \right) \frac{\sin \beta}{1 - 0.175 \cot \beta} + 0.25TW \quad (2.58)$$

where: R_f = the “fatigue” strength to rupture, and is determined in relation to the statistical limit of compression strength;

m = a coefficient of working condition, $m = 1.0$ for clear water, $m = 1.6$ for water carrying sediment; and

n = a coefficient of overload, $n = 4.0$ for natural conditions, $n = 2.25$ for laboratory experiments.

The other parameters are the same as defined in Section 2.4 for cohesionless materials.

Machado (1980) proposed a formula for jets impinging in different kinds of cohesionless materials, including rocks and gravels. He defined two phases of rock destruction:

- a) One in which the rock is subjected to high and non-uniform distributed pressures, but the rock still keeps its integrity.
- b) One in which the rock breaks apart and the small blocks are washed away.

Assuming that for total dissipation of the jet energy, no scour will occur, the maximum possible depth of scour (from the tailwater surface) will be:

$$D_{\max} = 2.98 C_v q^{0.5} \Delta H^{0.25} \quad (2.59)$$

where: C_v = the velocity coefficient of the outlet structure;

q = the unit discharge in m^2/s ; and

ΔH = the difference between the upstream reservoir elevation and the downstream tailwater elevation in m.

According to Machado this approach should be valid for all kinds of materials. D_{\max} is the depth at which the power of the jet is fully dissipated. He stated that this formula tends to over estimate the maximum depth of the scour hole.

CHAPTER 3

THEORETICAL CONSIDERATIONS

3.1 Introduction

Studies related to jet dynamics have been summarized in Section 2.2. From the studies reviewed, one concludes that the centerline velocity of the jet decreases as the jet transfers energy to the surrounding fluid by shear stress. The centerline velocity of the jet is inversely proportional to the square root of the distance from the issuance section to a section located downstream and is directly proportional to the square root of the thickness of the jet at issuance. Studies related to the pressures and shear stresses produced by an impinging jet on a plate have been summarized in Section 2.3 of the literature review. Hydrodynamic pressures (or heads) on a plate being impinged by a jet diminish as the tailwater depth increases. In addition, pressure fluctuations on the plate also diminish as the tailwater depth increases. Therefore, the potential for erosion of a cohesionless bed being impinged by a jet is expected to decrease as the tailwater depth increases.

The early studies of scour produced by an impinging jet incorporated the total fall height as a factor that affects the maximum depth of the scour hole (Thomas, 1953; Hallmark, 1955; Lencastre, 1961). The fall height was measured from the upstream water level to the downstream bed level. This approach does not take into account that an increase in the velocity of the jet occurs between the section of issuance and the tailwater

surface, and energy dissipation occurs after the jet enters the tailwater. Recent studies of scour caused by impinging jets take into consideration the fact that energy dissipation occurs after impingement.

The influence of the angle of impingement in jet scour has been taken into account by a few researchers. Hom-ma (1953) showed that the centerline velocity of an impinging jet decreases at a faster rate when the angle of impingement is different from vertical. Mirtskhulava et al. (1967) introduced a correction factor in an equation used to predict the maximum depth of a scour hole when the angle of impingement was greater than 15 degrees. Other authors have pointed out that the potential of scour is less when the jet is inclined, because the dissipation length of the centerline of the jet is longer. Scour is expected to decrease with an increase in the angle of impingement with respect to the vertical.

Extensive studies have been carried out by Shields and others to determine the threshold of motion for cohesionless materials in horizontal beds. The critical Shields parameter is a function of the dimensionless particle diameter, d_* , and the angle of repose of the material, ϕ , when d_* is less than 50. When d_* is greater than 50, the critical Shields parameter is solely a function of the angle of repose. The particle size diameter also influences the depth of scour produced by an impinging jet. Scimeni (Vanoni, 1975) showed that the depth of scour increased as the particles of a bed being impinged by a jet were made successively smaller and the rest of the conditions remained consistent. Many researchers consider that the characteristic dimension of the bed particles is important for the prediction of the maximum depth of the scour hole. However, no general agreement has been reached. The majority of the authors use d_{90} as the representative particle size for

calculating the depth of scour, but in many cases d_{50} was chosen as the representative particle size. Hallmark (1955) found that the material remaining in the bottom of the scour hole was approximately d_{85} . On the other hand, the roughness of the bed is often characterized as a function of d_{90} . For example, the Darcy-Weisbach grain friction factor is a function of d_{90} (Julien, 1995). The roughness of the bed affects the flow regime in an open channel flow situation.

The development of a theoretical model has to be compatible with observations made in the field and laboratory studies. Due to the complex nature of the processes involved, physical models are conducted to visualize the formation of the scour hole.

The various aspects of the mechanics of jet scour will be covered in this chapter to obtain a predictor of scour depth. The jet is released from a point located above the tailwater surface. The velocity across the jet is the average velocity at the issuance section. As the jet travels to the tailwater surface, an increase in the velocity of the jet occurs. If the trajectory is long enough, the jet disintegrates in discrete particles, and part of the kinetic energy of the jet is transformed into friction. Furthermore, as the jet entrains air, part of the energy is used to carry the air at the same velocity as the water. The power of the jet is partially dissipated in the tailwater. The jet forms a hole in the bed if the available power of the jet at the bed is sufficient to produce removal of the particles.

3.2 Initial Boundary Conditions

Boundary conditions such as the configuration of the issuing structure, tailwater depth, width of the downstream canyon, the nature of the jet (i.e., free-falling jet or adhering sheet jet), and existence of headwalls, are expected to affect the final dimensions

of the scour hole. For instance, if the tailwater surface is infinite and a rectangular jet is impinging on a very deep tailwater, no scour will occur and the jet downstream of the zone of impingement will be diffused in the longitudinal and lateral directions.

If the width of the downstream canyon is finite, but wider than the width of the jet at the zone of impingement and the tailwater depth is shallow enough so that erosion is occurring, a scour hole will be formed. Streamlines in the downstream direction will tend to diverge towards the banks, and depending on the ratio of canyon width to jet width at impingement (W_c / W_{ji}) and the angle of impingement, recirculation will occur, and backflows are expected. If the width of the canyon is approximately the same as the width of the jet in the zone of impingement, the streamlines of the flow downstream of the zone of impingement will be straight. Recirculation is unlikely to happen, because the walls will guide the flow in the downstream direction.

3.3 Scour Hole “Final” Boundary Conditions

As the scour hole is formed, deposition occurs downstream of the scour hole. Depending on the downstream tailwater depth, material will either deposit immediately downstream of the scour hole or it will be carried away. When the scour hole is close to equilibrium, lighter particles are carried away in the downstream direction, heavier particles remain at the bottom of the scour hole, and armoring takes place. Hydrodynamic forces acting on the particles have to overcome the component of the particles' weight parallel to the slope to remove them from the vicinity of the zone of impingement.

The depth of the scour hole is a function of the tailwater depth, discharge, bed material, and boundary conditions. Diffusion of the jet within the scour hole is expected to

be different from the diffusion in the tailwater above, where jet flow is less restricted. The side and longitudinal slopes of the scour hole will affect the size and shape of the jet because the walls of the scour hole will induce higher losses until the jet is not powerful enough to remove material from the bottom of the hole.

3.4 Scour Process

An impinging jet undergoes three distinct phases when scouring an erodible bed as shown in Figure 3.1. In Phase One, the jet is issued at a height z above the tailwater level. The initial velocity of the jet is V_0 and the width of the jet is b_0 . Velocity fluctuations exist across the jet at issuance but velocities become more homogeneous as the jet travels to the tailwater due to the interaction of water particles and air. A net gain in kinetic energy

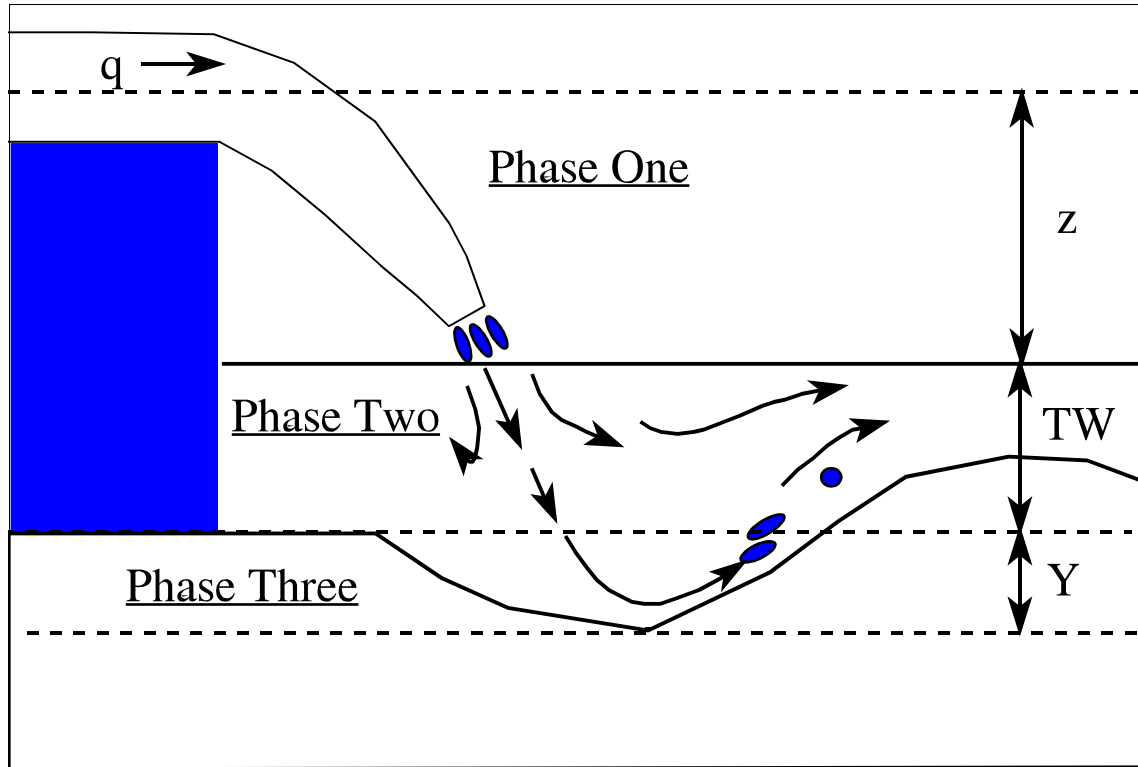


Figure 3.1. Phases of a scouring impinging jet.

is produced, due to gravitational acceleration. The jet impinges the bed at a higher velocity than the jet was issued, unless the jet disintegrates. The theoretical velocity of impingement is V_i , and the actual velocity of impingement is V_{iact} . The jet disintegrates if the trajectory of the jet, L , is large in comparison to the disintegration length, L_d , which is a function of the unit discharge of the jet, q , and the turbulence level at issuance, ε (McKeogh and Elsaywy, 1980; Ervine et al., 1997). If the jet disintegrates, the individual particles attain a terminal velocity corresponding to their ultimate diameter. Such velocity might be less than the velocity of issuance if the degree of the disintegration of the jet is high. In any case, the degree of jet disintegration depends upon the ratio L/L_d . The actual total available head at the tailwater surface, H_{act} , is expected to be less than the theoretical total available head, H_o . The jet impinges the bed at an angle, δ , with respect to the vertical.

In Phase Two, the jet dissipates energy after it impinges on the tailwater. The velocity of the jet is reduced as it penetrates the tailwater. The jet mixes with the surroundings, transferring part of its power to the once static fluid by shear stresses. The length of penetration of the centerline of the jet is $TW/\cos \delta$.

In Phase Three, the jet impinges the bed and creates a scour hole if the power of the jet is sufficient to cause the removal of the bed particles. The available head at the initial ground surface, H_{gs} , a characteristic width, b_{gs} , the characteristic particle size, d_n , and its drag coefficient, C_d , will determine the ultimate depth of scour below the initial ground surface, Y . The velocity necessary to move the characteristic particle is V_p . Mirtskhulava (1967) considered that the fall velocity of a particle, w , indicates its resistance to scour. The depth of scour varies with time. Because the forces available at the ground surface at

the beginning of the tests are very high, the rates of scour are high. The rate of scour decreases as time passes.

In addition, the nature of the fluid impinging the bed, and the density of the particles of the bed, ρ_s , must be taken into account. A fluid can be characterized by its viscosity, μ_w , and its density, ρ_w . The density of the air, ρ_a , and the viscosity of the air, μ_a , could also influence the depth of scour. Combining all of the variables of Phases one, two and three and the information of the soil and the fluids properties, the following function is obtained:

$$\begin{aligned} f_1(Y, V_o, b_o, \alpha, z, q, \epsilon, g, \rho_w, \mu_w, \mu_a, \rho_a, L, L_d, \delta, H_o, V_i, b_i, \\ TW, H_{gs}, b_{gs}, d_n, \rho_s, C_d, \theta, V_p, w, t) = 0 \end{aligned} \quad (3.1)$$

The Pi-Buckingham theorem, the results of previous studies, and the equation of energy will be used to identify the parameters of importance in the development of a scour hole. The variables of importance in each of the phases mentioned above will be assessed. Using the Pi-Buckingham theorem, and selecting TW , V_o , and μ_w as repeating variables, the following dimensionless parameters result:

$$\begin{aligned} f_2\left(\frac{Y}{TW}, \frac{b_o}{TW}, \alpha, \frac{z}{TW}, \frac{q}{V_o TW}, \epsilon, \frac{TW g}{V_o^2}, \frac{TW V_o \rho_w}{\mu_w}, \frac{\mu_a}{\mu_w}, \frac{TW V_o \rho_a}{\mu_w}, \right. \\ \left. \frac{H_o}{TW}, \frac{V_i}{V_o}, \frac{b_i}{TW}, \frac{L}{TW}, \frac{L_d}{TW}, \delta, \frac{H_{gs}}{TW}, \frac{b_{gs}}{TW}, \frac{d_n}{TW}, \frac{TW V_o \rho_s}{\mu_w}, \right. \\ \left. C_d, \theta, \frac{V_p}{V_o}, \frac{w}{V_o}, \frac{V_o t}{TW}\right) = 0 \end{aligned} \quad (3.2)$$

The physical processes occurring after the jet is issued will be taken into consideration in the derivations that follow to select the relevant dimensionless parameters.

3.5 Influence of Air Entrainment in the Available Power of the Jet at Impingement

A jet issued from a nozzle has different characteristics than the free overfall jet of Figure 3.1. Figure 3.2 shows a schematic drawing of a jet issuing from a nozzle and the analyses that follows relates to this condition.

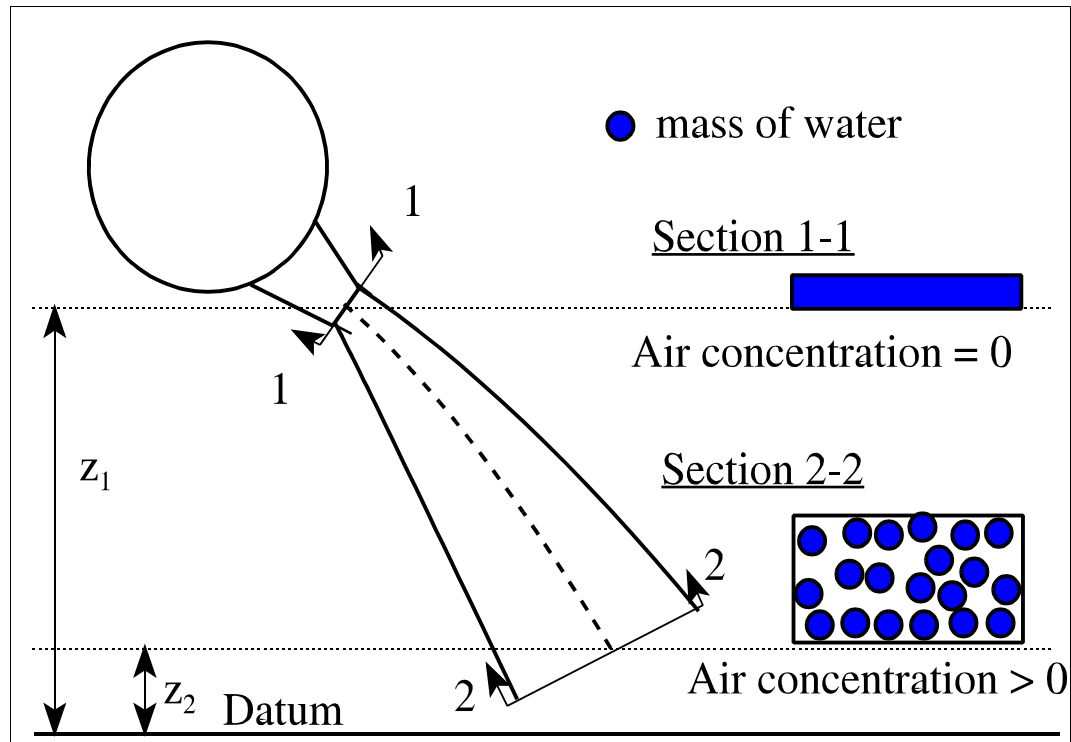


Figure 3.2. Sketch of air entrainment in a section of a jet.

The energy equation will be applied to show the influence of air entrainment on the velocity of impingement of a jet from a theoretical viewpoint. The unit discharge of the jet is constant. The air concentration is assumed to be zero at the section of issuance, and a positive value for sections downstream of the section of issuance. Section one is the section of issuance and section two is a section of the free jet. Between section one and section two air is entrained. The section of issuance is located at z_1 from a horizontal plane

of reference and section two is located at z_2 from the same plane of reference as seen in Figure 3.2. Water mass is m_w at any section and is constant. Air mass at section two is m_a . A fraction of the energy of the jet will be used to move the air mass at the same speed as the water. The energy equation is applied below:

$$m_w g z_1 + \frac{m_w V_1^2}{2} = (m_a + m_w) g z_2 + \frac{m_w V_w^2}{2} + \frac{m_a V_a^2}{2} \quad (3.3)$$

This equation can be written as:

$$z_1 + \frac{V_1^2}{2g} = \left[\frac{m_a + m_w}{m_w} \right] z_2 + \frac{V_w^2}{2g} + \left(\frac{m_a}{m_w} \right) \frac{V_a^2}{2g}$$

Air is moving at the same speed as the water in section two, therefore:

$$\frac{V_w^2}{2} = \frac{V_a^2}{2} \quad (3.4)$$

$$z_1 + \frac{V_1^2}{2g} = \left[\frac{m_a + m_w}{m_w} \right] z_2 + \left[\frac{m_w + m_a}{m_w} \right] \frac{V_2^2}{2g}$$

$$z_1 + \frac{V_1^2}{2g} = \left[\frac{m_a + m_w}{m_w} \right] \left(z_2 + \frac{V_2^2}{2g} \right)$$

But,

$$m_a = \rho_a \text{ Vol}_a, m_w = \rho_w \text{ Vol}_w \quad (3.5)$$

Consequently, after simplifications, the previous expression can be written as:

$$z_1 + \frac{V_1^2}{2g} = \left[\frac{\rho_a \text{Vol}_a}{\rho_w \text{Vol}_w} + 1 \right] \left(z_2 + \frac{V_2^2}{2g} \right) \quad (3.6)$$

This equation is theoretically valid for a jet that entrains air. It is important to point out that the density of the air is three orders of magnitude lower than the density of water (approximately 1.2 kg/m³ for air versus 1,000 kg/m³ for water). When air entrainment is zero the previous equation is Bernoulli's equation. Assuming air concentration is 90% by volume at section 2, the volume of air will be nine times greater than the volume of water, but because the density of water is almost 1,000 times the density of air, the term between brackets will be approximately 1.011. The previous considerations show that a small fraction of the energy of the flow is used to move the air entrained. Consequently, the available energy of the water fraction of the jet does not change significantly even when the air concentration is high. However, air entrainment is relevant because the total energy of the jet is expanded into a larger area before impingement. The air concentration of the jet at the tailwater surface influences the velocity decay of the centerline of the jet after impingement, as was pointed out by Bohrer and Abt (1996). The rate of decay depends upon the combined density of the jet.

3.6 Kinematics of Jet Travel

It has been shown in the previous section that the amount of energy used to entrain and move air at the same speed as the water is negligible in comparison to the total energy of a jet. A compact jet is a jet that does not entrain air and will be considered for

developing an expression to calculate the maximum depth of the scour hole. If noticeable differences exist between highly aerated jets and compact jets, correction factors will be introduced if sufficient data are available.

Mainly, two different structures can release a jet: pressurized conduits and open channels. If a rectangular pressurized conduit is considered, the exit velocity of the jet is:

$$v_o = \frac{q}{b_o} \quad (3.7)$$

where: q = is the discharge per unit width; and

b_o = the thickness of the nozzle or slot.

If the issuance section is located above the tailwater surface, the jet is an impinging jet. In the case of an open channel, a considerable difference in bed elevation must exist at a section of the channel so that a jet is formed and impinges against the lower water surface without submergence. The thickness of the jet at the brink according to Rouse (Hallmark, 1955) will be:

$$b_o = 0.715 y_c \quad (3.8)$$

Hallmark reported that the measurement of the thickness of the jet was difficult because of variations in flow depth at the brink of the free overfall. When the unit discharge is known but the depth at the brink is not known, one can assume that the thickness of the jet is the depth corresponding to the critical depth:

$$b_o = \left(\frac{q^2}{g} \right)^{1/3} \quad (3.9)$$

As the jet travels to the tailwater, an increase in kinetic energy occurs. The drop height is z and is equal to the difference in elevation between the centerline of the jet and the tailwater surface. If a free overfall is considered and the losses are neglected, the available head, H_o , is equal to:

$$H_o = \frac{V_o^2}{2g} + z + \frac{b_o}{2} \quad (3.10)$$

For a jet being released by a pressurized conduit, H_o , is:

$$H_o = \frac{V_o^2}{2g} + z \quad (3.11)$$

The jet will form a scour hole with a depth Y . A sketch with the important variables is given in Figure 3.3 and shows both a free overfall jet and a jet issuing from a nozzle. The depth of scour, Y , is measured from the initial bed elevation to the bottom of the scour hole. The tailwater depth is TW . The representative size diameter is d_n . Hoffman (1998), Bormann and Julien (1990), and others and have used d_{90} as the representative particle size for calculating the depth of scour. Field observations will be used to determine the representative size diameter.

The following deduction does not take into account friction of the jet in the air. The ballistic equation is used to calculate the angle of impingement of a jet. The angle of issuance, α , is the angle of the centerline of the nozzle with respect to the vertical. V_o is the velocity at the issuance section and t is the time of travel between the issuance section and the tailwater surface of a water particle moving on the centerline of the jet.

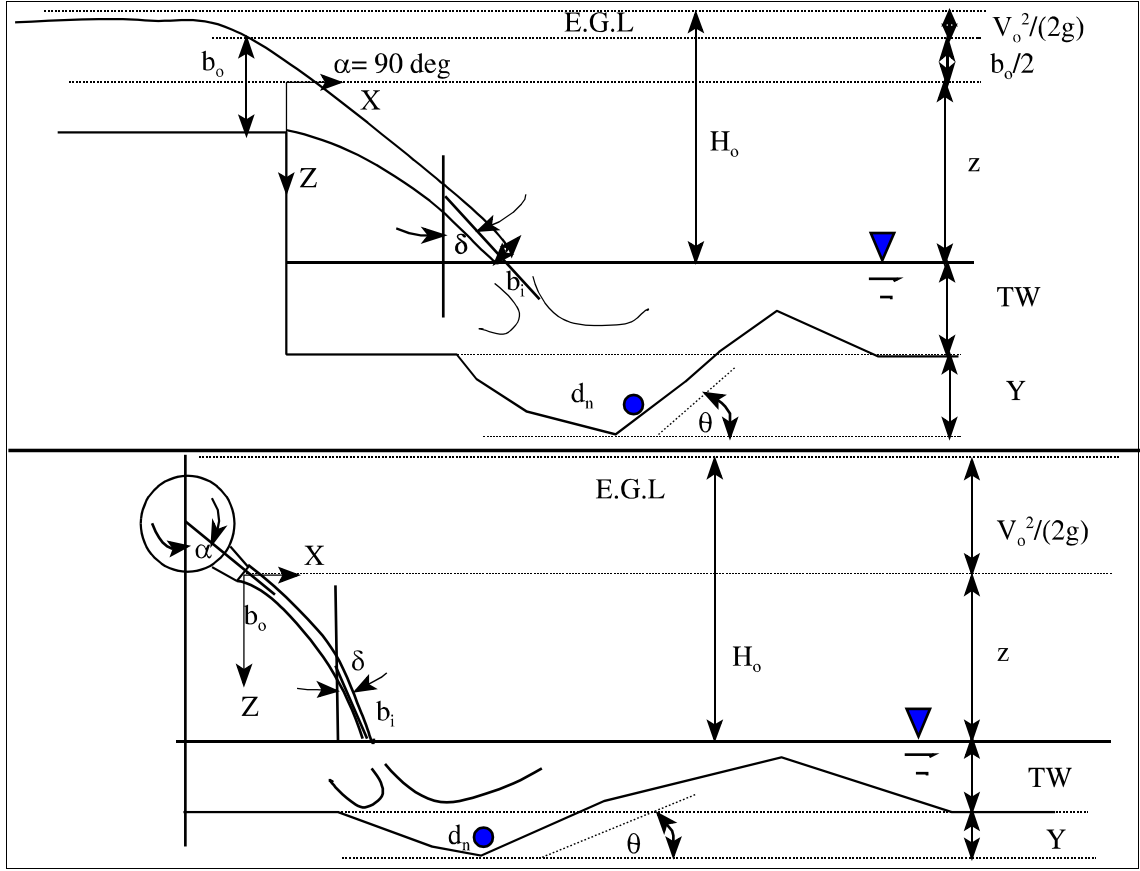


Figure 3.3. Variables of interest in this study.

If the distance from the point of release from the structure is located at a distance, z , from the tailwater elevation, and considering the acceleration of gravity:

$$z = (V_o \cos \alpha) (t) + \frac{gt^2}{2} \quad (3.12)$$

Equation (3.12) can be rearranged to find the time it takes a water particle to impinge the tailwater surface after it is released.

$$t = \frac{-V_o \cos \alpha + \sqrt{V_o^2 \cos^2 \alpha + 2gz}}{g} \quad (3.13)$$

Because velocity in the X direction is $V_o \sin \alpha$, the point of impingement at the tailwater surface will be at:

$$X = V_o \sin \alpha \left[\frac{\sqrt{V_o^2 \cos^2 \alpha + 2gz} - V_o \cos \alpha}{g} \right] \quad (3.14)$$

The vertical component of the velocity is:

$$V_y = V_o \cos \alpha + gt$$

$$V_y = V_o \cos \alpha + g \left[\frac{-V_o \cos \alpha + \sqrt{V_o^2 \cos^2 \alpha + 2gz}}{g} \right]$$

$$V_y = \sqrt{V_o^2 \cos^2 \alpha + 2gz} \quad (3.15)$$

Because V_x is a constant, the angle of impingement (measured from the vertical) will be:

$$\delta = \arctan \left(\frac{V_x}{V_y} \right)$$

or:

$$\delta = \arctan \left(\frac{V_o \sin \alpha}{\sqrt{(V_o \cos \alpha)^2 + 2gz}} \right) \quad (3.16)$$

This will also be the angle at which the bed will be impinged since the direction of the jet does not change significantly after it enters the tailwater. The magnitude of the velocity at impingement is:

$$V_i = \sqrt{(V_x)^2 + (V_y)^2}$$

$$V_i = \sqrt{((V_o \cos \alpha)^2 + 2gz) + (V_o \sin \alpha)^2}$$

Since $\cos^2 \alpha + \sin^2 \alpha = 1$, V_i can be written as:

$$V_i = \sqrt{(V_o)^2 + 2gz} \quad (3.17)$$

V_i can also be written as:

$$V_i = \sqrt{2g \left[\left(\frac{V_o^2}{2g} \right) + z \right]}$$

or if we call $H_o = \text{available head} = V^2 / 2g + z$; H_o is the theoretical available head at the tailwater surface (neglecting losses), then the theoretical velocity at impingement can be expressed as follows.

$$V_i = \sqrt{2g H_o} \quad (3.18)$$

3.7 Geometry of a Compact Falling Jet

The theoretical thickness of the jet at impingement is obtained using the principle of conservation of mass. The jet is assumed to be compact, so that the amount of air

entrained by the jet is negligible. The cross section of the jet is reduced as the jet falls. It is assumed that the width to thickness ratio is preserved throughout the trajectory of the jet unless the jet disintegrates. Therefore, $w_o/b_o = w_i/b_i = \text{constant}$ in Figure 3.4. Because the ratio of the dimensions of the cross section of the jet is assumed to be constant, the theoretical thickness of the jet at impingement is:

$$b_i = b_o \sqrt{V_o/V_i} \quad (3.19)$$

The geometry and the velocity distribution of the jet after it impinges the tailwater is expected to be a function of the thickness of the jet at the tailwater surface, b_i .

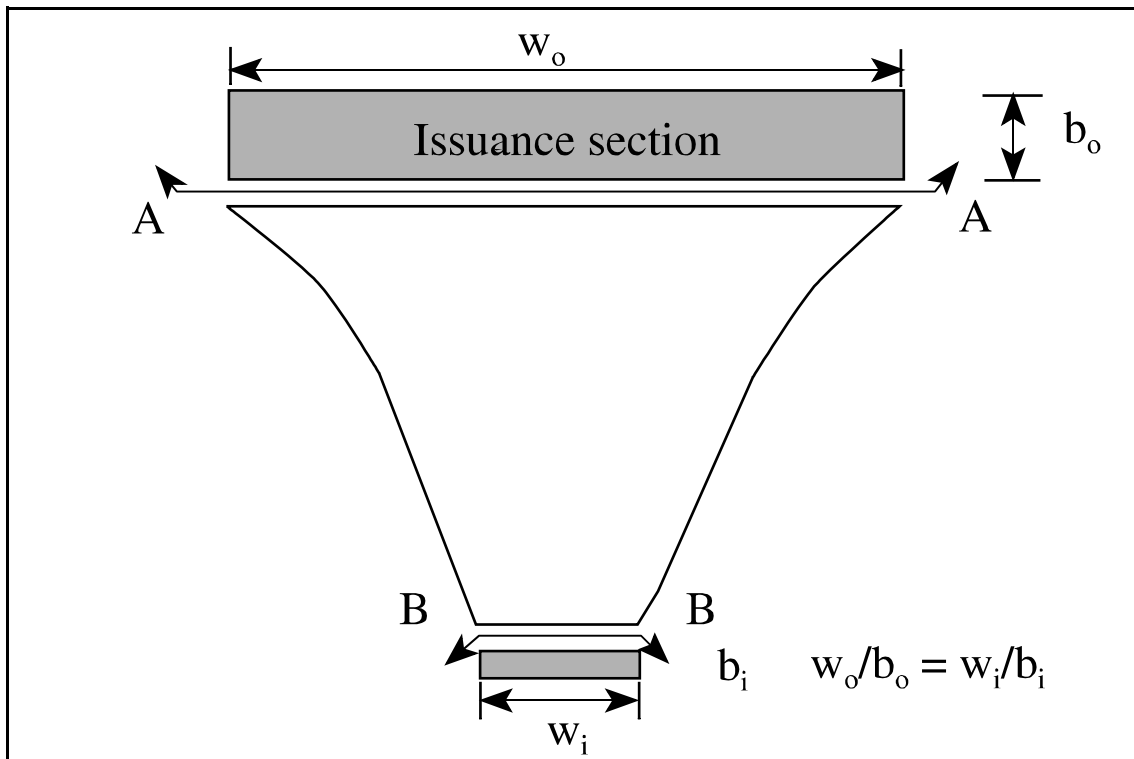


Figure 3.4. Geometry of a compact impinging jet.

3.8 Total Dynamic Available Head at the Tailwater Surface and Trajectory Length

As a falling jet travels to the tailwater, it gains speed and its cross section is reduced. If the velocity of a cross section of the jet is V and its thickness is b , the Froude number of the jet, $V/(g b)^{0.5}$, becomes a measure of the concentration of power or its intensity. The actual velocity of the jet at the tailwater surface, V_{iact} , would be equal to the theoretical velocity of impingement, V_i , if the conditions were ideal (i.e., without considering air friction and disintegration of the jet). However, in studies by Lencastre (1961), Lewis (1996) and Bohrer and Abt (1996), it was found that the actual velocity of impingement, V_{iact} , was less than the theoretical velocity of impingement, V_i . The actual velocity of impingement was as low as 70% of the theoretical velocity of impingement in Lencastre's studies when the fall height, z , was 15 times the thickness of the jet at issuance, b_o . The pressure available at a plate being impinged by a jet has been found to be both a function of L/L_d and TW/b_i . L is the trajectory length of the jet in the air. The disintegration length of an impinging jet, L_d , has been found to be a function of the unit discharge, q , and the turbulence level at issuance, ϵ according to the findings of McKeogh and Elsaywy (1980). Therefore, both the intensity of the jet given by the Froude number of the jet and its unit discharge need to be considered when deriving an expression for calculating the scouring potential of the jet. The process is assumed to be stationary (velocity and pressure fluctuations of the jet as it falls are expected to be periodic), therefore, the variable containing the time factor is neglected.

3.9 Phase Two Pressure Head Dissipation of an Impinging Jet

A purely theoretical analysis of pressure head dissipation is a very difficult task to accomplish with the mathematical tools presently available. The velocity of the jet is expected to diminish after it impinges the tailwater surface. Albertson et al. (1950) found a zone of establishment and a zone of established flow when studying submerged jets. In the zone of flow establishment, the centerline velocity of the jet was constant. The zone of established flow started where the centerline velocity of the jet started to diminish. The length of the zone of flow establishment was on the order of five to ten times the thickness of the jet at issuance. According to Hom-ma (1953), no distinct zones were found for impinging jets. Velocity decay of the centerline of the jet was detected immediately below the tailwater surface. Similar results were obtained by Bohrer and Abt (1997). Therefore, it will be assumed that velocity decay of the centerline of the jet takes place immediately after impingement. In Albertson et al.'s equation the centerline velocity of the jet is proportional to the product of the velocity of the jet at impingement multiplied and the square root of b_i/x , the ratio of the thickness of the jet at impingement and the distance "x" from the tailwater surface, as follows:

$$V_x = K V_i \sqrt{\frac{b_i}{x}} \quad (3.20)$$

If the jet impinges the tailwater surface at an angle δ , the trajectory of the jet in water, x , is equal to $TW/\cos \delta$. If $x = TW/\cos \delta$, Equation (3.20) can be rearranged as follows:

$$\frac{V_{TW/\cos \delta}}{V_i} = K \frac{1}{\sqrt{\frac{TW/\cos \delta}{b_i}}} \quad (3.21)$$

Equation (3.21) would approximately give the velocity of the jet at the ground surface if the free jet is free. However, velocities decrease in the impingement region according to Beltaos and Rajaratnam (1974). A relation between the ratio pressure heads at the bottom of a plunge pool to pressure heads at the tailwater surface (H_{gs}/H_o) and TW/b_i was found for vertical jets using Lencastre's data and is presented in Appendix A.

3.10 Pressure Distribution at the Bottom of a Plunge Pool

The reduction in available head of the jet after the jet enters the tailwater was discussed in a previous section. A jet with an available head at the tailwater surface, H_{act} , will have an available head, H_{gs} , and a width, b_{gs} , at the original bed surface as shown in Figure 3.5. A scour hole with a depth, Y , will be formed if the available energy of the jet exceeds the energy used in seepage flow and the energy necessary to overcome the resisting forces of the bed particles. Particles will be moved when the fluid moves at a velocity, V_p , which is sufficient to move the particles up the downstream slope, at an inclination θ . A drag coefficient, C_d , is usually associated with the size and shape of natural particles. The depth of the scour hole is also a function of the size of the particles and their submerged density, $\rho_s - \rho_w$. The particles at the bottom of the scour hole are characterized by a particle of diameter, d_n . The density of the jet and the tailwater are assumed to be the same.

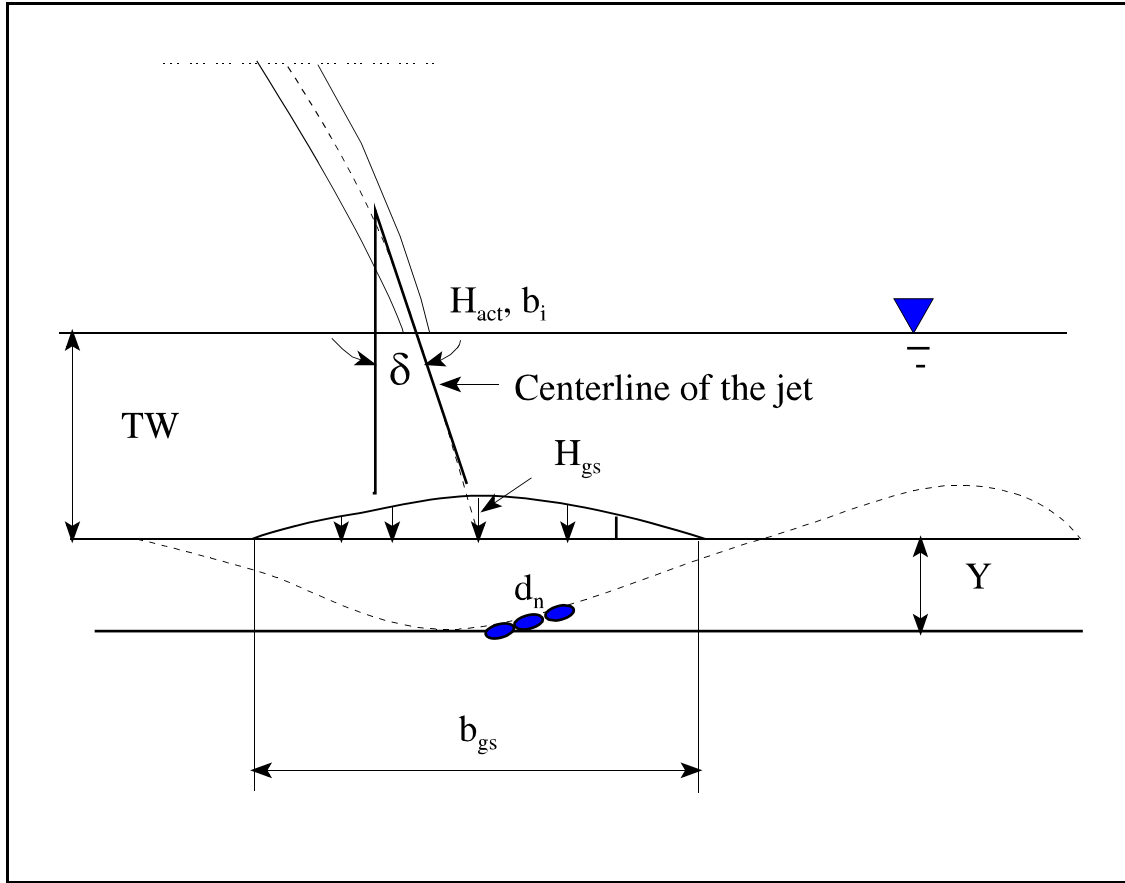


Figure 3.5. Variables of interest defining the depth of the scour hole.

3.11 Condition of Incipient Motion at the Bottom of a Scour Hole Using a Moment Model

The hydrodynamic moments applied to a particle of diameter d_n and specific gravity, G , have to overcome the resisting moments of the weight parallel to the slope and of the component of the weight perpendicular to the slope to induce motion in a particle. The downstream slope of the scour hole is θ (see Figure 3.6). The threshold condition of motion occurs when the driving moments exceed the resisting moments of the particle. Consequently:

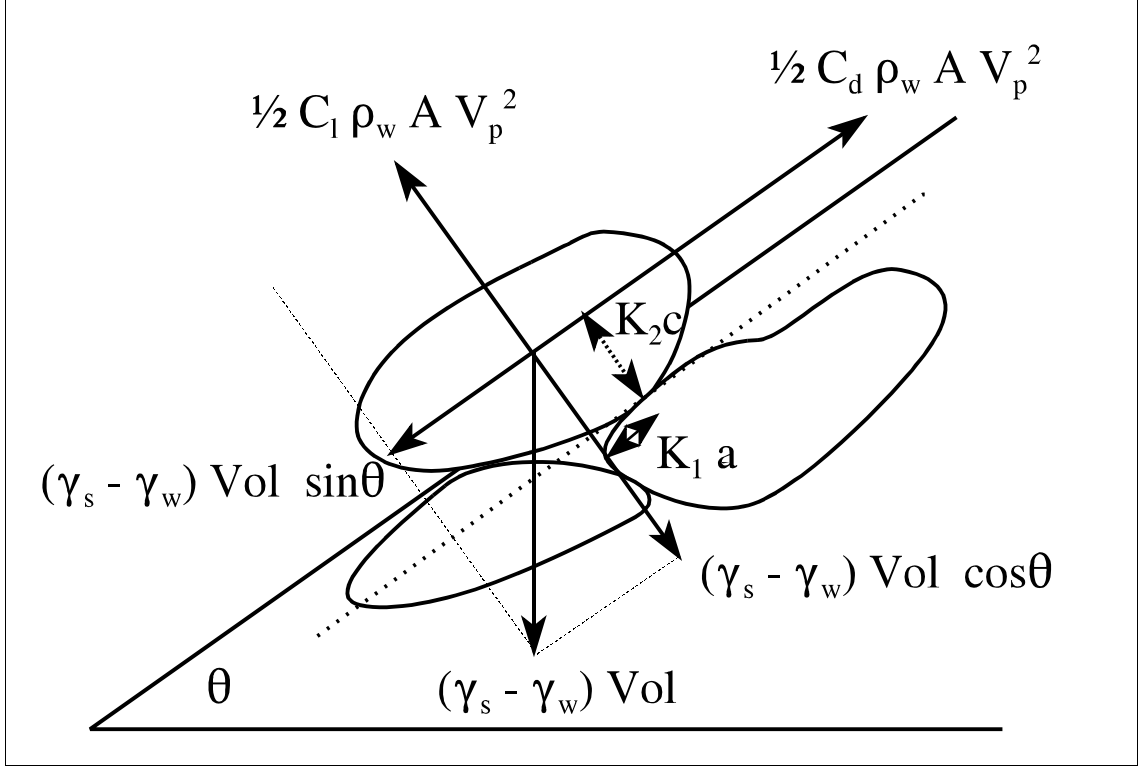


Figure 3.6. Moments acting on a particle located on the downstream slope of the scour hole.

$$(\mathbf{K}_1 \mathbf{a}) \frac{1}{2} \mathbf{C}_l \rho_w \mathbf{A} \mathbf{V}_p^2 + (\mathbf{K}_2 \mathbf{c}) \frac{1}{2} \mathbf{C}_d \rho_w \mathbf{A} \mathbf{V}_p^2 = (\gamma_s - \gamma_w) \mathbf{Vol} \sin \theta (\mathbf{K}_2 \mathbf{c}) + (\gamma_s - \gamma_w) \mathbf{Vol} \cos \theta (\mathbf{K}_1 \mathbf{a}) \quad (3.22)$$

The lift coefficient, C_l can be expressed as a fraction of the drag coefficient, C_d , so that

$C_l = K_3 C_d$. Considering that $\gamma_s = g \rho_s$, $\gamma_w = g \rho_w$, $\mathbf{Vol} = \pi d_n^3/6$, and $\mathbf{A} = \pi d_n^2/4$,

Equation (3.22) can be simplified and reduced as follows:

$$\mathbf{V}_p = \sqrt{\frac{4 \mathbf{g}}{3 \mathbf{C}_d} \left(\left(\frac{\rho_s}{\rho_w} \right) - 1 \right) d_n} \sqrt{\frac{\left[\sin \theta + \left(\frac{\mathbf{K}_1 \mathbf{a}}{\mathbf{K}_2 \mathbf{c}} \right) \cos \theta \right]}{1 + \mathbf{K}_3 \left(\frac{\mathbf{K}_1 \mathbf{a}}{\mathbf{K}_2 \mathbf{c}} \right)}} \quad (3.23)$$

The velocity of the particle traveling in a fluid in motion is approximately the velocity of the fluid that surrounds it. The drag coefficients for gravel, cobbles and larger particles has been found to be approximately 1.5. The acceleration of the gravity is approximately constant on Earth. Hence, the velocity required to remove particles from the bottom of the scour hole when particles are relatively large, is essentially a function of the characteristic particle size diameter, d_n ; the submerged specific gravity, $(\rho_s/\rho_w - 1)$; and the interlocking of the particles, given by $\{[\sin \theta + (K_1 a)/(K_2 c) \cos \theta]/[(1 + K_3 (K_1 a)/(K_2 c))]\}^{0.5}$. The ratio of moment arms, $(K_1 a)/(K_2 c)$ is assumed to be unity by Stevens and Simons (1971). In the data analysis, $(K_1 a)/(K_2 c)$ will be allowed to vary between 0.5 and 1.5, once the range of values of θ is known. The lift force is usually less than the drag force. This is especially true when the three dimensions of the particle are approximately similar, and when the flow is approximately parallel to the longest axis. Therefore K_3 , the lift coefficient to drag coefficient ratio, will be allowed to vary between 0.1 and 0.4 in the analysis.

3.12 Equation to Calculate the Depth of Scour Caused by a Rectangular Jet in a Cohesionless Bed

The processes occurring during the formation of a scour hole were described in Section 3.4. The variables of importance were specified. Using the Pi-Buckingham theorem, dimensionless parameters were found and summarized in Equation (3.2). Sections 3.5 through 3.11 served to assess the importance of the variables to use in the development of an expression to predict the maximum depth of the scour hole produced by an impinging jet. Assumptions made in the development of equations used to calculate

the final depth of scour will be explicitly stated. An equation used to predict the maximum depth of scour must include a term that summarizes the effect of jet travel in the air, the effect of energy dissipation in the tailwater depth, and the resistance of the bed to jet scour.

The capacity of penetration of the water by the jet is given by the available power of the jet at the tailwater surface and its unit discharge. In a rectangular jet, the discharge per unit length characterizes the flow, since the distribution of the flow is expected to be constant along its width. Combining (TWg/V_o^2) , V_i/V_o , and b_i/TW , the parameter $V_i^2/(g b_i)$ is obtained. This is a form of the Froude number, called the Froude number of the jet at impingement. This parameter represents the energy level of the jet per unit discharge at the tailwater surface. The area of an impinging jet diminishes as it falls due to an increase in velocity, unless it disintegrates. A higher impact Froude number in an impinging jet indicates a greater concentration of energy in a smaller area. Therefore, the Froude number is an indication of the capacity of penetration of the jet. Once the jet impacts the water it expands. It is assumed that the Froude number of the jet at impact determines the geometry of the jet after impingement.

The available power at the ground surface is the fraction of the power of the jet that remains after the jet penetrates the tailwater depth for a distance $TW/\cos \delta$. A scour hole is formed if the available power of the jet at the ground surface is greater than the resisting properties of the bed material. Taking into account the geometry of the impinging jet, b_i/TW and δ are combined and the parameter $TW/(b_i \cos \delta)$ is obtained. The dissipating power of the tailwater is given by the dimensionless parameter $(TW/\cos \delta)/b_i$.

From Equation (3.23), it can be inferred that the parameter representing the resisting properties of the bed material must include a term that contains the specific gravity, the

gravitational acceleration, and the characteristic particle size diameter. The combination of the parameters $(TW V_o \rho_s)/\mu_w$ and $(TW V_o \rho_w)/\mu_w$ results in the dimensionless parameter ρ_s/ρ_w , which is the specific gravity of the bed material, G .

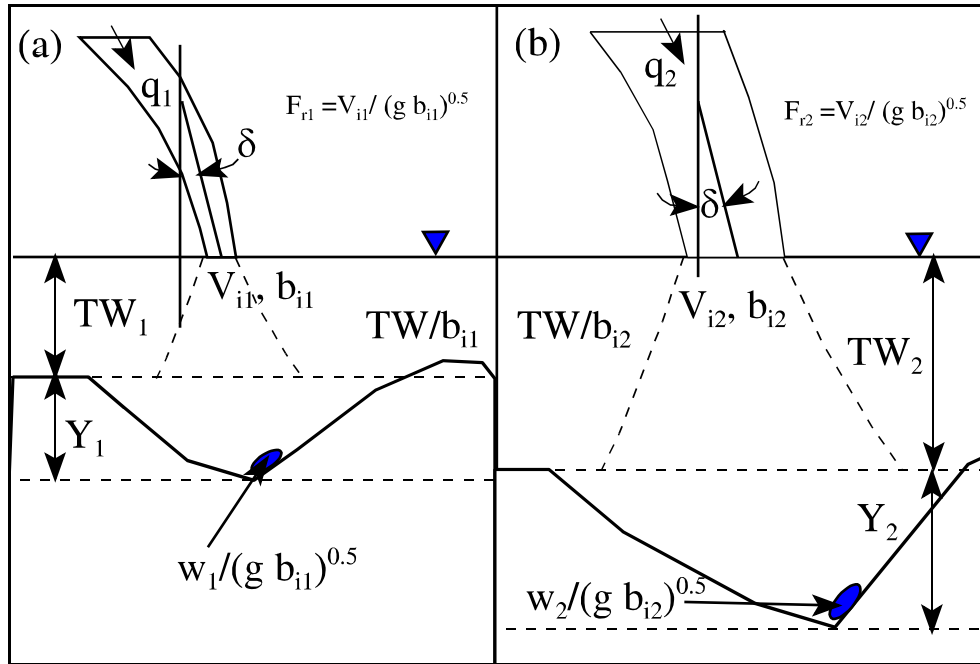
The fall velocity of a particle can be used as a parameter that indicates the particle's resistance to scour. When a particle attains its terminal velocity, the drag forces are equal to the submerged weight of the particle. If a particle is subjected to a velocity significantly greater than its fall velocity, it is expected to be carried away by the flow. Therefore, considering that a fluid such as water is isotropic, the minimum forces required to induce motion in a particle have to be in the same order of magnitude as the drag occurring when a particle is settling. Other considerations are also necessary. When a particle is placed on a bed, the interlocking with other particles increases the force required for dislodgement. The interlocking of the particles due to their position is considered to be random. In addition, the particle is not fully exposed to the flow due to the presence of other particles. Roughness also affects the flow pattern. The distance traveled by the jet in the scour hole and the pressure head distribution at the original ground surface is related to the velocity at the bottom of a scour hole, V_p . Furthermore, when the particles under consideration are greater than 1 mm, the drag coefficient is considered constant and equal to 1.5. The fall velocity of a coarse particle, w , is approximately given by (Julien, 1995):

$$w = \sqrt{(G - 1) g d_n} \quad (3.24)$$

The fall velocity, w , as presented in Equation (3.24) is the first term on the right hand side of Equation (3.23). Therefore, the particle entrainment velocity, V_p , is a function of the fall velocity of the particle, w , and the interlocking of the particles represented by

$[(\sin \theta + (K_1 a/K_2 c) \cos \theta)/(1 + K_3(K_1 a/K_2 c))]^{0.5}$ in Equation (3.23). The dimensionless particle fall velocity, $w/(g b_i)^{0.5}$, results from combining the dimensionless parameters w/V_o , $(TW g)/V_o^2$, and b_i/TW .

Figure 3.7 shows two impinging jets. In Figure 3.7(a), a thin jet impinges the tailwater surface with a thickness b_{i1} and velocity V_{i1} . The Froude number is equal to F_{r1} . The relative tailwater depth is TW_1/b_{i1} . In Figure 3.7(b), a thicker jets impacts a tailwater depth with a velocity V_{i2} and thickness b_{i2} . Assume that the dimensionless fall velocity of the particle, $w/(g b_i)^{0.5}$ is the same in both cases. Furthermore, the Froude number at the tailwater surface, $V_i/(g b_i)^{0.5}$, the relative tailwater depth, TW/b_i , and the angle of impingement, δ , are also the same. The distribution of the forces at the ground surface will be similar. The distribution of forces at the original ground surface determines the power of penetration of the jet.



Figures 3.7(a) and (b). Similarity between the pressure distribution of two jets.

The available power of each jet is reduced as the jets penetrate the bed. After the first jet scours the ground surface to a depth Y_1 , its power is reduced until it can barely lift the particles near the bottom of the scour hole. The second jet creates a scour hole with depth Y_2 . Geometric similarity exists between the two scour holes. The similarity between the depths of the scour holes produced by both jets will be given by the parameter Y^3g/q^2 .

$$\frac{(Y_1/(q_1^2/g)^{1/3})}{(Y_2/(q_2^2/g)^{1/3})} = 1 \quad (3.25)$$

The dimensionless parameters of importance in the development of an equation used to predict the depth of scour caused by impinging jets in cohesionless beds are summarized below:

$$f_5 \left(\frac{Y^3 g}{q^2}, \frac{V_i}{\sqrt{g} b_i}, \frac{(TW/\cos \delta)}{b_i}, \frac{w}{\sqrt{g} b_i}, \sqrt{\frac{\sin \theta + \left(\frac{K_1 a}{K_2 c} \right) \cos \theta}{1 + K_3 \left(\frac{K_1 a}{K_2 c} \right)}} \right) = 0 \quad (3.26)$$

Equation (3.26) can also be expressed as:

$$f_6 \left(\frac{Y^3 g}{q^2} \right) = f_7 \left(\frac{V_i}{\sqrt{g} b_i}, \frac{(TW/\cos \delta)}{b_i}, \frac{w}{\sqrt{g} b_i}, \sqrt{\frac{\sin \theta + \left(\frac{K_1 a}{K_2 c} \right) \cos \theta}{1 + K_3 \left(\frac{K_1 a}{K_2 c} \right)}} \right) \quad (3.27)$$

The parameter $(TW/\cos \delta)/b_i$ is obtained from the analysis of Lencastre's data. Taking the cubic root of the dimensionless parameter Y^3g/q^2 , a new parameter is obtained in the left hand side of Equation (3.27), $Y/(q^2/g)^{1/3}$. A jet penetrating a tailwater with a higher Froude number is expected to have relatively more power of penetration. Consequently, the relative depth of scour, $Y/(q^2/g)^{1/3}$, will be assumed to be directly proportional to a power of the Froude number of the jet at impingement. As the relative tailwater depth increases, the relative depth of scour decreases. Therefore, the relative depth of scour $Y/(q^2/g)^{1/3}$ will be assumed to be inversely proportional to a power of $(TW/\cos \delta)$. Furthermore, as the dimensionless fall velocity $w/(g b_i)^{0.5}$ increases, the relative depth of scour, $Y/(q^2/g)^{1/3}$, decreases. The relative depth of scour is inversely proportional to a power of $w/(g b_i)^{0.5}$. Considering that $y_c = (q^2/g)^{1/3}$, the final form of Equation (3.27) is given in Equation (3.28):

$$\frac{Y}{y_c} = K \frac{\left(\frac{V_i}{\sqrt{g b_i}} \right)^a}{\left[\frac{(TW/\cos \delta)}{b_i} \right]^b \left(\frac{w}{\sqrt{g b_i}} \right)^c} f \left(\sqrt{\frac{\left[\sin \theta + \left(\frac{K_1 a}{K_2 c} \right) \cos \theta \right]}{1 + K_3 \left(\frac{K_1 a}{K_2 c} \right)}} \right) \quad (3.28)$$

When the final equation is developed for practical use, a multiple correlation will be sought using the parameters proposed before, so that the residuals of the predicted values of scour with respect to the measured values of scour, are a minimum.

CHAPTER 4

RESEARCH FACILITIES, EQUIPMENT AND PROCEDURES

The experimental work for this study was conducted at the Dam Foundation Erosion (DFE) Facility. The DFE Facility consists of conveying structures and control valves, a jet diffuser, a tailbox, and outlet structures. Tests have been carried out since the completion of the construction and implementation of the DFE Facility. The description of the DFE Facility, the equipment used in the tests, and the procedures followed in the experimental phase of this study are given in the next pages.

4.1 The Dam Foundation Erosion Facility

The DFE Facility was built at the Engineering Research Center, Colorado State University (CSU), Foothills Campus and is shown in Figures 4.1 and 4.2. A 61 cm (24 in.) pipeline diverts flow from the main pipeline to the DFE Facility. Horsetooth Reservoir located west of the Foothills Campus provides water for all the experimental work conducted at the facilities. Head varied due to fluctuations in the reservoir level. A maximum static head of approximately 230 ft (70 m) was available. Flow was controlled by a 61 cm (24 in.) butterfly valve located approximately 183 m (600 ft) north of the DFE Facility. Flow could be monitored at the valve house by a digital output connected to the flow meter located at the Engineering Research Center. A 16 cm (6 in.) by-pass pipeline

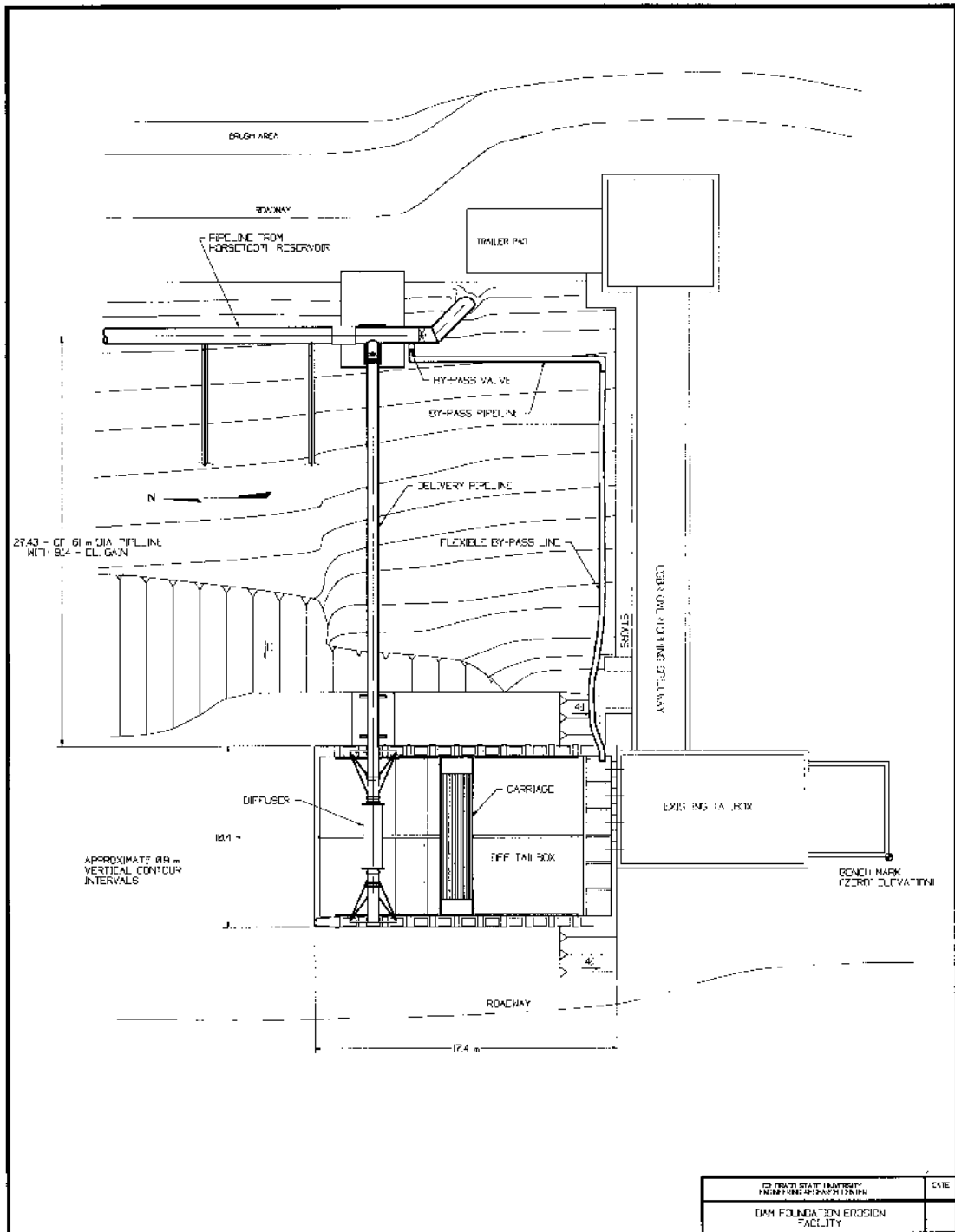


Figure 4.1. Dam Foundation Erosion Facility.

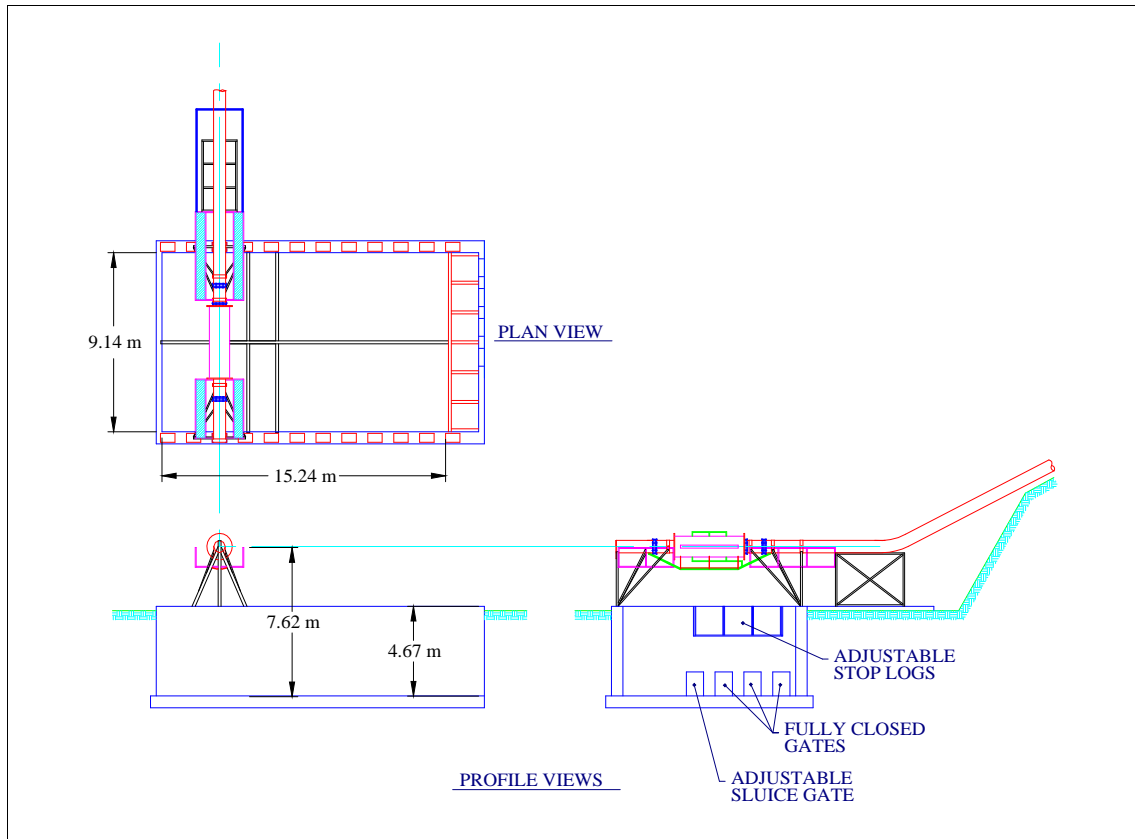


Figure 4.2. Dam Foundation Erosion Facility -- plan, side elevation and front elevation.

connected to a plastic sleeve allowed diversion of the flow for backfilling the tailbox or when it was necessary, such as at the end of a test to prevent further erosion of the bed. A diffuser was mounted on a supporting structure. The diffuser was a slotted 61 cm (24 in.) pipe inside a 106.7 cm (42 in.) pipe which contains the nozzle. At first a slot was used as an outlet. The nozzle was added after one trial run performed in June, 1996, because the distribution of the discharge across the outlet was very uneven. A nozzle was designed and attached to the 106.7 cm (42 in.) pipe. The nozzle was a metal prism open on two ends and had a rectangular converging section. It was 3.05 m (10 ft) wide by 8.73 cm (3 7/16 in.) high at the issuance section. The angle of the nozzle with respect to the vertical could be

adjusted by rotating the diffuser. Further information about the diffuser and Pitot tube installation can be found in Appendix B. Four Pitot tubes were installed at the issuance section to measure the velocity of the jet. The tailbox is a 16.76 m (55 ft) by 9.14 m (30 ft) by 4.57 m (15 ft) reinforced concrete structure in which material is placed for testing. Staff gages to establish elevations were painted on the east and west walls of the tailbox at 0 m, 1.52 m (5 ft), 3.05 m (10 ft), 4.57 m (15 ft), 7.62 m (25 ft) and 12.19 m (40 ft) from the north wall.

Divisions for the staff gage were painted every 3.05 cm (0.1 ft). At the end of the tailbox, an end basin is formed by placing metal sheets 1.83 m (6 ft) from the south wall of the tailbox. The end basin is used to backfill the tailbox with water without producing initial scour. A slide gate controls the tailwater elevation and is driven by an electric motor. The flow is conveyed to College Lake by an earth channel.

4.2 Test Procedures and Data Acquisition Equipment

Before testing began, an erodible bed was installed in the basin. The erodible bed was a 19.05 mm (3/4 in.) roadbase. The gradation of the bed material is shown in Figure 4.3. A crane was used to dump material in the tailbox and a crew of four people leveled the tailbox bed material to a specified ground elevation using shovels and rakes. The tailbox was filled with water to saturate the bed material. After settlement took place, more material was added to the tailbox to attain the specified elevation. The bed was surveyed before the test was conducted. Soil samples were collected. Some floating sentinel elements (tennis balls) were placed at different locations and buried at different depths. The tennis balls were painted with different colors for each location. Their

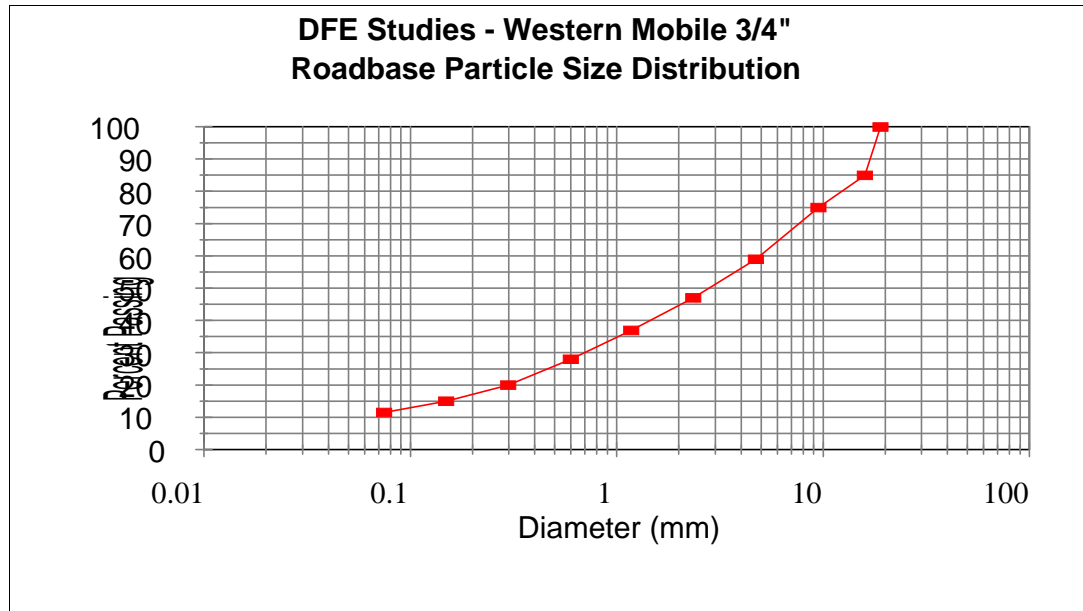


Figure 4.3. Gradation of bed material used in Dam Foundation Erosion Studies.

positions were documented using a tape to measure the distance from the north and east walls, and an engineer's level was used to record the elevation of the top of the tennis balls. For this study, the nozzle was set at three different angles: 15°, 25°, and 35° from vertical. The position of the nozzle was documented, as well as the target tailwater depth.

Safety and procedural checks were conducted before starting every test. The delivery valve was closed and the by-pass valve was opened. The main valve was opened slowly and discharge for filling the tailbox was never in excess of 0.283 m³/s (10 cfs) to prevent damage to the by-pass pipeline and the sleeve. Once the target tailwater elevation was attained, an operator opened the delivery valve to divert the flow to the DFE Facility, and the by-pass valve was closed as the flow was increased. Also, the delivery valve was opened as the main valve was opened so that the pressure at the junction of both pipes was less than 6.9 kPa (20 psi) at all times to prevent damage to the pipeline. This procedure continued until the target discharge was attained. Discharge was held constant

at $2.735 \text{ m}^3/\text{s}$ (96.6 cfs). A camcorder was used to record the tests and photographs were taken during the tests. Figure 4.4 shows the jet flowing at $2.735 \text{ m}^3/\text{s}$. This photograph was taken from the west side of the tailbox. Times were recorded as the discharge changed. The flow was considered stable after five minutes of continuous readings in which the average flow was approximately within 5.66 l/s (0.2 cfs) of the target discharge. The test started after the tailwater depth held constant and discharge readings fluctuated around the target discharge. Tailwater depths, discharges, and times were documented. The flow was kept at the test discharge for 104 minutes.



Figure 4.4. Photograph of the DFE Facility from the west side.

Readings of the velocity head at the nozzle and available head at the diffuser were taken during the tests. Piezometer readings were taken by the manometer installed in the northwest corner of the tailbox. Piezometers were connected to manometer tubes located

at the issuance section of the nozzle and also to the diffuser. Two people were necessary to read the pressure heads because of fluctuations of the water level. The readings did not change significantly in the first eight tests. No piezometer data was taken for the last four tests. Discharge was always set at 2.735 m³/s (96.6 cfs). Water depths upstream and downstream of the area of impingement of the jet were recorded as well. Tailwater depths were observed using the staff gages painted on both walls in the early stages of the project; and depth probes, as well as staff gages were used in the last four tests. Up to three staff gage readings were taken in the east and west walls at different times. Photographs of the jet and the area of impingement were taken using a Minolta Maxxum 7000i 35 mm camera with 35 - 80 mm zoom lenses. The jet and water surface in the tailbox were recorded using a JVC GRS77 - Super VHS compact videocamera from different angles at different times. The sentinel elements buried were uncovered and appeared in the surface while the discharge was being set. The color of the sentinel elements was also recorded, since at each location a different color was chosen. The time, the discharge, and the tailwater at which the floating sentinel elements appeared in the surface were also recorded.

After each test was concluded, tailwater depth was increased by closing the tailgate. Discharge was diminished gradually, trying to keep the tailwater elevation as high as possible, to prevent further scour. Lower discharges might have scoured the upstream end of the scour hole, possibly producing misleading results. In most cases, the tailgate started to be closed exactly 104 minutes after the specified discharge was attained. The flow was bypassed, and eventually shut down. When the main valve was completely closed, the tailbox was allowed to drain. Dewatering took place with the tailgate almost fully closed, so that the bed would not be seriously disturbed after the tests concluded. Photographs of

the mound and other distinct features were taken during dewatering, but most of the post-run data collection took place the next day. Photographs were taken from different angles. Also, video recording took place immediately after the photographs were taken.

Surveying was usually carried out one day after the tests were concluded. A 1.52 m (5 ft) by 1.52 m (5 ft) grid was used to document the final elevations. Extra points were taken near the deepest scour point, and where noticeable changes in slope occurred. Marks on the walls and on the structural elements were used as references to run a string and mark the lines on the ground. Figure 4.5 shows the bed being surveyed after a test. The depth was recorded either using a point gage placed on the carriage or an engineer's level and a Lietz fiberglass engineer's rod. Contour lines were plotted using Surfer[®] for Windows and lateral and longitudinal profiles of the scour hole were plotted using



Figure 4.5. Surveying of the bed after a test.

Grapher® for Windows. Both computer programs were developed by Golden software and allow one to view and analyze geometric characteristics of the scour hole. It was found that Surfer® was very sensitive to the type of algorithm used to calculate the contour lines. Linear interpolation was the algorithm that best reproduced the geometric characteristics of the scour hole. Comparisons between the photographs, video tapes and plots, and the outcome of the contour lines using different interpolations were made to choose the algorithm.

Soil samples were collected at the bottom of the scour hole for some tests performed in 1996. Soil samples were collected at different sections in the last four tests. They were collected at the upstream slope of the scour hole, at the bottom of the scour hole, at the downstream slope of the scour hole, and on top of the mound. Two and a half kilograms samples were stored in freezer bags and labeled for tests. Particle size distribution tests were carried out afterwards in the sedimentation laboratory of the Engineering Research Center. Particle size distribution tests were carried out following ASTM procedures and standards, with the exception that it was convenient to use different size sieves for most of the tests.

4.3 Velocity and Air Concentration Tests

Jet velocity and air concentration tests were carried out between erosion tests in 1997. A backflushing Pitot tube was used to measure velocities. Backflushing is used because a constant flow of water is run through it in a direction opposite to the velocity to be measured in order to prevent air bubbles from entering the Pitot tube ports. The Pitot tube was set at a fixed elevation. A probe was mounted near the Pitot tube to measure

air concentration. Both the backflushing Pitot tube and the air concentration probe were mounted on a circular plate that was connected to a wheel. The angle of the Pitot tube could be adjusted during the tests. Because of the highly turbulent jet flow, vibrations were expected, and the Pitot tube and the air probe were mounted on an arm attached to the boom of a hydraulic crane and then clamped to the carriage. The hydraulic crane was parked outside the DFE approximately near the zone of impingement of the jet. The boom was lowered until a target elevation was reached. The Pitot tube arm was bolted to two steel H beams that were welded to the DFE carriage. Two steel cables provided tension for fine adjustments. Final adjustments were made manually. The final elevation of the tip of the Pitot tube was checked using an engineer's level and a leveling rod. Filling of the tailbox was conducted in the same manner as the scour tests. After attaining the specified discharge, the tailgate was used to control the tailwater depth. The tailwater elevation was changed to observe changes in the measured velocities and air concentrations as the depth above the Pitot tube increased. A data acquisition program, DATAQ[®], was used to store data acquired during the velocity tests. A DATAQ[®] DI-220 digital/ analog data acquisition box was used as an interface and a Byte 386-SX computer was used to store data and process preliminary information. The angle of inclination of the backflushing Pitot tube was changed until a maximum velocity was obtained. The final elevation of the Pitot tube was checked after the tests were completed.

4.4 Fissured Rock Tests

Fissured rock tests were carried out at the DFE Facility. Blocks were utilized to simulate uniformly fissured rocks. They were 0.39 m (15 ½ in.) long, 0.20 m (8 in.)

wide, and 0.064 m (2 ½ in.) thick and they were flat on one side, fluted on the other side. A block is shown in Figure 4.6. A sliding test was carried out to determine the angle of friction of the blocks. Two blocks were placed on a movable flat surface, and two blocks were placed on top of them. The angle of inclination was varied until sliding was detected. The bottom blocks were fixed and stationary and the upper blocks started sliding at an angle of 36 degrees from horizontal. Blocks were installed in the DFE Facility in an area 6.1 m (20 ft) by 6.1 m (20 ft), as shown in Figure 4.7. The blocks were set at a 45° angle pointing upstream. The top edge of the blocks was set at an elevation of 2.13 m (7.00 ft) with respect to the reference level. The dimensions of the testing area, 6.1 m by 6.1 m (20 ft by 20 ft), were selected based upon the dimensions of the scour hole for low tailwater tests for an angle of issuance of 15 degrees from vertical.

Piezometers were installed in nine blocks in pairs, so that static pressure could be read. Tubes were laid from a manometer board located south of the tailbox to different positions within the testing section. They are labeled according to their position with respect to the center of the mat. The center block is labeled "C" and the other eight are labeled according to their position with respect to the center block. For example, the block N8 is a block located 8 ft (2.44 m) north of the center block, and W4 is a block located approximately 4 ft (1.22 m) west of the center block. Because two tubes were installed in each block as shown in Figure 4.6, numbers were used to identify their position. Tap 1 is the upper tap and tap 2 is the lower tap. Consequently, the full ID code for a tap is the block to which they belong and their position within the block. The lower tap of a block located 8 ft (2.40 m) south of the center block is S82. The arrangement of the manometer



Figure 4.6. Block used in a fissured rock test with tubes installed.



Figure 4.7. Simulated fractured rock testing surface.

tubes before the blocks are installed is shown in Figure 4.8. Piezometers are shown in Figure 4.6.



Figure 4.8. Piezometers setup prior to block installation.

The tailbox was backfilled using the by-pass conduit at a constant rate of $0.227 \text{ m}^3/\text{s}$ (8 cfs). When the tailwater elevation was 3.35 m (11 ft), the DFE valve was opened. The by-pass valve was slowly closed. The flow was increased until attaining the target initial discharge. The initial discharge was $0.99 \text{ m}^3/\text{s}$ (35 cfs). Tailwater depth was lowered to a minimum (depth corresponding to normal depth for that flow), and no scour was detected. Flow was increased until dislodgement of the blocks was detected. The tailbox was allowed to drain, and tests results were documented. Photographs were taken from different angles and a video camera was also used to record the outcome of this experiment.

A test was conducted in which the blocks were dislodged from the second layer. Discharge was increased from $1.416 \text{ m}^3/\text{s}$ (50 cfs) to $1.982 \text{ m}^3/\text{s}$ (70 cfs), when the bottom blocks were dislodged. The breadth of the jet was measured when the discharge was $1.416 \text{ m}^3/\text{s}$ (50 cfs) and when it was $1.982 \text{ m}^3/\text{s}$ (70 cfs). The tailbox was allowed to drain and photographs and video were taken again.

Finally, the discharge was increased to $2.775 \text{ m}^3/\text{s}$ (98 cfs) which corresponded to a unit discharge of $0.910 \text{ m}^2/\text{s}$. Several blocks were dislodged from the bottom layer and swept away. Blocks sunk into the hole while underlying material was being pumped out. Some top blocks and bottom blocks were broken. The maximum depth of scour was measured and photographs and video were taken.

CHAPTER 5

DATA COLLECTION

5.1 General

Twelve scour tests were conducted at the DFE Facility between August, 1996, and September, 1997, to study the influence of the angle of impingement and tailwater depth on the final dimensions of the scour hole. Discharge was held constant at $2.735 \text{ m}^3/\text{s}$ (96.6 cfs), which corresponded to a unit discharge of $0.897 \text{ m}^2/\text{s}$ ($9.66 \text{ ft}^2/\text{s}$). The duration of the tests was 104 minutes. A summary of the tests performed between August, 1996, and September, 1997, is shown in Table 5.1. The complete data set is presented in Appendix C. Tests were conducted trying to use similar tailwater depths for each set of tests conducted for the three different angles of issuance of the jet. This allowed a better comparison between tests. Figure 5.1 shows the relation between the depth of scour, Y , and the tailwater depth, TW , for each angle of issuance. In the first part of this study, the only variables that changed were the tailwater depth, bed elevation, and the angle of impingement. The rest of the variables, such as unit discharge, bed material, the characteristics of the nozzle, and the tailbox remained constant. Because the elevation of the point of issuance was approximately fixed (it changed slightly when the angle of issuance was changed), changing the tailwater elevation also affected the fall height of the jet.

Table 5.1. Summary of tests.

Angle of Nozzle from Vertical - α (deg)	Date of Test	Fall Height z (m)	Angle of Impingement δ (deg.)	Water Depth TW (m)	Δ TW - Drawdown (m)	Max Depth of Scour Hole - Y (m)
15	09/09/96	3.79	11.44	0.27	0.05	1.83
15	08/26/96	3.48	11.64	0.57	N/A	1.55
15	09/03/96	3.12	11.89	0.85	0.09	1.50
15	09/23/96	2.87	12.06	1.85	N/A	0.99
25	09/02/97	4.32	18.35	0.41	0.11	1.49
25	09/11/97	3.99	18.68	0.77	0.13	1.30
25	10/03/96	3.55	19.15	1.17	0.12	1.03
25	09/30/96	2.94	19.87	1.80	0.05	0.94
35	07/23/97	4.37	25.23	0.50	0.11	1.19
35	07/16/97	3.92	25.87	0.84	0.14	0.91
35	10/09/96	3.60	26.36	1.16	0.19	0.88
35	10/18/96	2.98	27.40	1.80	0.11	0.63

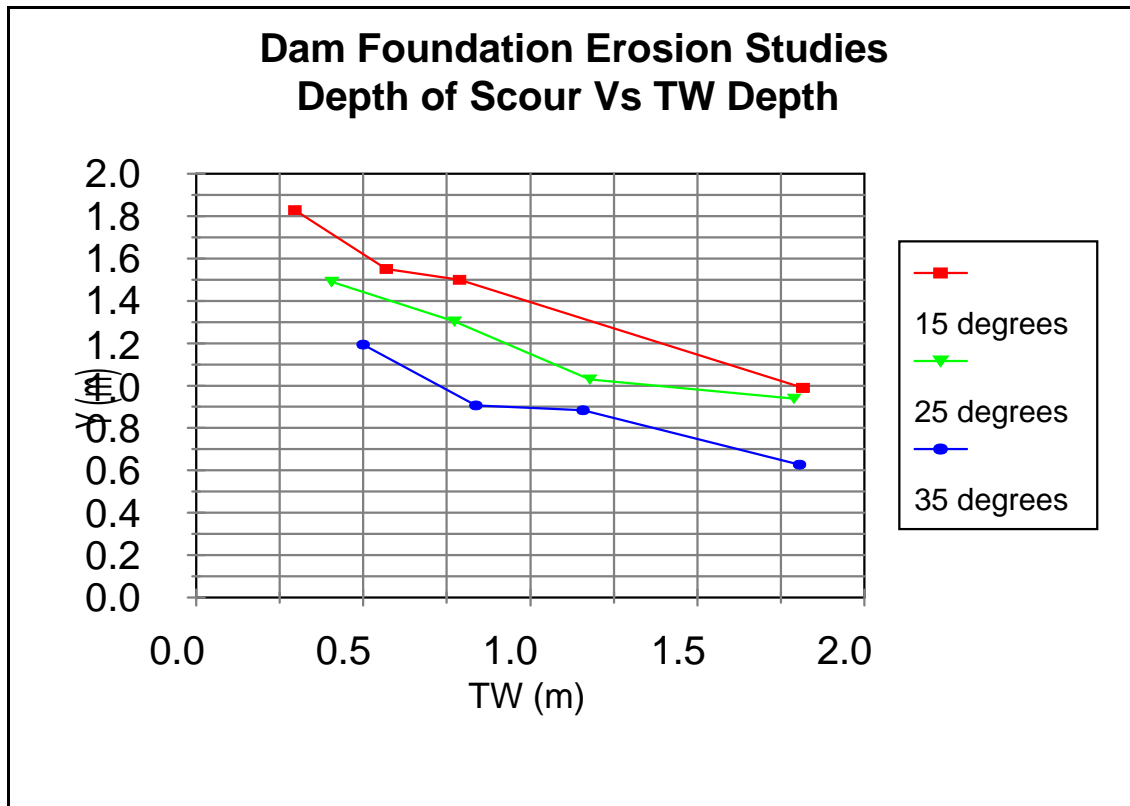


Figure 5.1. Depth of scour hole (Y) versus tailwater depth (TW).

Two scour tests were conducted using blocks to simulate fractured rock. Three thousand six hundred blocks were placed in two layers at a dip angle of 45 degrees. Discharge was increased until the first layer was dislodged from the matrix at a discharge of $1.13 \text{ m}^3/\text{s}$ (40 cfs). In a posterior test, discharge was increased several times. The depth of scour did not increase until the second layer was dislodged at $1.982 \text{ m}^3/\text{s}$ (70 cfs).

5.2 Appearance of the Jet

The flow was very turbulent at the section of issuance in tests conducted at the DFE Facility. Because of inertia, water particles tended to maintain the direction that they had at the issuance section. Jet particles did not follow a straight line because they were affected by the acceleration of gravity. The trajectory of the centerline of the jet and its edges can be described as a parabola, and the jet expanded. Due to this expansion, air was entrained and forced to travel at the same speed water particles were traveling. Although the thickness of the jet of issuance was approximately 8.7 cm, the thickness of the jet at impingement ranged from 0.90 m (2.95 ft) to 1.20 m (3.93 ft). Lateral expansion did not seem to be significant, as can be seen in Figure 5.2. The color of the water was white, indicating that significant air entrainment took place in the jet. Furthermore, significant agitation was observed in the water surface. Downstream of the area of impingement, large emergent bubbles formed a mound-shaped “boiling” surface. In contrast, recirculation was mild behind the zone of impingement. Velocity of the water upstream from the jet was low in comparison to the velocities downstream from the zone of impingement. The surface velocity was high downstream of the impingement area. One of the indicators of the surface velocity was the movement of the tennis balls after they were released. When

the angle of the nozzle was set at 35 degrees from the vertical, part of the flow seemed to bounce against the surface after impacting the tailwater surface. Tennis balls were thrown at the jet from the north wall at different positions. In most cases, they were carried away by the jet stream. However, when the balls were thrown near the edges, they passed through without significant deviation from their trajectory. This indicates that at least two zones exist within the jet. An inner section where the momentum is concentrated and an outer section where the jet's power per unit area decreases.



Figure 5.2. Front view of the jet. Some lateral expansion is observed.

5.3 Variation of Tailwater Depths in the Vicinity of the Zone of Impingement

Tailwater depths across the tailbox were not uniform. It has been observed in several tests that the tailwater is deeper downstream of the zone of impingement and

shallower upstream from the zone of impingement. Similar observations were made by Zahoor (1992) when studying a plunge pool stilling basin. In the tests performed at CSU the reference tailwater depth is the downstream water depth. On the average, tailwater downstream of the line of impingement was 15.2 cm (0.5 ft) deeper than upstream of the jet. Drawdowns observed upstream for the impact zone for most tests are given in Table 5.1.

5.4 Velocity Measurements Across the Nozzle

The Pitot tubes were calibrated prior to mounting and after the tests were conducted. Calibration data is given in Appendix D.1. Four Pitot tubes were placed along the centerline of the nozzle. The east Pitot tube was No.1, the middle ones were Nos. 2 and 3 and the west Pitot tube was No. 4. Pitot tubes Nos. 1, 2, 3, and 4 were placed at 0.46 m (1.5 ft), 1.22 m (4 ft), 1.83 m (6 ft), and 2.59 m (8.5 ft) from the east end of the nozzle, respectively. Velocity distribution was not uniform at the nozzle. Maximum velocities occurred in Pitot tube No. 3 as can be seen in Figure 5.3. Figure 5.3 corresponds to the velocity distribution of the first test, carried out on August 26, 1996. This velocity distribution is typical of subsequent tests. The minimum velocity was 10.25 m/s (33.63 ft/s) and the maximum was 11.07 m/s (36.32 ft/s). The mean of the four measurements is 10.64 m/s (34.91 ft/s). The average velocity calculated by dividing the total discharge by the area of the nozzle is 10.28 (m/s). Furthermore, comparisons between the discharge readings and the discharge calculated using the area-velocity method were made. Discrepancies between the average discharge and the discharge calculated using the area-

velocity method range from -0.84 % to 5.06 %. A complete set of velocity and discharge measurements is given in Appendix D.2.

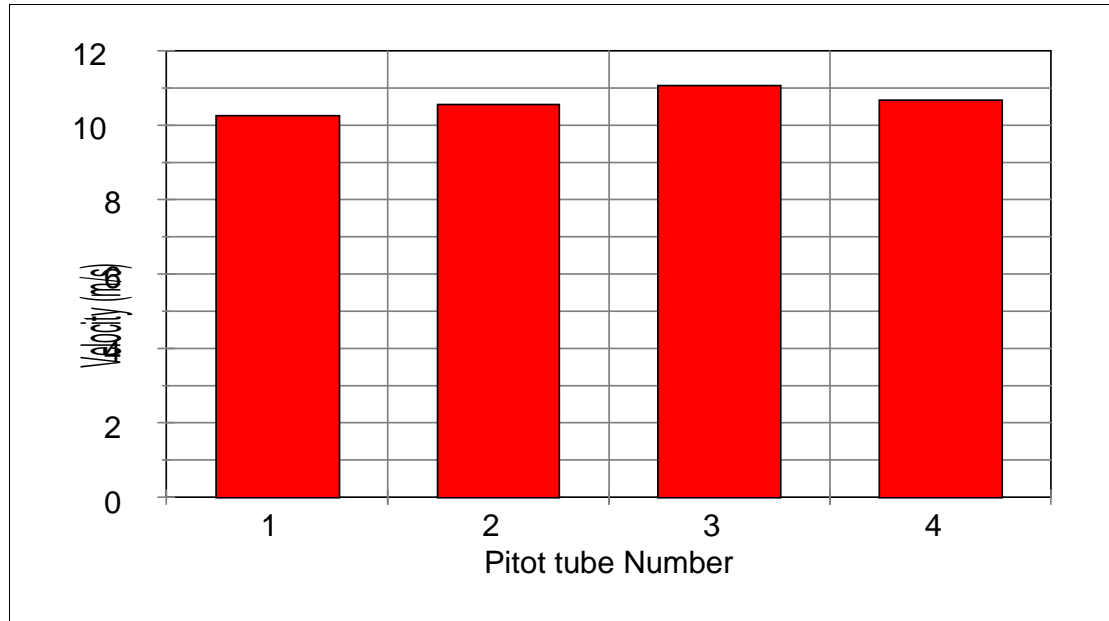


Figure 5.3. Typical velocity distribution across the nozzle. Test was conducted on August 26, 1996.

5.5 Effect of Time in Scour Hole Development

Because scour hole development could not be visually monitored due to high turbulence near the area of impingement and turbidity of the water, tennis balls, used as floating devices, were buried at different depths. Scour took place quickly as conditions changed with time. Tennis balls buried in the bed were uncovered and floated to the surface revealing the depth of scour at a particular location at a certain time. Tennis balls located in the vicinity of impingement appeared in the surface shortly after impingement started taking place. In most cases, tennis balls were found floating even before the specified discharge was attained.

Figure 5.4 shows rates of scour. Discharge, tailwater depths, and depths of scour were plotted versus time. For the September 11, 1997 test, depth of scour reached a maximum quickly after the tailwater depth was lowered to the specified elevation. Depth of scour is practically constant until the test is concluded. The final depth of scour is less than the maximum scour depth indicated by the release of the tennis ball. This indicates that the bed was fluidized, allowing the tennis ball to escape. Material settled after the test was concluded. Similar behavior was observed in the other tests. See Appendix E for the complete set of data.

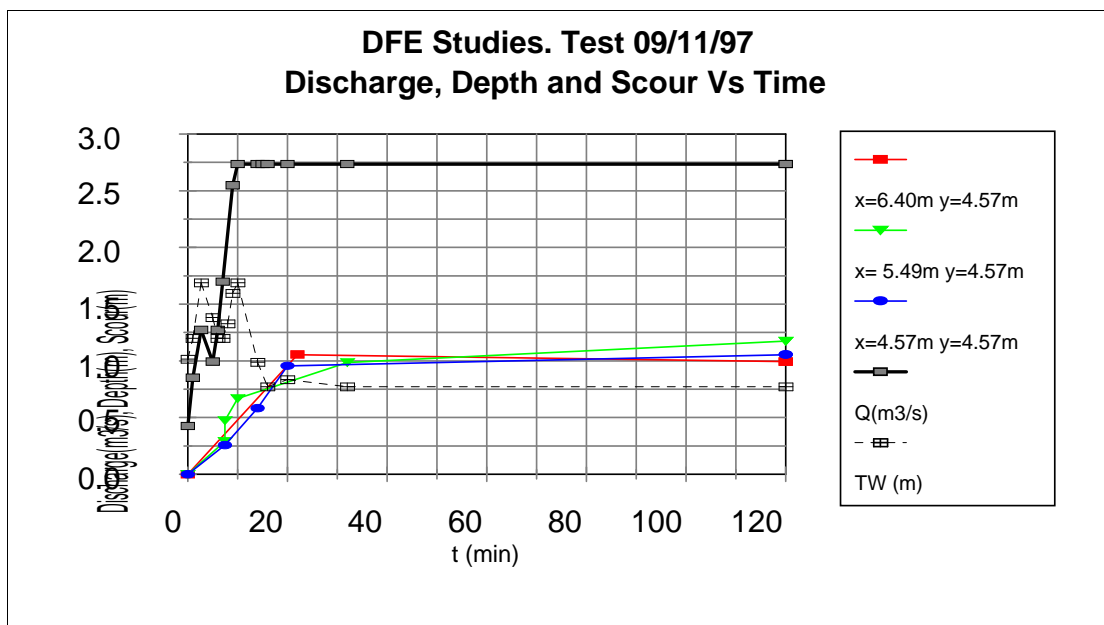


Figure 5.4. Typical scour development with time for points located along the centerline of the scour hole.

Tennis balls were also buried off the centerline of the tailbox. Limited data exist, because in some occasions, scour did not reach those locations. Scour stopped at a depth approximately equal to the depth of scour near the centerline of the scour hole. Depth of

scour versus time is a linear relation for these locations, so that scour apparently occurs at a steady, constant rate. Scour reaches a maximum depth between the time the deepest tennis ball is released and the end of the test. Depth of scour near the centerline of the impact point of the jet reached a maximum very quickly. Lateral scour occurred more slowly, but at a steady rate. See Figures E.3 and E.4 in Appendix E.

It is expected that lower discharges will produce scour closer to the issuance section during startup and shutdown. Greater discharges will produce scour further downstream, but the scour hole will have larger dimensions. Lower discharges will also produce lower unit discharges and the breakup lengths will be shorter. In most cases tailwater depth was increased at the end of the test, to prevent scour upstream of the area of impingement for the target discharge, but some extra scouring might have affected the upstream slope of the scour hole during shutdown. However, the maximum depth of the scour hole will not be affected by lower discharges, unless excessive scouring of the upstream slope produces deposition at the bottom of the scour hole, thus reducing the final depth of the scour hole.

5.6 Formation and Armoring of the Scour Hole and the Mound

Sorting took place in the development of the scour hole, and this effect was more noticeable in the vicinity of the area of impingement. The tailbox was filled to the target elevation with 19.05 mm (3/4 in.) roadbase. Roadbase contained material ranging from fine sand through coarse gravel. After the test was finished, most of the material on the surface of the bottom of the scour hole was mainly coarse gravel. It was also observed that in the upstream slope the predominant material was mainly composed of finer material.

Coarse gravel covered the downstream section of the scour hole. Figure 5.5(a) shows a typical gradation of bed material at different locations in and around the scour hole before and after the tests. Samples were collected in four different locations in the tests performed in 1997. Figure 5.5(b) shows the appearance of the bed material before the test and at different locations after the test. They were gathered at the upstream slope, at the bottom of the scour hole, at the lower sections of the downstream slope, and on the top of the mound formed downstream of the scour hole. The largest particles were found either in the bottom of the scour hole or the downstream slope. In the example shown in Figures 5.5(a) and 5.5(b) the largest particles were found at the downstream slope.

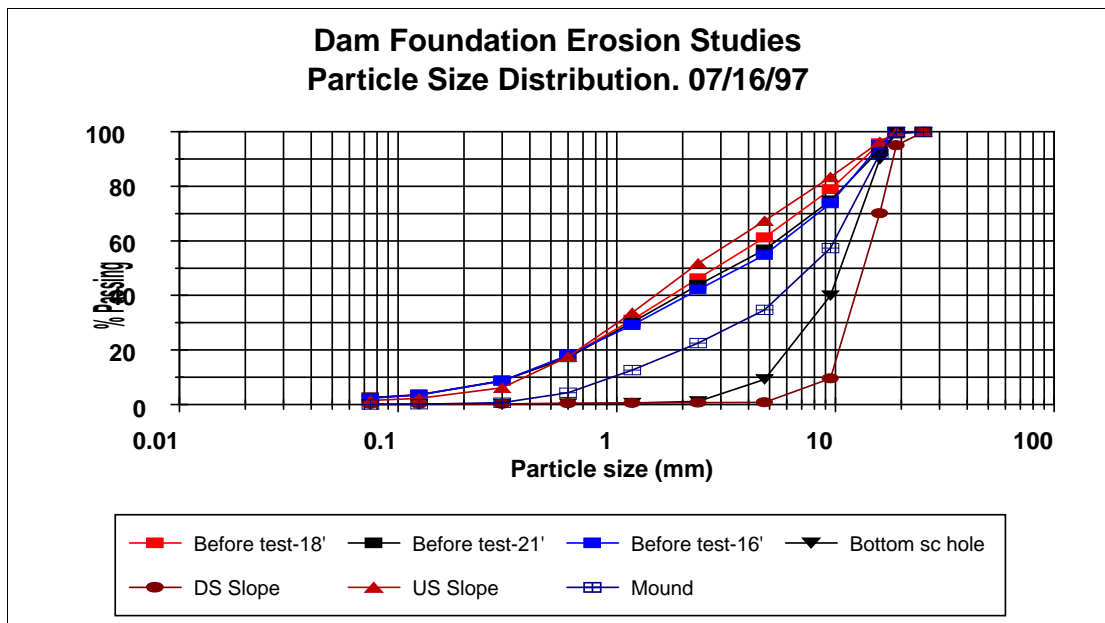


Figure 5.5(a). Typical particle size distribution of material in space after test.



Figure 5.5(b). Appearance of material gathered at different locations. From the upper left dish in clockwise rotation the location in which they were collected follows: downstream slope, upstream slope, original bed material, mound, and bottom of scour hole.

In the majority of previous investigations, both d_{85} and d_{90} have been used as the characteristic particle size to predict the depth of the scour hole caused by an impinging jet. Interestingly, the median size of the armored material corresponded to d_{85} of the original material in the tests conducted at the DFE Facility. Similar results were obtained by Hallmark (1955). Eventually, the weight of the particles deposited in the bottom of the scour hole will prevent further erosion, once the scour hole achieves a state of equilibrium.

The finest particles were found at the upstream slope. Table 5.2 is a summary of the median size of the particles found in different locations of the scour hole for the tests performed in 1997. A comprehensive data set is presented in Appendix F.

Table 5.2. Median size of particles found across the scour hole and the mound.

Date	Angle (deg.)	TW Depth m - (ft)	d ₅₀ Before the Test mm - (in.)	d ₅₀ US Slope mm - (in)	d ₅₀ Bottom of Scour Hole mm - (in.)	d ₅₀ DS Slope mm - (in.)	d ₅₀ Top of the Mound mm - (in.)
07/16/97	35	0.84 (2.75)	2.96, 3.48 (0.11, 0.137)	2.24 (0.088)	10.83 (0.426)	13.84 (0.545)	7.96 (0.313)
07/23/97	35	0.50 (1.64)	3.16, 3.68 (0.124, 0.145)	9.81 (0.386)	10.62 (0.418)	14.68 (0.578)	6.71 (0.264)
09/02/97	25	0.41 (1.33)	3.57, 2.77 (0.14, 0.11)	7.97 (0.313)	15.85 (0.624)	15.26 (0.601)	7.87 (0.310)
09/11/97	25	0.77 (2.55)	3.28, 3.74, 3.19 (0.129, 0.147, 0.126)	1.13 (0.044)	16.04 (0.631)	16.75 (0.659)	4.10 (0.161)

5.7 Geometry of the Scour Hole

The shape of the scour hole was approximately ellipsoidal. The top of the mound formed downstream of the scour hole was flat. A graphical representation of a typical scour hole can be seen in Figure 5.6. Several times, scour occurred when the tailbox was allowed to drain, scouring part of the mound and the sides of the scour hole near the east and the west walls. Some "rills" were produced downstream from the scour hole by dewatering of the tailbox after the tests were finished. This process did not affect the interior of the scour hole, although it may have affected the sides of the mound to a minor extent. Erosion along the sides of the basin occurred because of recirculation. A break in the downstream slope near the original ground surface was observed in almost all tests. The downstream slope became milder as it approached the original ground surface. A photograph of a scour hole can be seen in Figure 5.7. Contour maps, longitudinal and lateral profiles, and drawings of scour holes are available in Appendix G.

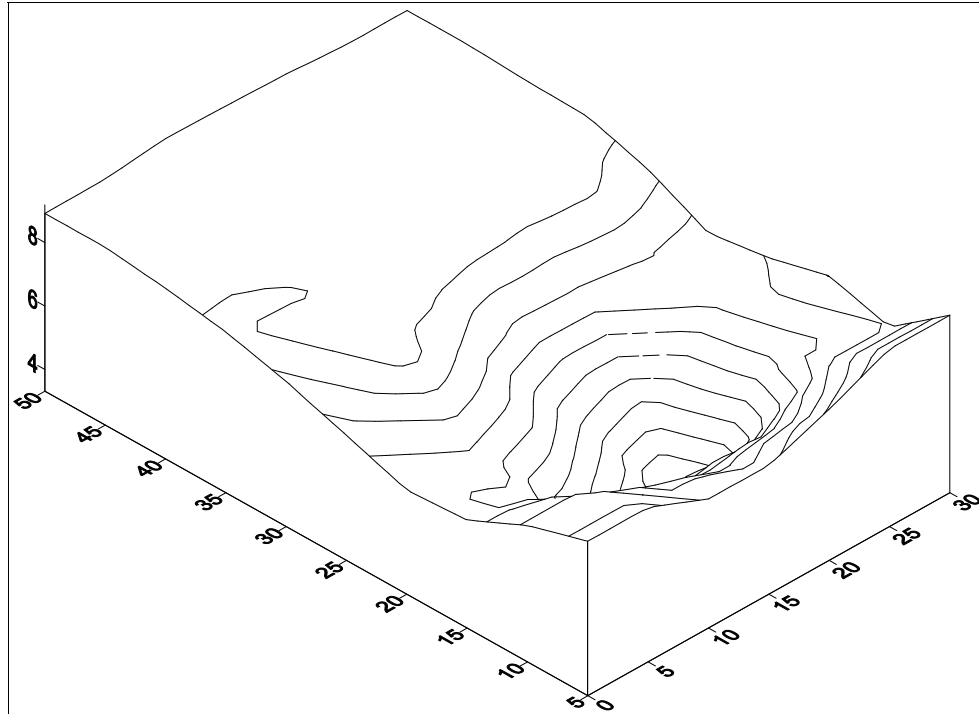


Figure 5.6. Three dimensional view of scour hole after test carried out on September 9, 1996. Dimensions are in feet.



Figure 5.7. Photograph of a scour hole.

5.8 Location of Deepest Points of Scour Hole and Highest Points of the Mound

Twelve tests were conducted at different nozzle angles and tailwater depths. When the angle of impingement was 15 degrees with respect to the vertical, the deepest points were found to be closer to the west side of the tailbox. Also, the mound was formed mainly on the southeast side of the tailbox. When the angle of impingement was 35 degrees, the mound was symmetrical along the longitudinal centerline.

5.9 Slopes of Scour Holes

In all cases, slopes were measured along the deepest point in the longitudinal direction and across the tailbox. Slopes of scour holes were steep, especially for the upstream side of the scour hole (on the order of 4:1 to 2:1). Table 5.3 gives the longitudinal slopes. Side slopes are given in Appendix G. Slopes were milder in the downstream face of the scour hole. Also, slope of the scour hole is flatter in the vicinity of the axis of maximum depth. This could be explained by the fact that the jet is stronger in the vicinity of the zone of impingement. This area was flattened, because the particles were removed outwards. Because of a longer trajectory path, the area of impingement is larger, and the upstream slope seems to be flatter for greater angles of the nozzle with respect to the horizontal.

In the tests performed in 1996 at CSU, it was observed that the downstream slope of the scour hole was approximately constant until a break in the slope occurred near the plane of the original bed level. The slope, in every case, was milder in the mound. This "break" in the slope was called "beaching" by Blaisdell (1989), and according to him "beaching" is not expected in prototype conditions.

Table 5.3. Longitudinal slopes.

Date	Angle of Nozzle	δ (deg.)	TW Depth m - (ft)	US Slope	DS Slope	θ (deg.)
08/26/96	15	11.636	0.57 (1.87)	0.55	0.50	26.6
09/03/96	15	11.887	0.85 (2.79)	0.50	0.46	24.5
09/09/96	15	11.438	0.27 (0.87)	0.46	0.46	24.6
09/23/96	15	12.064	1.85 (6.06)	0.50	0.49	26.2
09/30/96	25	19.875	1.80 (5.90)	0.37	0.44	23.6
10/03/96	25	19.150	1.17 (3.85)	0.26	0.58	29.9
09/02/97	25	18.346	0.41 (1.33)	0.53	0.46	24.9
09/11/97	25	18.683	0.77 (2.54)	0.49	0.49	26.0
10/09/96	35	26.360	1.16 (3.80)	0.24	0.38	20.9
10/18/96	35	27.395	1.80 (5.92)	0.35	0.29	16.0
07/16/97	35	25.869	0.84 (2.75)	0.33	0.34	18.6
07/23/97	35	25.229	0.50 (1.64)	0.48	0.33	17.2

5.10 Dimensionless Longitudinal Profiles of Scour Holes

Longitudinal profiles passing through the deepest point of the scour hole were obtained using Surfer[®] and Grapher[®] programs. Abscissas of the dimensionless longitudinal scour profiles were obtained by subtracting the distance from the north wall of the tailbox corresponding to the lowest point of the scour hole from the distance from the north wall of each point and dividing the result by the maximum depth of the scour hole.

$$Y^* = \frac{Y_{\phi} - Y_{\phi p}}{Y} \quad (5.1)$$

where: Y_{tb} = the horizontal distance of a point from the North wall of the tailbox,

Y_{dp} = the horizontal distance of the deepest point to the north wall; and

Y = the maximum depth of the scour hole.

Furthermore, the elevation of the lowest point, Z_{dp} , was subtracted from the elevation corresponding to each point, Z , and the result was divided by the maximum depth of the scour hole to obtain the dimensionless ordinates, Z^* , as follows:

$$Z^* = \frac{Z - Z_{dp}}{Y} \quad (5.2)$$

As a result, dimensionless scour hole profiles were obtained for each angle of issuance. The dimensionless scour profiles corresponding to the holes formed by jets issued at 15 degrees are shown in Figure 5.8. The downstream slope, measured downstream of the “bowl” at the bottom of the scour hole, is approximately constant for the four tests. The dimensionless profiles corresponding to angles of issuance of 25 and 35 degrees are given in Figures G.4 and G.5, respectively. The shape of two of the dimensionless profiles corresponding to tests in which the angle of issuance was set 35 degrees was different from the other two, which seemed to collapse in one. This could be the result of a larger breadth at the tailwater surface or post-run scour in the upstream slope. In the test performed on July 16, 1997 the tailwater was lowered rapidly at the end of the test. Deposition at the bottom of the scour hole occurred most likely during shutdown due to scour in the upstream slope. This would explain the distortion of the downstream slope near the bottom of the scour hole in this case. See Figures G.5 and G.14.

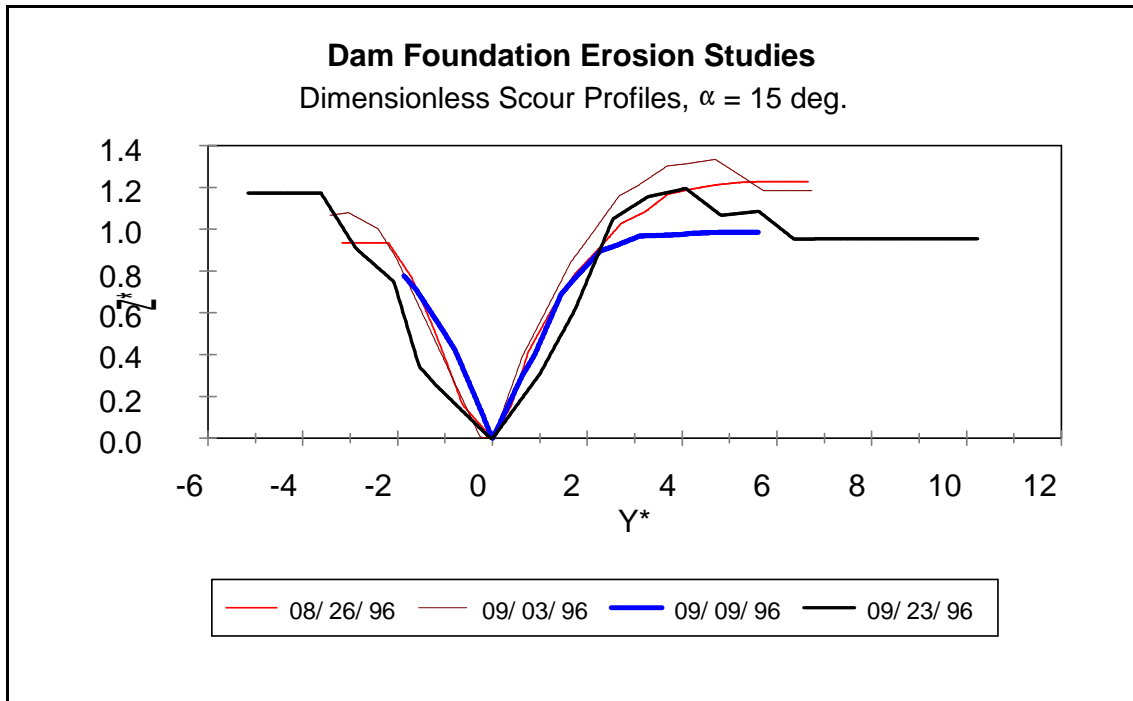


Figure 5.8. Dimensionless profiles of scour holes for an angle of issuance of 15 degrees.

5.11 Air Concentration and Velocities at the Section of Impingement and Below the Tailwater Surface

Air concentration and pressure differentials were recorded using an air concentration probe and a backflushing Pitot tube, respectively. Air concentration was high at the impact plane. The breadth of the jet changed when angles of issuance with respect to the vertical and the fall height changed. Larger breadths are expected for greater angles of issuance with respect to the vertical; therefore, greater air concentrations.

The tip of the Pitot tube and the air concentration probe were set at an elevation of 2.59 m (8.5 ft) for the test performed on July 29, 1997. The angle of issuance with respect to the vertical was 35 degrees. Tailwater was raised in 0.15 m (0.5 ft) increments and readings were taken for each tailwater elevation. Air concentration readings were fairly constant and equal to 96% until the Pitot tube was 0.30 m (1 ft) below the water surface,

as seen in Figure 5.9. For greater depths, air concentration decreased as the depth above the air concentration probe increased, as expected. Velocity voltage readings decreased as the depth above the Pitot tube increased, but they were above the calibration range. Velocities were on the order of 18.29 m/s (60 ft/s) until the probes were submerged approximately 0.45 m (1.48 ft). Velocities recorded at the tip of the Pitot tube decreased after the water surface was 0.45 m (1.48 ft) above the tip of the backflushing Pitot tube, as seen in Figure 5.10.

The tip of the Pitot tube was set at an elevation of 2.60 m (8.53 ft) for the tests performed on September 4, 1997. The angle of issuance with respect to the vertical was 25 degrees. When the depth above the probes was 0.30 m (1 ft), the measured air concentration was 100% as seen in Figure H.3. This indicates a reading error. When the water depth above the backflushing Pitot tube was greater than 0.3 m (1 ft), air concentration decreased until reaching an air concentration of 25% for a depth of 1.06 m (3.48 ft). Air concentrations are not available for greater depths. The variability of velocity readings was high. Velocities were on the order of 8 m/s (26.2 ft/s) to 12 m/s (39.37 ft/s) for depths on the order of 0.45 m (1.48 ft). Velocity decreased at greater depths and was on the order of 3 m/s (9.84 ft/s) for depths of approximately 1.05 m (3.44 ft/s). Other tests were carried out above the plane of impingement. The velocities taken using this procedure were higher than predicted using the ballistic equations. The calculated velocities of impingement are approximately 13 to 14 m/s (42.7 ft/s to 45.9 ft/s) (see Appendix B). Graphs and other information can be found in Appendix H.

The results presented in the previous paragraphs indicate that air concentration just below the plane of impingement remains constant up to a certain depth, where a noticeable

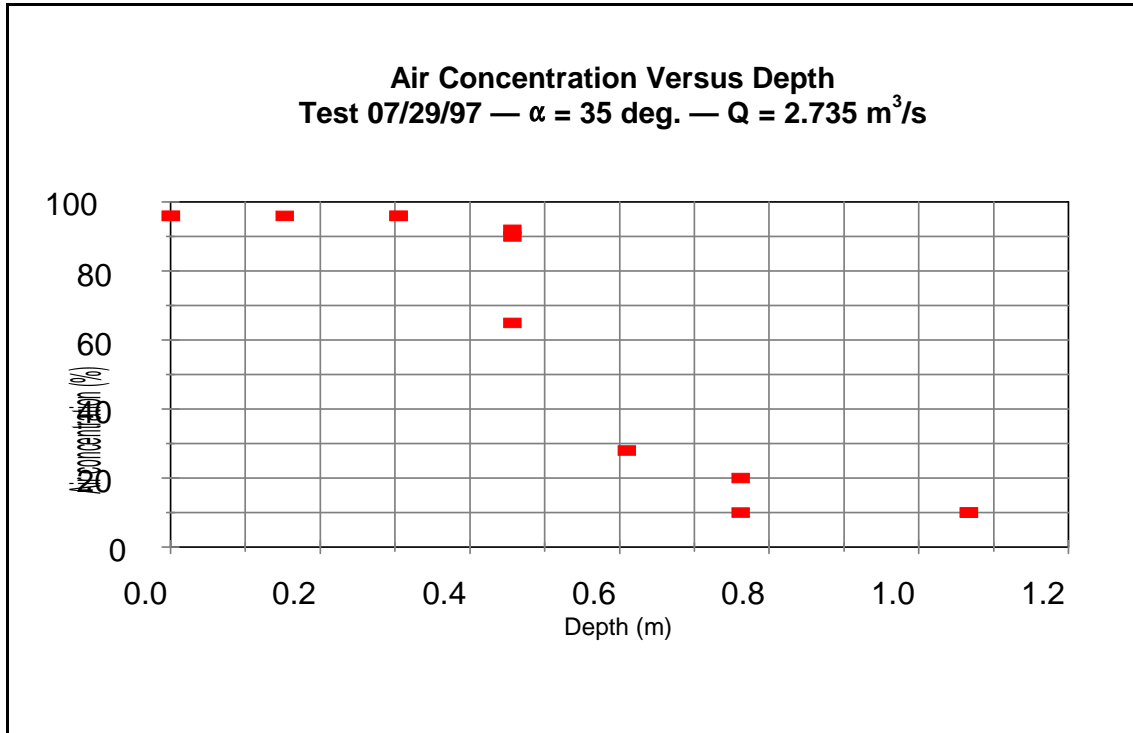


Figure 5.9. Depth of water above the Pitot tube versus air concentrations recorded on test conducted July 29, 1997. Unit discharge is $0.897 \text{ m}^2/\text{s}$.

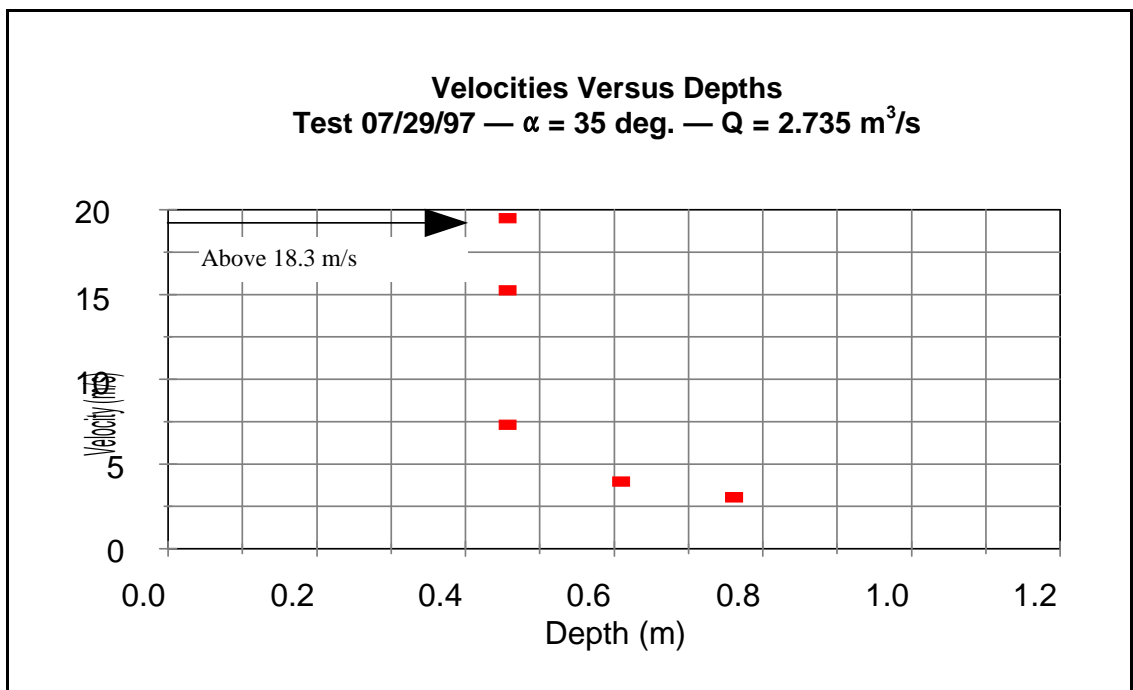


Figure 5.10. Measured velocities of the jet at different depths below the tailwater surface.

drop occurs. Velocity starts decreasing approximately at the same depth. Air concentrations and velocities diminish as the jet penetrates the tailwater.

5.12 Simulated Fractured Rock Tests

5.12.1 General

After backfilling the tailbox to a reference elevation of 3.35 m (11 ft), discharge was increased to 0.99 m³/s (35 cfs) and then to 1.13 m³/s (40 cfs). Tailwater depth was lowered by gradually opening the gate. Dislodgement of blocks was detected upstream of the jet impact area when the tailwater depth was approximately 0.21 m (0.7 ft) and the flow was 1.13 m³/s (40 cfs). At that moment, water depth was not being controlled by the downstream gate. No difference between the upstream tailwater depth and the downstream tailwater depth was observed for this discharge. Readings were taken for the upper tap and the lower tap of the nine different blocks chosen for installation and were plotted according to their position.

The shape of the scour hole was approximately ellipsoidal. Notes were taken of the final position and orientation of the more distant blocks. Most of the blocks were deposited with the longest axis perpendicular to the direction of the flow. It was noticed that downstream of the scour hole several rows of blocks had been disturbed by the jet. Blocks were standing several inches above their initial position, as if they were about to be dislodged.

5.12.2 Block failure at 1.13 m³/s (40 cfs)

The first blocks to be dislodged were located immediately upstream of the zone of impingement. The test was concluded a few minutes after movement was detected. A total of 23 blocks was found upstream of the jet impact zone. All of the twenty-three blocks lying outside the scour hole were deposited upstream of the scour hole. Figure 5.11 illustrates the process of dislodgement. The scour hole was not symmetrical. Up to five columns on the east side of the centerline of the scour hole, and up to eight columns west of the centerline of the scour hole were affected by the jet. Up to four rows of blocks were affected in the north south direction. Tailwater depth was approximately 0.21 m (0.7 ft). The scour hole can be seen in Figure 5.12. Piezometer readings were taken in a second test conducted at the same discharge, since they could not be taken when scour first occurred. Piezometer readings are given in Appendix I. The pressures measured near the bottom of the blocks were greater than the pressures measured near the top of the block in the vicinity of the zone of impingement as seen in Figure 5.13. A difference of 0.06 m (0.20 ft) in the piezometer readings was recorded. Pressures in excess of static have been calculated for blocks near the centerline of the jet, and, as an approximation, pressures in the bottom of the blocks are assumed to be the same as the pressures read in the tap No 2.

5.12.3 Block failure at 1.27 m³/s (45 cfs)

A second test was run at 1.27 m³/s (45 cfs) a few hours after the first test was concluded, and piezometer readings were taken. A 0.03 m (0.1 ft) difference in manometer elevation between the lower tap and the upper tap of the center block was

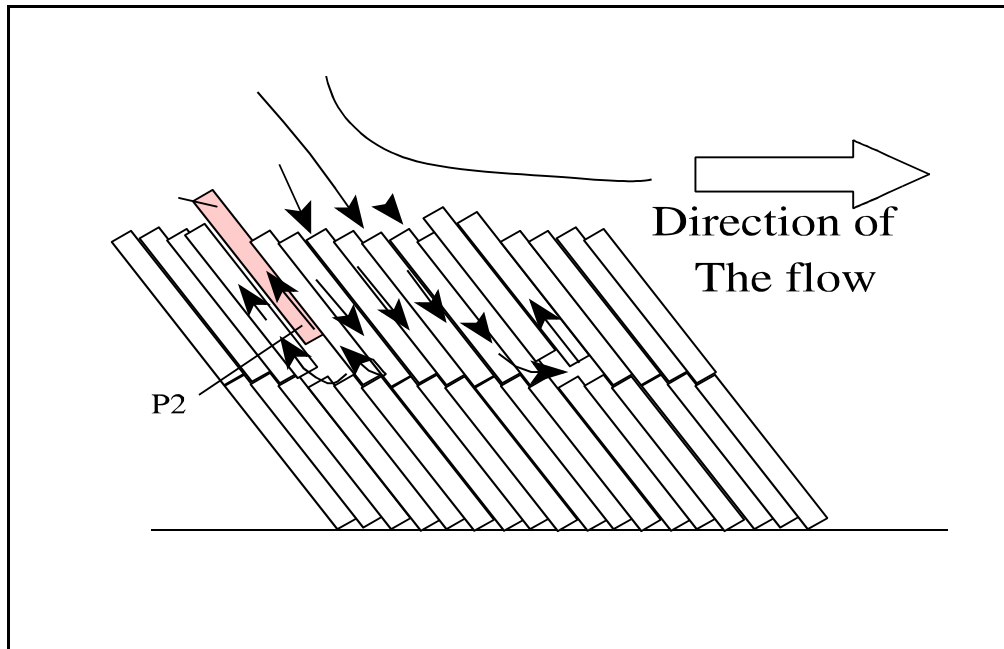


Figure 5.11. Mechanism of failure of fissured rocks under the action of the jet.



Figure 5.12. Mat after failure at $1.13 \text{ m}^3/\text{s}$ (40 cfs).

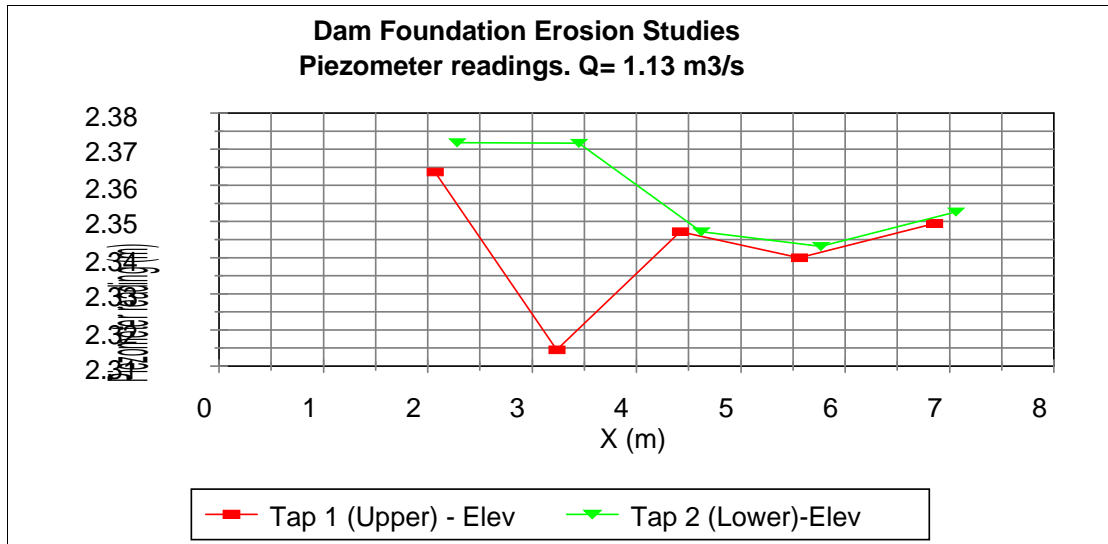


Figure 5.13. Piezometer readings in the north-south direction of the block setup across the centerline. $Q = 1.13 \text{ m}^3/\text{s}$ (40 cfs).

observed. The lower tap reading was again higher than the upper tap reading. The piezometer readings corresponding to $1.27 \text{ m}^3/\text{s}$ (45 cfs) can be seen in Figure 5.14.

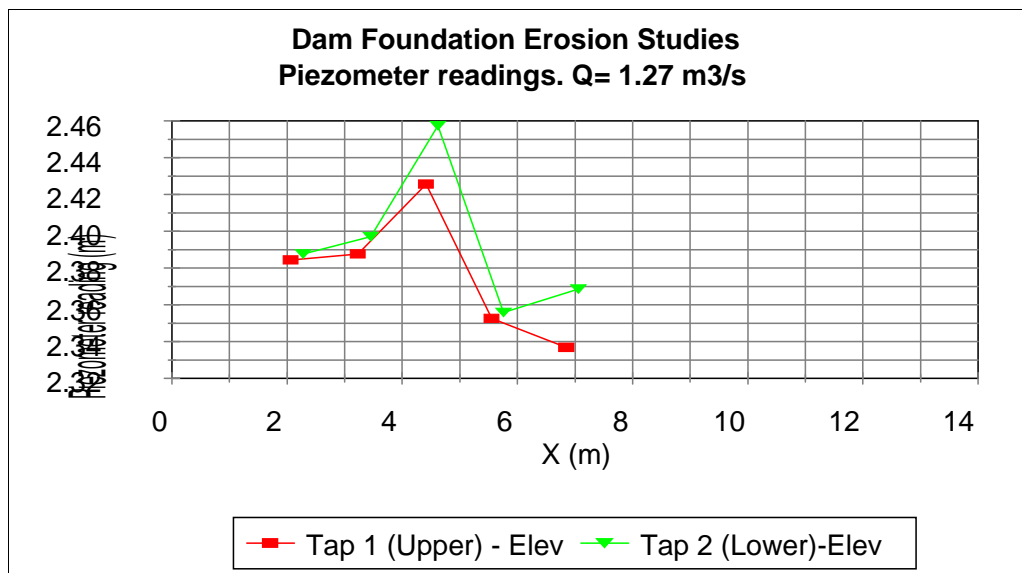


Figure 5.14. Piezometer readings at $1.27 \text{ m}^3/\text{s}$ (45 cfs) in the north-south direction of the testing surface along the centerline of the jet.

The size of the scour hole increased significantly. The approximate maximum dimension of the scour hole in the direction of the flow was 1.09 m (3.58 ft). The upstream end of the scour hole was at 3.28 m (10.75 ft) from the north wall and the downstream end of the scour hole was at 4.37 m (14.33 ft) from the north wall for a total length of 1.09 m (3.58 ft). The lateral dimension of the scour hole was 4.7 m (15.42 ft). No scour was detected in the unprotected areas of roadbase surrounding the simulated rock surface. In addition, scour did not occur near the edges of the simulated rock surface. The shape of some blocks near the center of the zone of impingement changed after the test. The corners and the edges of the blocks were apparently “sanded” by the abrasion between blocks and were rounded after the test was concluded. The hardness of the blocks is not known with certainty, but they probably correspond to the hardness of a 9.80 MPa (1,400 psi) concrete. A maximum of seven rows of blocks were dislodged from the testing section, approximately 3.81 m (12.5 ft) from the north wall. The approximate shape of the scour hole was an ellipse with its lateral axis measuring 2.6 m (8.67 ft) and its longitudinal axis (in the direction of the flow) measuring 1.03 m (3.38 ft). Two adjoining blocks were completely reversed in their respective positions. The fluted sides of the blocks were facing the south end of the tailbox after the test. Initially, they were facing the north side of the tailbox.

It is also important to point out the fact that photographic records (Figure 5.15) and video show that the center blocks of the testing surface were downstream of the centerline of the jet at impingement, and they were disturbed after the test at 1.27 m³/s (45 cfs). Manometer lines of the center block were exposed after the 1.27 m³/s (45 cfs) test, and this could affect posterior manometer readings.



Figure 5.15. Mat after failure at $1.27 \text{ m}^3/\text{s}$ (45 cfs).

5.12.4 Block failure at $1.42 \text{ m}^3/\text{s}$ (50 cfs)

The length and the width of the scour hole increased after a test was conducted at $1.42 \text{ m}^3/\text{s}$ (50 cfs). However, the depth of the scour hole remained constant, because the bottom layer remained in place. One block was lifted and deposited on top of the Pitot tube and air concentration probe. This indicates that the lift force of the jet was greater than the submerged weight of the block in that area. The depth of the scour hole did not increase with an increase in discharge (see Figure 5.16). A 0.19 m (0.62 ft) difference in water elevation between the lower tap and the upper tap was observed. Again, the lower tap reading was higher than the upper tap reading (see Figure 5.17). The readings for the blocks placed at 2.44 m (8 ft) from the center block (in either direction) showed an



Figure 5.16. Mat after failure at $1.42 \text{ m}^3/\text{s}$ (50 cfs).

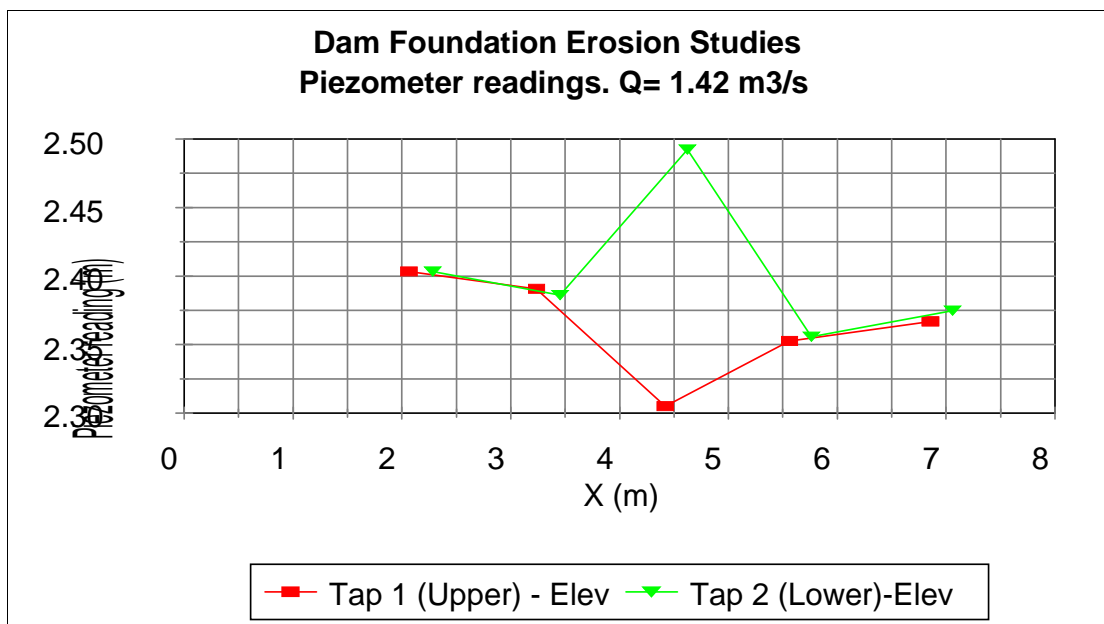


Figure 5.17. Piezometer readings at $1.42 \text{ m}^3/\text{s}$ (50 cfs) in the north-south direction of the testing surface along the centerline of the jet.

increasing trend in water elevation with discharge, but were always higher than the west depth probe readings. For the blocks located 1.22 m (4 ft) west and 1.22 m (4 ft) east from the center block, water elevation readings were higher than the blocks located 2.44 m (8 ft) west and 2.44 m (8 ft) east of the center block. Static pressures at the bottom of the blocks were higher than the static pressure corresponding to the water depth near the zone of impact. The width of the jet at issuance is 3.05 m (10 ft), so if the cross section of the jet did not increase laterally, it would extend 1.52 m (5 ft) west and 1.52 m (5 ft) east of the centerline. In reality, downstream of the issuance section, the jet expands mainly in the upstream and downstream directions.

5.12.5 Block failure at 1.98 m³/s (70 cfs)

The next series of block tests were conducted on September 17, 1998. The objective of the tests was to dislodge the bottom layer from the block matrix. The tailbox was filled following the same procedures used in previous tests. Discharge was increased to 1.27 m³/s (45 cfs), and then increased to 1.42 m³/s (50 cfs). Measurements of the thickness of the jet at impingement were taken. A weight was attached to a string which, in turn, was attached to the center of a rope that was run between the east wall and the west wall of the DFE Facility. The walls were marked upstream and downstream of the jet immediately after the weight touched the jet at the tailwater surface. The thickness of the jet was 1.45 m (4.76 ft) when the discharge was 1.42 m³/s (50 cfs). Flow was stopped. Because no scour was detected, discharge was increased to 1.56 m³/s (55 cfs). Piezometer readings were taken at the 18 piezometers in the blocks and at the nozzle. The nozzle readings indicated that velocity changed across the width of the nozzle when the flow was

1.56 m³/s (55 cfs). The minimum velocity was 6.28 m/s (20.61 ft/s) in Pitot tube No. 1. The maximum velocity was 6.83 m/s (22.42 ft/s) in Pitot tube No. 3. Discharge was diverted, allowing dewatering of the tailbox. Photographs and video were taken. The dimensions of the scour hole increased longitudinally and laterally.

Discharge was increased to 1.77 m³/s (62.5 cfs) in approximately 0.06 m³/s (2 cfs) increments. The scour hole was closely monitored. One member of the DFE team stood in the water upstream of the zone of impingement observing the scour hole. The tailbox was dewatered again and no scour was observed.

Discharge was increased to 1.83 m³/s (64.5 cfs), then to 67 cfs (1.90 m³/s), and then to 1.98 m³/s (70 cfs). Measurement of the thickness of the jet was performed again at 1.98 m³/s (70 cfs). The thickness of the jet at the tailwater surface was 1.63 m (5.35 ft). Failure was detected when the color of the flow downstream of the impingement area changed suddenly. Granular material was pumped from underneath the bottom layer of blocks and formed a brown plume that was clearly detected. This indicated that significant movement of the bottom layer had occurred, because removal of the bottom blocks allowed smaller material to be pumped out of the bottom of the scour hole. The flow was stopped shortly after the plume was detected. Photographs and video were taken. Two blocks were dislodged from the bottom layer, and a hole was observed. The hole can be seen in Figure 5.18. Also, a depression of the tops of the blocks was evident in the areas surrounding the location where dislodgement took place. Upstream of the hole in the bottom layer, several blocks were standing above their original position as if they were about to be dislodged, as can be seen in Figure 5.19. The edges of some blocks were rounded by the apparent abrasion resulting from blocks moving relative to each other. The

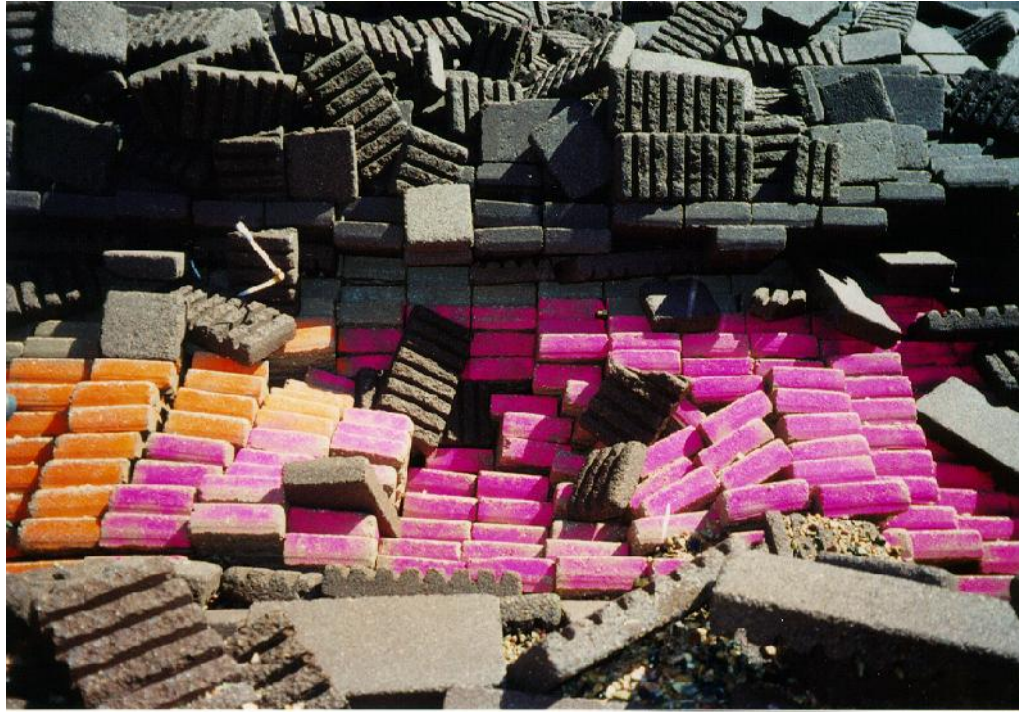


Figure 5.18. Photograph of the scour hole after test conducted at $1.98 \text{ m}^3/\text{s}$ (70 cfs).



Figure 5.19. Detail showing the blocks protruding above their initial position.

dimensions of the scour hole continually increased in the lateral and longitudinal directions. A mound of blocks was formed downstream of the scour hole. The size of the mound increased as more blocks were dislodged during the tests. The transport capacity of the flow was not sufficient to move the blocks very far from the zone of impingement in the downstream direction. The depth of scour was measured on the projection of the two layers on a vertical plane. Therefore, the depth of scour is 0.56 m (1.84 ft) when the bottom layer failed.

Finally, a test was conducted under the maximum discharge possible, $2.78 \text{ m}^3/\text{s}$ (98 cfs) which corresponded to a unit discharge of $0.91 \text{ m}^2/\text{s}$ ($9.8 \text{ ft}^2/\text{s}$). The dimensions of the scour hole increased. The blocks sank into the hole as the underlying material was being pumped out. The tailwater depth was 0.30 m (1 ft), and the depth of scour was 1.43 m (4.69 ft) at the end of the test. (See Figure 5.20.)



Figure 5.20. Photograph of the scour hole after test conducted at $2.78 \text{ m}^3/\text{s}$ (98 cfs).

CHAPTER 6

DATA ANALYSIS AND DISCUSSION

6.1 Introduction

Equations developed in the theoretical analysis and field observations will be used to find expressions that adequately predict the depths of scour holes produced by impinging jets in streambeds composed of cohesionless materials. Tailwater depths and angles of issuance of the jet were changed in the experimental phase of the present study. However, the bed material and the unit discharge remained constant. To validate Equation (3.28), data from previous investigations will be used in addition to data gathered in this study. Laboratory data related to scour produced by impinging jets were found in the literature review. However, complete sets of variables of interest were not reported in many investigations. For instance, the complete particle size distribution of the bed material was not available in the majority of reports that were reviewed. In some cases, the characteristic particle size was documented, but a complete description of the particle size distribution was not provided. In other cases, the total depth of scour measured from the tailwater surface was reported but tailwater depths were not included.

The boundary conditions for selecting appropriate sets of data were also taken into account. Data sets are limited to rectangular impinging jets. Jets had approximately a rectangular shape and the width of the jet was several times larger than the thickness of the

jets at the issuance section. The fall height was also taken into account. Data were taken into consideration if they were gathered in experiments where the jet underwent a free fall. Data were discarded when the jet was submerged or semi-submerged at the issuance section. A summary of data used for finding an equation that describes the geometry of the scour hole for impinging rectangular jets is given in Table 6.1.

Table 6.1. Summary of data used in this study.

Study	Type of Jet	q (m^2/s)	d_{85} (mm)	z/b_o	V_o/V_i
Present Study (DFE) 1997	Rectangular impinging pressurized	0.897	16	34.1-50.2	0.76-0.82
DFE-Model 1996	Rectangular impinging pressurized	0.178	6	30.1	0.670
DFE-Block	Rectangular impinging pressurized	0.372	213	51.1-51.7	0.412
Hallmark A 1955	Rectangular impinging free overfall	0.011-0.046	13	10.3-44.5	0.10-0.21
Thomas I- 1953	Rectangular impinging free overfall	0.011-0.047	7	1.76-50.1	0.10-0.46
Thomas II	Idem	0.011-0.046	10	1.8-50.1	0.10-0.43
Lencastre a (1961)	Rectangular impinging free overfall	0.023-0.134	48	5-23	0.02-0.25
Lencastre b	Idem	0.08-0.147	62	3.7-11.5	0.18-0.41

6.2 Angle of Downstream Slope Versus Angle of Impingement

A relation between the angle of the downstream slope of the scour hole and the angle of impingement was found in the experimental phase of this study. The downstream

slope remained approximately constant until the angle of impingement was greater than 18 degrees. Then, a linear relation existed between the downstream slope of the scour hole and the angle of impingement. Therefore, if θ is the downstream slope of the scour hole, and δ is the angle of impingement with respect to the vertical, the previous statement can be expressed mathematically as follows: $\theta = \theta_0$ if $\delta \leq \delta_0$; and $\theta = \theta_1 - C\delta$ if $\delta > \delta_0$; where θ_0 , θ_1 and C are constants.

Data in Table 6.2 were used to develop a relation between the angle of impingement and the downstream slope of the scour hole. The points in the sloping portion of the curve in Figure 6.1 were used for the regression analysis. Using data from this study it has been found that a relation exists between the angle of impingement and the downstream slope of the scour hole.

Table 6.2. Angle of downstream slopes versus angles of impingement.

Angle of impingement δ (deg.)	Angle of DS slope θ (deg.)
19.88	23.56
29.36	20.91
27.40	15.96
25.87	18.62
25.23	17.22
18.35	24.89
18.68	26.01
19.15	29.90

A linear relation of the type:

$$\theta = C - C_1 \delta \quad (6.1)$$

is sought when δ is greater than 18 degrees;

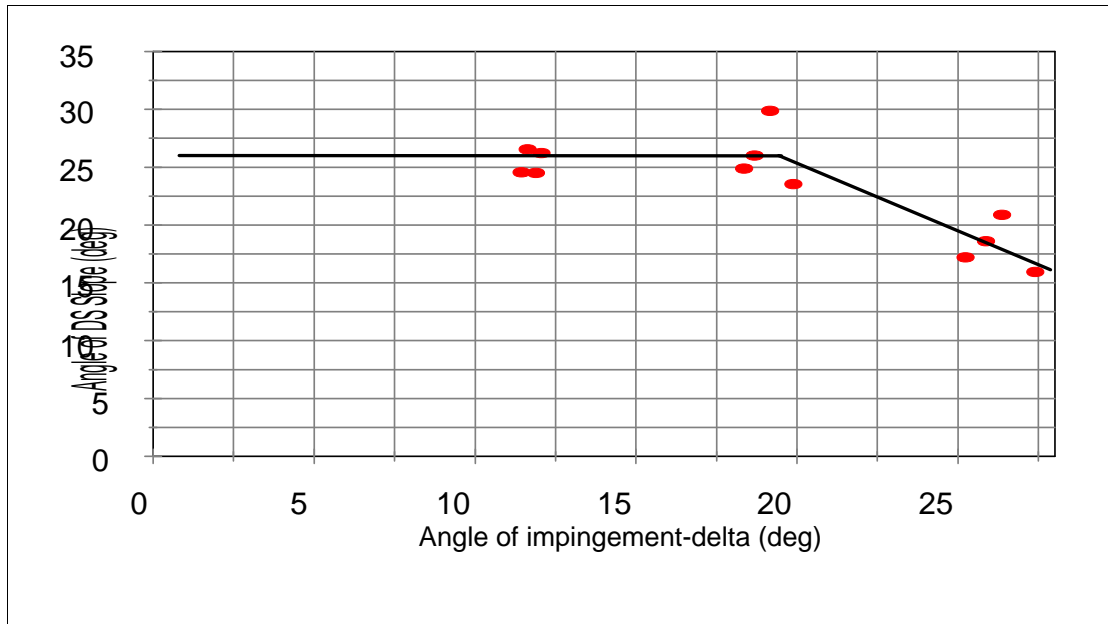


Figure 6.1. Angle of downstream slope (θ) versus angle of impingement (δ).

where: θ = the downstream slope of the scour hole;

C = a constant, in degrees;

C_1 = a constant; and

δ = the angle of impingement measured from the vertical.

A linear regression analysis was performed using Quattro-Pro[®]. The following is the output of the linear regression:

C (deg.) = 46.58

Estimated standard error of C = 2.43

R^2 = 0.78

No of observations = 8

Degrees of freedom = 6

$$C_1 = -1.081$$

$$\text{Standard error of } C_1 = 0.234$$

If the angle of impingement, δ , is less than 18 degrees, the downstream slope of the scour hole is approximately constant and equal to 26 degrees. Mirtskhulava et al. (1967) included a correction factor equal to $\sin (90 - \delta)/[1-0.175 \cot (90 - \delta)]$ for calculating the maximum depth of a scour hole if the angle of impingement with respect to the vertical exceeded 15 degrees.

The particle entrainment velocity, V_p , was found to be a function of the particle fall velocity, w , and an interlocking factor. The interlocking factor is given by $[(\sin \theta + (K_1 a / K_2 c) \cos \theta) / (1 + K_3 (K_1 a / K_2 c))]^{0.5}$. Hence, the interlocking factor is a function of the inclination of the downstream slope of the scour hole, θ , the moment arm ratio, $K_1 a / (K_2 c)$, and the lift coefficient to drag coefficient ratio, $K_3 = C_L / C_d$. Values of θ have been recorded for the studies considered for analysis. They vary approximately from 15 degrees to 30 degrees. For practical applications (Stevens and Simons, 1971), it is assumed that $K_1 a / (K_2 c)$ is equal to one. However, it will be assumed that $K_1 a / (K_2 c)$ varies between 0.5 and 1.5. The influence of the lift force is usually neglected, but it will be assumed that the lift coefficient varies between 10 percent and 40 percent of the drag coefficient. The results are presented graphically in Figure 6.2. The interlocking factor roughly varies between 0.9 and 1.2 with an average value of approximately 1.05 for the range of values of $K_1 a / (K_2 c)$ and K_3 given above. The interlocking factor will not be considered in the final development of an equation to predict the depth of scour caused by an impinging jet on a cohesionless bed. It does not change significantly with changes in values of $K_1 a / (K_2 c)$ and K_3 . Calculations are included in Appendix J.

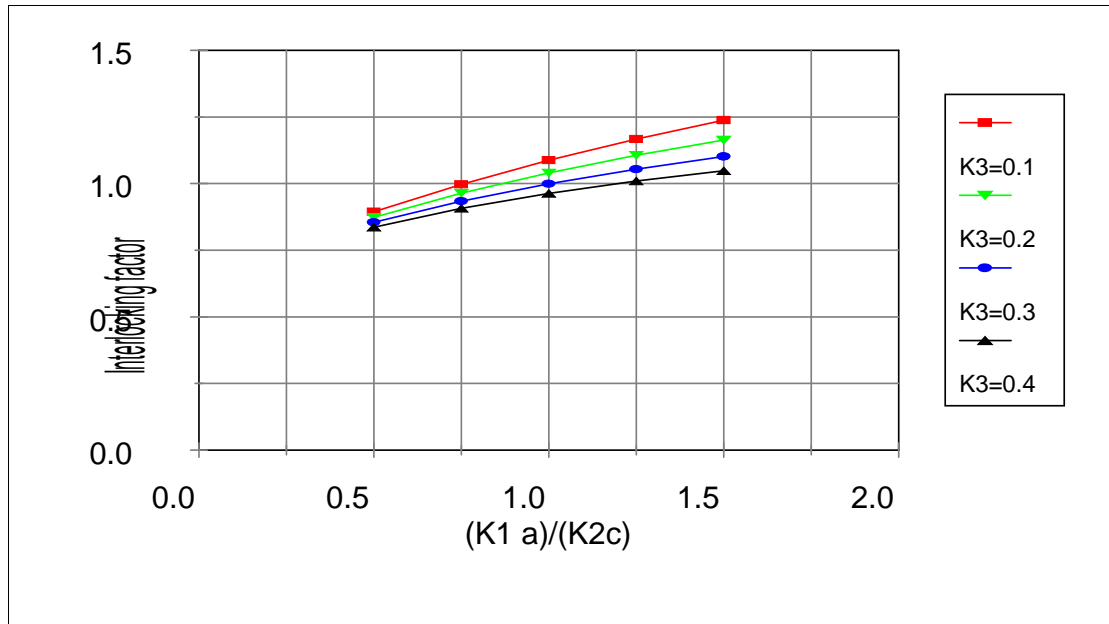


Figure 6.2. Interlocking factor as a function of the moment arm ratio, $(K_1 a)/(K_2 c)$, and the lift coefficient to drag coefficient ratio, K_3 .

6.3 Position of the Deepest Point of the Scour Hole

Because the angle of impingement affects the final depth of the scour hole, changes in tailwater elevation will change the angle of impingement, especially if the tailwater depth is of the same order of magnitude as the fall height. Apparently, the angle of the centerline of the jet changes slightly as it enters the tailwater in the direction of the flow. A comparison was made between the horizontal distance of the deepest point to the north wall and the predicted distance to the north wall, using the calculated angle of impingement from Equation (3.16). For an angle of issuance of 15 degrees, the deepest point was downstream of the calculated position. For other angles, the location of the deepest point varied around the calculated line of impingement. Calculations are given in Table G.5. Apparently, for steep angles of impingement a shift of the deepest point in the downstream direction is expected.

6.4 Drawdown Depth

Drawdown depth is the difference in elevation between the downstream tailwater surface and the upstream tailwater surface. Data collected during the experimental phase of this study suggested that a relation existed between the angle of impingement and the drawdown depth. The angle of impingement, δ , was approximately constant when the angle of issuance was held constant. Apparently, the drawdown depth is mainly a function of the unit discharge of the jet. Drawdown was noticeable when the discharge was 2.735 m³/s (96.6 cfs). This discharge was used during the cohesionless materials scour tests. However, drawdown was not apparent when the discharge was between 0.99 m³/s (35 cfs) and 1.42 m³/s (50 cfs). Zahoor (1992) developed an equation that relates the unit discharge, the Froude number at impingement, the angle of impingement, and the exit channel depth of a plunge pool to the drawdown depth. When Zahoor's equation is used for predicting the drawdown depth using DFE Studies data, it overestimates the drawdown (see Appendix K).

Table 6.3 shows the angles of issuance, the angles of impingement and the corresponding drawdown depths collected in the experimental phase of this study.

Table 6.3. Drawdown depths versus calculated angles of impingement.

α (deg.)	δ (deg.)	Drawdown (m)
15	11.44	0.05
15	11.89	0.09
25	18.35	0.11
25	18.68	0.13
25	19.15	0.12
25	19.87	0.05
35	25.23	0.11
35	25.87	0.14
35	26.36	0.19
35	27.40	0.11

A regression analysis was run for the purpose of illustration. The parameters found in the linear regression are listed below:

Constant (m)	=	0.0190
Estimated standard error of constant	=	0.0344
R^2	=	0.3856
No of observations	=	10
Degrees of freedom	=	8
a_δ (m/deg.)	=	0.0045
Standard error of a_δ (m/deg.)	=	0.0020

The regression coefficient $R^2 = 0.39$ is very low, which indicates that the angle of impingement and the drawdown depth are not strongly correlated. Other factors might affect the drawdown depth. However, Figure 6.3 indicates that drawdown depths, h_o , tend to increase with an increase in the angle of impingement with respect to the vertical, δ .

The drawdown depth when the unit discharge is $0.372 \text{ m}^2/\text{s}$ (9.66 cfs/ft) can be expressed as:

$$h_o = 0.0190 + 0.0045 \delta \quad (6.2)$$

More data is necessary to derive a general relation between the drawdown depth h_o and the pertinent variables.

6.5 Representative Particle Size

Bed material was collected after the tests were concluded. The median particle size of the samples collected in the bottom of the scour hole and in the downstream slope was

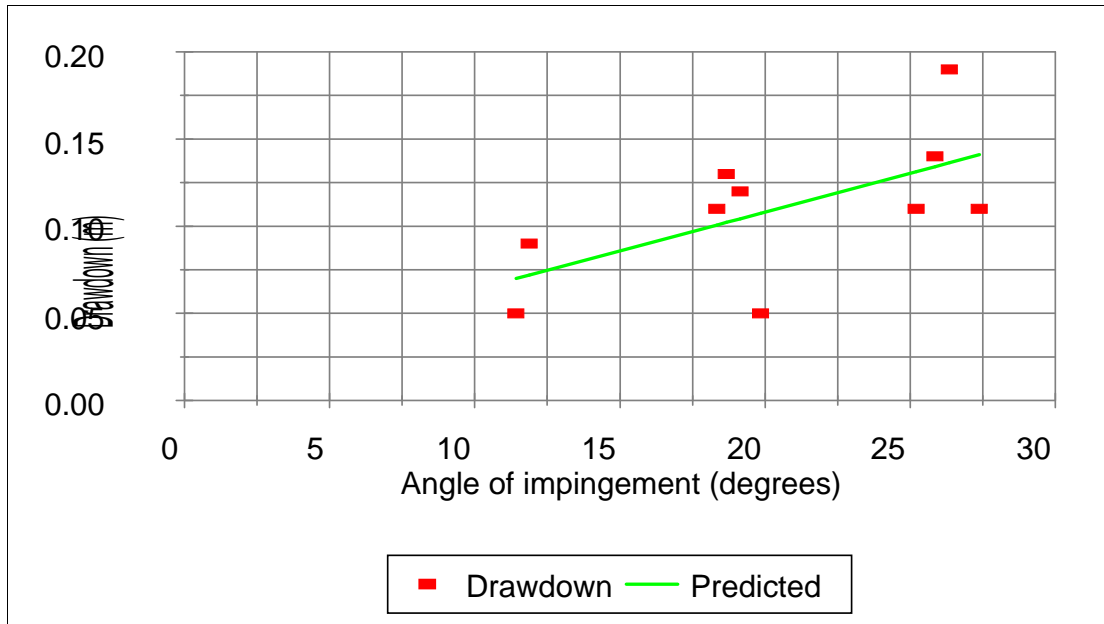


Figure 6.3. Drawdown depths versus angles of impingement for DFE studies.

approximately the nominal diameter corresponding to d_{85} of the original bed material. Similar results were obtained by Hallmark (1955). He reported that the addition of a small amount of armoring material produced a significant decrease on the ultimate depth of scour. This finding supports the idea that the depth of scour depends upon the coarser fractions of the original bed material. At the beginning of the test, the jet impinged on the bed after traveling a distance of $TW/\cos \delta$. Large and small particles were carried away and they deposited downstream of the scour hole. As the test progressed, the scour hole deepened. The heavier particles remained in place, the lighter ones were carried away, and armoring occurred. If the specific weight of the particles is considered constant, the heavier particles will also be the larger ones. Particles will be removed from the bottom of the scour hole when the hydrodynamic forces in the direction of the downstream slope are greater than the component of the weight parallel to the downstream slope and the friction between the moving particles and the subjacent ones. A summary of the median size particle of material

found in different sections of the scour hole with respect to the original bed material is shown in Table 6.4. The characteristic particle size in the final equation used for predicting the depth of scour, Y , will be d_{85} .

Table 6.4. Median diameter of material found in different sections of the scour hole with respect to initial bed particle size distribution.

Date of Test	δ (deg.)	d_{50} Initial			d_{50} Upstream	d_{50} Bottom	d_{50} Downstream	d_{50} Mound
10/03/96	19.15	n/a	n/a	n/a	n/a	d_{84}	n/a	n/a
7/17/97	25.87	d_{51}	d_{50}	d_{50}	d_{46}	d_{77}	d_{82}	d_{70}
7/24/97	25.23	d_{51}	d_{52}	-	d_{75}	d_{77}	d_{83}	d_{66}
09/02/97	18.35	d_{53}	d_{49}		d_{70}	d_{85}	d_{85}	d_{69}
09/11/97	18.68	d_{52}	d_{54}	d_{51}	d_{36}	d_{85}	d_{89}	d_{56}

6.6 Time Dependency of Depth of Scour

Floating sentinel elements (tennis balls) were placed before the tests at various depths. Although sentinel elements were also placed outside the longitudinal centerline of the bed, scour was detected outside the centerline only in two occasions. The following observations refer to scour occurring at locations along the centerline of the bed closest to the deepest points of the scour holes. The appearance of the tennis balls on the water surface indicated the depth of scour at a particular location at time t . The ratio of the depth of scour at a certain time to the final depth of scour, Y_t/Y_f , has been plotted against the ratio of the time to the total time of the test, t/T_f . The total time of scour, T_f , includes the necessary time to attain the specified discharge and the specified tailwater depth. It ranges between 114 minutes to 119 minutes. Scour occurs very rapidly near the centerline of the jet, as can be seen in Figure 6.4. Between 40 percent and 60 percent of the total depth of

scour is attained in less than 15% of the total time of the tests in each case. This means that 50 percent of the total depth of scour is reached in the first 20 minutes in most cases.

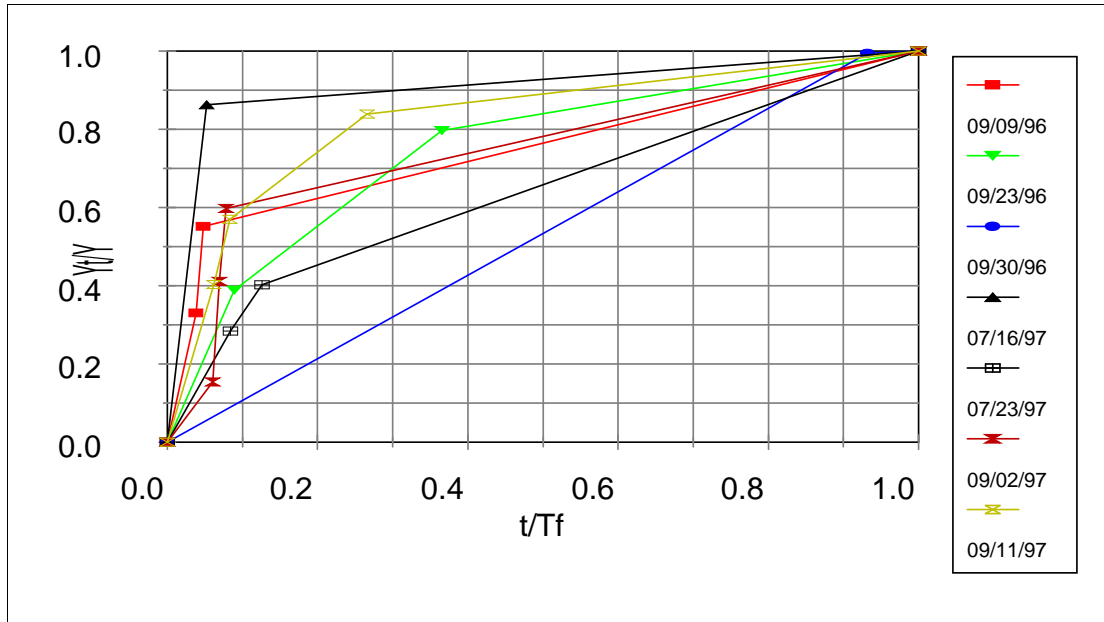


Figure 6.4. Ratios of depths of scour at certain times to the final depth of scour (Y_t/Y) versus ratios of time to the total time of tests (t/T_f).

6.7 Predictors of Scour Depth

6.7.1 Compact jets

Data from studies conducted by Thomas (1953), Hallmark (1955) and Lencastre (1961) were found in the literature review. They corresponded to laboratory tests in which scour occurred at the base of free overfalls. Photographic records indicated that air was not entrained before impingement. Therefore, the jets were classified as compact jets. Available data were separated in two groups, since the physical processes occurring in the jets before impingement were different. In the case of compact jets, the cross section is

reduced as the jet falls. Highly aerated jets, on the other hand, expand as they fall. Equation (6.3) is Equation (3.28) in which the interlocking factor has been eliminated and the fall velocity is calculated using d_{85} as the characteristic particle size. The parameters in Equation (6.3) for compact jets are given in Table 6.5.

$$\frac{Y}{y_c} = K \frac{\left(\frac{V_i}{\sqrt{g b_i}} \right)^a}{\left[\frac{(TW/\cos \delta)}{b_i} \right]^b \left(\frac{w}{\sqrt{g b_i}} \right)^c} \quad (6.3)$$

Table 6.5. Parameters of compact jets in Equation (6.3).

Parameter	Value	Std Error	CV(%)	Dependencies
K	0.965	0.122	12.67	0.978
a	0.719	0.055	7.64	0.977
b	0.124	0.023	18.18	0.886
c	1.257	0.093	7.42	0.525

The final form of the equation that predicts the depth of scour caused by a compact impinging rectangular jet on a cohesionless bed is given in Equation (6.4) as shown below.

$$\frac{Y}{y_c} = 0.965 \frac{\left(\frac{V_i}{\sqrt{g b_i}} \right)^{0.72}}{\left[\frac{(TW/\cos \delta)}{b_i} \right]^{0.12} \left(\frac{w}{\sqrt{g b_i}} \right)^{1.26}} \quad (6.4)$$

Figure 6.5 on the next page, shows a comparison between the predicted values of the relative depth of scour, Y/y_c , and the measured values of the relative depth of scour. A simple regression analysis yielded a regression coefficient R^2 of 0.77. Estimates of the depths of scour were plotted against the measured depths of scour in Figure 6.6 (next page).

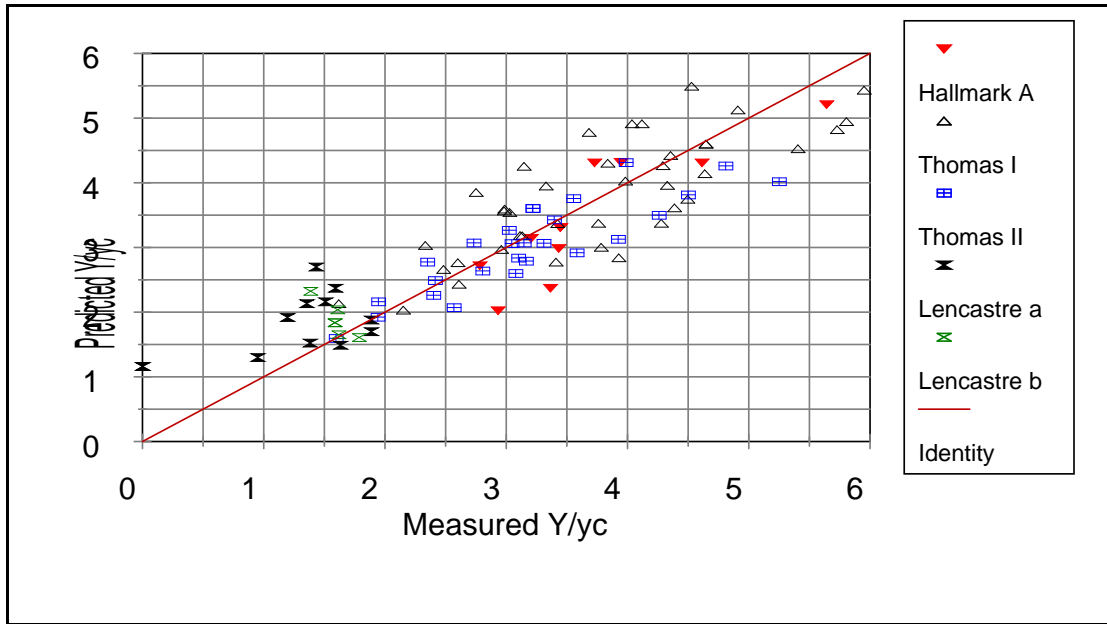


Figure 6.5. Predicted values of Y/y_c versus measured values of Y/y_c for compact jets.

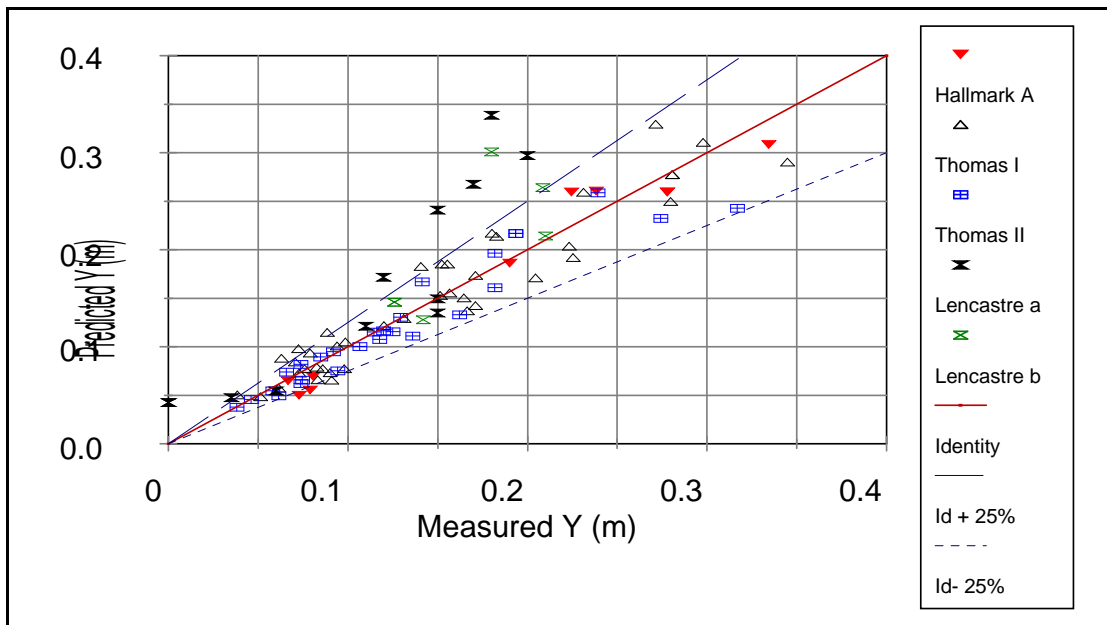


Figure 6.6. Predicted values of depth of scour versus measured values of depth of scour using Equation (6.4). The upper line (broken) corresponds to the values overestimated by 25% and the lower line (dotted) corresponds to the values underestimated by 25%.

The regression coefficient, R^2 , for the depths of scour was 0.80. In 81.3 % of the cases, the estimates of scour depth were within 25% of the measured values of scour. Furthermore, in 89 % of the cases, the predicted values were within 35% of the measured depth of scour.

Compact jet data has been extracted from the investigations conducted by Hallmark, Thomas and Lencastre. Their data included points taken for low tailwater depths in which the depth of scour increased slightly with an increase in tailwater depth. These points departed also from the expression proposed in this study for calculating the scour due to compact jets. When the tailwater depth was low, the depth of scour was approximately constant, suggesting that the forces available at the original ground surface remained unchanged until a critical depth was reached. The points that tended to overestimate the relative scour depth Y/y_c in Figure 6.6 correspond to tests in which the tailwater depth and the discharge were low. Also, as the tailwater depth decreased, the fall height increased. The fall height to the thickness of the jet ratio in Hallmark and Thomas' experiments was as high as 48. Disintegration of the jet could have affected the actual available head at the tailwater surface. Since the actual available head was not measured at the tailwater surface, no information exists that can confirm the loss of power of the jet due to disintegration. In any case, low tailwater scour tests produce data that departs from the general trend. In general, it is considered that pressures fluctuate with time, and that the ultimate depth of scour is a function of the total dynamic pressures available at the ground surface and the bed material. Since the tailwater depth attenuates pressure fluctuations, a minimum tailwater depth might be necessary to cause a significant decrease in maximum dynamic pressures. Dissipation of the energy of the jet might not occur until

a certain depth is reached. The potential for scour decreases thereafter. Furthermore, when the tailwater depth is very shallow, the bed level can be significantly lowered, due to the high stresses near the zone of impingement. The initial tailwater depth would not be representative of the tailwater depth during the formation of the scour hole in that case.

Lencastre used the largest particles in the compact jet database. In the series labeled "Lencastre a," he used 44 mm gravel and in the series labeled "Lencastre b," he used cubes with a 50 mm edge. In the "Lencastre b" tests, the cubes were placed in rows. If the calculated depth of scour was between two horizontal planes of fracture, it should be expected that scour would just penetrate to the plane immediately above of the calculated position of the bottom of the scour hole. In that case, overestimation of the depth of scour occurs as it can be seen in Figure 6.6.

Large particles also increase the roughness of the bottom of the scour hole and the area surrounding it. After the jet impacts the bottom, the jet tends to follow the contours of the downstream slope of the scour hole. If the jet encounters a rougher surface, the flow will tend to separate and the transport capacity of the jet in the downstream slope is lost to friction. For all the scour tests considered in this analysis, the dimensionless particle fall velocity, $w/(g b_i)^{0.5}$, represented adequately the resisting properties of the bed material, regardless of shape. The coefficients of variation of the parameters K , a , b , and c , are acceptable for this type of test. In contrast, the dependencies reported in Table 6.8 are very high. This could mean that one or more factors can be removed and still obtain an expression that produce similar results. However, removing any of the factors that are believed to be related to the potential for scour, causes a decrease in the accuracy of the

predictions. It is believed that “critical tailwater phenomenon” causes the dependencies to be high. When the tailwater depth is low, the scour is approximately constant.

6.7.2 Highly aerated (diverging) jets

Data gathered during the experimental phase of the Dam Foundation Erosion Studies was separated from the data obtained by other researchers. Bohrer and Abt (1996) concluded that the dissipation of the jet, after it enters the tailwater, varies as air entrainment increases. Also, the area of the cross section of a compact impinging jet is reduced as it falls and the velocity increases. In the Dam Foundation Erosion Studies, the jet was always a diverging jet. The cross section of the jet increased as the jet traveled to the tailwater. While the thickness of the jet was 8.7 cm (0.087 m) at issuance, it was 1 m (3.28 ft) to 1.5 m (4.92 ft) thick at the tailwater surface.

From the data presented in Section 5.1, it is evident that the tailwater depth and the angle of issuance play a major role in the development of scour holes. If the conditions of discharge, angle of impingement, and bed material remain constant, less scour is expected when the tailwater depth increases. In tests carried out by other researchers, it was noticed that a critical tailwater depth existed for which the depth of the scour hole was a maximum. All of them carried out tests using laboratory waterfalls, and the jets did not entrain significant amounts of air. Probably their capacity of penetration was not affected until a certain tailwater depth was reached. In the highly aerated jets used at the DFE facility, the influence of tailwater depth on the scouring capacity of the jets was more noticeable.

In twelve tests conducted at the DFE Facility the same unit discharge and same bed material were used. The only variables were the tailwater depth, the angle of impingement, and the available head. The available head did not vary significantly throughout the tests. It ranged from 8.80 m (28.87 ft) to 10.18 m (33.40 ft). The unit discharge also remained constant. The angle of impingement proved to be a major factor in the formation of the scour hole. When the jet impinged the bed at steeper angles relative to the horizontal, the scour holes were deeper when the rest of the conditions remained approximately constant, as can be seen in Figure 5.1. If the discharge, material, and tailwater depth remain constant, then an increase in the angle of the nozzle from the vertical will result in less scour. This can be attributed to longer trajectory lengths of the jet in water, $TW/\cos \delta$.

Hom-ma (1953) measured the velocity of the centerline of the jet below the tailwater surface. He found different expressions to describe the jet velocity for different angles of impingement and Reynolds numbers. Therefore, the influence of the angle of impingement in the rate of energy dissipation with larger tailwater depths has to be analyzed, because it appears that for more oblique angles, the influence of tailwater depth grows in importance.

At first, both the compact jet scour data and the diverging jet scour data were considered the same population. A regression analysis carried out using both compact jet data and highly aerated jet data showed significant dispersion in the predicted values of the compact jet data. Table 6.6 shows the parameters in Equation (6.3) obtained for diverging jets. They correspond to the data gathered in the experimental part of the Dam Foundation Erosion Studies.

Table 6.6. Parameters for highly aerated jets (diverging jets) in Equation (6.3).

Parameter	Value	Std Error	CV(%)	Dependencies
K	3.111	3.162	101.6	0.999
a	0.070	0.373	534.1	0.999
b	0.390	0.065	16.69	0.928
c	1.132	0.222	19.57	0.902

The final form of the equation used to predict the depth of scour produced by a rectangular impinging jet is given in Equation (6.5) as shown below:

$$\frac{Y}{y_c} = 3.111 \frac{\left(\frac{V_i}{\sqrt{g b_i}} \right)^{0.07}}{\left[\frac{(TW/\cos \delta)}{b_i} \right]^{0.39} \left(\frac{w}{\sqrt{g b_i}} \right)^{1.13}} \quad (6.5)$$

The exponent of the variable $(TW/\cos \delta)/b_i$ is 0.39. For compact jets, the exponent associated with the same variable is 0.12. This indicates that the effect of tailwater depth on the reduction of potential of scour is much more pronounced in highly aerated jets. An analogy can be made if aerated jets are considered as a collection of jets, as opposed to a solid one. After the jets impinges the tailwater, mutual interference between the jets causes a more drastic velocity decay. In addition, emerging bubbles carry part of the energy of the jet as they rise to the surface. Again, the resisting properties of the bed material can be characterized by $w/(g b_i)^{0.5}$. The exponent of $w/(g b_i)^{0.5}$ in the case of compact jets is 1.26, and in the case of diverging jets is 1.13. These values are not significantly different. Values of the predicted relative depths of scour, Y/y_c , were plotted against the measured relative depths of scour and presented in Figure 6.7. A simple

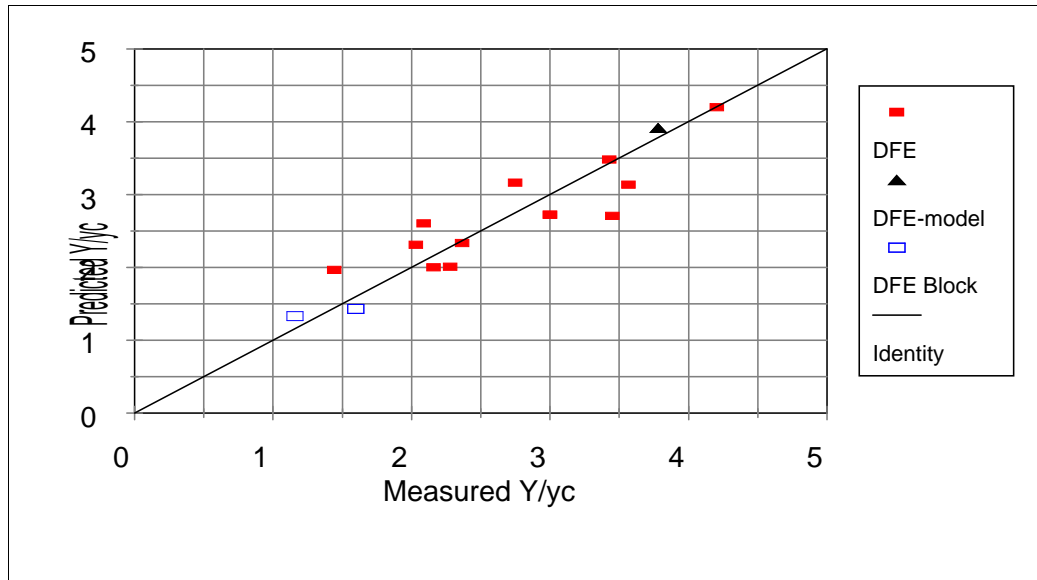


Figure 6.7. Predicted relative depth of scour versus measured relative depth of scour for highly aerated jets using Equation (6.5).

regression analysis yielded a regression coefficient R^2 of 0.80. Predicted depths of scour were plotted against the measured values of depth of scour in Figure 6.8. A simple regression analysis yielded a regression coefficient R^2 of 0.88. Equation (6.5) predicted the maximum depth of scour within 25% of the measured value in fourteen of the fifteen points (which would be 93.3 % of the cases). Furthermore, all of the predicted depths of scour but one fell within 35% of the measured values. The points corresponding to the fissured block tests and the point corresponding to the test conducted at the DFE model facility showed good agreement with the other twelve points. Forces have been calculated based on the measured pressures and the average area of the bottom of the blocks in Table I.5. Notice that calculated bottom forces are on the order of magnitude of the submerged weight of the blocks that were removed for the 1.42 m³/s (50 cfs) test. The submerged weight is approximately 3.08 kg (6.7 lbs) and the calculated bottom force is 1.97 kg (4.4 lbs).

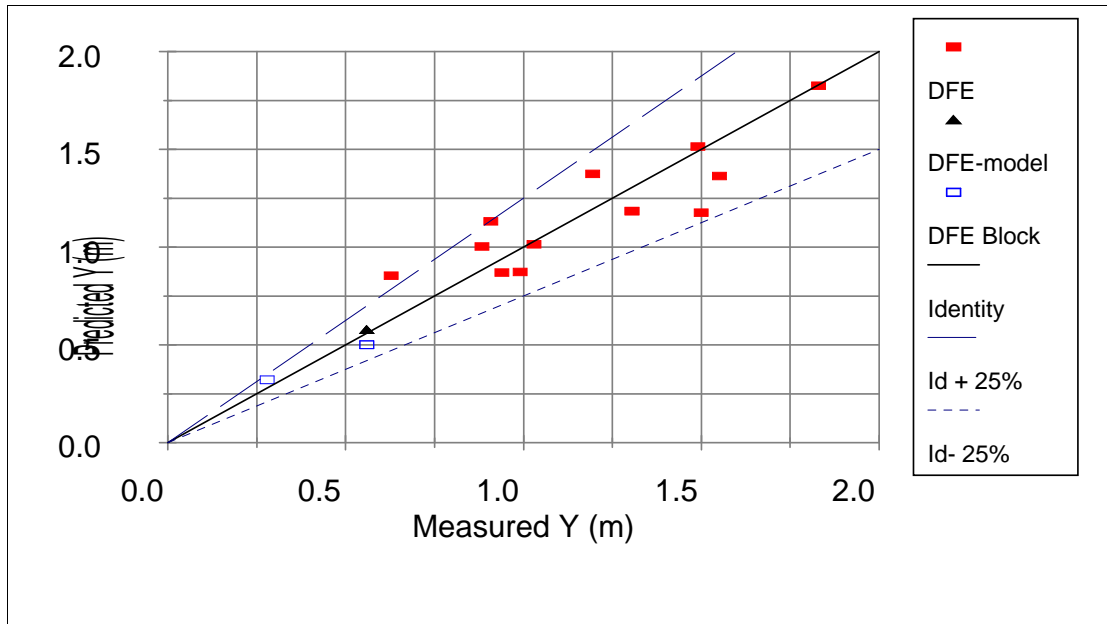


Figure 6.8. Predicted depths of scour using Equation (6.5) versus measured depths of scour. The upper broken line indicates an overestimation of 25% and the lower dotted line indicates an underestimation of 25%.

Twelve of the data points were gathered at the Dam Foundation Erosion Prototype facility using the same unit discharge and the same bed material for all tests. One test was conducted at the DFE model facility, and two were the simulated fractured rock test conducted at the Dam Foundation Erosion Facility.

The dependencies in this case are high because in twelve of the fifteen tests the discharge and the bed material were constant, and the only variables of importance were the tailwater depth and the angle of impingement. The coefficients of variation of K and “ a ” are very high in comparison to the coefficient of variation of the other parameters. In posterior analysis, the Froude number of the jet at the tailwater surface was eliminated because the parameter “ a ” was almost zero and its coefficient of variation was very high. The newly obtained parameters are presented in Table 6.7 and in Equation (6.6).

Table 6.7. Parameters for highly aerated (diverging) jets discarding the Froude number of the jet at impingement.

Parameter	Value	Std Error	CV(%)	Dependencies
K	3.755	0.586	15.61	0.947
b	0.388	0.062	15.96	0.927
c	1.124	0.208	18.48	0.898

$$\frac{Y}{y_c} = \frac{3.755}{\left[\frac{(TW/\cos \delta)}{b_i} \right]^{0.39} \left(\frac{w}{\sqrt{g b_i}} \right)^{1.12}} \quad (6.6)$$

A plot of the predicted relative depths of scour versus the measured relative depth of scour is given in Figure 6.9. A plot of the predicted depths of scour versus the measured depths of scour is given in Figure 6.10. The predictions of the depths of scour obtained suppressing the variable $V_i/(g b_i)^{0.5}$ are similar to the predictions in which the variable is considered. However, the coefficients of variation of K, b, and c decreased drastically. This result can be explained since the Froude number of the jet at impingement, $V_i/(g b_i)^{0.5}$, is almost constant in the 15 tests considered for the analysis of highly aerated jets as seen in Table C.2.2 in Appendix C.

In the compact jet data set, Lencastre's b data set can be considered representative of a simulated fissured rock. Cubes were orderly placed in the bed and very tightly packed. In the highly-aerated jet data set, rectangular blocks were used to simulate fissured rock in the DFE studies. The predicted values of scour caused by the jet in blocks were within 25% of the measured values. Also, scour predicted in the cubic blocks closely followed the measured values of scour. Fissured rock in which no cementing material fills the

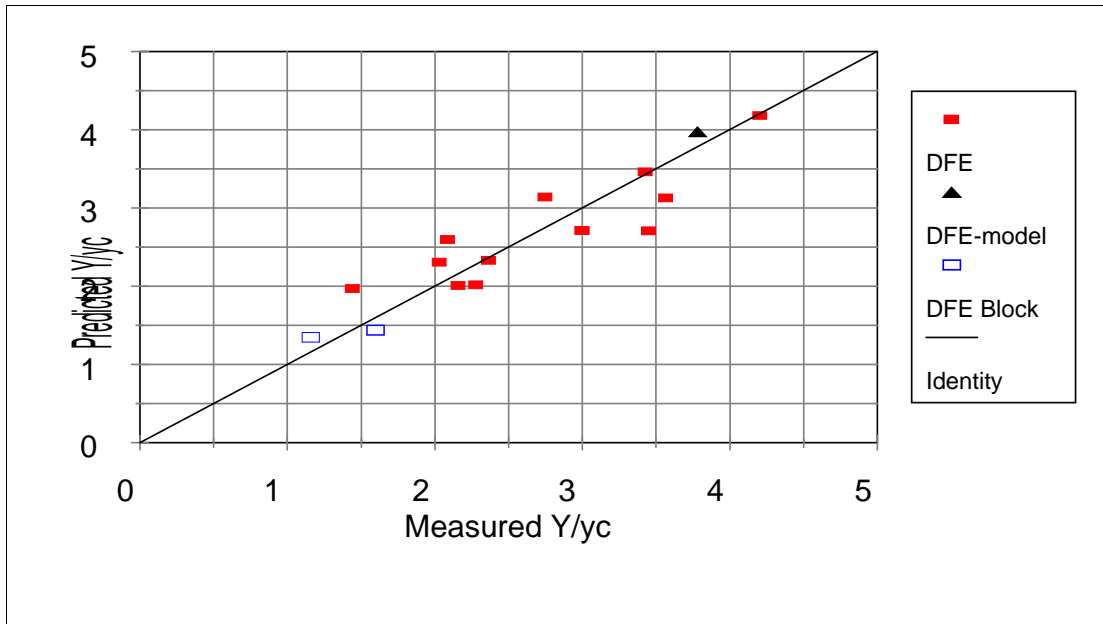


Figure 6.9. Predicted values of the relative depths of scour versus the measured values of the depths of scour using Equation (6.6).

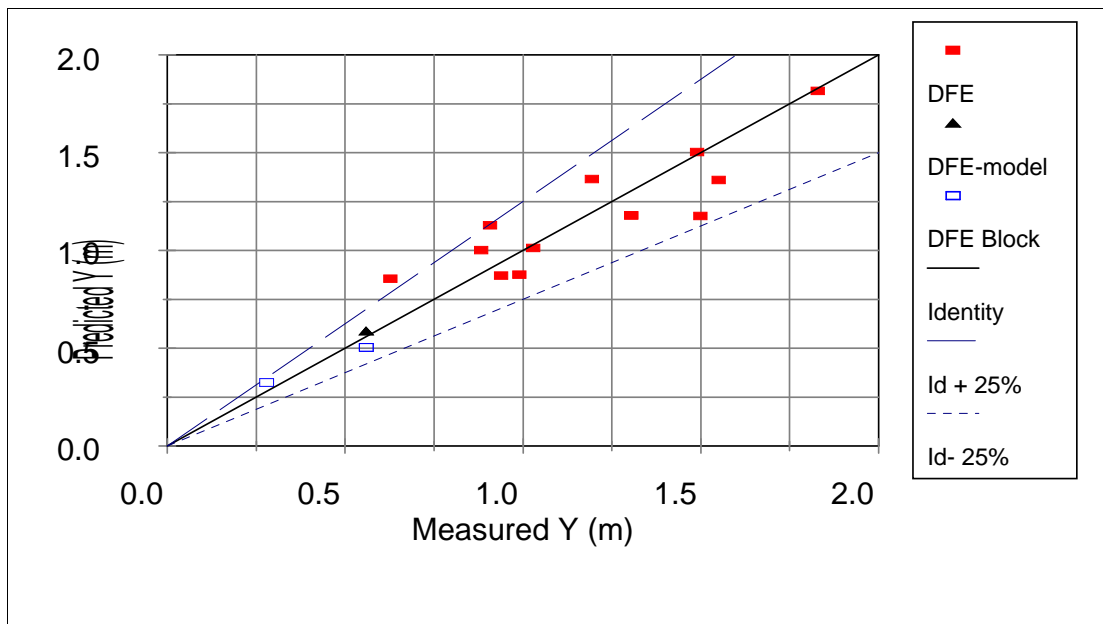


Figure 6.10. Predicted depths of scour using Equation (6.6). The upper broken line represents an overestimation of 25%. The lower dotted line represents an underestimation of 25% of the measured values.

joints between blocks might be treated as a cohesionless material. However, the following considerations should be taken into account:

- 1) A representative “rock size” and depth has to be chosen for each layer.
- 2) The particle fall velocity, w , is calculated using d_{85} , which is the equivalent diameter for which 85% of the particles are finer by weight. In the DFE erosion tests and in Lencastre b series the blocks were uniform. Therefore, d_{85} was equal to d_{50} . When the blocks of a rock mass are not very uniform, provisions need to be taken to choose a representative rock size.
- 3) The depths of the rock layers have to be taken into account when calculating the depth of a scour hole. A layer is not removed (consequently, the depth of scour does not increase) until the threshold for removing the fractured blocks of rocks is exceeded.

Equation (6.4), developed for compact jets, was used to predict the depth of scour caused by compact jets and highly aerated jets. Predicted depths of scour were plotted against measured depths of scour and presented in Figure 6.11. Equation (6.4) tends to overestimate the depth of scour caused by highly aerated impinging jets.

Equation (6.5), developed using highly aerated jets data, was used to predict the depth of scour caused by both compact jets and highly aerated jets. The predicted values of depth of scour were plotted against the measured values of depths of scour as shown in Figure 6.12. The depths of scour caused by compact jets are clearly underestimated when using Equation (6.5). The limit between highly aerated jets and compact jets remains to be established.

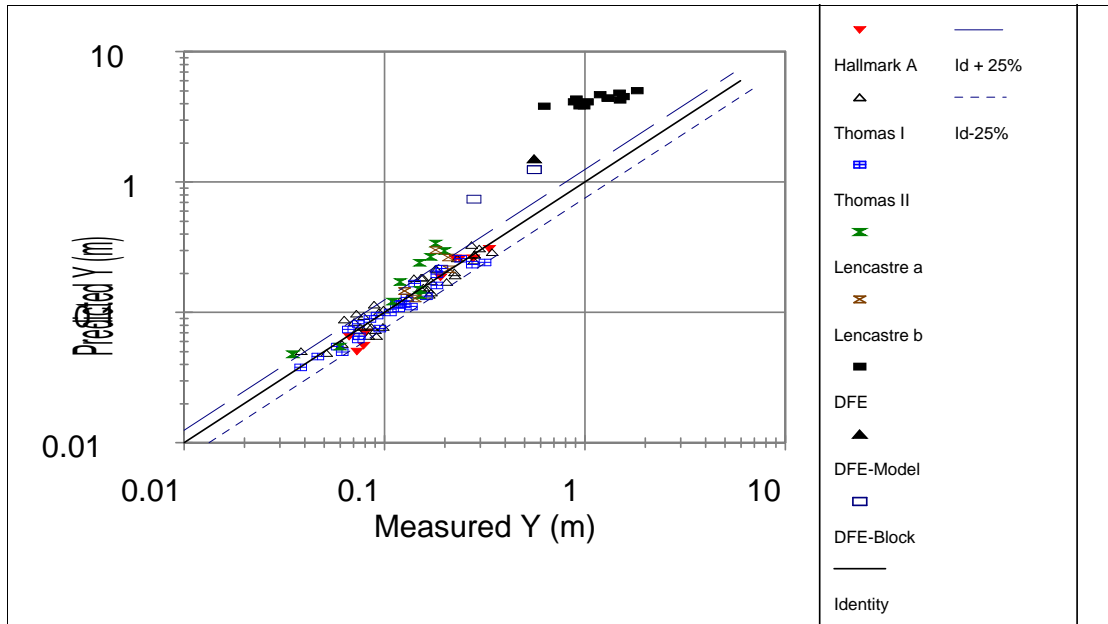


Figure 6.11. Predicted values of depths of scour using Equation (6.4). The depths of scour of highly aerated jets tends to be overestimated.

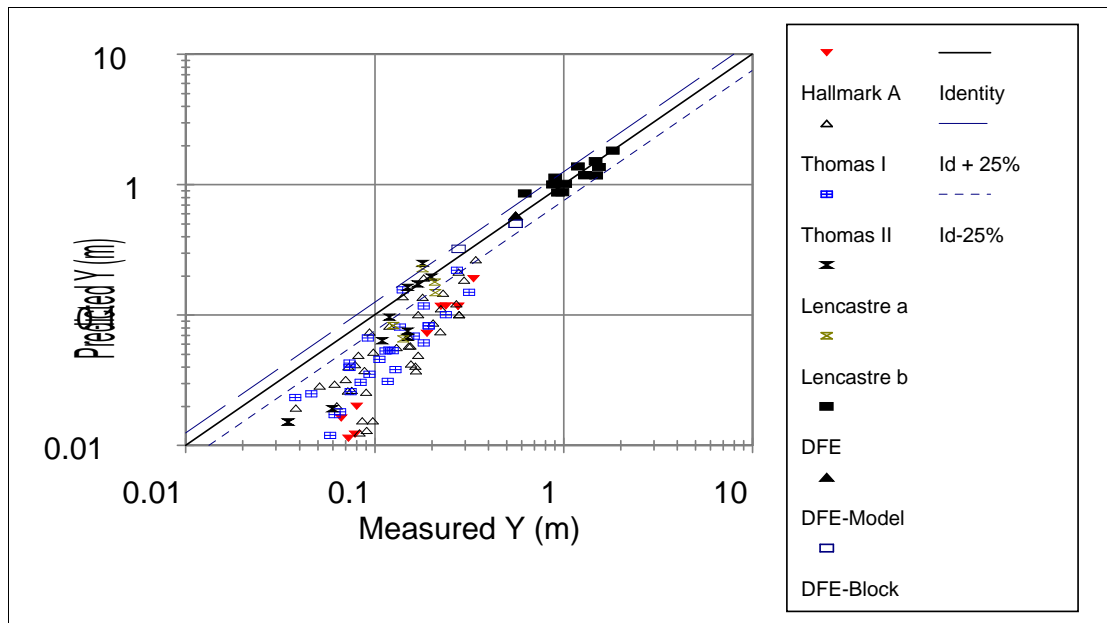


Figure 6.12. Predicted values of depths of scour using Equation (6.5). The depths of scour of compact jets tend to be underestimated.

A parameter that has not been studied by other researchers is the diverging angle of the jet. The diverging angle of the jet is the angle at which the jet spreads as it travels from the outlet (in this case the nozzle) to the tailwater. It is expected that narrower jets will produce deeper scour holes than thicker jets with the same (unit) discharge, because the rate of energy per unit area will be greater. The concept of an effective area of impingement could be a general parameter to take into account in order to study scour holes produced by aerated jets.

A factor that can influence the potential of scour of the jet is jet disintegration. As the trajectory length of the jet in the air increases, the potential for disintegration increases. Dynamic pressure coefficients at the bottom of a plunge pool decreased dramatically as the ratio of the trajectory length to the disintegration length approached 0.9 and were almost negligible as they approached 2 in experiments carried out by Ervine et al. (1997). Horeni's equation is used to calculate the disintegration length of the jet in Table 6.8. The trajectory length of the jet is approximated as $z/\cos \alpha$, where z is the fall height measured from the centerline of the nozzle to the tailwater surface and α is the angle of issuance. The ratio of the approximate trajectory length, $z/\cos \alpha$, to the disintegration length, L_d , is given in the last column of Table 6.8. The ratio of disintegration, $(z/\cos \alpha)/L_d$ ranges from 0.76 to 0.92 when α is 35 degrees, from 0.56 to 0.82 when α is 25 degrees, and from 0.51 to 0.68 when α is 15 degrees. The value of n in Equation (6.3) is lower when the angle of issuance is 35 degrees, but remains approximately constant when the angle of issuance is less than 25 degrees. The previous results might indicate that there is a relation between the degree of disintegration of a jet at impingement and its potential for scour.

Table 6.8. Ratios of approximate length of jet to disintegration length using Horeni's equation.

q (m ² /s)	α (deg.)	z (m)	δ (deg.)	cos δ	L _d (m)	(z/cos α)/L _d
0.897	15	3.79	11.388	0.980	5.796	0.622
0.897	15	3.48	11.568	0.980	5.796	0.557
0.897	15	3.12	11.796	0.979	5.796	0.677
0.897	15	2.87	11.956	0.978	5.796	0.513
0.897	25	4.33	17.749	0.952	5.796	0.823
0.897	25	3.90	18.031	0.951	5.796	0.759
0.897	25	3.55	18.418	0.949	5.796	0.676
0.897	25	2.94	19.009	0.945	5.796	0.559
0.897	35	4.37	23.437	0.918	5.796	0.920
0.897	35	3.92	23.907	0.914	5.796	0.926
0.897	35	3.60	24.264	0.912	5.796	0.759
0.897	35	2.98	25.002	0.906	5.796	0.628

6.8 Comparison Between Maximum Depth of Scour Using Mason's Formulae and the Actual Depth of Scour

Mason and Arumugan (1985) developed two formulae for predicting the maximum depth of scour holes for two different situations. The first formula was developed for predicting the maximum depth of scour produced by an impinging jet in model studies.

The second formula was developed for prototype situations. The formula for models is:

$$D = 3.27 \frac{q^{0.6} H_o^{0.05} TW^{0.15}}{g^{0.30} d_{50}^{0.1}} \quad (2.48)$$

where: D = the maximum depth of the scour hole measured from the water surface;

q = the unit discharge;

H_o = the difference in elevation between the upstream water level and the downstream water level;

TW = the tailwater depth;

g = the acceleration of gravity; and

d_{50} = the median size diameter.

Because the formula proposed by Mason calculates the depth of scour below the tailwater surface, D , the depth of scour below the original ground surface, Y , will be given by the difference between D and the tailwater depth, TW . The negative values of Y correspond to points in which the predicted depth of scour, D , was less than the tailwater depth, TW . Using Mason and Arumugan's model equation, the depth of scour is overpredicted for DFE data and underpredicted for model studies, as can be seen in Figures 6.13 and 6.14. The depth of scour is overpredicted for DFE data and model studies when Mason and Arumugan's prototype equation is used, as seen in Figure 6.14.

In Mason and Arumugan's model and prototype equation, the depth of scour below the water surface, D , is directly proportional to a power of the tailwater depth ($TW^{0.15}$). This contradicts the fact that the longer the trajectory of the jet in water, the more energy is dissipated and less energy is available to scour the bed. In model experiments, the depth of scour was reported to increase as the tailwater depth increased until a critical tailwater depth was reached. It decreased thereafter. The concept of a critical tailwater depth for which the depth of scour was a maximum was expressed by Thomas (1953), Hallmark (1955), Lencastre (1961) and others. Mason used a very extensive database to obtain the model and prototype formulae for calculating the maximum depth of a scour hole. He used Lencastre's and Thomas' data in addition to other data sets to obtain the model equation. His equation was developed by trial and error until the sum of the variances were minimal. When the tailwater depth is low, distortions such as the occurrence of a critical depth for which scour is a maximum result.

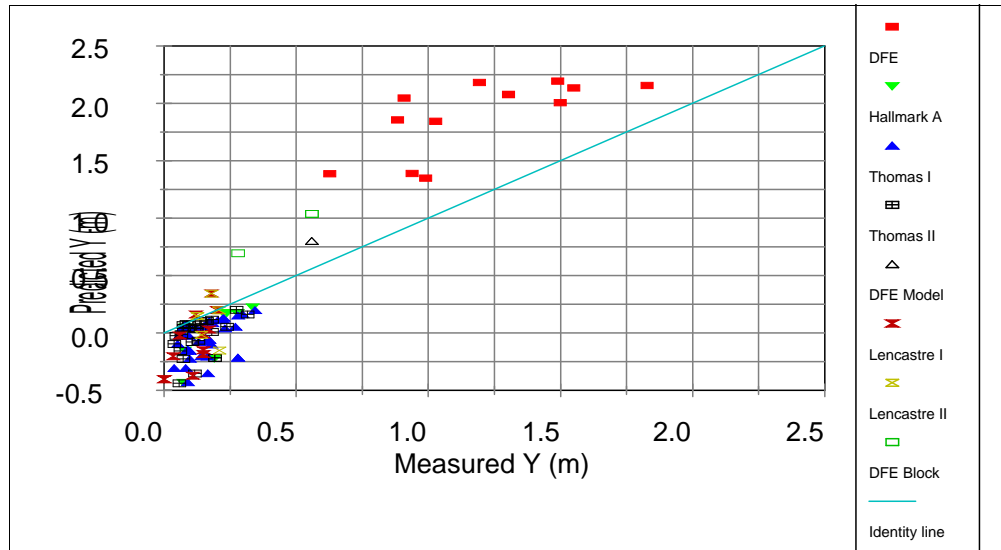


Figure 6.13. Predicted values of scour using Mason and Arumugan's model equation versus predicted measured values of scour. Negative values of Y indicate that the estimated value of depth below the tailwater surface was lower than the tailwater depth.

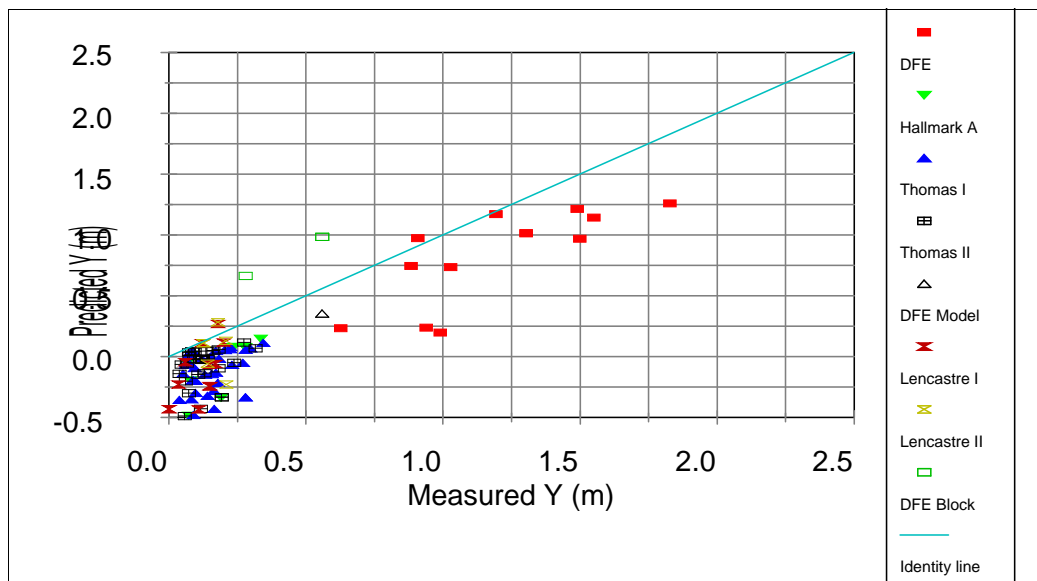


Figure 6.14. Predicted values of scour using Mason and Arumugan's prototype equation versus measured values of scour. Negative values of Y indicate that the estimated value of depth below the tailwater surface was lower than the tailwater depth.

Because the distance from the brink of the laboratory waterfalls to the downstream level was kept approximately constant for every data set, a decrease in tailwater depth results in an increase in the fall height. The jet disintegrates if the fall height is large in comparison to the disintegration length, which is associated with the unit discharge. For those cases, the depth of scour could possibly seem to be directly proportional to a power of the tailwater depth, as opposed to inversely proportional to a power of the tailwater depth. In Thomas, Hallmark and Lencastre's studies, plots of the depth of scour versus tailwater depth were given. They show that when the tailwater depth is very low the depth of scour appears to increase with an increase in tailwater depth until reaching the "critical" tailwater depth. It decreases thereafter. Thomas (1953) and Hallmark (1955) gathered the majority of their data when the tailwater depth was very low.

Mason's model equation was taken as a basis for his prototype equation. The exponent associated with the tailwater depth was kept constant. The other exponents changed. As a result, adjusting factors are used. Mason's prototype equation overpredicts the maximum depth of scour as seen in Figure 6.14.

Equation (2.55) was proposed by Hoffman (1998) to predict the depth of scour produced by 2-D impinging jets on cohesionless beds. Data gathered during the DFE studies was used to compare with Hoffman's equation to predict the depths of scour. Predicted values of the depth of scour were plotted against the measured values in Figure 6.15 as shown below. The depth of scour is clearly overestimated.

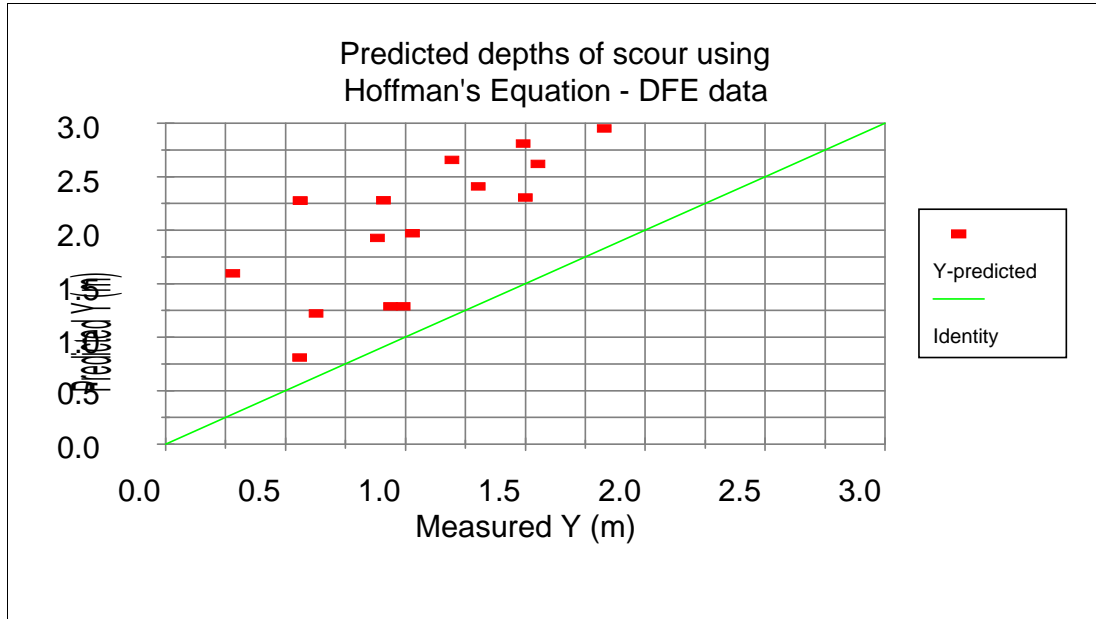


Figure 6.15. Predicted depths of scour using Equation (2.53) (Hoffman, 1998).

Machado (1980) proposed the use of two equations to calculate the depth of scour caused by jet. Equation (2.44) was developed to predict the depth of scour produced in granular materials caused by an impinging jet. Equation (2.59) was developed to predict the depth of scour occurring in any material. The main assumption of Equation (2.59) is that scour ceases where the power of the jet is entirely dissipated. Machado pointed out that Equation (2.59) might overestimate the depth of scour. Both Equation (2.44) and Equation (2.59) clearly overpredict the depth of scour as seen in Figures 6.16 and 6.17, respectively.

Depths of scour below the tailwater surface were calculated using Equation (2.42), proposed by Mirtshkulava et al. (1967). A plot of the predicted depths of scour using Equation (2.42) and the measured depths of scour is presented in Figure 6.18. Again, the depths of scour are largely overestimated. Calculations of the depths of scour are given in Appendix L.

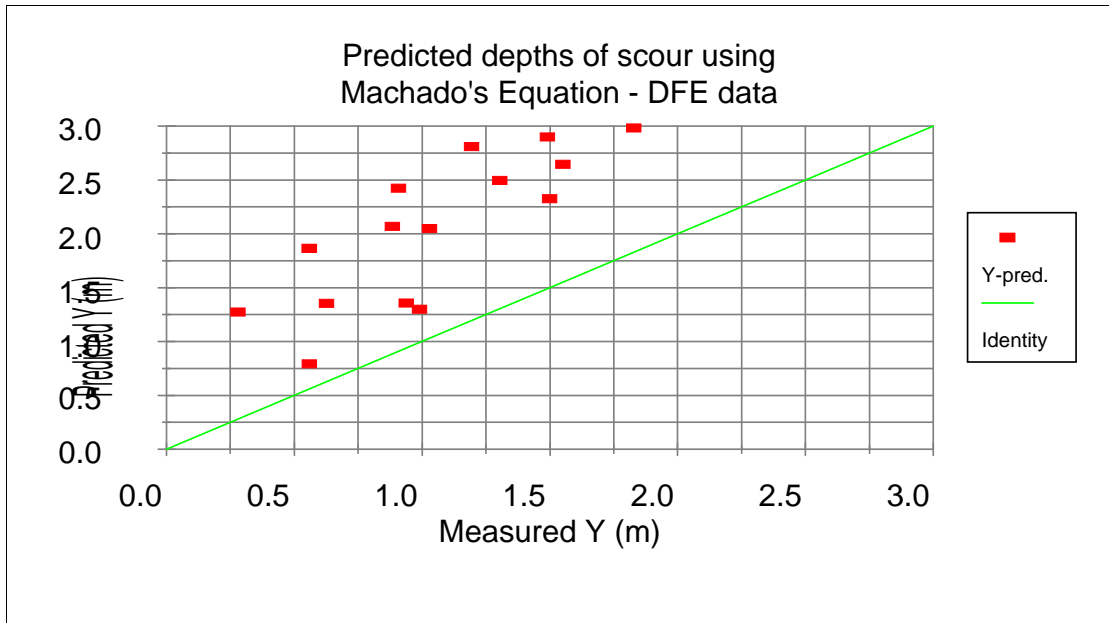


Figure 6.16. Predicted depths of scour using Equation (2.44) (Machado, 1980).

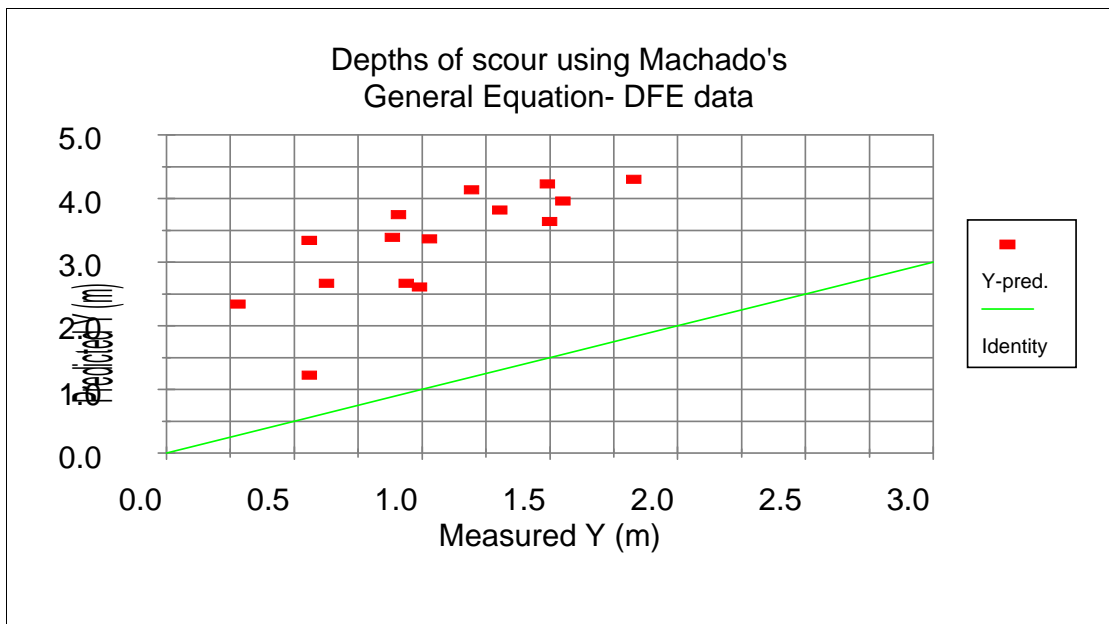


Figure 6.17. Predicted depths of scour using Equation (2.59) (Machado, 1980).

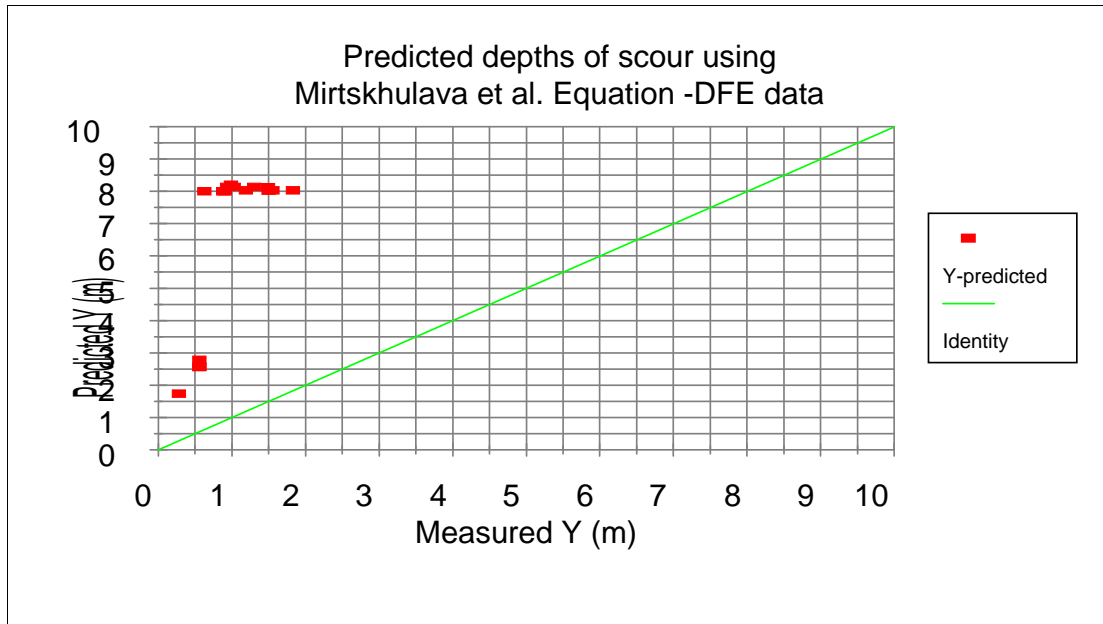


Figure 6.18. Predicted depths of scour using Equation (2.42) (Mirtskhulava et al., 1980).

6.9 Alternative Methods to Calculate the Depth of Scour Produced by Impinging Jets

Alternative methods to predict the depth of scour produced by impinging jets on cohesionless beds and fractured rock are presented in this section. First, a method proposed by Annandale (1995) is used to predict scour in a cohesionless bed. However, it can not be applied directly in all cases. The tailwater dissipated a significant amount of the power of the jet in the cohesionless (granular) material tests. Therefore, the dissipation of the jet in water must be taken into account. Annandale's method is used to estimate the power per unit area based upon the erodibility of the bed material. The particle velocity is in turn obtained from an expression that relates the power per unit area to the velocity of the jet. A correction factor is used to account for the fact that the particle is located on a slope as opposed to a flat bed. The minimum velocity required to entrain a particle located on the downstream slope of the scour hole is compared to the velocity calculated using Bohrer's

equation. The equation presented by Bohrer et al. (1996) for fully developed jets is used to predict the velocity of the jets below the tailwater surface. In the simulated fractured rock tests, the tailwater depth was minimal, and the prediction of the power per unit area necessary to dislodge the first layer is made directly. The measured power per unit area is compared to the predicted power per unit area and the discrepancy is close to 20%.

Equation (3.23) is used to calculate the threshold velocity of a particle located on the slope on the downstream side of a scour hole. The threshold velocities are compared to the velocities calculated using Bohrer's equation.

In addition, the velocities calculated using Bohrer's equation at the original bed surface were compared to the depths of scour measured along the centerline of the jet, $Y/\cos \delta$. Velocities calculated at the original bed surface using Bohrer's equation, V_L , appeared to be correlated to $Y/\cos \delta$.

6.9.1 Power per unit area versus erodibility

An analysis was conducted to check whether Annandale's approach is applicable to calculate the extent of erosion produced by an impinging jet on a cohesionless bed and simulated fractured rock. Annandale's approach is referred to in at least three publications (Annandale, 1995; Wittler et al., 1998; Annandale et al., 1998). In the first paper, Annandale's method is presented for general use. In the last two papers, Annandale's approach is used to specifically check the applicability of the method to calculate the depth of scour produced by impinging jets. Annandale (1995) presented two graphs correlating the power per unit area to the erodibility of the bed material. The first graph is for granular

materials. Using the data given in the first graph, the threshold required to erode smaller granular materials is given by Equation (6.7).

$$P_{crit} = K_h^{1/2} \quad (6.7)$$

In the second graph, in which a similar relation is presented for larger bed materials, the power per unit length required to erode larger materials such as rocks, is given approximately by Equation (6.8).

$$P_{crit} = K_h^{3/4} \quad (6.8)$$

6.9.2 Calculation of maximum depth of scour using equation of Bohrer et al. and Annandale's approach

The power of a stream having a specific weight γ , a discharge Q , and an available head H , is given by:

$$Power = \gamma Q H \quad (6.9)$$

Consequently, the power per unit area, P , is given by:

$$P = \frac{\gamma Q H}{A} \quad (6.10)$$

The average velocity of a jet at any point is given by Q/A . In addition, the excess available head at a point located at a distance "L" from the point of impingement is given by the velocity head of the jet at that point. Therefore "H" is equal to $V^2/(2g)$. Replacing in Equation (6.10), and taking into account that $\gamma = \rho g$, the power per unit area can also be obtained using the following expression:

$$P = \frac{\rho V^3}{2} \quad (6.11)$$

If the critical power per unit area for dislodging a particle is known, the critical velocity can be found using Equation (6.11). Most of the data obtained by Annandale to predict the erodibility of small cohesionless materials was obtained from flume tests. The streamlines were nearly parallel to the bed. Shear stresses in the bed were increased by changing the flow conditions (i.e., lowering the water level, increasing the discharge, etc.). In a cohesionless bed, the smaller particles are the first to be separated from the bed matrix, while the larger particles remain in place. In an open channel flow regime, the direction of the flow does not change drastically as scour takes place when lowering of the bed occurs. However, when a scour hole is produced by the impact of a jet, the direction of the flow changes near the bed surface. Part of the available power of the jet diffuses laterally, and the jet spreads in the downstream direction creating vortices and turbulence as seen in Figure 6.19. Therefore, not all of the available kinetic energy of the jet near the bottom of the scour hole is used to continue the process of erosion of the bed.

The minimum velocity of entrainment calculated using Annandale's method and Equation (6.11) is multiplied by a correction factor to account for the fact that the particle motion takes place on the downstream slope as opposed to a flat bed. Bormann (1990) developed a method to calculate the relationship between the critical shear stresses at the threshold of erosion on a slope and the critical shear stresses at the threshold of erosion in a flat bed. The resulting expression is given in Equation (6.12) and is similar to one proposed by Simons and Stevens (1971).

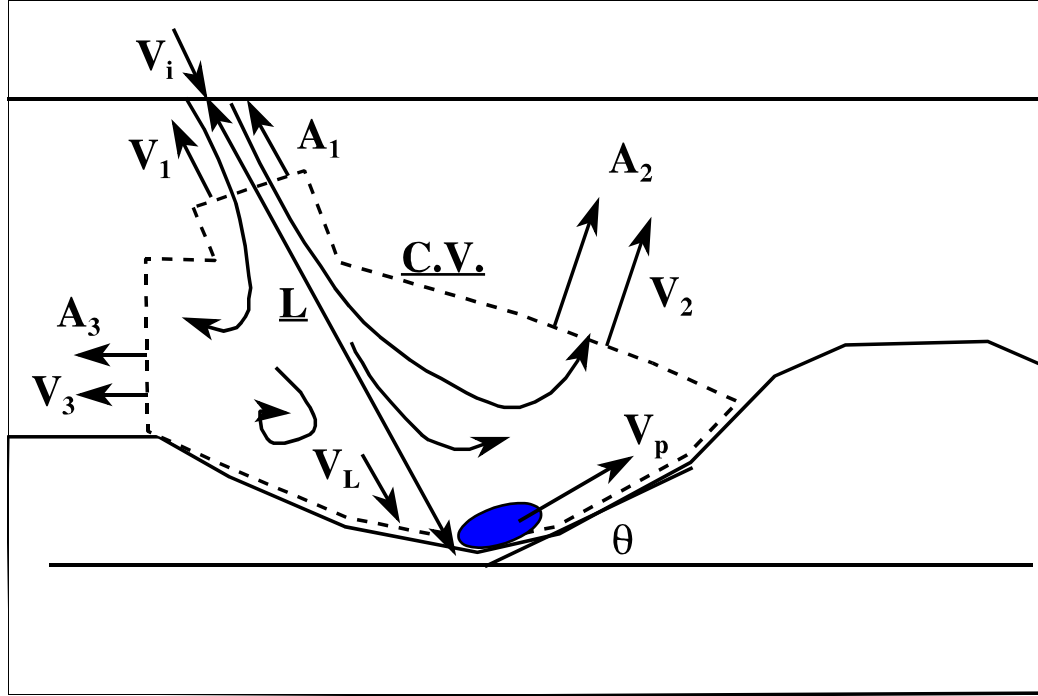


Figure 6.19. Diagram showing the calculated velocity, V_L , and the velocity of the particle, V_p .

$$\frac{\tau_{\theta}}{\tau_{crit}} = \frac{\cos(\theta) (\tan(\phi) + \tan(\theta))}{\tan(\phi)} \quad (6.12)$$

In Equation (6.12), θ is the downstream slope of the scour hole, ϕ is the angle of repose of the bed material, τ_{crit} is the critical shear stress on a flat slope, and τ_{θ} is the critical shear stress on an slope. Following the derivations by Bormann (1988), the shear stresses are proportional to the square of the velocities necessary to produce dislodgement. Provided that the bed material remains constant, the ratios of the velocities necessary to produce dislodgement, V_p/V_{crit} will be proportional to the square root of the ratio of the shear stresses, $\tau_{\theta}/\tau_{crit}$. The correction factor of the particle velocity at a slope θ is $(\tau_{\theta}/\tau_{crit})^{0.5}$.

The velocity at a distance “L” from the tailwater surface can be calculated using the equation by Bohrer et al. (1998) for fully developed jets:

$$-\ln\left(\frac{V_L}{V_i}\right) = -0.5812 \ln\left[\left(\frac{\rho_i}{\rho_w}\right) \left(\frac{V_i^2}{gL}\right)\right] + 2.107 \quad (2.19)$$

In which V_L is the velocity of the jet at a distance L from the tailwater surface, V_i is the velocity of the jet at the tailwater surface, ρ_i is the density of the aerated jet, ρ_w is the density of the water, and g is the acceleration of gravity.

The methodology for analysis follows. The erodibility index is calculated for d_{50} in Table 6.9 for the purpose of comparison, with the erodibility index of d_{85} . The erodibility index is calculated for d_{85} in Table 6.10. The characteristic particle size is assumed to be d_{85} instead of d_{50} because the particles found at the bottom of the scour hole had a median particle size equivalent to d_{85} of the original bed material. Then, the necessary power per unit area to cause incipient motion is calculated from Annandale’s expression.

The respective minimum velocity to produce entrainment of the bed material is obtained from Equation (6.11) (see Table 6.10). The velocity of the jet at a distance L from the tailwater surface is obtained using Equation (2.19) and presented in Table 6.11. L is the distance measured along the centerline of the jet from the tailwater surface to the bottom of the scour hole. Consequently, L is equal to $[(TW+Y)/\cos \delta]$. The entrainment velocity found in Table 6.10 is multiplied by the correction factor and presented in Table 6.12. The velocity V_L is compared to the calculated values of the bottom velocity and they exceed the corrected threshold velocity approximately by a factor of three (see Table 6.12). The ratio mean of the ratio V_L/V_p has a relatively low variability of 14.3 percent. Notice that V_L is one order of magnitude greater than the bottom velocity calculated using d_{50} .

Table 6.9. Erodibility of the granular material used in the Dam Foundation Erosion Studies (d_{50}).

Parameter	Value
M_s	0.07
d_{50} (m)	0.00296
$K_b = 1,000 d_{50}^3$	0.00002593
K_d (approximately tan 35 deg.)	0.7002
$J_s = 1$ for granular material	1
K_h	0.000001271
$P_{crit} (kW/m^2) = K_h^{0.5}$	0.0011
V_b (m/s)	0.131

Table 6.10. Erodibility of the granular material used in the Dam Foundation Erosion Studies (d_{85}).

Parameter	Value
M_s	0.07
d_{85} (m)	0.016
$K_b = 1,000 d_{85}^3$	0.0040975
K_d (approx tan 35 deg.)	0.7002
$J_s = 1$ for granular material	1
K_h	0.00020084
$P_{crit} (kW/m^2) = K_h^{0.5}$	0.01417
V_b (m/s)	0.305

Table 6.11. Velocities V_L calculated at a distance $L = (TW+Y)/\cos \delta$ from the tailwater surface using Bohrer's equation.

Study	V_i (m/s)	TW (m)	Y (m)	$\cos \delta$	$L = (TW+Y)/\cos \delta$ (m)	Air conc.	ρ_i (kg/m ³)	ρ_w (Kg/m ³)	ρ_i/ρ_w	$\ln (\rho_i/\rho_w^* V_i^2/(2gL))$	V_L (m/s)
DFE	13.50	0.57	1.55	0.98	2.17	0.94	61.128	1,000	0.061	-0.6443	1.13
DFE	13.24	0.85	1.50	0.98	2.40	0.94	61.128	1,000	0.061	-0.7876	1.02
DFE	13.72	0.27	1.83	0.98	2.14	0.94	61.128	1,000	0.061	-0.5984	1.18
DFE	13.05	1.85	0.99	0.98	2.90	0.94	61.128	1,000	0.061	-1.0044	0.89
DFE	13.10	1.80	0.94	0.95	2.89	0.94	61.128	1,000	0.061	-0.9952	0.89
DFE	13.56	1.17	1.03	0.95	2.32	0.94	61.128	1,000	0.061	-0.7065	1.09
DFE	13.59	1.16	0.88	0.91	2.24	0.94	61.128	1,000	0.061	-0.6655	1.12
DFE	13.14	1.80	0.63	0.91	2.68	0.94	61.128	1,000	0.061	-0.9142	0.94
DFE	13.82	0.84	0.91	0.91	1.91	0.94	61.128	1,000	0.061	-0.4729	1.28
DFE	14.13	0.50	1.19	0.92	1.85	0.94	61.128	1,000	0.061	-0.3945	1.37
DFE	14.10	0.41	1.49	0.95	1.99	0.94	61.128	1,000	0.061	-0.4736	1.30
DFE	13.87	0.77	1.30	0.95	2.19	0.94	61.128	1,000	0.061	-0.6009	1.19
Avg (m/s)											1.116
Std dev (m/s)											0.152
CV											0.136

Table 6.12. Comparison between estimated scour threshold velocities at the bottom of scour holes and calculated velocities at a distance $(TW + Y)/\cos \delta$.

$V_b - d_{85}$ (m/s)	θ (deg.)	ϕ (deg.)	τ/τ_{cr}	$(\tau/\tau_{cr})^{0.5}$	$V_p = V_b * (\tau/\tau_{cr})^{0.5}$ (m/s)	V_L (m/s)	V_L/V_p
0.305	26.565	35	1.533	1.238	0.378	1.129	2.991
0.305	24.513	35	1.502	1.226	0.374	1.018	2.725
0.305	24.560	35	1.503	1.226	0.374	1.179	3.153
0.305	26.243	35	1.528	1.236	0.377	0.886	2.349
0.305	23.557	35	1.487	1.220	0.372	0.894	2.403
0.305	29.899	35	1.579	1.257	0.383	1.093	2.854
0.305	20.907	35	1.444	1.202	0.366	1.123	3.064
0.305	15.961	35	1.354	1.164	0.355	0.939	2.647
0.305	18.624	35	1.404	1.185	0.361	1.277	3.534
0.305	17.223	35	1.378	1.174	0.358	1.366	3.818
0.305	24.891	35	1.508	1.228	0.374	1.302	3.478
0.305	26.012	35	1.525	1.235	0.377	1.189	3.158
						Min	2.349
						Max	3.818
						Mean	3.015
						SD	0.431
						CV	0.143

6.9.3 Simulated fractured rock test

The erodibility of fractured rock and the power required to dislodge a layer was calculated using Annandale's equation. The power per unit area acting on the blocks is assumed to be the power per unit area at the tailwater surface. The tailwater depth was low in the fractured rock tests. Therefore, the effects of tailwater dissipation are neglected. The calculation of the erodibility of the blocks is given in Table 6.13. The hydraulic conditions under which dislodgement occurred are given in Table 6.14. The required power per unit area to produce dislodgement of the blocks is approximately 25 kW/m², and the available power per unit area from the jet at DFE is approximately 21 kW/m². The discrepancy is 19.1%, which is acceptable, given the empirical nature of Annandale's approach. This result indicates that Annandale's approach might be directly applied for

predicting the dislodgement of the upper layer of a mass of fractured rock when the tailwater depth is low near the zone of impact of the jet.

Table 6.13. Erodibility of the blocks used in the Dam Foundation Erosion Studies.

Parameter	Value
M_s'	17.7
M_s (corrected for densities)	11.021
J_x	0.064
J_y	0.20
J_z	0.39
$RQD (105-10/(J_x \cdot J_y \cdot J_z)^{0.33})$	47.51
J_n (joint set number = 3)	2.73
K_b	17.4
K_d (approximately $\tan 36$ deg.)	0.7265
J_s (take $r = 1:2$, angle 45 deg. dipping in direction of flow)	0.535
K_h	74.55
$P_{crit} (kW/m^2) = K_h^{0.75}$	25.37

Table 6.14. Hydraulic conditions at the threshold of erosion. Simulated fissured rock tests.

Parameter	Value
Specific gravity of the fluid, γ , (N/m^3)	9806
Q (m^3/s)	1.13
Width (m)	3.05
q (m^2/s)	0.3705
Initial Velocity, V_o , (m/s)	4.2584
Velocity Head (m)	0.9246
z (m)	4.51
Velocity head at impingement, $V_i^2/(2g)$ (m)	5.44
Power of the jet (kW)	60.279
Width of the jet (m)	3.04
Thickness of the jet (m)	0.95
Area of the Jet (m^2)	3.4
Power per unit Area (kW/m^2)	20.87

6.9.4 Comparison between the calculated velocity of the jet, V_L , and the velocity of the particle at the downstream slope calculated using Equation (3.23)

Equation (3.23), developed in Section 3.11, is used to predict the minimum velocity, V_p , that induces motion of a particle whose specific gravity and size are known.

Then, the equation proposed by Bohrer et al. is used to calculate the velocity at a distance $(TW + Y)/\cos \delta$ from the tailwater surface.

$$V_p = \sqrt{\frac{4g}{3C_d} \left(\left(\frac{\rho_s}{\rho_w} \right) - 1 \right) d_n} \sqrt{\frac{\sin \theta + \left(\frac{K_1 a}{K_2 c} \right) \cos \theta}{1 + K_3 \left(\frac{K_1 a}{K_2 c} \right)}} \quad (3.23)$$

In which V_p is the velocity of the particle parallel to the downstream slope, g is the gravity acceleration, C_d is the drag coefficient of the particles, ρ_s is the density of the bed material, ρ_w is the density of water, d_n is the characteristic particle diameter, and θ is the angle of the downstream slope with respect to the horizontal. The drag coefficient, C_d , is assumed to be 1.5 (for coarse sand and larger particles). The ratio of moment arms of the forces acting on the particles, $(K_1 a/K_2 c)$, is assumed to be one. The lift coefficient to drag coefficient ratio, represented by K_3 , is assumed to be 0.20. Those velocities were compared to the velocities calculated using Bohrer's equation in Table 6.15. Bohrer's equation calculates the velocity of a jet at a distance "L" from the point of impingement. Again, L is $(TW + Y)/\cos \delta$ at the bottom of a scour hole. The velocities calculated using Bohrer's equation (in Table 6.11) are approximately two and a half times the velocities found using Equation (3.23). This result is expected, since there are losses due to turbulence at the bottom of the scour hole. In addition, the downstream slope of the scour hole, a solid boundary, forces the jet to change its direction. The variability of the ratio V_L/V_p is low. The calculated coefficient of variation of the mean of the ratio V_L/V_p is 14%.

This indicates that the results are consistent, and in general, there is no significant dispersion of the ratio V_L/V_p when the bed material is constant.

Table 6.15. Comparison between the calculated velocity at the bottom of the scour hole from Equation (3.23) and the threshold velocity, V_p .

θ (deg)	d_{85} (m)	G	V_p (Equation (3.23)) (m/s)	L (m)	V_L (m/s)	V_L/V_p (m/s)
26.565	0.016	2.65	0.439	2.17	1.129	2.571
24.513	0.016	2.65	0.436	2.40	1.018	2.333
24.560	0.016	2.65	0.437	2.14	1.179	2.700
26.243	0.016	2.65	0.439	2.90	0.886	2.018
23.557	0.016	2.65	0.435	2.89	0.894	2.054
29.899	0.016	2.65	0.443	2.32	1.093	2.467
20.907	0.016	2.65	0.431	2.24	1.123	2.605
15.961	0.016	2.65	0.422	2.68	0.939	2.227
18.624	0.016	2.65	0.427	1.91	1.277	2.991
17.223	0.016	2.65	0.424	1.85	1.366	3.221
24.891	0.016	2.65	0.437	1.99	1.302	2.980
26.012	0.016	2.65	0.439	2.19	1.189	2.712
					Min	2.018
					Max	3.221
					Mean	2.573
					Std	0.361
					CV	0.140

6.9.5 Depth of scour versus calculated velocity at the initial bed surface

The velocity of impingement of the jet at the tailwater surface was approximately constant for the 12 tests conducted using roadbase. As the tailwater depth, TW, and the angle of impingement, δ , increased, the depth of scour, Y, decreased. When the trajectory length of the centerline of the jet $TW/\cos \delta$, increases, the velocity is expected to decrease in Bohrer's equation. The velocities at a distance $TW/\cos \delta$ from the point of impingement were calculated using Bohrer's equation for fully developed jets. The lengths of scour, $Y/\cos \delta$, were correlated to the velocities at a distance $TW/\cos \delta$ from the impingement point. A relationship of the form.

$$(Y/\cos \delta) = a (V_L)^b \quad (6.13)$$

was found and is presented in Figure 6.20 in which a is equal to 0.829 and b is equal to 0.578. The linear regression coefficient found between $\ln(Y/\cos \delta)$ and $\ln(V_L)$ was $R^2 = 0.715$. The variables of importance are shown in Table 6.16. More tests have to be conducted under different conditions to develop a general relation that can be used to predict the depth of scour caused by an impinging jet on a cohesionless bed.

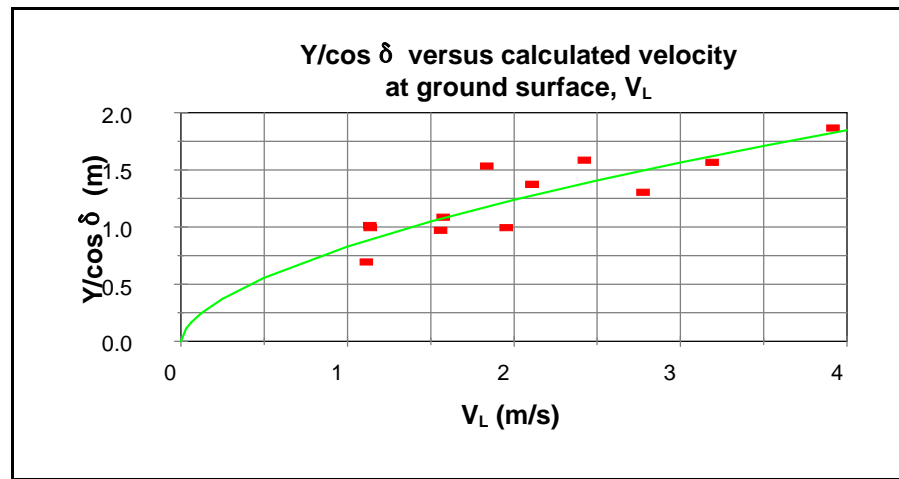


Figure 6.20. Depths of scour along the centerline of the jet versus estimated velocities V_L at a distance $TW/\cos \delta$ from the point of impingement.

Table 6.16. Lengths of scour $Y/\cos \delta$ versus estimated velocities at original bed surface V_L .

Study	V_i	TW	Y	$\cos \delta$	L	Air Conc.	ρ_i	ρ_w	ρ_i/ρ_w	$\ln(\rho_i/\rho_w \cdot V_i^2/(2gTW))$	$V(TW/\cos \delta)$	$Y/\cos \delta$	$\ln(V_{TW}/\cos \delta)$	$\ln(Y/\cos \delta)$	$(Y/\cos \delta)'$
	(m/s)	(m)	(m)		(m)		(kg/m ³)	(kg/m ³)			(m/s)	(m)			(m)
DFE	13.50	0.57	1.55	0.98	2.17	0.94	61.128	1,000	0.061	0.6700	2.424	1.584	0.885	0.460	1.383
DFE	13.24	0.85	1.50	0.98	2.40	0.94	61.128	1,000	0.061	0.2289	1.839	1.532	0.609	0.427	1.179
DFE	13.72	0.27	1.83	0.98	2.14	0.94	61.128	1,000	0.061	1.4681	3.917	1.866	1.365	0.624	1.826
DFE	13.05	1.85	0.99	0.98	2.90	0.94	61.128	1,000	0.061	-0.5750	1.137	1.013	0.128	0.012	0.893
DFE	13.10	1.80	0.94	0.95	2.89	0.94	61.128	1,000	0.061	-0.5751	1.141	0.993	0.132	-0.007	0.895
DFE	13.56	1.17	1.03	0.95	2.32	0.94	61.128	1,000	0.061	-0.0768	1.576	1.085	0.455	0.081	1.079
DFE	13.59	1.16	0.88	0.91	2.24	0.94	61.128	1,000	0.061	-0.0984	1.561	0.970	0.445	-0.031	1.072
DFE	13.14	1.80	0.63	0.91	2.68	0.94	61.128	1,000	0.061	-0.6156	1.117	0.693	0.111	-0.367	0.884
DFE	13.82	0.84	0.91	0.91	1.91	0.94	61.128	1,000	0.061	0.2612	1.956	0.994	0.671	-0.006	1.222
DFE	14.13	0.50	1.19	0.92	1.85	0.94	61.128	1,000	0.061	0.8264	2.778	1.302	1.022	0.264	1.497
DFE	14.10	0.41	1.49	0.95	1.99	0.94	61.128	1,000	0.061	1.0690	3.192	1.565	1.161	0.448	1.622
DFE	13.87	0.77	1.30	0.95	2.19	0.94	61.128	1,000	0.061	0.3868	2.111	1.372	0.747	0.316	1.277

CHAPTER 7

CONCLUSIONS AND RECOMMENDATIONS

7.1 Summary

The need to find an equation that accurately predicts the depth of scour caused by overtopping of a dam at its foundation prompted the U.S. Bureau of Reclamation and Colorado State University to conduct a research program. An equation that predicts the depth of scour produced by an impinging jet on a cohesionless bed was developed using the Pi-Buckingham theorem and the results of studies conducted by other researchers who studied the mechanics of jets and jet scour. Equation (3.28) was developed assuming the jet does not entrain air. It takes into account the effect of tailwater depth and angle of impingement on the depth of scour. Furthermore, the resistance of the bed to erosion is given by the fall velocity of a particle whose diameter is d_n .

The Dam Foundation Erosion (DFE) Facility was built at Colorado State University to simulate overtopping of a concrete dam. Material used for testing was placed in a 16.76 m (55 ft) by 9.14 m (30 ft) tailbox, and a jet was issued by a rectangular nozzle located above the tailwater surface. The study was limited to study scour produced by jet impingement in cohesionless beds.

The first test series consisted of twelve scour tests conducted using 19 mm (3/4 in.) roadbase, a cohesionless material. Tennis balls were buried as floating elements to detect

the depth of scour near the centerline of the jet at different times. The angle of issuance was changed in ten degree increments. The nozzle was set at 15 degrees, 25 degrees and 35 degrees with respect to the vertical. Four tailwater depths were tested for each of the angles of issuance. The net duration of the tests, after the specified tailwater depth and the specified discharge were attained, was 104 minutes. The specified discharge was 2.734 m³/s (96.6 cfs) and corresponded to a unit discharge of 0.897 m²/s (9.66 cfs/ft). Scour occurred very rapidly as indicated by the release of the tennis balls and at least 50 % occurred in the first 20 minutes of the tests. Bed material was collected at five different positions in the scour hole and the mound and the particle size distribution analysis showed that armoring occurred near the bottom of the scour hole. The median size of the particles found near the bottom of the scour hole was d_{85} of the original bed material. The testing area was surveyed after each test was conducted and the depths of scour below the original bed surface were plotted against the tailwater depths and angles of issuance. The plot showed that the depth of scour decreased as the tailwater depth increased when the rest of the conditions remained constant. Also, steeper angles of impingement produced deeper depths of scour. The scour holes were ellipsoidal in most cases. An interesting relationship between the downstream slope and the angle of impingement was found. The downstream slope of the scour hole remained constant until the angle of impingement was 18 degrees. It decreased thereafter.

The jet issued at the Dam Foundation Erosion Facility can be considered as a highly aerated jet. Readings taken at DFE indicated that the air concentration of the jet was on the order of 92% to 96% at the tailwater surface. Also, the apparent color of the jet was

white in all cases. This indicates that significant amounts of air were entrained by the jet as it traveled to the tailwater.

Attempts to measure the velocity of the impinging jet before it impinged the tailwater surface and after it impinged the tailwater surface were made using a backflushing Pitot tube. Air concentration was also measured using an air concentration probe. Unit discharge was held constant. Depth above the Pitot tube and air concentration probe was varied. Air concentrations and velocities were approximately constant until the depth above the measuring devices was approximately 0.35 m (1.15 ft). Both decreased noticeably with further increase of the depth. Calibration of the backflushing Pitot tube was made before and after the tests. The measured velocities of the jets and their respective air concentrations decreased as they moved away from the tailwater surface. However, the measured values of the velocity of the jet at impingement were always greater than the theoretical values. Consequently, the velocity and air concentration data was considered only for qualitatively describing the velocity decay of the jet in water.

The second test series was conducted to simulate the effect of impinging jets on a bed composed of fractured rock. Fractured rock was simulated by placing lightweight concrete blocks in two layers. They were fluted on one side, flat on the other side. They were 0.39 m (15.5 in.) high, 20 cm (8 in.) wide, and 0.064 m (2.5 in.) thick. Piezometer tubes were installed near the top and near the bottom of the blocks in 9 locations, along and across the centerline of the testing surface.

Discharge was increased until dislodgement occurred at $1.13 \text{ m}^3/\text{s}$ (40 cfs). The corresponding unit discharge was $0.371 \text{ m}^2/\text{s}$ (4 cfs). Piezometer readings were taken and indicated that the pressures at the bottom of the scour hole were greater than the pressure

near the top of the blocks near the centerline of the jet. Blocks were deposited upstream of the zone of impingement. Discharge was increased to $1.27 \text{ m}^3/\text{s}$ (45 cfs), and $1.42 \text{ m}^3/\text{s}$ (50 cfs). The dimensions of the scour hole increased in the longitudinal and lateral directions. However, the depth of scour did not increase. A second test was conducted with an initial discharge of $1.42 \text{ m}^3/\text{s}$ (50 cfs). The tailwater depth was not controlled by the downstream slide gate. Discharge was increased until the bottom layer failed at $1.982 \text{ m}^3/\text{s}$ (70 cfs). The corresponding unit discharge was $0.650 \text{ m}^2/\text{s}$ ($7 \text{ ft}^2/\text{s}$). A plume of earth was detected downstream of the zone of impingement. This indicated that significant movement had occurred in the bottom layer. Visual inspection confirmed that three blocks had been removed from the bottom layer.

Two equations were developed using data from previous studies and from this study. Both equations were obtained using Equation (3.28) as a basis. In Equation (3.28), the unit discharge, the velocity of the jet at impingement, the thickness of the jet at impingement, the tailwater depth, the angle of impingement, and the bed material are known.

Data gathered by Thomas (1953), Hallmark (1955) and Lencastre (1961) were used to develop Equation (6.4), which predicts the depth of scour produced by compact jets. Equation (6.4) predicted the depth of scour within 25% of the predicted depth of scour in 81% of the cases. Furthermore, the prediction of the depth of scour was within 35% in 89% of the cases. This shows a significant improvement with respect to previous studies. When Equation (6.4) is used to predict the depth of scour produced by a highly aerated jet, the depth of scour is overestimated.

Data obtained in the Dam Foundation Studies experimental program were used to develop Equation (6.5), which predicts the depth of the scour hole when the jet is highly aerated. The predicted values of the depths of scour fell within 25% of the measured values in 93 % of the cases. Equation (6.5) clearly underpredicts the depths of scour caused by compact jets. In general, a significant improvement in the prediction of depths of scour was obtained when the physical processes occurring in the formation of a scour hole were taken into account.

7.2 Conclusions

1. Three factors were found to affect the depth of scour caused by an impinging jet on a cohesionless bed: the tailwater depth, the angle of impingement, and the degree of aeration of the jet. The depth of scour caused by a highly aerated jet decreased with an increase in tailwater depth when the air concentration of the jet at impact was approximately 94% and the unit discharge was $0.897 \text{ m}^2/\text{s}$. An increase of the angle of impingement with respect to the vertical also reduced the depth of scour for similar tailwater depths. A regression analysis was run using data taken by other researchers in which the jets did not entrain appreciable amounts of air. It was concluded that such data belongs to a different population than the data taken in this study. Two equations are proposed to calculate the depth of scour, according to the degree of air entrainment. Equation (6.4) is used for calculating the depth of scour caused by compact jets (jets that do not entrain air).

$$\frac{Y}{y_c} = 0.965 \frac{\left(\frac{V_i}{\sqrt{g b_i}} \right)^{0.72}}{\left[\frac{(TW/\cos \delta)}{b_i} \right]^{0.12} \left(\frac{w}{\sqrt{g b_i}} \right)^{1.26}} \quad (6.4)$$

Equation (6.5) is used for calculating the depth of scour caused by highly aerated jets.

$$\frac{Y}{y_c} = 3.111 \frac{\left(\frac{V_i}{\sqrt{g b_i}} \right)^{0.07}}{\left[\frac{(TW/\cos \delta)}{b_i} \right]^{0.39} \left(\frac{w}{\sqrt{g b_i}} \right)^{1.13}} \quad (6.5)$$

Both equations adequately predict the depth of scour caused by impinging jets on cohesionless beds.

2. A matrix formed by blocks can be considered a collection of large cohesionless materials when there is no cementing material between the blocks. The equations developed for both compact jets and highly aerated jets can be applied to matrices formed by blocks that simulate fissured rock. In both cases, the depths of scour of blocks were adequately predicted.
3. Scour takes place in steps in a simulated fissured rock mass. The depth of scour does not increase until the threshold for removing a block from a layer has been exceeded.
4. Surveys conducted in this study and by Hallmark (1955) show that the median size of the particles remaining at the bottom of the scour hole and the downstream slope is approximately d_{85} of the original bed material. If the bed

is composed by cohesionless materials of different sizes, the representative particle used to calculate the depth of scour is d_{85} .

5. The downstream slope of a scour hole, θ , is a function of the angle of impingement with respect to the vertical, δ . It is constant until the angle of impingement is approximately 18 degrees. It decreases thereafter with an increase in δ .
6. The rate of scour caused by a highly aerated jet on a cohesionless bed is high at the beginning of a test and decreases rapidly as the test progresses. Approximately 50% of the scour occurred during the first 20 minutes of the test while the total testing time was 104 minutes.

7.3 Recommendations for Future Research

Any investigation conducted to develop new technology leaves questions unanswered, raises new questions, and provides preliminary information on how to improve the existing database. This study is no exception and recommendations to improve the knowledge in the field of jet scour follow.

The database of scour caused by highly aerated jets on cohesionless beds needs to be increased. The granular media tests produced twelve points obtained using the same unit discharge and the same bed material. Two additional points were obtained using a two-layer block setup whose layers failed at two different discharges, and an extra point was obtained in the model facility using a smaller granular material. Tests should be carried out at different discharges and using bed materials of different sizes. The tailwater depths and angles of issuance should be similar to those used in this study. Once the

database for highly aerated jets is increased, a new regression analysis should be carried out using Equation (3.28) as a basis.

It is believed that studying the velocity distribution of the jet near the bottom of preformed scour holes would greatly improve the knowledge of the processes leading to scour. Special attention should be given to study the effect of roughness of the bed material on the velocity distribution of the jet. Furthermore, the disintegration of a jet in air, in conjunction with power dissipation in water, affects the available pressures at the original ground surface. Therefore, the scouring capacity of the jet is affected by jet disintegration in air. In order to measure velocities of the jet in air and water, the accuracy of the backflushing Pitot tube needs to be improved or a more accurate device to measure velocities of two-phase flows needs to be invented.

Two expressions have been proposed in this study to predict the depth of scour caused by a rectangular impinging jet on a cohesionless bed. One expression was obtained when jet entrainment was minimal. The second expression was obtained using data when the jet was highly aerated. However, definite limits for the application of both equations are yet to be given. Research needs to be conducted to determine the air concentration limits of highly aerated jets and compact jets, and whether an intermediate condition (as suggested by the studies of Bohrer et al.) exists.

REFERENCES

- Abt, S.R, Lewis, T., Annandale, G., Mefford, B., Ruff, J., Wittler, R., Adhya, K., and Morris, D. (1995). "Pit 4 dam, slab and buttress foundation scale model simulation." U.S. Bureau of Reclamation, Denver, CO.
- Albertson, M.L., Dai, Y.B., Jensen, R.A., and Rouse, H. (1950). "Diffusion of submerged jets." Transactions ASCE, 115:639-664.
- Annandale, G.W. (1995). "Erodibility." J. Hydr. Res., Delft, The Netherlands, 33(4):471-494.
- Bell, F.G. (1992). Engineering in rock masses. Butterworth Heinmann Ed. Kent, Great Britain.
- Beltaos, S. (1976). "Oblique impingement of plane turbulent jets." J. Hydr. Div., ASCE, 102(9):1177-1192.
- Beltaos, S., and Rajaratnam, N. (1974). "Impinging circular turbulent jets." J. Hydr. Div., ASCE, 100(10):1313-1328.
- Blaisdell, F.W., and Anderson C. (1989). " Scour at cantilevered pipe outlets, plunge pipe pool energy dissipator design criteria." Agricultural Research Service. Springfield, VA.
- Blaisdell, F.W. (1983). "Analysis of scour observations at cantilevered pipe outlets." Agricultural Research Service, Springfield, VA.

- Blaisdell, F.W., and Anderson, C. (1991). "Pipe plunge pool energy dissipator." *J. Hydr. Engrg.*, ASCE, 117(3):303-323.
- Bohrer, J.G., and Abt, S.R. (1996). "Plunge pool velocity prediction of rectangular, free falling jets." Department of Civil Engineering, Colorado State University, Ft. Collins, CO.
- Bormann, N.E., and Julien, P.Y. (1991). "Scour downstream of grade control structures." *J. Hydr. Engrg.*, ASCE, 117(5):579-594.
- Chang, H.H. (1988). *Fluvial processes in river engineering*. John Wiley & Sons, New York, NY.
- Coleman, N.L. (1979). "Bed particle Reynolds modelling for fluid drag." *J. Hydr. Res.*, Delft, The Netherlands, 17(2):91-105.
- Davis, A.C., Ellett, B.G.S., and Jacob, R.P. (1998). "Flow measurement in sloping channels with rectangular free overfalls." *J. Hyd. Engrg.*, 124(7):760-763.
- Doddiah, D. (1949). "Comparison of scour caused by hollow and solid jets of water." M.S. Thesis, Colorado State University, Fort Collins, CO.
- Doehring, F.K. (1987). "The influence of drop height on outlet scour." M.S. Thesis. Colorado State University, Fort Collins, CO.
- Ervine, D.A., Falvey, H.T., and Withers, W.A. (1997). "Pressure fluctuations on plunge pool floors." *J. Hydr. Res.*, Delft, The Netherlands, 35(2):257-279.
- George, R.L. (1980). "Impinging jets." U.S. Department of the Interior, Water and Power Resources Service, Springfield, VA.
- Hallmark, D.E. (1955). "Influence of particle size gradation on scour at the base of a free overfall." M.S. Thesis, Colorado State University, Fort Collins, CO.

- Hamilton, K.J., and Abt, S.R. (1997). "Dam foundation erosion, phase III - clear water experiments 1:3 scale model facility, plunge pool circulation at dam foundations." Colorado State University, Fort Collins, CO.
- Hoffman, G. (1998). "Jet scour in equilibrium phase." J. Hydr. Engrg., ASCE, 124(4): 430-437.
- Hom-ma, M. (1953). "An experimental study on water fall." Proceedings Minnesota International Hydraulics Convention, Minneapolis, MN, pp. 477-481.
- Julien, P.Y. (1995). Erosion and sedimentation. Cambridge University Press, New York, NY.
- Laursen, E.M. (1952). "Observations on the nature of scour." Proc. 5th Hydraulic Conference, University of Iowa, Iowa City, IA, Bulletin 34, pp. 179-197.
- Lencastre, A. (1961). "Descarregadores de Lamina Livre, bases para o seu estudo e dimensionamento." Memoria No.174, National Laboratory of Civil Engineering. Ministry of Public Works, Lisboa, Portugal.
- Leutheusser, H.J., and Birk, W.M. (1991). "Drownproofing of low overflow structures." J. Hydr. Engrg., 117(2):205-213.
- Lewis, T.M. (1996). "Prediction of velocities within jets formed by overtopping Steep dams." M.S. Thesis, Colorado State University, Fort Collins, CO.
- Machado, L.I. (1980). "Formulas para calcular o limite da erosao em leitos rocosos ou Granulares." XIII Seminário Nacional de Grandes Barragens, Tema 1, Rio de Janeiro, Brazil, pp. 35-52.
- Mason, P.J., and Arumugan, K. (1985). "Free jet scour below dams and flip buckets." J. Hydr. Engrg., ASCE, 111(2):220-235.

- Mason, P.J. (1989). "Effects of air entrainment on plunge pool scour." J. Hydr Engrg., ASCE, 115(3):385-399.
- McKeogh E.J., and Elsayy, E.M. (1980). "Air retained in pool by plunging water jet." J. Hydr. Div., ASCE, 106(10):1577-1593.
- Mendoza-Cabrales, C. (1980). "Headwall influence on scour at culver outlets." M.S. Thesis, Colorado State University, Fort Collins, CO.
- Mirtskhulava, E., Dolidze I.V., and Magomedova, A.V. (1967). "Mechanism and computation of local and general scour in non-cohesive, cohesive soils and rock beds." Proceedings, Twelfth Congress of International Association for Hydraulic Research, Colorado State University, Fort Collins, CO, pp. C20 (1-8).
- Novak, P. (1984). Developments in hydraulic engineering. Vol 2. Elsevier Applied Science Publishers. Belfast, Northern Ireland.
- Rajaratnam, N. (1976). Turbulent jets. Elsevier Scientific Publishing Company, Amsterdam, The Netherlands.
- Rajaratnam, N. (1981a). "Erosion of a loose polysterene bed by obliquely impinging circular turbulent air jets." Technical Report WRE 81-2, Department of Civil Engineering, University of Alberta, Edmonton, Alberta, Canada.
- Rajaratnam, N. (1981b). "Erosion of sand beds by circular impinging water jets with minimum tailwater." Technical Report Water Resources Engineering Group 81-3, Department of Civil Engineering, University of Alberta, Edmonton, Alberta, Canada.
- Rajaratnam, N., and Pochylko, D.S. (1981c). "Further studies on the erosion of sand beds by plane water jets." Technical Report Water Resources Engineering Group 81-4,

Department of Civil Engineering, University of Alberta, Edmonton, Alberta, Canada.

Rajaratnam, N., and Albers C. (1998). "Water distribution in very high velocity water jets in air." *J. of Hyd. Engrg.*, 124(6):647-650.

Shafai-Bajestan M. (1989). "Riprap criteria at pipe outlet." Dissertation, Colorado State University, Fort Collins, CO.

Stein, O.R., and Julien P.Y. (1994). "Sediment concentration below free overfall." *J. Hydr. Engrg.*, 120(9):1043-1059.

Stevens, M.A., and Simons, D.B. (1971). "Stability analysis for coarse granular materials on slopes." *River Mechanics, Volume I* (Edited and Published by H.W. Shen), Fort Collins, CO.

Streeter, V. L., and Wylie, B. (1985). *Fluid mechanics. Eight Edition*, McGraw-Hill Inc., New York, NY.

Thomas, R. (1953). "Scour in a gravel bed at the base of a free overfall." M.S. Thesis, Colorado State University, Fort Collins, CO.

U.S. Bureau of Reclamation (1987). *Design of small dams*. Department of the Interior, Denver, Colorado.

Vanoni, V. (1975). *Sedimentation engineering*. ASCE, New York, NY.

Zahoor, T. (1992). "Evaluation of flip bucket-plunge pool energy dissipator." Dissertation, Colorado State University, Fort Collins, CO.

APPENDIX A

INFLUENCE OF TW/b_i ON PRESSURE DISSIPATION

APPENDIX A

INFLUENCE OF TW/b_i ON PRESSURE DISSIPATION

In this Appendix, Lencastre's data was used to find an expression that relates the average available head at the tailwater surface to average values of the available head at the bottom of a plunge pool. A short discussion is included.

Data in Table A.1. was extracted from Lencastre's graph (Figure 2.6 in Chapter 2) and corresponds to dimensionless excess pressures at the centerline of the jet.

Table A.1. Relative pressure heads at a plate for different relative water depths. Data is taken from Lencastre (1961).

TW/b_i	$(H_{gs})/H_{act}$
0.0	1.000
5.7	0.473
10.6	0.250
15.1	0.100
19.7	0.060
24.2	0.020

A relation of the type:

$$\frac{H_{gs}}{H_{act}} = \frac{1}{\left(\frac{TW}{b_i} + c_1 \right)^{c_2}}$$

can be used to obtain a mathematical expression that describes the relation between the pressure head in a non-erodible smooth surface and the total available head at the plane of impingement. The following expression was obtained:

$$\frac{H_p}{H_{act}} = \frac{1}{\left(\frac{TW}{b_i} + 1\right)^{0.6337}} \quad (A.1)$$

The coefficient of variation for c_1 is 18.55% and for c_2 is 17.12%. A graph comparing the points calculated using the above expression with the points given in Table A.1 is given in Figure A.1. Pressures at the centerline of the jet are further dissipated in the scour hole. The jet is not expanding freely. The maximum depth of the scour hole is determined by the capacity of the jet to remove material from the bottom of the scour hole.

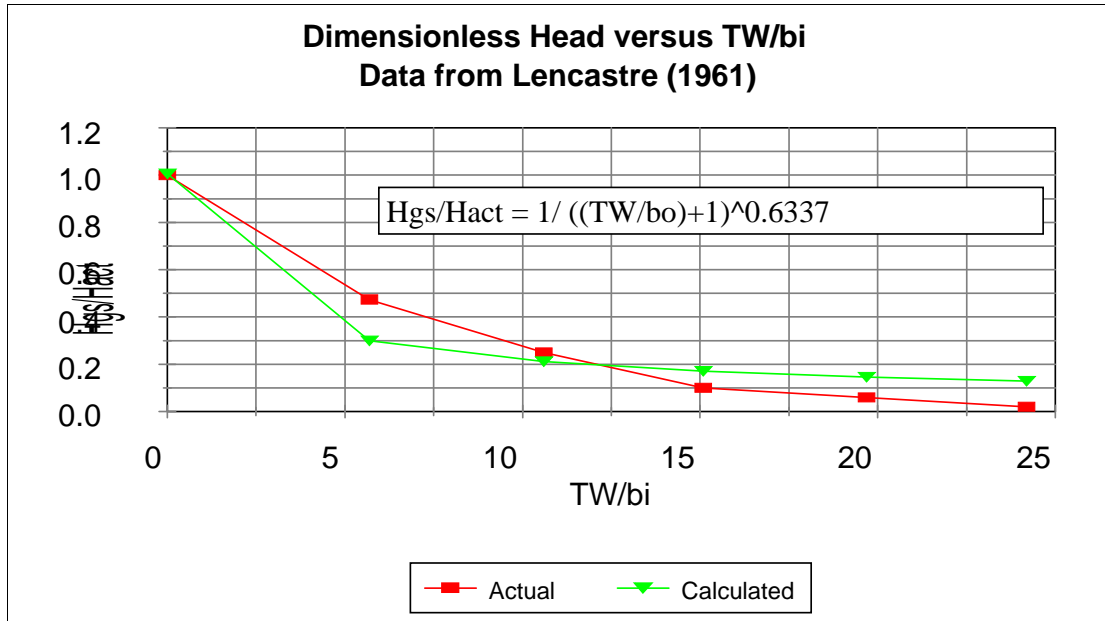


Figure A.1. Excess dimensionless mean pressure heads of a jet impinging on a plate with a dimensionless tailwater depth TW/b_i .

The previous expression was developed for a vertical jet. If the jet is inclined, the trajectory length of the jet in the water before it impinges the plate, TW_{δ} , is:

$$TW_{\delta} = \frac{TW}{\cos \delta} \quad (A.2)$$

The following expression takes into account the dissipation of the head pressures in a longer path when the jet is inclined:

$$\frac{H_g}{H_{act}} = \frac{1}{\left(\frac{TW}{b_i \cos \delta} + c_1 \right)^{c_2}} \quad (A.3)$$

As the jet scours the bed, the boundary conditions change with time. The jet is not impinging on a flat, non-erodible surface. On the other hand, the jet is not free in the vicinity of the zone of impingement. Velocities are expected to decay even more drastically within the scour hole, until the hydrodynamic forces of the jet cannot remove particles from the bottom of the scour hole.

APPENDIX B
DAM FOUNDATION EROSION FACILITY
&
NOZZLE AND DIFFUSER DIAGRAMS

APPENDIX B
DAM FOUNDATION EROSION FACILITY
&
NOZZLE AND DIFFUSER DIAGRAMS

The diagrams of the Dam Foundation Erosion Facility, where the experimental phase of this study was conducted, are given in Appendix B. Important features are also included. Figure B.1 is a general plan of the DFE facility. Figure B.2 shows a cross section of the diffuser and the nozzle. Figure B.3 illustrates the front view of the diffuser and the slot where the nozzle is attached. The position of the Pitot tubes along the centerline of the nozzle is given in Figure B.4. An elevation of the DFE facility with the positions of the diffuser, the manometer and the Pitot tube is given in Figure B.5.

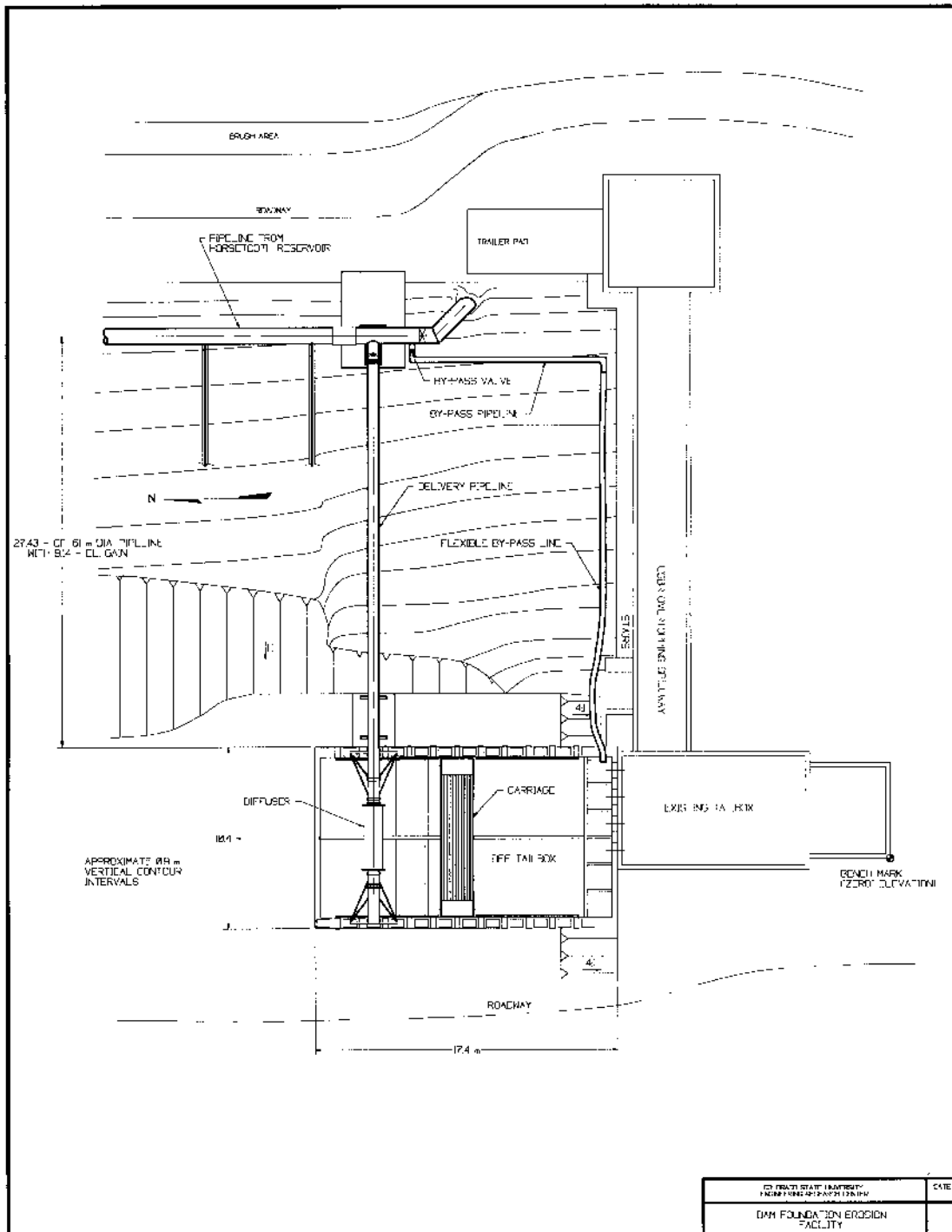


Figure B.1. Dam Foundation Erosion Facility.

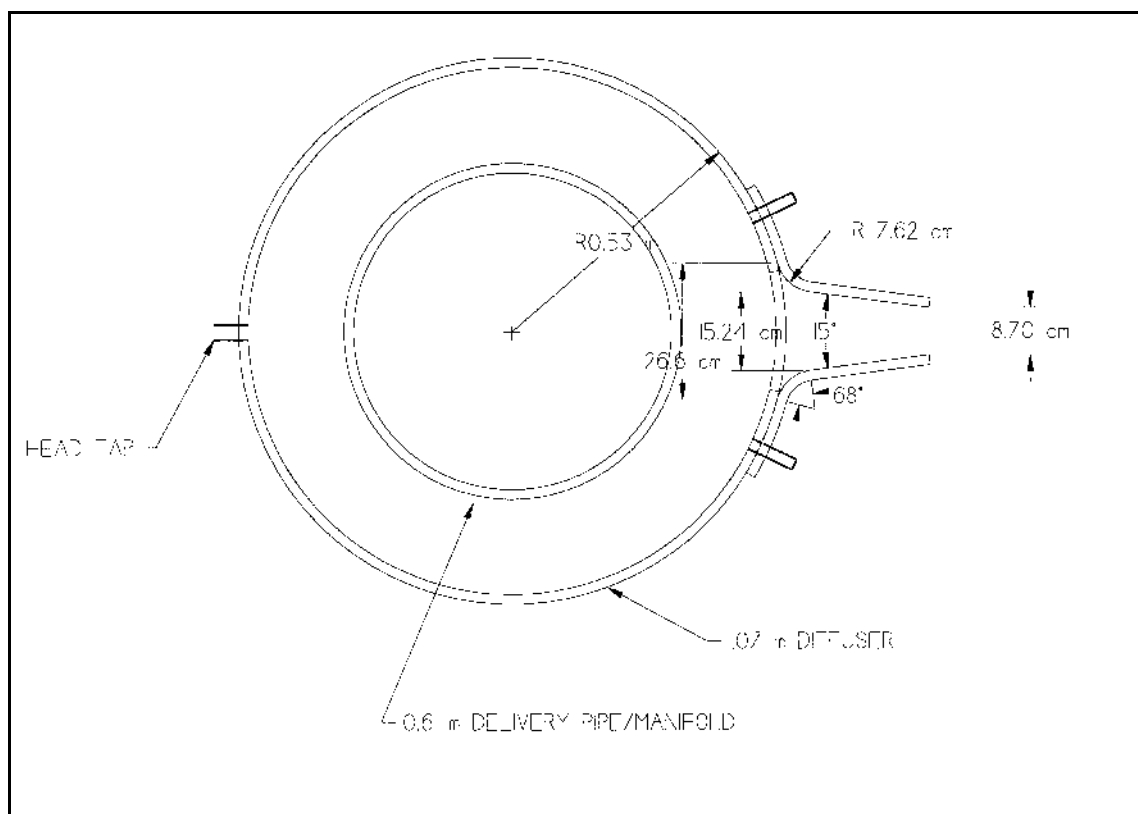


Figure B.2. Dam Foundation Erosion Facility diffuser.

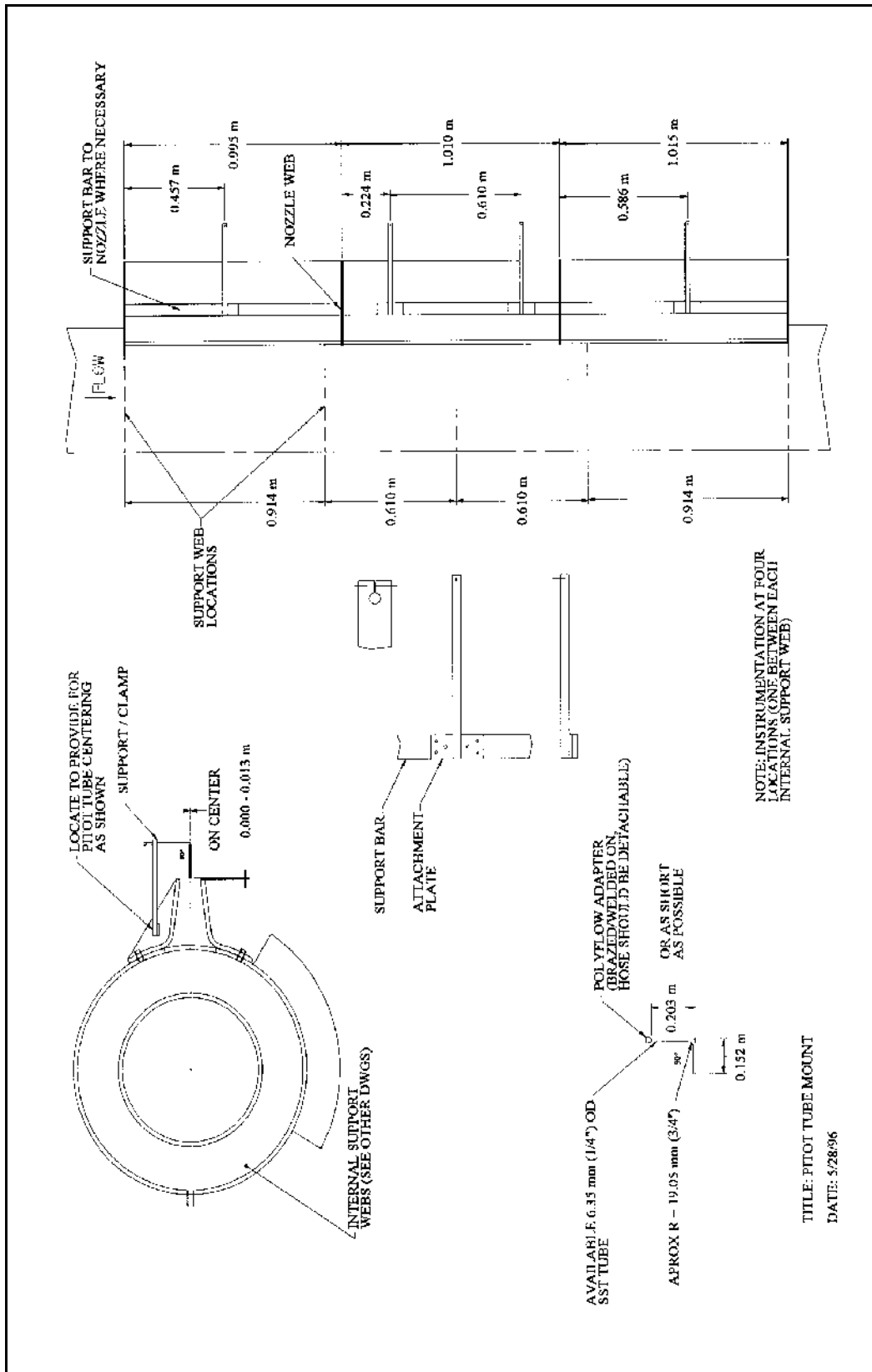


Figure B.4. Mounting of Pitot tubes.

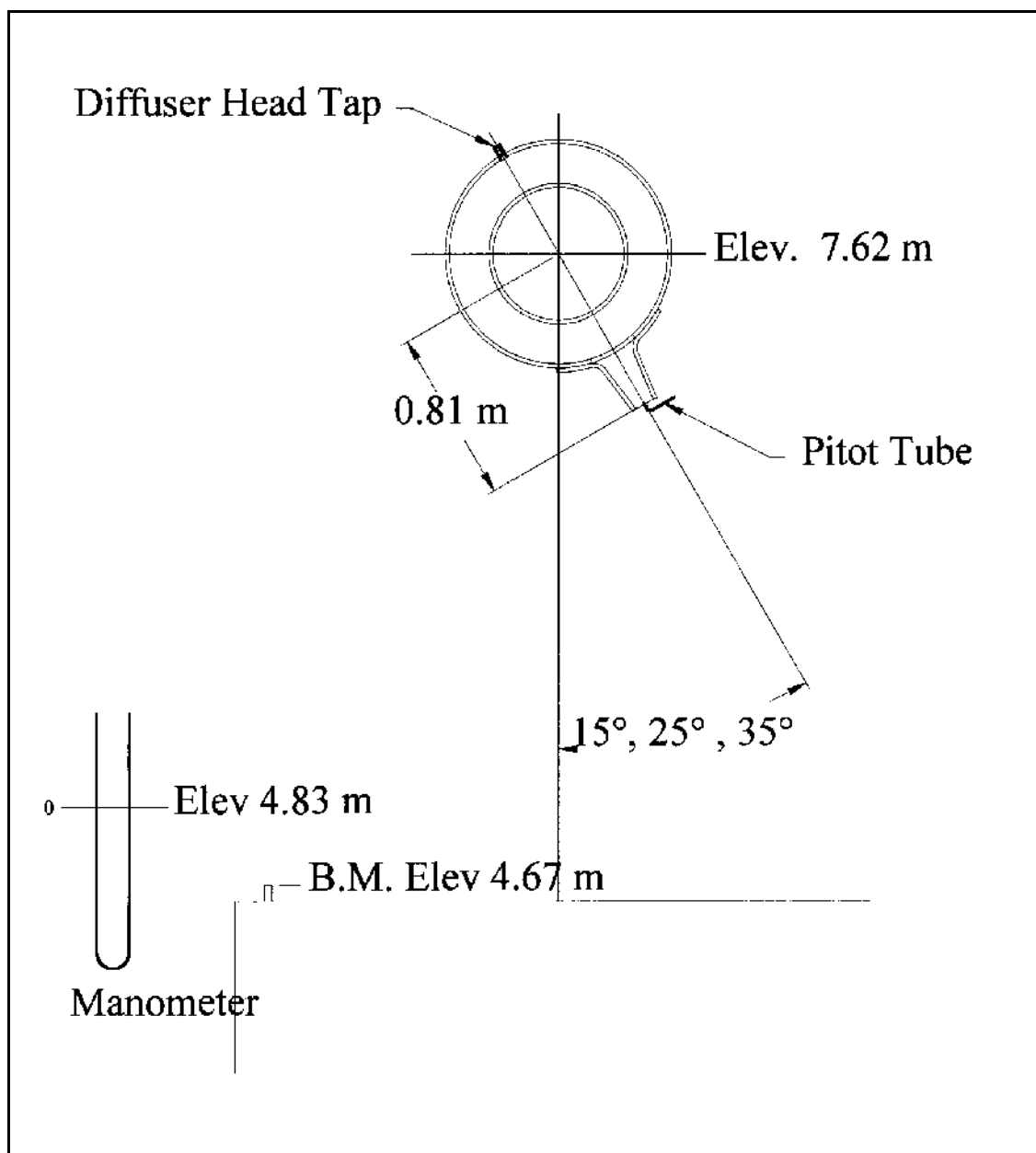


Figure B.5. Position of manometers and Pitot tubes.

APPENDIX C

DATA USED IN THIS STUDY/CALCULATIONS

APPENDIX C

DATA USED IN THIS STUDY/CALCULATIONS

Appendix C condenses the data used in the analysis to obtain equations to predict the depth of scour caused by compact jets (in Tables C.1.1 - C.1.7) and highly aerated jets (DFE data, in Tables C.2.1 - C.2.7). Regression analysis for the compact jet data and for the highly aerated jet data has been included. Predictions of the depths of scour using Equations (6.4) and (6.5) for both compact jet data and highly aerated data are also included.

Table C.1.1. Compact jet data used in this study.

Study	q	Y	b _o	Ref. Depth	dz	z	α	V _o	V _i	b _i	H _o	cos δ	d _{gs}	d ₅₀	TW	G	T	v	w	z/b _o
	(m ² /s)	(m)	(m)	(m)	(m)	(m)	(deg.)	(m/s)	(m/s)	(m)	(m)		(m)	(m)	(m)		°C	(m ² /s)	(m/s)	
Hallmark A	0.045	0.190	0.059	0.059	0.610	0.64	90	0.763	3.622	0.027	0.669	0.979	0.013	0.006	0.61	2.65	10	1.308E-06	0.451	10.28
Hallmark A	0.045	0.334	0.059	0.059	1.181	1.21	90	0.762	4.932	0.023	1.240	0.988	0.013	0.006	0.04	2.65	10	1.308E-06	0.451	19.94
Hallmark A	0.046	0.238	0.060	0.060	1.067	1.10	90	0.770	4.702	0.024	1.127	0.987	0.013	0.006	0.15	2.65	10	1.308E-06	0.451	17.67
Hallmark A	0.012	0.073	0.025	0.025	0.610	0.62	90	0.494	3.527	0.009	0.634	0.990	0.013	0.006	0.61	2.65	10	1.308E-06	0.451	24.54
Hallmark A	0.012	0.067	0.024	0.024	1.067	1.08	90	0.485	4.625	0.008	1.091	0.995	0.013	0.006	0.15	2.65	10	1.308E-06	0.451	44.53
Hallmark A	0.011	0.079	0.023	0.023	0.914	0.93	90	0.480	4.289	0.008	0.938	0.994	0.013	0.006	0.30	2.65	10	1.308E-06	0.451	39.01
Hallmark A	0.011	0.080	0.023	0.023	1.143	1.15	90	0.480	4.783	0.007	1.166	0.995	0.013	0.006	0.08	2.65	10	1.308E-06	0.451	48.76
Hallmark A	0.046	0.225	0.060	0.060	1.067	1.10	90	0.768	4.701	0.024	1.127	0.987	0.013	0.006	0.15	2.65	10	1.308E-06	0.451	17.72
Hallmark A	0.046	0.278	0.060	0.060	1.067	1.10	90	0.768	4.701	0.024	1.127	0.987	0.013	0.006	0.15	2.65	10	1.308E-06	0.451	17.72
Thomas I	0.012	0.083	0.024	0.024	0.279	0.29	90	0.485	2.436	0.011	0.303	0.981	0.007	0.006	0.04	2.65	10	1.308E-06	0.339	11.63
Thomas I	0.012	0.073	0.025	0.025	0.241	0.25	90	0.491	2.282	0.011	0.265	0.978	0.007	0.006	0.08	2.65	10	1.308E-06	0.339	9.80
Thomas I	0.011	0.062	0.024	0.024	0.164	0.18	90	0.481	1.919	0.012	0.188	0.970	0.007	0.006	0.15	2.65	10	1.308E-06	0.339	6.97
Thomas I	0.012	0.052	0.024	0.024	0.088	0.10	90	0.485	1.483	0.014	0.112	0.951	0.007	0.006	0.23	2.65	10	1.308E-06	0.339	3.68
Thomas I	0.023	0.171	0.038	0.038	0.248	0.27	90	0.611	2.367	0.019	0.286	0.968	0.007	0.006	0.08	2.65	10	1.308E-06	0.339	6.51
Thomas I	0.024	0.120	0.038	0.038	0.172	0.19	90	0.613	2.029	0.021	0.210	0.957	0.007	0.006	0.15	2.65	10	1.308E-06	0.339	4.48
Thomas I	0.023	0.094	0.038	0.038	0.095	0.11	90	0.610	1.616	0.023	0.133	0.936	0.007	0.006	0.23	2.65	10	1.308E-06	0.339	2.51
Thomas I	0.046	0.345	0.060	0.060	0.259	0.29	90	0.768	2.501	0.033	0.319	0.956	0.007	0.006	0.08	2.65	10	1.308E-06	0.339	4.30
Thomas I	0.046	0.280	0.060	0.060	0.186	0.22	90	0.769	2.196	0.036	0.246	0.944	0.007	0.006	0.15	2.65	10	1.308E-06	0.339	3.08
Thomas I	0.046	0.183	0.060	0.060	0.106	0.14	90	0.770	1.808	0.039	0.167	0.920	0.007	0.006	0.23	2.65	10	1.308E-06	0.339	1.76
Thomas I	0.011	0.079	0.024	0.024	0.583	0.60	90	0.482	3.450	0.009	0.607	0.990	0.007	0.006	0.04	2.65	10	1.308E-06	0.339	24.61
Thomas I	0.011	0.071	0.024	0.024	0.545	0.56	90	0.482	3.340	0.009	0.569	0.990	0.007	0.006	0.08	2.65	10	1.308E-06	0.339	23.01
Thomas I	0.012	0.076	0.024	0.024	0.466	0.48	90	0.489	3.102	0.010	0.491	0.988	0.007	0.006	0.15	2.65	10	1.308E-06	0.339	19.16
Thomas I	0.013	0.090	0.026	0.026	0.318	0.33	90	0.509	2.599	0.012	0.344	0.981	0.007	0.006	0.30	2.65	10	1.308E-06	0.339	12.03
Thomas I	0.011	0.038	0.024	0.024	0.164	0.18	90	0.482	1.920	0.012	0.188	0.970	0.007	0.006	0.46	2.65	10	1.308E-06	0.339	6.93
Thomas I	0.024	0.226	0.039	0.039	0.580	0.60	90	0.617	3.484	0.016	0.619	0.985	0.007	0.006	0.05	2.65	10	1.308E-06	0.339	14.94
Thomas I	0.023	0.205	0.038	0.038	0.552	0.57	90	0.609	3.402	0.016	0.590	0.984	0.007	0.006	0.08	2.65	10	1.308E-06	0.339	14.60
Thomas I	0.023	0.151	0.038	0.038	0.480	0.50	90	0.611	3.188	0.017	0.518	0.982	0.007	0.006	0.15	2.65	10	1.308E-06	0.339	12.63
Thomas I	0.024	0.131	0.038	0.038	0.324	0.34	90	0.613	2.666	0.018	0.362	0.975	0.007	0.006	0.30	2.65	10	1.308E-06	0.339	8.45
Thomas I	0.023	0.099	0.038	0.038	0.174	0.19	90	0.610	2.041	0.021	0.212	0.958	0.007	0.006	0.46	2.65	10	1.308E-06	0.339	4.60
Thomas I	0.047	0.298	0.061	0.061	0.488	0.52	90	0.771	3.279	0.029	0.548	0.973	0.007	0.006	0.15	2.65	10	1.308E-06	0.339	8.04
Thomas I	0.046	0.231	0.060	0.060	0.335	0.37	90	0.769	2.784	0.032	0.395	0.964	0.007	0.006	0.30	2.65	10	1.308E-06	0.339	5.56
Thomas I	0.046	0.180	0.060	0.060	0.183	0.21	90	0.770	2.183	0.036	0.243	0.943	0.007	0.006	0.46	2.65	10	1.308E-06	0.339	3.02
Thomas I	0.046	0.141	0.060	0.060	0.082	0.11	90	0.769	1.670	0.041	0.142	0.908	0.007	0.006	0.56	2.65	10	1.308E-06	0.339	1.36

Table C.1.1 (cont.). Compact jet data used in this study.

Study	q	Y	b ₀	Ref. Depth	dz	z	α	V ₀	V _i	b _i	H ₀	cos δ	d _{gs}	d ₅₀	TW	G	T	v	w	z/b ₀
	(m ² /s)	(m)	(m)	(m)	(m)	(m)	(deg.)	(m/s)	(m/s)	(m)	(m)		(m)	(m)	(m)		°C	(m ² /s)	(m/s)	
Thomas I	0.011	0.073	0.023	0.023	1.155	1.17	90	0.476	4.806	0.007	1.178	0.995	0.007	0.006	0.08	2.65	10	1.308E-06	0.339	50.08
Thomas I	0.011	0.063	0.023	0.023	1.084	1.10	90	0.474	4.660	0.007	1.107	0.995	0.007	0.006	0.15	2.65	10	1.308E-06	0.339	47.31
Thomas I	0.011	0.098	0.023	0.023	0.926	0.94	90	0.474	4.314	0.008	0.949	0.994	0.007	0.006	0.30	2.65	10	1.308E-06	0.339	40.39
Thomas I	0.010	0.083	0.022	0.022	0.773	0.78	90	0.465	3.949	0.008	0.795	0.993	0.007	0.006	0.46	2.65	10	1.308E-06	0.339	35.14
Thomas I	0.011	0.086	0.023	0.023	0.926	0.94	90	0.474	4.314	0.008	0.949	0.994	0.007	0.006	0.30	2.65	10	1.308E-06	0.339	40.39
Thomas I	0.011	0.091	0.023	0.023	0.636	0.65	90	0.477	3.597	0.008	0.660	0.991	0.007	0.006	0.59	2.65	10	1.308E-06	0.339	27.45
Thomas I	0.023	0.223	0.038	0.038	1.162	1.18	90	0.607	4.850	0.013	1.199	0.992	0.007	0.006	0.08	2.65	10	1.308E-06	0.339	30.97
Thomas I	0.023	0.155	0.038	0.038	1.086	1.10	90	0.608	4.694	0.014	1.123	0.992	0.007	0.006	0.15	2.65	10	1.308E-06	0.339	28.78
Thomas I	0.023	0.152	0.038	0.038	1.086	1.10	90	0.608	4.694	0.014	1.123	0.992	0.007	0.006	0.15	2.65	10	1.308E-06	0.339	28.78
Thomas I	0.024	0.171	0.039	0.039	0.934	0.95	90	0.620	4.369	0.015	0.973	0.990	0.007	0.006	0.30	2.65	10	1.308E-06	0.339	23.81
Thomas I	0.022	0.157	0.036	0.036	0.933	0.95	90	0.598	4.360	0.014	0.969	0.991	0.007	0.006	0.30	2.65	10	1.308E-06	0.339	25.56
Thomas I	0.023	0.165	0.038	0.038	0.781	0.80	90	0.611	4.008	0.015	0.819	0.989	0.007	0.006	0.46	2.65	10	1.308E-06	0.339	20.54
Thomas I	0.023	0.166	0.038	0.038	0.629	0.65	90	0.610	3.615	0.016	0.666	0.986	0.007	0.006	0.61	2.65	10	1.308E-06	0.339	16.57
Thomas I	0.046	0.272	0.060	0.060	0.944	0.97	90	0.767	4.438	0.025	1.004	0.985	0.007	0.006	0.30	2.65	10	1.308E-06	0.339	15.75
Thomas I	0.046	0.281	0.060	0.060	0.640	0.67	90	0.770	3.706	0.028	0.700	0.979	0.007	0.006	0.61	2.65	10	1.308E-06	0.339	10.60
Thomas II	0.012	0.074	0.024	0.024	0.279	0.29	90	0.485	2.436	0.011	0.303	0.981	0.010	0.006	0.04	2.65	10	1.308E-06	0.411	11.63
Thomas II	0.012	0.046	0.024	0.024	0.164	0.18	90	0.483	1.921	0.012	0.188	0.970	0.010	0.006	0.15	2.65	10	1.308E-06	0.411	6.90
Thomas II	0.012	0.038	0.024	0.024	0.088	0.10	90	0.483	1.482	0.014	0.112	0.951	0.010	0.006	0.23	2.65	10	1.308E-06	0.411	3.70
Thomas II	0.023	0.136	0.038	0.038	0.245	0.26	90	0.611	2.354	0.019	0.283	0.968	0.010	0.006	0.08	2.65	10	1.308E-06	0.411	6.43
Thomas II	0.023	0.092	0.038	0.038	0.171	0.19	90	0.612	2.027	0.021	0.210	0.957	0.010	0.006	0.15	2.65	10	1.308E-06	0.411	4.50
Thomas II	0.047	0.274	0.061	0.061	0.259	0.29	90	0.773	2.505	0.034	0.320	0.956	0.010	0.006	0.08	2.65	10	1.308E-06	0.411	4.25
Thomas II	0.046	0.141	0.060	0.060	0.106	0.14	90	0.768	1.806	0.039	0.166	0.920	0.010	0.006	0.23	2.65	10	1.308E-06	0.411	1.77
Thomas II	0.012	0.094	0.024	0.024	0.584	0.60	90	0.486	3.452	0.009	0.608	0.990	0.010	0.006	0.04	2.65	10	1.308E-06	0.411	24.23
Thomas II	0.011	0.075	0.024	0.024	0.545	0.56	90	0.481	3.340	0.009	0.569	0.990	0.010	0.006	0.08	2.65	10	1.308E-06	0.411	23.13
Thomas II	0.012	0.062	0.024	0.024	0.317	0.33	90	0.485	2.585	0.010	0.341	0.983	0.010	0.006	0.30	2.65	10	1.308E-06	0.411	13.22
Thomas II	0.023	0.162	0.038	0.038	0.543	0.56	90	0.611	3.376	0.016	0.581	0.984	0.010	0.006	0.09	2.65	10	1.308E-06	0.411	14.29
Thomas II	0.023	0.125	0.038	0.038	0.458	0.48	90	0.608	3.117	0.017	0.496	0.981	0.010	0.006	0.17	2.65	10	1.308E-06	0.411	12.14
Thomas II	0.023	0.115	0.038	0.038	0.458	0.48	90	0.607	3.117	0.017	0.495	0.982	0.010	0.006	0.17	2.65	10	1.308E-06	0.411	12.17
Thomas II	0.023	0.120	0.038	0.038	0.455	0.47	90	0.611	3.109	0.017	0.493	0.981	0.010	0.006	0.17	2.65	10	1.308E-06	0.411	11.96
Thomas II	0.023	0.107	0.038	0.038	0.324	0.34	90	0.611	2.664	0.018	0.362	0.975	0.010	0.006	0.30	2.65	10	1.308E-06	0.411	8.52
Thomas II	0.023	0.074	0.038	0.038	0.171	0.19	90	0.609	2.025	0.021	0.209	0.958	0.010	0.006	0.46	2.65	10	1.308E-06	0.411	4.53
Thomas II	0.046	0.317	0.060	0.060	0.487	0.52	90	0.770	3.278	0.029	0.548	0.974	0.010	0.006	0.15	2.65	10	1.308E-06	0.411	8.07
Thomas II	0.046	0.182	0.060	0.060	0.304	0.33	90	0.768	2.674	0.032	0.365	0.961	0.010	0.006	0.34	2.65	10	1.308E-06	0.411	5.06

Table C.1.1 (cont.). Compact jet data used in this study.

Study	q	Y	b _o	Ref. Depth	dz	z	α	V _o	V _i	b _i	H _o	cos δ	d _{gs}	d ₅₀	TW	G	T	v	w	z/b _o
	(m ² /s)	(m)	(m)	(m)	(m)	(m)	(deg.)	(m/s)	(m/s)	(m)	(m)		(m)	(m)	(m)		°C	(m ² /s)	(m/s)	
Thomas II	0.012	0.066	0.024	0.024	1.076	1.09	90	0.486	4.644	0.008	1.100	0.995	0.010	0.006	0.16	2.65	10	1.308E-06	0.411	44.67
Thomas II	0.012	0.058	0.024	0.024	0.622	0.63	90	0.487	3.559	0.009	0.646	0.991	0.010	0.006	0.61	2.65	10	1.308E-06	0.411	25.68
Thomas II	0.023	0.182	0.038	0.038	1.159	1.18	90	0.609	4.845	0.013	1.197	0.992	0.010	0.006	0.08	2.65	10	1.308E-06	0.411	30.64
Thomas II	0.023	0.130	0.038	0.038	0.933	0.95	90	0.612	4.365	0.014	0.972	0.990	0.010	0.006	0.30	2.65	10	1.308E-06	0.411	24.48
Thomas II	0.023	0.118	0.038	0.038	0.629	0.65	90	0.610	3.615	0.016	0.666	0.986	0.010	0.006	0.61	2.65	10	1.308E-06	0.411	16.57
Thomas II	0.046	0.239	0.060	0.060	0.944	0.97	90	0.767	4.438	0.025	1.004	0.985	0.010	0.006	0.30	2.65	10	1.308E-06	0.411	15.75
Thomas II	0.046	0.194	0.060	0.060	0.640	0.67	90	0.768	3.705	0.027	0.700	0.979	0.010	0.006	0.61	2.65	10	1.308E-06	0.411	10.64
Lencastre a	0.139	0.200	0.150	0.150	0.950	1.03	90	0.927	4.578	0.067	1.069	0.980	0.048	0.044	0.40	2.70	10	1.308E-06	0.895	6.33
Lencastre a	0.139	0.170	0.150	0.150	0.750	0.83	90	0.927	4.128	0.071	0.869	0.976	0.048	0.044	0.60	2.70	10	1.308E-06	0.895	5.00
Lencastre a	0.070	0.150	0.100	0.100	0.940	0.99	90	0.701	4.462	0.040	1.015	0.988	0.048	0.044	0.41	2.70	10	1.308E-06	0.895	9.40
Lencastre a	0.139	0.180	0.150	0.150	1.150	1.23	90	0.927	4.988	0.065	1.269	0.983	0.048	0.044	0.20	2.70	10	1.308E-06	0.895	7.67
Lencastre a	0.070	0.150	0.100	0.100	0.750	0.80	90	0.701	4.023	0.042	0.825	0.985	0.048	0.044	0.60	2.70	10	1.308E-06	0.895	7.50
Lencastre a	0.139	0.150	0.150	0.150	0.550	0.62	90	0.927	3.622	0.076	0.669	0.969	0.048	0.044	0.80	2.70	10	1.308E-06	0.895	3.67
Lencastre a	0.070	0.120	0.100	0.100	1.150	1.20	90	0.701	4.902	0.038	1.225	0.990	0.048	0.044	0.20	2.70	10	1.308E-06	0.895	11.50
Lencastre a	0.070	0.110	0.100	0.100	0.550	0.60	90	0.701	3.501	0.045	0.625	0.981	0.048	0.044	0.80	2.70	10	1.308E-06	0.895	5.50
Lencastre a	0.022	0.060	0.050	0.050	1.150	1.18	90	0.440	4.821	0.015	1.185	0.996	0.048	0.044	0.20	2.70	10	1.308E-06	0.895	23.00
Lencastre a	0.022	0.035	0.050	0.050	0.950	0.97	90	0.440	4.395	0.016	0.985	0.995	0.048	0.044	0.40	2.70	10	1.308E-06	0.895	19.00
Lencastre a	0.022	0.000	0.050	0.050	0.740	0.77	90	0.440	3.898	0.017	0.775	0.994	0.048	0.044	0.61	2.70	10	1.308E-06	0.895	14.80
Lencastre b	0.146	0.209	0.150	0.150	0.950	1.03	90	0.973	4.588	0.069	1.073	0.978	0.062	0.062	0.40	2.70	10	1.308E-06	1.017	6.33
Lencastre b	0.146	0.210	0.150	0.150	0.550	0.62	90	0.973	3.634	0.078	0.673	0.966	0.062	0.062	0.80	2.70	10	1.308E-06	1.017	3.67
Lencastre b	0.070	0.142	0.100	0.100	0.950	1.00	90	0.700	4.484	0.040	1.025	0.988	0.062	0.062	0.40	2.70	10	1.308E-06	1.017	9.50
Lencastre b	0.146	0.180	0.150	0.150	1.150	1.23	90	0.973	4.997	0.066	1.273	0.982	0.062	0.062	0.20	2.70	10	1.308E-06	1.017	7.67
Lencastre b	0.070	0.126	0.100	0.100	1.150	1.20	90	0.700	4.901	0.038	1.225	0.990	0.062	0.062	0.20	2.70	10	1.308E-06	1.017	11.50

Table C.1.2. Dimensionless parameters in Equation (6.3) -- compact jet data.

Study	q (m ² /s)	$\frac{V_i}{(g b_i)^{0.5}}$	$\frac{(TW/\cos \delta)}{b_i}$	$\frac{w}{(g b_i)^{0.5}}$	y_c (m)	Y/y_c
Hallmark A	0.045	7.011	22.887	0.874	0.059	3.206
Hallmark A	0.045	10.321	1.656	0.945	0.059	5.644
Hallmark A	0.046	9.608	6.324	0.923	0.060	3.948
Hallmark A	0.012	11.685	66.236	1.496	0.025	2.932
Hallmark A	0.012	16.772	19.758	1.637	0.024	2.786
Hallmark A	0.011	15.469	39.127	1.628	0.023	3.367
Hallmark A	0.011	17.728	10.317	1.673	0.023	3.432
Hallmark A	0.046	9.623	6.344	0.924	0.060	3.731
Hallmark A	0.046	9.623	6.344	0.924	0.060	4.617
Thomas I	0.012	7.526	3.635	1.047	0.024	3.448
Thomas I	0.012	6.822	6.832	1.013	0.025	2.962
Thomas I	0.011	5.642	13.316	0.997	0.024	2.612
Thomas I	0.012	4.047	17.560	0.925	0.024	2.150
Thomas I	0.023	5.438	4.074	0.779	0.038	4.496
Thomas I	0.024	4.463	7.555	0.746	0.038	3.133
Thomas I	0.023	3.380	10.486	0.709	0.038	2.483
Thomas I	0.046	4.372	2.389	0.593	0.060	5.730
Thomas I	0.046	3.713	4.436	0.573	0.060	4.641
Thomas I	0.046	2.910	6.309	0.546	0.060	3.029
Thomas I	0.011	11.707	4.342	1.150	0.024	3.331
Thomas I	0.011	11.242	8.551	1.141	0.024	2.983
Thomas I	0.012	10.080	15.973	1.101	0.024	3.118
Thomas I	0.013	7.671	26.530	1.000	0.026	3.411
Thomas I	0.011	5.626	39.691	0.993	0.024	1.620
Thomas I	0.024	8.704	2.841	0.847	0.039	5.807
Thomas I	0.023	8.588	4.837	0.856	0.038	5.406
Thomas I	0.023	7.891	9.267	0.839	0.038	3.983
Thomas I	0.024	6.278	17.012	0.798	0.038	3.427
Thomas I	0.023	4.526	23.014	0.752	0.038	2.604
Thomas I	0.047	6.107	5.327	0.631	0.061	4.913
Thomas I	0.046	4.995	9.981	0.608	0.060	3.837
Thomas I	0.046	3.682	13.526	0.572	0.060	2.989
Thomas I	0.046	2.637	15.012	0.535	0.060	2.336
Thomas I	0.012	17.902	5.041	1.242	0.024	3.682
Thomas I	0.011	18.022	10.559	1.271	0.023	3.146

Table C.1.2 (cont.). Dimensionless parameters in Equation (6.3) -- compact jet data.

Study	q (m ² /s)	$\frac{V_i}{(g b_i)^{0.5}}$	$\frac{(TW/\cos \delta)}{b_i}$	$\frac{w}{(g b_i)^{0.5}}$	y_c (m)	Y/y_c
Thomas I	0.011	17.403	20.112	1.266	0.023	2.752
Thomas I	0.011	15.801	40.347	1.242	0.023	4.281
Thomas I	0.010	14.516	61.011	1.246	0.022	3.782
Thomas I	0.011	15.801	40.347	1.242	0.023	3.763
Thomas I	0.011	12.501	71.026	1.178	0.023	3.931
Thomas I	0.023	13.445	5.787	0.940	0.038	5.954
Thomas I	0.023	12.863	11.316	0.929	0.038	4.120
Thomas I	0.023	12.863	11.316	0.929	0.038	4.040
Thomas I	0.024	11.474	20.823	0.890	0.039	4.358
Thomas I	0.022	11.974	22.759	0.931	0.036	4.293
Thomas I	0.023	10.505	31.154	0.888	0.038	4.328
Thomas I	0.023	9.250	39.686	0.867	0.038	4.388
Thomas I	0.046	8.977	12.410	0.686	0.060	4.529
Thomas I	0.046	7.135	22.634	0.653	0.060	4.650
Thomas II	0.012	7.526	3.635	1.269	0.024	3.079
Thomas II	0.012	5.611	13.147	1.200	0.024	1.944
Thomas II	0.012	4.056	17.667	1.124	0.024	1.599
Thomas II	0.023	5.402	4.227	0.942	0.038	3.582
Thomas II	0.023	4.474	7.602	0.906	0.038	2.414
Thomas II	0.047	4.349	2.356	0.713	0.061	4.502
Thomas II	0.046	2.914	6.337	0.662	0.060	2.352
Thomas II	0.012	11.597	4.258	1.380	0.024	3.923
Thomas II	0.011	11.278	8.608	1.387	0.024	3.168
Thomas II	0.012	8.105	29.894	1.288	0.024	2.570
Thomas II	0.023	8.478	5.362	1.031	0.038	4.264
Thomas II	0.023	7.712	10.436	1.016	0.038	3.312
Thomas II	0.023	7.723	10.470	1.018	0.038	3.046
Thomas II	0.023	7.648	10.505	1.010	0.038	3.150
Thomas II	0.023	6.304	17.174	0.972	0.038	2.805
Thomas II	0.023	4.491	23.016	0.911	0.038	1.950
Thomas II	0.046	6.120	5.352	0.767	0.060	5.251
Thomas II	0.046	4.757	10.826	0.731	0.060	3.026
Thomas II	0.012	18.033	4.905	1.515	0.024	3.556
Thomas II	0.012	16.803	20.061	1.486	0.024	2.733
Thomas II	0.012	12.008	68.681	1.386	0.024	2.404

Table C.1.2 (cont.). Dimensionless parameters in Equation (6.3) -- compact jet data.

Study	q (m ² /s)	$\frac{V_i}{(g b_i)^{0.5}}$	$\frac{(TW/\cos \delta)}{b_i}$	$\frac{w}{(g b_i)^{0.5}}$	y_c (m)	Y/y_c
Thomas II	0.023	13.359	5.955	1.132	0.038	4.810
Thomas II	0.023	11.669	21.566	1.098	0.038	3.397
Thomas II	0.023	9.250	39.686	1.051	0.038	3.102
Thomas II	0.046	8.977	12.410	0.831	0.060	3.990
Thomas II	0.046	7.150	22.743	0.793	0.060	3.219
Lencastre a	0.139	5.628	6.048	1.100	0.125	1.595
Lencastre a	0.139	4.945	8.652	1.072	0.125	1.356
Lencastre a	0.070	7.157	10.471	1.435	0.079	1.888
Lencastre a	0.139	6.265	3.146	1.123	0.125	1.436
Lencastre a	0.070	6.287	14.589	1.398	0.079	1.888
Lencastre a	0.139	4.199	10.883	1.037	0.125	1.196
Lencastre a	0.070	8.049	5.342	1.469	0.079	1.511
Lencastre a	0.070	5.286	18.234	1.350	0.079	1.385
Lencastre a	0.022	12.525	13.295	2.324	0.037	1.636
Lencastre a	0.022	11.158	25.410	2.271	0.037	0.954
Lencastre a	0.022	9.605	36.544	2.204	0.037	0.000
Lencastre b	0.146	5.574	5.918	1.235	0.130	1.610
Lencastre b	0.146	4.165	10.668	1.166	0.130	1.621
Lencastre b	0.070	7.203	10.246	1.634	0.079	1.791
Lencastre b	0.146	6.202	3.078	1.262	0.130	1.390
Lencastre b	0.070	8.052	5.346	1.671	0.079	1.590

Table C.1.3. Measured values of Y/y_c and summary of predicted values of Y/y_c using Equation (6.4) for each data set -- compact jet data.

Measured Y/y_c	Predicted Y/y_c					Identity
	Hallmark A	Thomas I	Thomas II	Lencastre a	Lencastre b	
3.206	3.143					
5.644	5.212					
3.948	4.320					
2.932	2.025					
2.786	2.722					
3.367	2.376					
3.432	2.987					
3.731	4.314					
4.617	4.314					
3.448	3.310					
2.962		2.972				
2.612		2.438				
2.150		2.037				
4.496		3.749				
3.133		3.182				
2.483		2.665				
5.730		4.828				
4.641		4.146				
3.029		3.544				
3.331		3.954				
2.983		3.567				
3.118		3.190				
3.411		2.778				
1.620		2.134				
5.807		4.949				
5.406		4.529				
3.983		4.029				
3.427		3.375				
2.604		2.771				
4.913		5.132				
3.837		4.307				
2.989		3.600				
2.336		3.037				
3.682		4.783				

Table C.1.3 (cont.). Measured values of Y/y_c and summary of predicted values of Y/y_c using Equation (6.4) for each data set -- compact jet data.

Measured Y/y_c	Predicted Y/y_c					Identity
	Hallmark A	Thomas I	Thomas II	Lencastre a	Lencastre b	
3.146		4.259				
2.752		3.854				
4.281		3.379				
3.782		3.007				
3.763		3.379				
3.931		2.844				
5.954		5.434				
4.120		4.915				
4.040		4.915				
4.358		4.428				
4.293		4.268				
4.328		3.963				
4.388		3.618				
4.529		5.495				
4.650		4.601				
3.079			2.601			
1.944			1.927			
1.599			1.596			
3.582			2.923			
2.414			2.493			
4.502			3.819			
2.352			2.778			
3.923			3.132			
3.168			2.795			
2.570			2.074			
4.264			3.504			
3.312			3.071			
3.046			3.066			
3.150			3.072			
2.805			2.640			
1.950			2.166			
5.251			4.023			
3.026			3.269			
3.556			3.758			

Table C.1.3 (cont.). Measured values of Y/y_c and summary of predicted values of Y/y_c using Equation (6.4) for each data set -- compact jet data.

Measured Y/y_c	Predicted Y/y_c					Identity
	Hallmark A	Thomas I	Thomas II	Lencastre a	Lencastre b	
2.733			3.074			
2.404			2.263			
4.810			4.263			
3.397			3.429			
3.102			2.842			
3.990			4.318			
3.219			3.607			
1.595				2.372		
1.356				2.135		
1.888				1.885		
1.436				2.704		
1.888				1.703		
1.196				1.923		
1.511				2.165		
1.385				1.527		
1.636				1.492		
0.954				1.305		
0.000				1.163		
1.610					2.040	
1.621					1.655	
1.791					1.613	
1.390					2.325	
1.590					1.842	
0.000						0.000
6.000						6.000

Table C.1.4. Predicted values of Y/y_c using Equation (6.4) and measured values of Y/y_c used to calculate the regression coefficient -- compact jet data.

Predicted Y/y_c	Measured Y/y_c
3.143	3.206
5.212	5.644
4.320	3.948
2.025	2.932
2.722	2.786
2.376	3.367
2.987	3.432
4.314	3.731
4.314	4.617
3.310	3.448
2.972	2.962
2.438	2.612
2.037	2.150
3.749	4.496
3.182	3.133
2.665	2.483
4.828	5.730
4.146	4.641
3.544	3.029
3.954	3.331
3.567	2.983
3.190	3.118
2.778	3.411
2.134	1.620
4.949	5.807
4.529	5.406
4.029	3.983
3.375	3.427
2.771	2.604
5.132	4.913
4.307	3.837
3.600	2.989
3.037	2.336
4.783	3.682
4.259	3.146
3.854	2.752

Table C.1.4 (cont.). Predicted values of Y/y_c using Equation (6.4) and measured values of Y/y_c used to calculate the regression coefficient -- compact jet data.

Predicted Y/y_c	Measured Y/y_c
3.379	4.281
3.007	3.782
3.379	3.763
2.844	3.931
5.434	5.954
4.915	4.120
4.915	4.040
4.428	4.358
4.268	4.293
3.963	4.328
3.618	4.388
5.495	4.529
4.601	4.650
2.601	3.079
1.927	1.944
1.596	1.599
2.923	3.582
2.493	2.414
3.819	4.502
2.778	2.352
3.132	3.923
2.795	3.168
2.074	2.570
3.504	4.264
3.071	3.312
3.066	3.046
3.072	3.150
2.640	2.805
2.166	1.950
4.023	5.251
3.269	3.026
3.758	3.556
3.074	2.733
2.263	2.404
4.263	4.810

Table C.1.4 (cont.). Predicted values of Y/y_c using Equation (6.4) and measured values of Y/y_c used to calculate the regression coefficient -- compact jet data.

Predicted Y/y_c	Measured Y/y_c
3.429	3.397
2.842	3.102
4.318	3.990
3.607	3.219
2.372	1.595
2.135	1.356
1.885	1.888
2.704	1.436
1.703	1.888
1.923	1.196
2.165	1.511
1.527	1.385
1.492	1.636
1.305	0.954
1.163	0.000
2.040	1.610
1.655	1.621
1.613	1.791
2.325	1.390
1.842	1.590

Regression Output:

Constant	0
Std Err of Y Est	0.582
R Squared	0.774
No. of Observations	91
Degrees of Freedom	90
X Coefficient(s)	0.999
Std Err of Coef.	0.018

Table C.1.5. Summary of measured values of scour and predicted values of scour using Equation (6.4) for each data set -- compact jet data.

Measured Y (m)	Predicted Y (m)							
	Hallmark A	Thomas I	Thomas II	Lencastre a	Lencastre b	Identity	Id + 25%	Id - 25%
0.190	0.186							
0.334	0.309							
0.238	0.261							
0.073	0.050							
0.067	0.065							
0.079	0.056							
0.080	0.070							
0.225	0.260							
0.278	0.260							
0.083		0.079						
0.073		0.073						
0.062		0.057						
0.052		0.049						
0.171		0.143						
0.120		0.122						
0.094		0.101						
0.345		0.291						
0.280		0.250						
0.183		0.214						
0.079		0.094						
0.071		0.085						
0.076		0.078						
0.090		0.073						
0.038		0.051						
0.226		0.192						
0.205		0.171						
0.151		0.153						
0.131		0.129						
0.099		0.105						
0.298		0.311						
0.231		0.260						
0.180		0.217						
0.141		0.183						
0.089		0.115						
0.073		0.098						
0.063		0.088						
0.098		0.077						
0.083		0.066						
0.086		0.077						
0.091		0.066						
0.223		0.204						

Table C.1.5 (cont.). Summary of measured values of scour and predicted values of scour using Equation (6.4) for each data set -- compact jet data.

Measured Y (m)	Predicted Y (m)							
	Hallmark A	Thomas I	Thomas II	Lencastre a	Lencastre b	Identity	Id + 25%	Id - 25%
0.155		0.185						
0.152		0.185						
0.171		0.174						
0.157		0.156						
0.165		0.151						
0.166		0.137						
0.272		0.330						
0.281		0.278						
0.074			0.062					
0.046			0.046					
0.038			0.038					
0.136			0.111					
0.092			0.095					
0.274			0.233					
0.141			0.167					
0.094			0.075					
0.075			0.066					
0.062			0.050					
0.162			0.133					
0.125			0.116					
0.115			0.115					
0.120			0.117					
0.107			0.100					
0.074			0.082					
0.317			0.243					
0.182			0.197					
0.085			0.090					
0.066			0.074					
0.058			0.055					
0.182			0.161					
0.130			0.131					
0.118			0.108					
0.239			0.259					
0.194			0.217					
0.200				0.297				
0.170				0.268				
0.150				0.150				
0.180				0.339				
0.150				0.135				
0.150				0.241				
0.120				0.172				

Table C.1.5 (cont.). Summary of measured values of scour and predicted values of scour using Equation (6.4) for each data set -- compact jet data.

Measured Y (m)	Predicted Y (m)							
	Hallmark A	Thomas I	Thomas II	Lencastre a	Lencastre b	Identity	Id + 25%	Id - 25%
0.110				0.121				
0.060				0.055				
0.035				0.048				
0.000				0.043				
0.209					0.264			
0.210					0.214			
0.142					0.128			
0.180					0.301			
0.126					0.146			
0.000						0.000		
0.400						0.400		
0.000							0.000	
0.325							0.406	
0.000								0.000
0.400								0.300

Table C.1.6. Predicted values of Y using Equation (6.4)
and measured values of Y used to calculate
the regression coefficient -- compact jet data.

Predicted Y (m)	Measured Y (m)
0.186	0.190
0.309	0.334
0.261	0.238
0.050	0.073
0.065	0.067
0.056	0.079
0.070	0.080
0.260	0.225
0.260	0.278
0.079	0.083
0.073	0.073
0.057	0.062
0.049	0.052
0.143	0.171
0.122	0.120
0.101	0.094
0.291	0.345
0.250	0.280
0.214	0.183
0.094	0.079
0.085	0.071
0.078	0.076
0.073	0.090
0.051	0.038
0.192	0.226
0.171	0.205
0.153	0.151
0.129	0.131
0.105	0.099
0.311	0.298
0.260	0.231
0.217	0.180
0.183	0.141
0.115	0.089
0.098	0.073

Table C.1.6 (cont.). Predicted values of Y using Equation (6.4) and measured values of Y used to calculate the regression coefficient -- compact jet data.

Predicted Y (m)	Measured Y (m)
0.088	0.063
0.077	0.098
0.066	0.083
0.077	0.086
0.066	0.091
0.204	0.223
0.185	0.155
0.185	0.152
0.174	0.171
0.156	0.157
0.151	0.165
0.137	0.166
0.330	0.272
0.278	0.281
0.062	0.074
0.046	0.046
0.038	0.038
0.111	0.136
0.095	0.092
0.233	0.274
0.167	0.141
0.075	0.094
0.066	0.075
0.050	0.062
0.133	0.162
0.116	0.125
0.115	0.115
0.117	0.120
0.100	0.107
0.082	0.074
0.243	0.317
0.197	0.182
0.090	0.085
0.074	0.066

Table C.1.6 (cont.). Predicted values of Y using Equation (6.4) and measured values of Y used to calculate the regression coefficient -- compact jet data.

Predicted Y (m)	Measured Y (m)
0.055	0.058
0.161	0.182
0.131	0.130
0.108	0.118
0.259	0.239
0.217	0.194
0.297	0.200
0.268	0.170
0.150	0.150
0.339	0.180
0.135	0.150
0.241	0.150
0.172	0.120
0.121	0.110
0.055	0.060
0.048	0.035
0.043	0.000
0.264	0.209
0.214	0.210
0.128	0.142
0.301	0.180
0.146	0.126

Regression Output:

Constant	0
Std Err of Y Est	0.034
R Squared	0.801
No. of Observations	91
Degrees of Freedom	90
X Coefficient(s)	0.927
Std Err of Coef.	0.021

Table C.1.7. Number of predictions falling within 25% of measured values and within 35% of measured values -- compact jet data.

Study	Measured Y (m)	Predicted Y (m)	Id - 25%	Id + 25%	Within 25%?	Count	Id - 35%	Id + 35%	Within 35%?	Count
Hallmark A	0.190	0.186	0.143	0.238	YES	1	0.124	0.257	YES	1
Hallmark A	0.334	0.309	0.251	0.418	YES	2	0.217	0.451	YES	2
Hallmark A	0.238	0.261	0.179	0.298	YES	3	0.155	0.322	YES	3
Hallmark A	0.073	0.050	0.055	0.091	NO	3	0.047	0.098	YES	4
Hallmark A	0.067	0.065	0.050	0.083	YES	4	0.043	0.090	YES	5
Hallmark A	0.079	0.056	0.059	0.099	NO	4	0.051	0.107	YES	6
Hallmark A	0.080	0.070	0.060	0.101	YES	5	0.052	0.109	YES	7
Hallmark A	0.225	0.260	0.168	0.281	YES	6	0.146	0.303	YES	8
Hallmark A	0.278	0.260	0.208	0.347	YES	7	0.181	0.375	YES	9
Thomas I	0.083	0.079	0.062	0.103	YES	8	0.054	0.112	YES	10
Thomas I	0.073	0.073	0.055	0.091	YES	9	0.047	0.098	YES	11
Thomas I	0.062	0.057	0.046	0.077	YES	10	0.040	0.083	YES	12
Thomas I	0.052	0.049	0.039	0.064	YES	11	0.033	0.070	YES	13
Thomas I	0.171	0.143	0.128	0.214	YES	12	0.111	0.231	YES	14
Thomas I	0.120	0.122	0.090	0.150	YES	13	0.078	0.162	YES	15
Thomas I	0.094	0.101	0.071	0.118	YES	14	0.061	0.127	YES	16
Thomas I	0.345	0.291	0.259	0.431	YES	15	0.224	0.466	YES	17
Thomas I	0.280	0.250	0.210	0.350	YES	16	0.182	0.378	YES	18
Thomas I	0.183	0.214	0.137	0.229	YES	17	0.119	0.247	YES	19
Thomas I	0.079	0.094	0.059	0.099	YES	18	0.051	0.107	YES	20
Thomas I	0.071	0.085	0.053	0.088	YES	19	0.046	0.095	YES	21
Thomas I	0.076	0.078	0.057	0.095	YES	20	0.049	0.102	YES	22
Thomas I	0.090	0.073	0.068	0.113	YES	21	0.059	0.122	YES	23
Thomas I	0.038	0.051	0.029	0.048	NO	21	0.025	0.052	YES	24
Thomas I	0.226	0.192	0.169	0.282	YES	22	0.147	0.304	YES	25
Thomas I	0.205	0.171	0.153	0.256	YES	23	0.133	0.276	YES	26
Thomas I	0.151	0.153	0.114	0.189	YES	24	0.098	0.205	YES	27
Thomas I	0.131	0.129	0.099	0.164	YES	25	0.085	0.177	YES	28
Thomas I	0.099	0.105	0.074	0.123	YES	26	0.064	0.133	YES	29
Thomas I	0.298	0.311	0.223	0.372	YES	27	0.194	0.402	YES	30
Thomas I	0.231	0.260	0.174	0.289	YES	28	0.150	0.312	YES	31
Thomas I	0.180	0.217	0.135	0.226	YES	29	0.117	0.244	YES	32
Thomas I	0.141	0.183	0.106	0.176	NO	29	0.092	0.190	YES	33
Thomas I	0.089	0.115	0.067	0.111	NO	29	0.058	0.120	YES	34
Thomas I	0.073	0.098	0.054	0.091	NO	29	0.047	0.098	NO	34
Thomas I	0.063	0.088	0.047	0.079	NO	29	0.041	0.085	NO	34
Thomas I	0.098	0.077	0.074	0.123	YES	30	0.064	0.132	YES	35
Thomas I	0.083	0.066	0.062	0.104	YES	31	0.054	0.112	YES	36
Thomas I	0.086	0.077	0.065	0.108	YES	32	0.056	0.116	YES	37
Thomas I	0.091	0.066	0.068	0.114	NO	32	0.059	0.123	YES	38
Thomas I	0.223	0.204	0.168	0.279	YES	33	0.145	0.302	YES	39
Thomas I	0.155	0.185	0.117	0.194	YES	34	0.101	0.210	YES	40
Thomas I	0.152	0.185	0.114	0.191	YES	35	0.099	0.206	YES	41
Thomas I	0.171	0.174	0.128	0.214	YES	36	0.111	0.231	YES	42
Thomas I	0.157	0.156	0.118	0.196	YES	37	0.102	0.212	YES	43
Thomas I	0.165	0.151	0.123	0.206	YES	38	0.107	0.222	YES	44
Thomas I	0.166	0.137	0.125	0.208	YES	39	0.108	0.225	YES	45

Table C.1.7 (cont.). Number of predictions falling within 25% of measured values and within 35% of measured values -- compact jet data.

	Measured Y	Predicted Y	Id - 25%	Id + 25%	Within 25%?	Count	Id - 35%	Id + 35%	Within 35%?	Count	
Study	(m)	(m)									
Thomas I	0.272	0.330	0.204	0.339	YES	40	0.177	0.367	YES	46	
Thomas I	0.281	0.278	0.211	0.351	YES	41	0.182	0.379	YES	47	
Thomas II	0.074	0.062	0.055	0.092	YES	42	0.048	0.100	YES	48	
Thomas II	0.046	0.046	0.035	0.058	YES	43	0.030	0.063	YES	49	
Thomas II	0.038	0.038	0.029	0.048	YES	44	0.025	0.051	YES	50	
Thomas II	0.136	0.111	0.102	0.170	YES	45	0.089	0.184	YES	51	
Thomas II	0.092	0.095	0.069	0.115	YES	46	0.060	0.124	YES	52	
Thomas II	0.274	0.233	0.206	0.343	YES	47	0.178	0.370	YES	53	
Thomas II	0.141	0.167	0.106	0.177	YES	48	0.092	0.191	YES	54	
Thomas II	0.094	0.075	0.071	0.118	YES	49	0.061	0.128	YES	55	
Thomas II	0.075	0.066	0.056	0.093	YES	50	0.049	0.101	YES	56	
Thomas II	0.062	0.050	0.046	0.077	YES	51	0.040	0.083	YES	57	
Thomas II	0.162	0.133	0.122	0.203	YES	52	0.105	0.219	YES	58	
Thomas II	0.125	0.116	0.094	0.156	YES	53	0.081	0.169	YES	59	
Thomas II	0.115	0.115	0.086	0.143	YES	54	0.074	0.155	YES	60	
Thomas II	0.120	0.117	0.090	0.150	YES	55	0.078	0.162	YES	61	
Thomas II	0.107	0.100	0.080	0.133	YES	56	0.069	0.144	YES	62	
Thomas II	0.074	0.082	0.055	0.092	YES	57	0.048	0.100	YES	63	
Thomas II	0.317	0.243	0.238	0.396	YES	58	0.206	0.428	YES	64	
Thomas II	0.182	0.197	0.136	0.227	YES	59	0.118	0.246	YES	65	
Thomas II	0.085	0.090	0.064	0.106	YES	60	0.055	0.114	YES	66	
Thomas II	0.066	0.074	0.049	0.082	YES	61	0.043	0.089	YES	67	
Thomas II	0.058	0.055	0.044	0.073	YES	62	0.038	0.079	YES	68	
Thomas II	0.182	0.161	0.136	0.227	YES	63	0.118	0.246	YES	69	
Thomas II	0.130	0.131	0.097	0.162	YES	64	0.084	0.175	YES	70	
Thomas II	0.118	0.108	0.088	0.147	YES	65	0.076	0.159	YES	71	
Thomas II	0.239	0.259	0.179	0.299	YES	66	0.156	0.323	YES	72	
Thomas II	0.194	0.217	0.145	0.242	YES	67	0.126	0.261	YES	73	
Lencastre a	0.200	0.297	0.150	0.250	NO	67	0.130	0.270	NO	73	
Lencastre a	0.170	0.268	0.128	0.213	NO	67	0.111	0.230	NO	73	
Lencastre a	0.150	0.150	0.113	0.188	YES	68	0.098	0.203	YES	74	
Lencastre a	0.180	0.339	0.135	0.225	NO	68	0.117	0.243	NO	74	
Lencastre a	0.150	0.135	0.113	0.188	YES	69	0.098	0.203	YES	75	
Lencastre a	0.150	0.241	0.113	0.188	NO	69	0.098	0.203	NO	75	
Lencastre a	0.120	0.172	0.090	0.150	NO	69	0.078	0.162	NO	75	
Lencastre a	0.110	0.121	0.083	0.138	YES	70	0.072	0.149	YES	76	
Lencastre a	0.060	0.055	0.045	0.075	YES	71	0.039	0.081	YES	77	
Lencastre a	0.035	0.048	0.026	0.044	NO	71	0.023	0.047	NO	77	
Lencastre a	0.000	0.043	0.000	0.000	NO	71	0.000	0.000	NO	77	
Lencastre b	0.209	0.264	0.156	0.261	NO	71	0.136	0.281	YES	78	
Lencastre b	0.210	0.214	0.158	0.263	YES	72	0.137	0.284	YES	79	
Lencastre b	0.142	0.128	0.107	0.178	YES	73	0.092	0.192	YES	80	
Lencastre b	0.180	0.301	0.135	0.225	NO	73	0.117	0.243	NO	80	
Lencastre b	0.126	0.146	0.095	0.158	YES	74	0.082	0.170	YES	81	
Total YES						74	Total YES				81
Total						91	Total				91
% Yes						81.32	% Yes				89.01

Table C.2.1. Highly aerated jet data used in this study.

Study	q (m ² /s)	Y (m)	b _o (m)	Ref. Depth (m)	dz (m)	z (m)	α (deg.)	V _o (m/s)	V _i (m/s)	b _i (m)	H _o (m)	cos δ	d ₈₅ (m)	d ₅₀ (m)	TW (m)	G	T °C	v (m ² /s)	w (m/s)	z/b _o
DFE	0.897	1.55	0.087			3.48	15	10.279	13.190	0.077	8.871	0.980	0.0160	0.00296	0.57	2.65	10	1.308E-06	0.509	39.90
DFE	0.897	1.50	0.087			3.12	15	10.279	12.915	0.078	8.505	0.979	0.0160	0.00296	0.85	2.65	10	1.308E-06	0.509	35.71
DFE	0.897	1.83	0.087			3.79	15	10.279	13.415	0.076	9.176	0.981	0.0160	0.00296	0.27	2.65	10	1.308E-06	0.509	43.39
DFE	0.897	0.99	0.087			2.87	15	10.279	12.729	0.078	8.261	0.979	0.0160	0.00296	1.85	2.65	10	1.308E-06	0.509	32.92
DFE	0.897	0.94	0.087			2.94	25	10.279	12.777	0.078	8.325	0.947	0.0160	0.00296	1.80	2.65	10	1.308E-06	0.509	33.65
DFE	0.897	1.03	0.087			3.55	25	10.279	13.242	0.077	8.940	0.950	0.0160	0.00296	1.17	2.65	10	1.308E-06	0.509	40.70
DFE	0.897	0.88	0.087			3.60	35	10.279	13.278	0.077	8.989	0.914	0.0160	0.00296	1.16	2.65	10	1.308E-06	0.509	41.26
DFE	0.897	0.63	0.087			2.98	35	10.279	12.813	0.078	8.371	0.908	0.0160	0.00296	1.80	2.65	10	1.308E-06	0.509	34.17
DFE	0.897	0.91	0.087			3.92	35	10.279	13.512	0.076	9.309	0.917	0.0160	0.00296	0.84	2.65	10	1.308E-06	0.509	44.93
DFE	0.897	1.19	0.087			4.37	35	10.279	13.831	0.075	9.754	0.920	0.0160	0.00296	0.50	2.65	10	1.308E-06	0.509	50.02
DFE	0.897	1.49	0.087			4.32	25	10.279	13.801	0.075	9.711	0.954	0.0160	0.00296	0.41	2.65	10	1.308E-06	0.509	49.53
DFE	0.897	1.30	0.087			3.99	25	10.279	13.560	0.076	9.376	0.952	0.0160	0.00296	0.77	2.65	10	1.308E-06	0.509	45.69
DFE-Model	0.178	0.56	0.041		1.219	1.22	18	4.40	6.58	0.033	2.21	0.979	0.0055	0.00043	0.18	2.65	10	1.308E-06	0.298	30.08
DFE-Rock	0.372	0.28	0.087			4.51	15	4.26	10.32	0.056	5.43	0.994	0.2131	0.21300	0.21	1.65	10	1.308E-06	1.165	51.65
DFE-Rock	0.650	0.56	0.087			4.45	15	7.47	11.96	0.069	7.30	0.987	0.2131	0.21300	0.29	1.65	10	1.308E-06	1.165	51.14

Table C.2.2. Dimensionless parameters in Equation (6.3) -- highly aerated jet data.

Study	q (m ² /s)	$\frac{V_i}{(g b_i)^{0.5}}$	$\frac{(TW/\cos \delta)}{b_i}$	$\frac{w}{(g b_i)^{0.5}}$	y_c (m)	Y/y_c
DFE	0.897	15.172	7.544	0.585	0.435	3.569
DFE	0.897	14.778	11.147	0.582	0.435	3.450
DFE	0.897	15.496	3.537	0.588	0.435	4.207
DFE	0.897	14.512	24.050	0.580	0.435	2.279
DFE	0.897	14.581	24.255	0.581	0.435	2.160
DFE	0.897	15.246	16.055	0.586	0.435	2.368
DFE	0.897	15.298	16.497	0.586	0.435	2.033
DFE	0.897	14.631	25.399	0.581	0.435	1.444
DFE	0.897	15.636	12.009	0.589	0.435	2.090
DFE	0.897	16.099	7.219	0.592	0.435	2.749
DFE	0.897	16.055	5.640	0.592	0.435	3.429
DFE	0.897	15.706	10.694	0.589	0.435	3.001
DFE-Model	0.178	11.537	5.633	0.523	0.148	3.780
DFE-Rock	0.372	13.923	3.767	1.572	0.241	1.159
DFE-Rock	0.650	14.569	4.265	1.419	0.351	1.597

Table C.2.3. Measured values of Y/y_c and summary of predicted values of Y/y_c using Equation (6.5) by data set -- highly aerated jet data.

Measured Y/y_c	Predicted Y/y_c			
	DFE	DFE-model	DFE Block	Identity
3.569	3.139			
3.450	2.707			
4.207	4.202			
2.279	2.012			
2.160	2.004			
2.368	2.337			
2.033	2.311			
1.444	1.967			
2.090	2.606			
2.749	3.163			
3.429	3.484			
3.001	2.725			
3.780		3.918		
1.159			1.336	
1.597			1.434	
0.000				0.000
5.000				5.000

Table C.2.4. Predicted values of Y/y_c using Equation (6.5) and measured values of Y/y_c used to calculate the regression coefficient — highly aerated jet data.

Predicted Y/y_c	Measured Y/y_c
3.139	3.569
2.707	3.450
4.202	4.207
2.012	2.279
2.004	2.160
2.337	2.368
2.311	2.033
1.967	1.444
2.606	2.090
3.163	2.749
3.484	3.429
2.725	3.001
3.918	3.780
1.336	1.159
1.434	1.597

Regression Output:

Constant	0
Std Err of Y Est	0.356
R Squared	0.849
No. of Observations	15
Degrees of Freedom	14
X Coefficient(s)	0.999
Std Err of Coef.	0.033

Table C.2.5. Summary of measured values of scour and predicted values of scour using Equation (6.5) for each data set -- highly aerated jet data.

Measured Y (m)	Predicted Y (m)					
	DFE	DFE- Model	DFE Block	Identity	Id + 25%	Id - 25%
1.551	1.364					
1.500	1.177					
1.829	1.827					
0.991	0.875					
0.939	0.871					
1.029	1.016					
0.884	1.005					
0.628	0.855					
0.908	1.133					
1.195	1.375					
1.490	1.514					
1.305	1.184					
0.560		0.580				
0.280			0.323			
0.560			0.503			
0.000				0.000		
2.000				2.000		
0.000					0.000	
1.600					2.000	
0.000						0.000
2.700						2.025

Table C.2.6. Predicted values of Y using Equation (6.5) and measured values of Y used to calculate the regression coefficient -- highly aerated jet data.

Y-Measured (m)	Y-Predicted (m)
1.55	1.36
1.50	1.18
1.83	1.83
0.99	0.87
0.94	0.87
1.03	1.02
0.88	1.00
0.63	0.86
0.91	1.13
1.19	1.38
1.49	1.51
1.30	1.18
0.56	0.58
0.28	0.32
0.56	0.50

Regression Output:

Constant	0
Std Err of Y Est	0.152
R Squared	0.876
No. of Observations	15
Degrees of Freedom	14
X Coefficient(s)	1.005
Std Err of Coef.	0.035

Table C.2.7. Number of predictions falling within 25% of measured values and within 35% of measured values -- highly aerated jet data.

Study	Measured Y (m)	Predicted Y (m)	Id -25% (m)	Id+25% (m)	Within 25%? (m)	Count	Id -35% (m)	Id+ 35% (m)	Within 35%? (m)	Count
DFE	1.551	1.364	1.164	1.939	YES	1	1.008	2.094	YES	1
DFE	1.500	1.177	1.125	1.875	YES	2	0.975	2.024	YES	2
DFE	1.829	1.827	1.372	2.286	YES	3	1.189	2.469	YES	3
DFE	0.991	0.875	0.743	1.238	YES	4	0.644	1.337	YES	4
DFE	0.939	0.871	0.704	1.173	YES	5	0.610	1.267	YES	5
DFE	1.029	1.016	0.772	1.287	YES	6	0.669	1.390	YES	6
DFE	0.884	1.005	0.663	1.105	YES	7	0.575	1.193	YES	7
DFE	0.628	0.855	0.471	0.785	NO	7	0.408	0.848	NO	7
DFE	0.908	1.133	0.681	1.135	YES	8	0.590	1.226	YES	8
DFE	1.195	1.375	0.896	1.494	YES	9	0.777	1.613	YES	9
DFE	1.490	1.514	1.118	1.863	YES	10	0.969	2.012	YES	10
DFE	1.305	1.184	0.978	1.631	YES	11	0.848	1.761	YES	11
DFE-Model	0.560	0.580	0.420	0.700	YES	12	0.364	0.755	YES	12
DFE-Rock	0.280	0.323	0.210	0.350	YES	13	0.182	0.378	YES	13
DFE- Rock	0.560	0.503	0.420	0.700	YES	14	0.364	0.756	YES	14
					Total YES	14			Total YES	14
					Total	15			Total	15
					% Yes	93.33			% Yes	93.33

Table C.3.1. Highly aerated jet data used in this study.

Study	q (m ² /s)	Y (m)	b ₀ (m)	Ref. Depth (m)	dz (m)	z (m)	α (deg.)	V ₀ (m/s)	V _i (m/s)	b _i (m)	H ₀ (m)	cos δ	d ₈₅ (m)	d ₅₀ (m)	TW (m)	G	T °C	v (m ² /s)	w (m/s)	z/b ₀
DFE	0.897	1.55	0.087			3.48	15	10.279	13.190	0.077	8.871	0.980	0.0160	0.00296	0.57	2.65	10.1308E-06	0.509	39.90	
DFE	0.897	1.50	0.087			3.12	15	10.279	12.915	0.078	8.505	0.979	0.0160	0.00296	0.85	2.65	10.1308E-06	0.509	35.71	
DFE	0.897	1.83	0.087			3.79	15	10.279	13.415	0.076	9.176	0.981	0.0160	0.00296	0.27	2.65	10.1308E-06	0.509	43.39	
DFE	0.897	0.99	0.087			2.87	15	10.279	12.729	0.078	8.261	0.979	0.0160	0.00296	1.85	2.65	10.1308E-06	0.509	32.92	
DFE	0.897	0.94	0.087			2.94	25	10.279	12.777	0.078	8.325	0.947	0.0160	0.00296	1.80	2.65	10.1308E-06	0.509	33.65	
DFE	0.897	1.03	0.087			3.55	25	10.279	13.242	0.077	8.940	0.950	0.0160	0.00296	1.17	2.65	10.1308E-06	0.509	40.70	
DFE	0.897	0.88	0.087			3.60	35	10.279	13.278	0.077	8.989	0.914	0.0160	0.00296	1.16	2.65	10.1308E-06	0.509	41.26	
DFE	0.897	0.63	0.087			2.98	35	10.279	12.813	0.078	8.371	0.908	0.0160	0.00296	1.80	2.65	10.1308E-06	0.509	34.17	
DFE	0.897	0.91	0.087			3.92	35	10.279	13.512	0.076	9.309	0.917	0.0160	0.00296	0.84	2.65	10.1308E-06	0.509	44.93	
DFE	0.897	1.19	0.087			4.37	35	10.279	13.831	0.075	9.754	0.920	0.0160	0.00296	0.50	2.65	10.1308E-06	0.509	50.02	
DFE	0.897	1.49	0.087			4.32	25	10.279	13.801	0.075	9.711	0.954	0.0160	0.00296	0.41	2.65	10.1308E-06	0.509	49.53	
DFE	0.897	1.30	0.087			3.99	25	10.279	13.560	0.076	9.376	0.952	0.0160	0.00296	0.77	2.65	10.1308E-06	0.509	45.69	
DFE-Model	0.178	0.56	0.041		1.219	1.22	18	4.40	6.58	0.033	2.21	0.979	0.0055	0.00043	0.18	2.65	10.1308E-06	0.298	30.08	
DFE-Rock	0.372	0.28	0.087			4.51	15	4.26	10.32	0.056	5.43	0.994	0.2131	0.21300	0.21	1.65	10.1308E-06	1.165	51.65	
DFE-Rock	0.650	0.56	0.087			4.45	15	7.47	11.96	0.069	7.30	0.987	0.2131	0.21300	0.29	1.65	10.1308E-06	1.165	51.14	

Table C.3.2. Dimensionless parameters used to develop Equation (6.6).

Study	q (m ² /s)	$\frac{(TW/\cos \delta)}{b_i}$	$\frac{w}{(g b_i)^{0.5}}$	y_c (m)	Y/y_c
DFE	0.897	7.544	0.585	0.435	3.569
DFE	0.897	11.147	0.582	0.435	3.450
DFE	0.897	3.537	0.588	0.435	4.207
DFE	0.897	24.050	0.580	0.435	2.279
DFE	0.897	24.255	0.581	0.435	2.160
DFE	0.897	16.055	0.586	0.435	2.368
DFE	0.897	16.497	0.586	0.435	2.033
DFE	0.897	25.399	0.581	0.435	1.444
DFE	0.897	12.009	0.589	0.435	2.090
DFE	0.897	7.219	0.592	0.435	2.749
DFE	0.897	5.640	0.592	0.435	3.429
DFE	0.897	10.694	0.589	0.435	3.001
DFE-Model	0.178	5.633	0.523	0.148	3.780
DFE-Rock	0.372	3.767	1.572	0.241	1.159
DFE-Rock	0.650	4.265	1.419	0.351	1.597

Table C.3.3. Measured values of Y/y_c and summary of predicted values of Y/y_c using Equation (6.6) for each data set -- highly aerated jet data.

Measured Y/y_c	Predicted Y/y_c			Identity
	DFE	DFE-Model	DFE Block	
3.569	3.131			
3.450	2.707			
4.207	4.180			
2.279	2.017			
2.160	2.008			
2.368	2.333			
2.033	2.307			
1.444	1.971			
2.090	2.597			
2.749	3.143			
3.429	3.460			
3.001	2.713			
3.780		3.978		
1.159			1.350	
1.597			1.443	
0.000				0.000
5.000				5.000

Table C.3.4. Predicted values of Y/y_c using Equation (6.6) and measured values of Y/y_c used to calculate the regression coefficient -- highly aerated jet data.

Predicted Y/y_c	Measured Y/y_c
3.131	3.569
2.707	3.450
4.180	4.207
2.017	2.279
2.008	2.160
2.333	2.368
2.307	2.033
1.971	1.444
2.597	2.090
3.143	2.749
3.460	3.429
2.713	3.001
3.978	3.780
1.350	1.159
1.443	1.597

Regression Output:

Constant	0
Std Err of Y Est	0.357
R Squared	0.849
No. of Observations	15
Degrees of Freedom	14
X Coefficient(s)	1.000
Std Err of Coef.	0.034

Table C.3.5. Summary of measured values of scour and predicted values of scour using Equation (6.6) for each data set -- highly aerated jet data.

Measured Y (m)	Predicted Y (m)					
	DFE	DFE-Model	DFE Block	Identity	Id + 25%	Id - 25%
1.551	1.361					
1.500	1.177					
1.829	1.817					
0.991	0.877					
0.939	0.873					
1.029	1.014					
0.884	1.003					
0.628	0.857					
0.908	1.129					
1.195	1.366					
1.490	1.504					
1.305	1.179					
0.560		0.589				
0.280			0.326			
0.560			0.506			
0.000				0.000		
2.000				2.000		
0.000					0.000	
1.600					2.000	
0.000						0.000
2.700						2.025

Table C.3.6. Predicted values of Y using Equation (6.6) and measured values of Y used to calculate the regression coefficient -- highly aerated jet data.

Y-Measured (m)	Y-Predicted (m)
1.55	1.36
1.50	1.18
1.83	1.82
0.99	0.88
0.94	0.87
1.03	1.01
0.88	1.00
0.63	0.86
0.91	1.13
1.19	1.37
1.49	1.50
1.30	1.18
0.56	0.59
0.28	0.33
0.56	0.51

Regression Output:

Constant	0
Std Err of Y Est	0.149
R Squared	0.856
No. of Observations	15
Degrees of Freedom	14
X Coefficient(s)	0.975
Std Err of Coef.	0.034

Table C.3.7. Computation of predicted values falling within 25% of measured values and within 35% of measured values -- highly aerated jet data.

Measured Y	Predicted Y	Id-25%	Id+25%	Within 25%?	Count	Id-35%	Id+35%	Within 35%?	Count		
(m)	(m)	(m)	(m)	(m)		(m)	(m)	(m)			
1.551	1.361	1.164	1.939	YES	1	1.008	2.094	YES	1		
1.500	1.177	1.125	1.875	YES	2	0.975	2.024	YES	2		
1.829	1.817	1.372	2.286	YES	3	1.189	2.469	YES	3		
0.991	0.877	0.743	1.238	YES	4	0.644	1.337	YES	4		
0.939	0.873	0.704	1.173	YES	5	0.610	1.267	YES	5		
1.029	1.014	0.772	1.287	YES	6	0.669	1.390	YES	6		
0.884	1.003	0.663	1.105	YES	7	0.575	1.193	YES	7		
0.628	0.857	0.471	0.785	NO	7	0.408	0.848	NO	7		
0.908	1.129	0.681	1.135	YES	8	0.590	1.226	YES	8		
1.195	1.366	0.896	1.494	YES	9	0.777	1.613	YES	9		
1.490	1.504	1.118	1.863	YES	10	0.969	2.012	YES	10		
1.305	1.179	0.978	1.631	YES	11	0.848	1.761	YES	11		
0.560	0.589	0.420	0.700	YES	12	0.364	0.755	YES	12		
0.280	0.326	0.210	0.350	YES	13	0.182	0.378	YES	13		
0.560	0.506	0.420	0.700	YES	14	0.364	0.756	YES	14		
				Total YES	14					Total YES	14
				Total	15					Total	15
				% Yes	93.33					% Yes	93.33

Table C.4.1. Prediction of depth of scour using compact jet formula Equation (6.4) -- compact jet data and highly aerated jet data.

Measured Y (m)	Predicted Y (m)										
	Hallmark A	Thomas I	Thomas II	Lencastre a	Lencastre b	DFE	DFE- Model	DFE- Block	Identity	Id + 25%	Id-25%
0.190	0.186										
0.334	0.309										
0.238	0.261										
0.073	0.050										
0.067	0.065										
0.079	0.056										
0.080	0.070										
0.225	0.260										
0.278	0.260										
0.083		0.079									
0.073		0.073									
0.062		0.057									
0.052		0.049									
0.171		0.143									
0.120		0.122									
0.094		0.101									
0.345		0.291									
0.280		0.250									
0.183		0.214									
0.079		0.094									
0.071		0.085									
0.076		0.078									
0.090		0.073									
0.038		0.051									
0.226		0.192									
0.205		0.171									
0.151		0.153									
0.131		0.129									
0.099		0.105									
0.298		0.311									
0.231		0.260									
0.180		0.217									
0.141		0.183									
0.089		0.115									
0.073		0.098									
0.063		0.088									
0.098		0.077									
0.083		0.066									
0.086		0.077									
0.091		0.066									
0.223		0.204									
0.155		0.185									
0.152		0.185									
0.171		0.174									
0.157		0.156									
0.165		0.151									
0.166		0.137									

Table C.4.1 (cont.). Prediction of depth of scour using compact jet formula Equation (6.4) -- compact jet data and highly aerated jet data.

Measured Y (m)	Predicted Y (m)										
	Hallmark A	Thomas I	Thomas II	Lencastre a	Lencastre b	DFE	DFE- Model	DFE- Block	Identity	Id + 25%	Id-25%
0.272		0.330									
0.281		0.278									
0.074			0.062								
0.046			0.046								
0.038			0.038								
0.136			0.111								
0.092			0.095								
0.274			0.233								
0.141			0.167								
0.094			0.075								
0.075			0.066								
0.062			0.050								
0.162			0.133								
0.125			0.116								
0.115			0.115								
0.120			0.117								
0.107			0.100								
0.074			0.082								
0.317			0.243								
0.182			0.197								
0.085			0.090								
0.066			0.074								
0.058			0.055								
0.182			0.161								
0.130			0.131								
0.118			0.108								
0.239			0.259								
0.194			0.217								
0.200				0.297							
0.170				0.268							
0.150				0.150							
0.180				0.339							
0.150				0.135							
0.150				0.241							
0.120				0.172							
0.110				0.121							
0.060				0.055							
0.035				0.048							
0.209					0.264						
0.210					0.214						
0.142					0.128						
0.180					0.301						
0.126					0.146						
1.551						4.521					
1.500						4.254					
1.829						5.015					

Table C.4.1 (cont.). Prediction of depth of scour using compact jet formula Equation (6.4) -- compact jet data and highly aerated jet data.

Measured Y (m)	Predicted Y (m)										
	Hallmark A	Thomas I	Thomas II	Lencastre a	Lencastre b	DFE	DFE- Model	DFE- Block	Identity	Id + 25%	Id-25%
0.991						3.835					
0.939						3.839					
1.029						4.126					
0.884						4.119					
0.628						3.824					
0.908						4.328					
1.195						4.673					
1.490						4.812					
1.305						4.400					
0.560							1.510				
0.280								0.743			
0.560								1.249			
0.010									0.010		
6.000									6.000		
0.010										0.013	
5.500										6.875	
0.010											0.008
7.000											5.250

Table C.5.1. Prediction of depths of scour using highly-aerated jet formula Equation (6.5) -- compact jet data and highly aerated jet data.

Measured Y (m)	Predicted Y (m)										
	Hallmark A	Thomas I	Thomas II	Lencastre a	Lencastre b	DFE	DFE- Model	DFE- Block	Identity	Id + 25%	Id-25%
0.190	0.073										
0.334	0.190										
0.238	0.117										
0.073	0.011										
0.067	0.016										
0.079	0.012										
0.080	0.020										
0.225	0.117										
0.278	0.117										
0.083		0.049									
0.073		0.040									
0.062		0.030									
0.052		0.029									
0.171		0.101									
0.120		0.082									
0.094		0.074									
0.345		0.265									
0.280		0.213									
0.183		0.193									
0.079		0.042									
0.071		0.032									
0.076		0.026									
0.090		0.026									
0.038		0.019									
0.226		0.112									
0.205		0.087									
0.151		0.069									
0.131		0.057									
0.099		0.052									
0.298		0.185									
0.231		0.147									
0.180		0.137									
0.141		0.138									
0.089		0.038									
0.073		0.026									
0.063		0.020									
0.098		0.016									
0.083		0.012									
0.086		0.016									
0.091		0.013									
0.223		0.075									
0.155		0.058									
0.152		0.058									
0.171		0.049									
0.157		0.042									

Table C.5.1 (cont.). Prediction of depths of scour using highly-aerated jet formula Equation (6.5) -- compact jet data and highly aerated jet data.

Measured Y (m)	Predicted Y (m)										
	Hallmark A	Thomas I	Thomas II	Lencastre a	Lencastre b	DFE	DFE- Model	DFE- Block	Identity	Id + 25%	Id-25%
0.165		0.040									
0.166		0.037									
0.272		0.122									
0.281		0.101									
0.074			0.040								
0.046			0.025								
0.038			0.023								
0.136			0.081								
0.092			0.067								
0.274			0.221								
0.141			0.156								
0.094			0.035								
0.075			0.026								
0.062			0.017								
0.162			0.069								
0.125			0.053								
0.115			0.053								
0.120			0.054								
0.107			0.046								
0.074			0.043								
0.317			0.150								
0.182			0.118								
0.085			0.031								
0.066			0.018								
0.058			0.012								
0.182			0.061								
0.130			0.038								
0.118			0.031								
0.239			0.101								
0.194			0.083								
0.200				0.196							
0.170				0.174							
0.150				0.075							
0.180				0.249							
0.150				0.068							
0.150				0.163							
0.120				0.096							
0.110				0.064							
0.060				0.019							
0.035				0.015							
0.209					0.179						
0.210					0.149						
0.142					0.066						
0.180					0.227						
0.126					0.083						

Table C.5.1 (cont.). Prediction of depths of scour using highly-aerated jet formula Equation (6.5) -- compact jet data and highly aerated jet data.

Measured Y (m)	Predicted Y (m)										
	Hallmark A	Thomas I	Thomas II	Lencastre a	Lencastre b	DFE	DFE- Model	DFE- Block	Identity	Id + 25%	Id-25%
1.551						1.364					
1.500						1.177					
1.829						1.827					
0.991						0.875					
0.939						0.871					
1.029						1.016					
0.884						1.005					
0.628						0.855					
0.908						1.133					
1.195						1.375					
1.490						1.514					
1.305						1.184					
0.560							0.580				
0.280								0.323			
0.560								0.503			
0.010									0.010		
10.000									10.000		
0.010										0.013	
10.000										12.500	
0.010											0.008
13.500											10.125

APPENDIX D

MANOMETER READINGS AT DFE DIFFUSER AND NOZZLE

APPENDIX D

MANOMETER READINGS AT DFE DIFFUSER AND NOZZLE

Table D.1. shows the calibration data for the four Pitot tubes installed at the nozzle of the DFE facility. Table D.2 shows the manometer readings at the diffuser and at the nozzle, as well as velocities and discharge measurements using the area-velocity method. The discrepancies between the measured discharge and the one calculated by the area-velocity method are less than 5% in most cases.

Table D.1. DFE nozzle Pitot tube calibration.

(Using Calibration stand with U-tube Manometer)

Water depth on atmospheric side (cm) = 0.7

Elevation of pitot tube w.r.t. zero (cm), Y_o = 8.7 Y_o (ft) = 0.29

Pitot Tube #1 (East)

Velocity (ft/s)	Pressure side, Y1 (cm)	Atm side, Y2 (cm)	H ₂ O, Y3 (cm)	Y1 (ft)	Y2 (ft)	Y3 (ft)	H _o (ft)	V (ft/s)	C _v
5	1.4	0.8	1.5	0.05	0.03	0.05	1.24	8.95	0.559
10	2.2	1.6	2.3	0.07	0.05	0.08	1.93	11.15	0.897
15	4.2	3.6	4.3	0.14	0.12	0.14	3.65	15.33	0.978
20	7.1	6.4	7.1	0.23	0.21	0.23	6.10	19.82	1.009
25	11.2	10.6	11.3	0.37	0.35	0.37	9.67	24.95	1.002
30	15.5	14.8	15.5	0.51	0.49	0.51	13.32	29.29	1.024
35	21.8	20.9	21.6	0.72	0.69	0.71	18.65	34.65	1.010
40	27.9	27	27.7	0.92	0.89	0.91	23.89	39.22	1.020
45	37.1	35.9	36.6	1.22	1.18	1.20	31.66	45.16	0.997
50	46.2	44.8	45.5	1.52	1.47	1.49	39.40	50.37	0.993

Pitot Tube #2

Velocity (ft/s)	Pressure side, Y1 (cm)	Atm side, Y2 (cm)	H ₂ O, Y3 (cm)	Y1 (ft)	Y2 (ft)	Y3 (ft)	H _o (ft)	V (ft/s)	C _v
5	1.2	0.9	1.6	0.04	0.03	0.05	1.21	8.81	0.567
10	2.1	1.6	2.3	0.07	0.05	0.08	1.89	11.03	0.906
15	3.8	3.3	4	0.12	0.11	0.13	3.35	14.69	1.021
20	7	6.4	7.1	0.23	0.21	0.23	6.06	19.75	1.013
25	11	10.4	11.1	0.36	0.34	0.36	9.50	24.73	1.011
30	15.2	15	15.7	0.50	0.49	0.52	13.28	29.25	1.026
35	21.7	20.7	21.4	0.71	0.68	0.70	18.52	34.53	1.014
40	28.6	27.7	28.4	0.94	0.91	0.93	24.49	39.71	1.007
45	38.7	37.5	38.2	1.27	1.23	1.25	33.04	46.13	0.976
50	48.4	47.5	48.2	1.59	1.56	1.58	41.51	51.70	0.967

Table D.1 (cont.). DFE nozzle Pitot tube calibration.

Pitot Tube #3

Velocity (ft/s)	Pressure side, Y1 (cm)	Atm side, Y2 (cm)	H ₂ O, Y3 (cm)	Y1 (ft)	Y2 (ft)	Y3 (ft)	H ₀ (ft)	V (ft/s)	C _v
5	1.4	0.9	1.6	0.05	0.03	0.05	1.29	9.11	0.549
10	2.2	1.8	2.5	0.07	0.06	0.08	2.02	11.41	0.877
15	4.4	3.9	4.6	0.14	0.13	0.15	3.87	15.78	0.950
20	7.3	6.7	7.4	0.24	0.22	0.24	6.32	20.17	0.992
25	11.2	10.7	11.4	0.37	0.35	0.37	9.71	25.01	1.000
30	15.7	15.1	15.8	0.52	0.50	0.52	13.54	29.52	1.016
35	21.5	20.8	21.5	0.71	0.68	0.71	18.48	34.50	1.015
40	27.7	26.8	27.5	0.91	0.88	0.90	23.72	39.08	1.023
45	36.7	35.7	36.4	1.20	1.17	1.19	31.41	44.97	1.001
50	45.7	44.5	45.2	1.50	1.46	1.48	39.06	50.15	0.997

Pitot Tube #4 (West)

Velocity (ft/s)	Pressure side, Y1 (cm)	Atm side, Y2 (cm)	H ₂ O, Y3 (cm)	Y1 (ft)	Y2 (ft)	Y3 (ft)	H ₀ (ft)	V (ft/s)	C _v
5	1.4	0.8	1.5	0.05	0.03	0.05	1.24	8.95	0.559
10	2.2	1.6	2.3	0.07	0.05	0.08	1.93	11.15	0.897
15	4.2	3.6	4.3	0.14	0.12	0.14	3.65	15.33	0.978
20	7.1	6.4	7.1	0.23	0.21	0.23	6.10	19.82	1.009
25	11.2	10.6	11.3	0.37	0.35	0.37	9.67	24.95	1.002
30	15.5	14.8	15.5	0.51	0.49	0.51	13.32	29.29	1.024
35	21.8	20.9	21.6	0.72	0.69	0.71	18.65	34.65	1.010
40	27.9	27	27.7	0.92	0.89	0.91	23.89	39.22	1.020
45	37.1	35.9	36.6	1.22	1.18	1.20	31.66	45.16	0.997
50	46.2	44.8	45.5	1.52	1.47	1.49	39.40	50.37	0.993

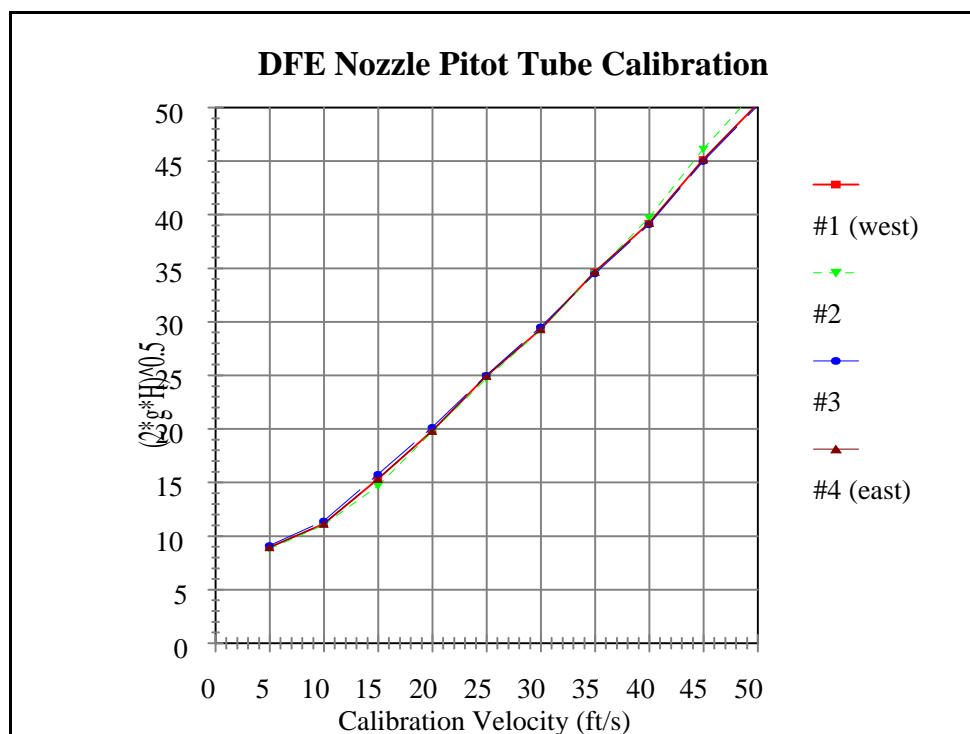


Figure D.1. DFE nozzle Pitot tube calibration.

Table D.2. Manometer readings at DFE diffuser and nozzle.

Eo = 15.85 ft													
Specific Weight of Water = 62.4 lb/ft ³													
Specific Weight of Mercury = 847 lb/ft ³													
Date: 8/26/96													
Discharge = 96.6 cfs													
Angle of Jet = 15 deg.													
Tailwater = 11 ft													
Nozzle	Angle of Jet (deg.)	El.	Y1 (cm)	Y2 (cm)	YH20 (cm)	Y1 (ft)	Y2 (ft)	Y3 (ft)	H (ft)	C _v	V (ft/s)	E1 + v2/2g (ft)	Q _i (cfs)
1	15	22.43	30.5	24.4	29.8	1.00	0.80	0.18	17.09	1.014	33.64	40.01	0.788 26.50
2	15	22.43	31.6	25.6	30.5	1.04	0.84	0.16	18.07	1.015	34.62	41.04	0.645 22.32
3	15	22.43	33.9	27.3	32.6	1.11	0.90	0.17	19.79	1.017	36.31	42.90	0.645 23.40
4	15	22.43	32.7	25.9	31.4	1.07	0.85	0.18	18.67	1.010	35.03	41.48	0.788 27.59
Diffuser	Angle of Jet (deg.)	El.	Y1 (cm)	Y2 (cm)	YH20 (cm)	Y1 (ft)	Y2 (ft)	Y3 (ft)	H1 (ft)	E1 + H1 (ft)			
1	15	26.68	33.2	26.7	32.3	1.09	0.88	0.18	14.99	41.67			
2	15	26.68	31.5	24.7	30.2	1.03	0.81	0.18	13.39	40.07			
3	15	26.68	35.9	29.4	34.7	1.18	0.96	0.17	17.30	43.98			
4	15	26.68	35.2	28.8	34.4	1.15	0.94	0.18	16.75	43.44			
										Total Q	(cfs)		
											99.81		
										Meas. Q (cfs)	96.60		
										Discrep (%)	3.33		
Date: 9/3/96													
Discharge = 96.6													
Angle of Jet = 15 deg.													
Tailwater = 12 ft													
No Manometer Data													

Table D.2 (cont.). Manometer readings at DFE diffuser and nozzle.

Date: 9/9/96													
Discharge = 96.6 cfs													
Angle of Jet = 15 deg.													
Tailwater = 10 ft													
Nozzle	Angle of Jet (deg.)	E1.	Y1 (cm)	Y2 (cm)	YH20 (cm)	Y1 (ft)	Y2 (ft)	Y3 (ft)	H1 (ft)	C _v	V (ft/s)	E1 + v ² /2g (ft)	Q _i (cfs)
1	15	22.43	31.1	24.6	30.1	1.02	0.81	0.18	17.43	1.013	33.95	40.33	0.788 26.74
2	15	22.43	32.7	25.6	30.9	1.07	0.84	0.17	18.53	1.015	35.06	41.52	0.645 22.60
3	15	22.43	34.5	28.2	33.7	1.13	0.93	0.18	20.44	1.018	36.94	43.62	0.645 23.81
4	15	22.43	33.6	27.2	32.6	1.10	0.89	0.18	19.62	1.012	35.97	42.52	0.788 28.34
Diffuser	Angle of Jet (deg.)	E1.	Y1 (cm)	Y2 (cm)	YH20 (cm)	Y1 (ft)	Y2 (ft)	Y3 (ft)	H1 (ft)	E1 + H1 (ft)		Total Q (cfs)	
1	15	26.68	34.0	27.1	32.3	1.12	0.89	0.17	15.49	42.17			
2	15	26.68	31.9	25.1	30.6	1.05	0.82	0.18	13.74	40.42		Meas. Q (cfs)	96.60
3	15	26.68	36.7	30.4	35.8	1.20	1.00	0.18	18.08	44.76		Discrep (%)	5.06
4	15	26.68	36.1	29.4	34.7	1.18	0.96	0.17	17.38	44.07			

Table D.2 (cont.). Manometer readings at DFE diffuser and nozzle.

Date: 9/23/96													
Discharge = 96.6 cfs													
Angle of Jet = 15 deg.													
Tailwater = 13 ft													
Nozzle	Angle of Jet (deg.)	E1.	Y1 (cm)	Y2 (cm)	YH20 (cm)	Y1 (ft)	Y2 (ft)	Y3 (ft)	H1 (ft)	C _v	V (ft/s)	EGL Elev. E1 + v ² /2g (ft)	Oi (cfs)
1	15	22.43	31.5	24.4	29.6	1.03	0.80	0.17	17.50	1.013	34.01	40.39	0.788 26.79
2	15	22.43	25.5	18.4	24.0	0.84	0.60	0.18	12.35	1.022	28.84	35.34	0.645 18.59
3	15	22.43	29.8	23.0	28.7	0.98	0.75	0.19	16.19	1.015	32.79	39.12	0.645 21.13
4	15	22.43	35.1	28.6	33.5	1.15	0.94	0.16	20.85	1.014	37.17	43.88	0.788 29.28
Diffuser	Angle of Jet (deg.)	E1.	Y1 (cm)	Y2 (cm)	YH20 (cm)	Y1 (ft)	Y2 (ft)	Y3 (ft)	H1 (ft)	E1 + H1 (ft)		Total Q (cfs)	
1	15	26.68	33.8	26.5	32.4	1.11	0.87	0.19	15.16	41.84			
2	15	26.68	24.9	18.0	23.5	0.82	0.59	0.18	7.67	34.36		Meas. Q (cfs)	96.60
3	15	26.68	36.8	27.5	35.4	1.21	0.90	0.26	16.91	43.59		Discrep (%)	-0.84
4	15	26.68	34.0	27.1	32.5	1.12	0.89	0.18	15.49	42.17			

Table D.2 (cont.). Manometer readings at DFE diffuser and nozzle.

Date: 9/30/96														
Discharge = 96.6														
Angle of Jet = 25 deg.														
Tailwater = 13 ft														
Nozzle	Angle of Jet (deg.)	E1.	Y1 (cm)	Y2 (cm)	YH20 (cm)	Y1 (ft)	Y2 (ft)	Y3 (ft)	H1 (ft)	C _v	V (ft/s)	E1 + v ² /2g (ft)	A (ft ²)	Q _i (cfs)
1	25	22.59	31.5	24.7	30.0	1.03	0.81	0.17	17.48	1.013	33.99	40.53	0.788	26.77
2	25	22.59	32.9	26.0	30.9	1.08	0.85	0.16	18.62	1.014	35.11	41.73	0.645	22.63
3	25	22.59	34.8	28.2	33.5	1.14	0.93	0.17	20.40	1.018	36.90	43.73	0.645	23.78
4	25	22.59	33.5	27.3	32.2	1.10	0.90	0.16	19.45	1.012	35.80	42.49	0.788	28.20
Diffuser	Angle of Jet (deg.)	E1.	Y1 (cm)	Y2 (cm)	YH20 (cm)	Y1 (ft)	Y2 (ft)	Y3 (ft)	H1 (ft)	E1 + H1 (ft)		Total Q (cfs)		
1	25	26.58	34.3	27.6	33.0	1.13	0.91	0.18	15.95	42.52			Meas. Q (cfs)	96.60
2	25	26.58	32.0	25.4	30.5	1.05	0.83	0.17	14.00	40.58			Discrep (%)	4.96
3	25	26.58	36.7	30.3	35.9	1.20	0.99	0.18	18.15	44.72				
4	25	26.58	35.9	29.2	34.4	1.18	0.96	0.17	17.31	43.89				

Date: 10/3/96													
Discharge = 96.6 cfs													
Angle of Jet = 25 deg.													
Tailwater = 11 ft													
No Manometer Data - Ground Surface at 7 ft													

Table D.2 (cont.). Manometer readings at DFE diffuser and nozzle.

Date: 10/9/96

Discharge = 96.6 cfs

Angle of Jet = 35 deg.

Tailwater = 11 ft

Nozzle	Angle of Jet (deg.)	E1.	Y1 (cm)	Y2 (cm)	YH20 (cm)	Y1 (ft)	Y2 (ft)	Y3 (ft)	H1 (ft)	C _v	V (ft/s)	EGL Elev. E1 + v ² /2g (ft)	A (ft ²)	Q _i (cfs)
1	35	22.82	32.2	25.2	30.7	1.06	0.83	0.18	17.77	1.012	34.24	41.03		
2	35	22.82	32.5	25.2	30.7	1.07	0.83	0.18	17.89	1.015	34.47	41.27		
3	35	22.82								N/A	N/A	N/A		
4	35	22.82	33.9	27.0	32.4	1.11	0.89	0.18	19.27	1.011	35.62	42.52		

Diffuser

Angle of Jet (deg.)

E1.

Y1 (cm)

Y2 (cm)

YH20 (cm)

Y1 (ft)

Y2 (ft)

Y3 (ft)

H1 (ft)

E1 + H1 (ft)

1	35	26.42	34.5	27.5	33.5	1.13	0.90	0.20	16.16			42.58		
2	35	26.42	32.4	25.3	30.5	1.06	0.83	0.17	14.28			40.70		
3	35	26.42	37.2	30.2	35.7	1.22	0.99	0.18	18.46			44.88		
4	35	26.42	37.2	30.2	35.6	1.22	0.99	0.18	18.46			44.88		

Date: 10/18/96

Discharge = 96.6 cfs

Angle of Jet = 35 deg.

Tailwater = 13 ft

No Manometer Data

APPENDIX E

DEPTH OF SCOUR VERSUS TIME AT VARIOUS LOCATIONS --
DFE STUDIES

APPENDIX E
DEPTH OF SCOUR VERSUS TIME AT VARIOUS LOCATIONS --
DFE STUDIES

Appendix E condenses the information related to the depth of scour at different points of the bed during the tests. Tennis balls were buried in different locations. Each location was assigned a color. When the tennis balls floated to the surface, the time of appearance was recorded.

Table E.1. Dam Foundation Erosion Studies -- depth of scour hole with respect to time (SI units), 09/09/96, 09/23/96, 09/30/96, 07/16/97.

Date	09/09/96				
G.S (m)	2.783				
Angle (deg.)	15				
t	t' (min)	Level (m)	z (m)	Scour Rate (m/min)	Q (m³/s)
02:55 PM	0	2.783	0.000	0.000	0.000
03:00 PM	5	2.326	0.457	0.091	2.172
03:01 PM	6	2.021	0.762	0.305	2.430
04:49 PM	104	1.402	1.381	0.006	2.735
Date	09/23/96				
G.S (m)	2.115				
Angle (deg.)	15				
t	t' (min)	Level (m)	z (m)	Scour Rate (m/min)	Q (m³/s)
10:51 AM	0	2.115	0.000		0.000
11:01 AM	10	1.792	0.323	0.032	2.735
11:32 AM	41	1.454	0.661	0.011	2.735
12:43 PM	112	1.286	0.829	0.002	2.735
Date	09/30/96				
G.S (m)	2.149				
Angle (deg.)	25				
t	t' (min)	Level (m)	z (m)	Scour Rate (m/min)	Q (m³/s)
10:58 AM	0	2.149	0.000	0.000	0
12:35 PM	97	1.527	0.622	0.006	N/A
12:42 PM	104	1.524	0.625	0.000	N/A
Date	07/16/97				
G.S (m)	2.195				
Angle (deg.)	35				
X (m)	6.858				
t	t' (min)	Level (m)	z (m)	Scour Rate (m/min)	Q (m³/s)
01:33 PM	0	2.195	0.000		1.133
01:39 PM	6	1.615	0.579	0.097	2.322
03:27 PM	114	1.524	0.671	0.001	2.735
X (m)	5.486				
t	t' (min)	Level (m)	z (m)	Scour Rate (m/min)	Q (m³/s)
01:33 PM	0	2.195	0.000		
01:48 PM	15	1.756	0.439	0.029	
01:50 PM	17	1.539	0.655	0.108	2.735
03:27 PM	114	1.603	0.591	-0.001	2.735
X (m)	4.572				
t	t' (min)	Level (m)	z (m)	Scour Rate (m/min)	Q (m³/s)
01:33 PM	0	2.195	0.000		0
01:48 PM	15	1.911	0.283	0.019	2.735
02:10 PM	37	1.582	0.613	0.015	2.735
03:27 PM	114	1.661	0.533	-0.001	2.735
Side scour					
X (m)	5.486				
Y (m)	7.62				
t	t' (min)	Level (m)	z (m)	Scour Rate (m/min)	Q (m³/s)
01:33 PM	0	2.195	0.000		
02:20 PM	47	1.893	0.302	0.006	2.735
02:50 PM	77	1.643	0.552	0.008	2.735
03:27 PM	114	1.372	0.823	0.007	2.735

Table E.2. Dam Foundation Erosion Studies -- depth of scour hole with respect to time (SI units), summary of 07/16/97.

t' (min)	X = 6.86 m Y = 4.57 m	X = 5.49 m Y = 4.57 m	X = 4.57 m Y = 4.57 m	X = 5.49 m Y = 7.62 m	Q (m ³ /s)	TW (m)
0	0.000					
6	0.579					
114	0.671					
0		0.000				
15		0.439				
17		0.655				
114		0.591				
0			0.000			
15			0.283			
37			0.613			
114			0.533			
0				0.000		
47				0.302		
77				0.552		
114				0.823		
0					1.133	
2					1.416	
7					2.322	
10					2.735	
15					2.735	
17					2.735	
37					2.735	
47					2.735	
77					2.735	
114					2.735	
2						1.250
7						1.311
15						0.701
17						0.793
37						0.823
47						0.823
77						0.823
114						0.823

Table E.3. Dam Foundation Erosion Studies -- depth of scour hole with respect to time (SI units), 07/23/97.

Date	7/23/97
GS (m)	2.088
Angle	35
X (m)	7.62

t	t' (min)	Level (m)	z (m)	Scour Rate (m/min)	Q (m ³ /s)
01:55 PM	0	2.088	0.000		0.425
02:05 PM	10	1.786	0.302	0.030	2.549
02:10 PM	15	1.661	0.427	0.025	2.735
03:54 PM	119	1.027	1.061	0.006	2.735

X (m) 6.401

t	t' (min)	Level (m)	z (m)	Scour Rate (m/min)	Q (m ³ /s)
01:55 PM	0	2.088	0.000		0.425
02:05 PM	10	1.826	0.262	0.026	2.549
02:10 PM	15	1.603	0.485	0.045	2.735
03:54 PM	119	1.100	0.988	0.005	2.735

X (m) 5.486

t	t' (min)	Level (m)	z (m)	Scour Rate (m/min)	Q (m ³ /s)
01:55 PM	0	2.088	0.000		0.425
02:13 PM	18	1.673	0.415	0.023	2.549
02:17 PM	22	1.430	0.658	0.061	2.735
03:54 PM	119	1.335	0.753	0.001	2.735

X (m) 4.572

t	t' (min)	Level (m)	z (m)	Scour Rate (m/min)	Q (m ³ /s)
01:55 PM	0	2.088	0.000		
02:16 PM	21	1.759	0.329	0.016	
03:54 PM	119	1.631	0.457	0.001	

X (m) 5.486
Y (m) 7.620

t	t' (min)	Level (m)	z (m)	Scour Rate (m/min)	Q (m ³ /s)
01:55 PM	0	2.088	0.000		0.425
02:27 PM	32	1.747	0.341	0.011	2.735
02:45 PM	50	1.615	0.472	0.007	2.735
03:54 PM	119	1.073	1.015	0.008	2.735

Table E.4. Dam Foundation Erosion Studies -- depth of scour hole with respect to time (SI units), summary of 07/23/97.

t (min)	X = 7.62 m Y = 4.57 m	X = 6.86 m Y = 4.57 m	X = 5.49 m Y = 4.57 m	X = 4.57 m Y = 4.57 m	X = 5.49 m Y = 7.62 m	Q (m ³ /s)	TW (m)
0	0.000						
10	0.302						
15	0.427						
119	1.061						
0		0.000					
10		0.262					
15		0.485					
119		0.988					
0			0.000				
18			0.415				
22			0.658				
119			0.753				
0				0.000			
21				0.329			
119				0.457			
0					0.000		
32					0.341		
50					0.472		
119					1.015		
0						0.425	
6						1.416	
10						2.549	
15						2.735	
18						2.735	
32						2.735	
119						2.735	
0							1.143
6							1.326
15							1.265
18							0.655
32							0.503
119							0.503

Table E.5. Dam Foundation Erosion Studies -- depth of scour hole with respect to time (SI units), 09/02/97.

Date	09/02/97				
GS (m)	2.15				
Angle	25				
X (m)	6.401				

t	t' (min)	Level (m)	z (m)	Scour Rate (m/min)	Q (m ³ /s)
03:02 PM	0	2.155	0.000		0.283
03:19 PM	17	1.518	0.637	0.037	2.735
04:57 PM	115	0.975	1.180	0.006	2.735

X (m)	5.486				
-------	-------	--	--	--	--

t	t' (min)	Level (m)	z (m)	Scour Rate (m/min)	Q (m ³ /s)
03:02 PM	0	2.155	0.000		0.283
03:09 PM	7	1.945	0.210	0.030	1.699
03:10 PM	8	1.594	0.561	0.351	2.265
03:11 PM	9	1.341	0.814	0.253	2.549
04:57 PM	115	0.792	1.362	0.005	2.735

X (m)	4.572				
-------	-------	--	--	--	--

t	t' (min)	Level (m)	z (m)	Scour Rate (m/min)	Q (m ³ /s)
03:02 PM	0	2.155	0.000		0.283
03:08 PM	6	1.932	0.223	0.037	1.416
03:10 PM	8	1.814	0.341	0.059	2.265
03:11 PM	9	1.670	0.485	0.143	2.549
04:57 PM	115	0.954	1.201	0.007	2.735

Table E.6. Dam Foundation Erosion Studies -- depth of scour hole with respect to time (SI units), summary of 09/02/97.

t (min)	X = 6.40 m Y = 4.57 m	X = 5.49 m Y = 4.57 m	X = 4.57 m Y = 4.57 m	Q (m ³ /s)	TW (m)
0	0.000				
17	0.637				
115	1.180				
0		0.000			
7		0.210			
8		0.561			
9		0.814			
115		1.362			
0			0.000		
6			0.223		
8			0.341		
9			0.485		
115			1.201		
0				0.283	
2				0.481	
3				0.991	
6				1.416	
7				1.699	
8				2.265	
9				2.549	
11				2.735	
13				2.735	
15				2.735	
17				2.735	
115				2.735	
0					1.289
2					1.289
3					1.350
6					1.320
9					1.440
13					0.985
15					0.588
17					0.436
115					0.436

Table E.7. Dam Foundation Erosion Studies -- depth of scour hole with respect to time (SI units), 09/11/97.

Date	09/11/97				
GS (m)	2.120				
Angle	25				
X (m)	6.401				

t	t' (min)	Level (m)	z (m)	Scour Rate (m/min)	Q (m ³ /s)
10:48:00 AM	0	2.121	0.000		0.425
11:10:00 AM	22	1.067	1.055	0.048	2.735
12:48:00 PM	120	1.128	0.994	-0.001	2.735

X (m) 5.486

t	t' (min)	Level (m)	z (m)	Scour Rate (m/min)	Q (m ³ /s)
10:48:00 AM	0	2.121	0.000		0.425
10:55:30 AM	7.5	1.829	0.293	0.039	1.699
10:55:30 AM	7.5	1.646	0.475		1.699
10:58:00 AM	10	1.451	0.671	0.078	2.735
11:10:00 AM	32	1.134	0.988	0.014	2.735
12:48:00 PM	120	0.945	1.177	0.002	2.735

X (m) 4.572

t	t' (min)	Level (m)	z (m)	Scour Rate (m/min)	Q (m ³ /s)
10:48:00 AM	0	2.121	0.000		0.425
10:55:30 AM	7.5	1.862	0.259	0.035	1.699
11:02:00 AM	14	1.536	0.585	0.050	2.735
11:08:00 AM	20	1.164	0.957	0.062	2.735
12:48:00 PM	120	1.067	1.055	0.001	2.735

Table E.8. Dam Foundation Erosion Studies -- depth of scour hole with respect to time (SI units), summary of 09/11/97.

t (min)	X = 6.40 m Y = 4.57 m	X = 5.49 m Y = 4.57 m	X = 4.57 m Y = 4.57 m	Q (m ³ /s)	TW (m)
0	0.00				
22	1.05				
120	0.99				
0		0.00			
7.5		0.29			
7.5		0.48			
10		0.67			
32		0.99			
120		1.18			
0			0.00		
7.5			0.26		
14			0.59		
20			0.96		
120			1.05		
0				0.425	
1				0.850	
2.75				1.274	
5				0.991	
6				1.274	
7				1.699	
9				2.549	
10				2.735	
14				2.735	
15				2.735	
16				2.735	
20				2.735	
32				2.735	
120				2.735	
0					1.018
1					1.201
2.75					1.689
5					1.384
6					1.201
7					1.201
8					1.329
9					1.597
10					1.689
14					0.989
16					0.774
20					0.835
32					0.774
120					0.774

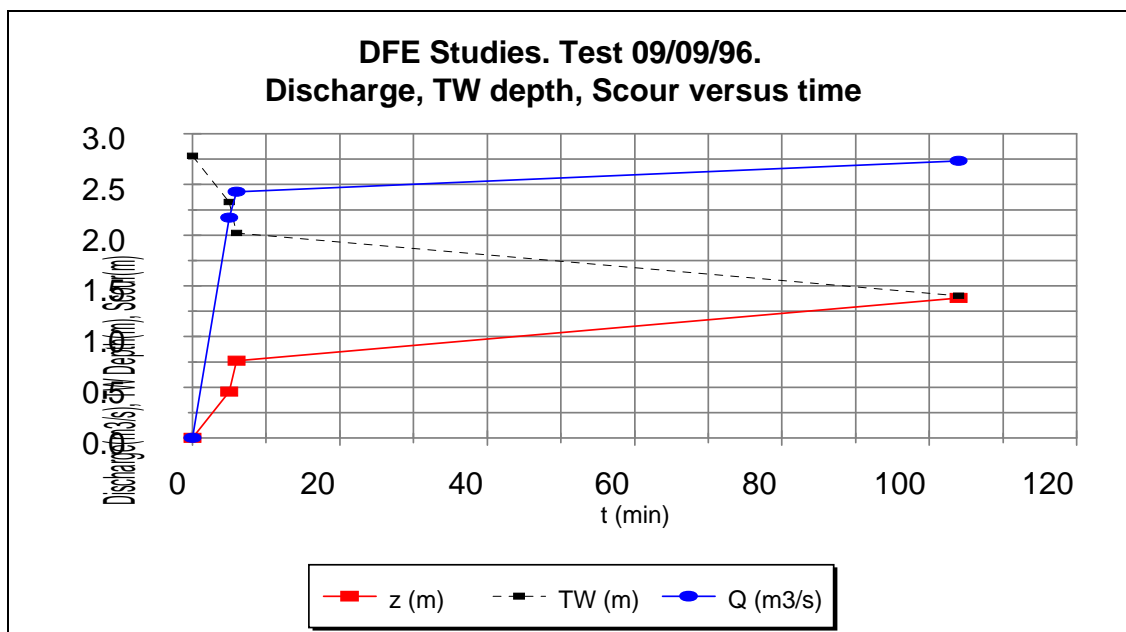


Figure E.1. Dam Foundation Erosion Studies — discharge, TW depth, and scour depth versus time for 09/09/96.

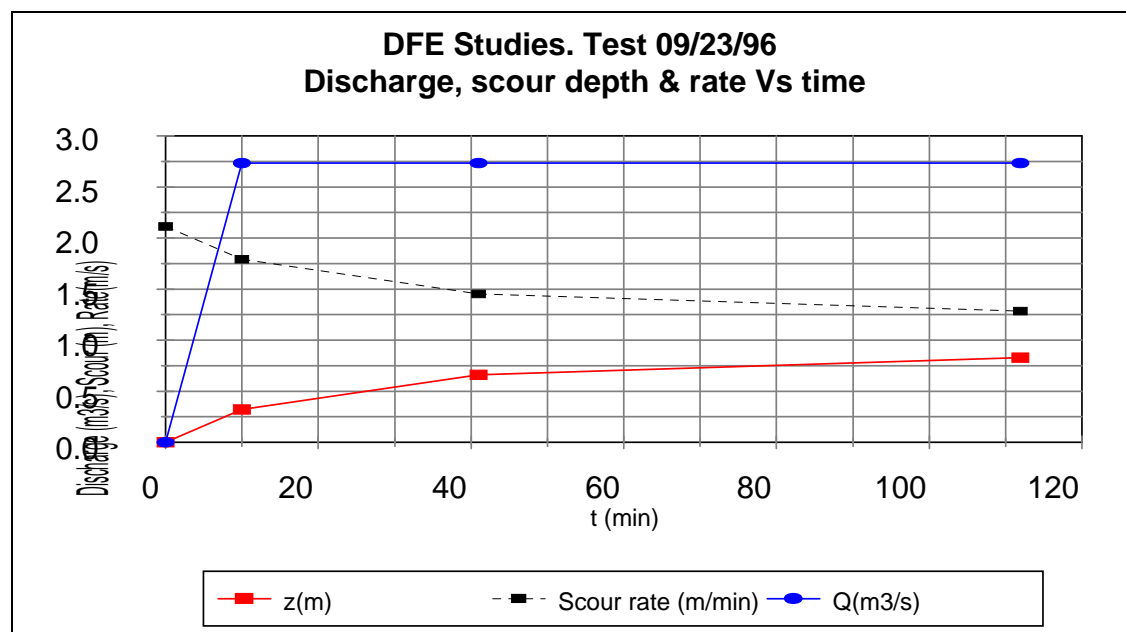


Figure E.2. Dam Foundation Erosion Studies — discharge, scour depth, and rate versus time for 09/23/96.

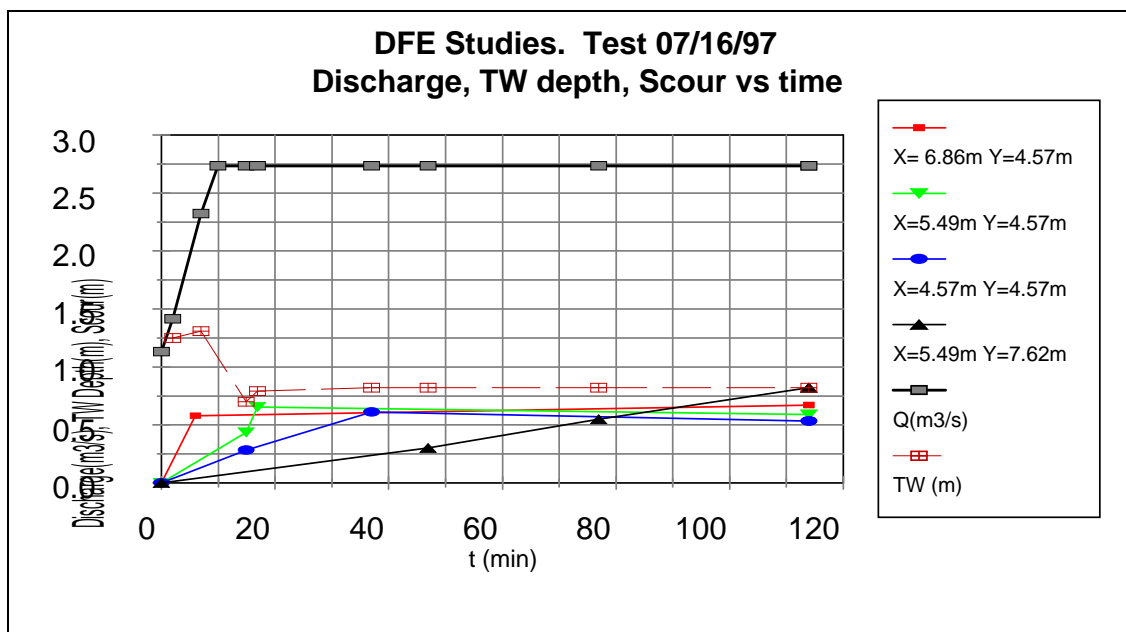


Figure E.3. Dam Foundation Erosion Studies — discharge, TW depth, and scour depth versus time for 07/16/97.

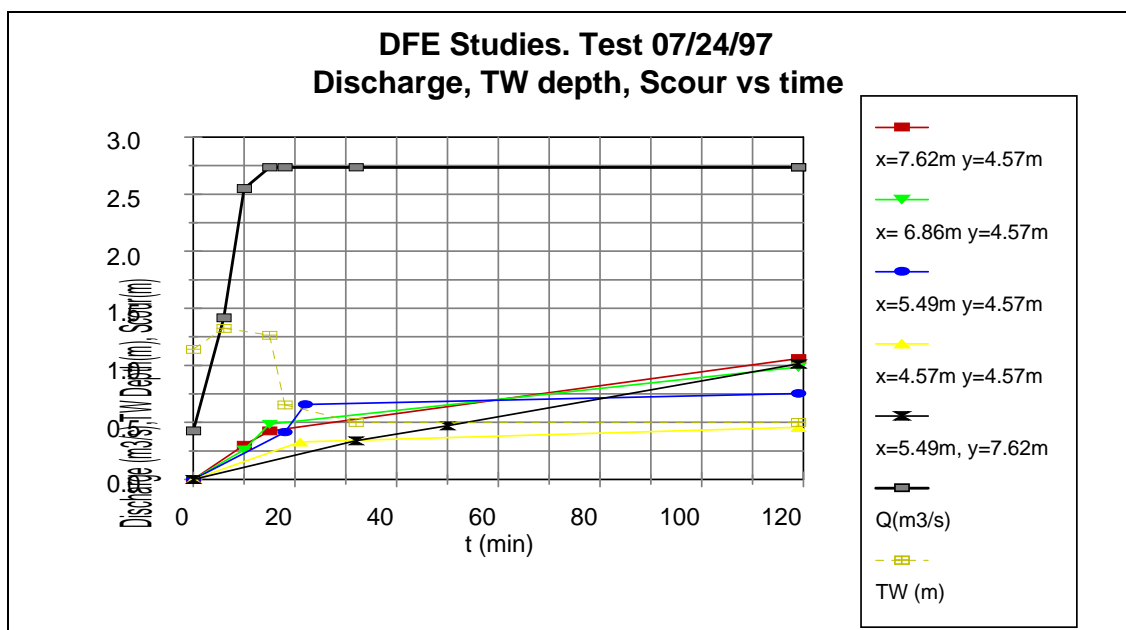


Figure E.4. Dam Foundation Erosion Studies — discharge, TW depth, and scour depth versus time for 07/24/97.

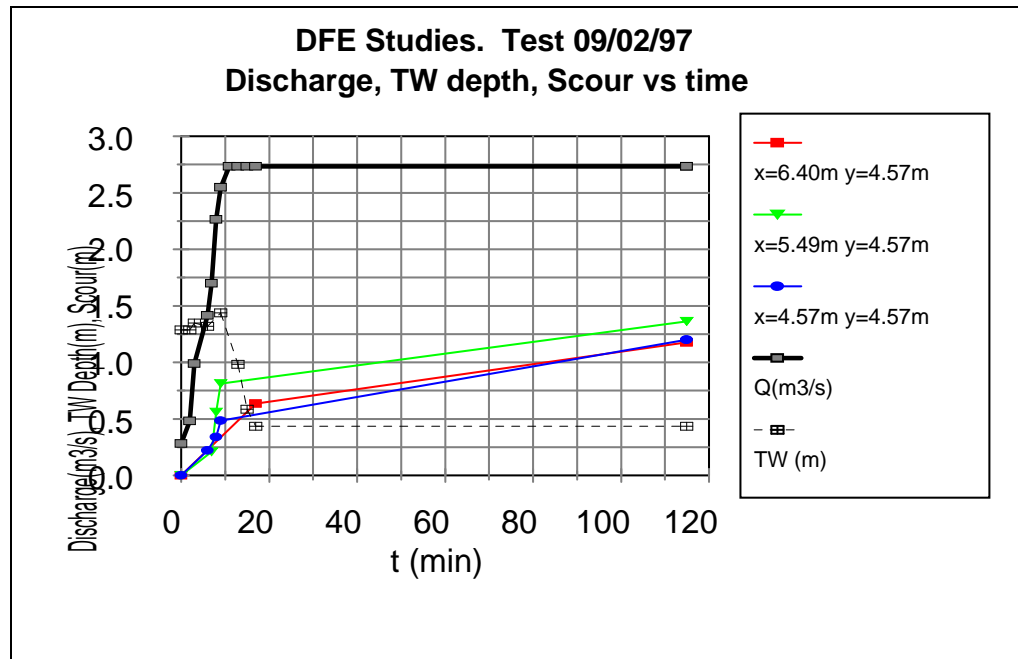


Figure E.5. Dam Foundation Erosion Studies — discharge, TW depth, and scour depth versus time for 09/02/97.

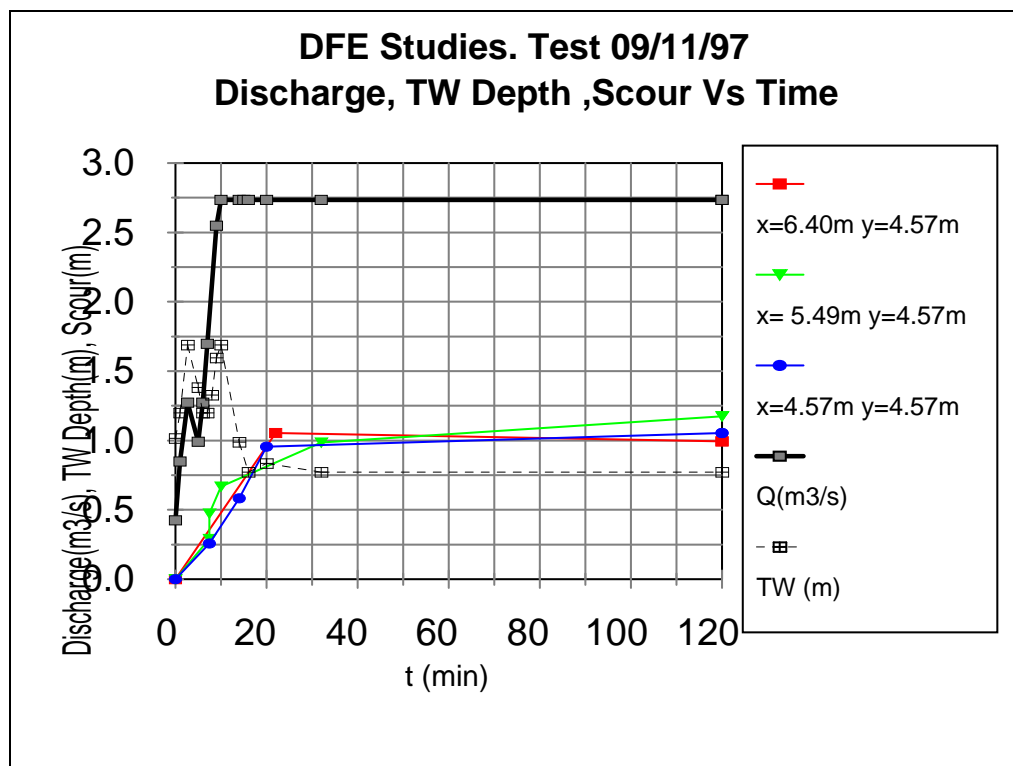


Figure E.6. Dam Foundation Erosion Studies — discharge, TW depth, and scour depth versus time for 09/11/97.

APPENDIX F

PARTICLE SIZE DISTRIBUTION OF
BEFORE AND AFTER THE TESTS

&

PARTICLE SIZE DISTRIBUTION IN HALLMARK AND THOMAS TESTS

APPENDIX F
PARTICLE SIZE DISTRIBUTION OF
BEFORE AND AFTER THE TESTS
&
PARTICLE SIZE DISTRIBUTION IN HALLMARK AND THOMAS TESTS

The size distribution of the particles before and after the tests is given in Appendix F. Soil samples were collected before the tests near the zone of impingement. After the tests, soil samples were collected at the upstream slope, the bottom, and the downstream slope of the scour hole. In addition, samples were collected at the top of the mound formed downstream of the scour hole. Graphs of the particle size distribution using Hallmark's data were also included for comparison.

Table F.1. Particle size distribution data from DFE Studies.

Sieve #	Opening (mm)	WM 3/4" Road Base
1"	25.400	100
3/4"	19.050	100
5/8"	16.000	85
3/8"	9.520	75
No. 4	4.750	59
No. 8	2.360	47
No. 16	1.180	37
No. 30	0.600	28
No. 50	0.300	20
No. 100	0.150	15
No. 200	0.075	11.52
d_{50} (mm)		2.96
d_{85} (mm)		16.00

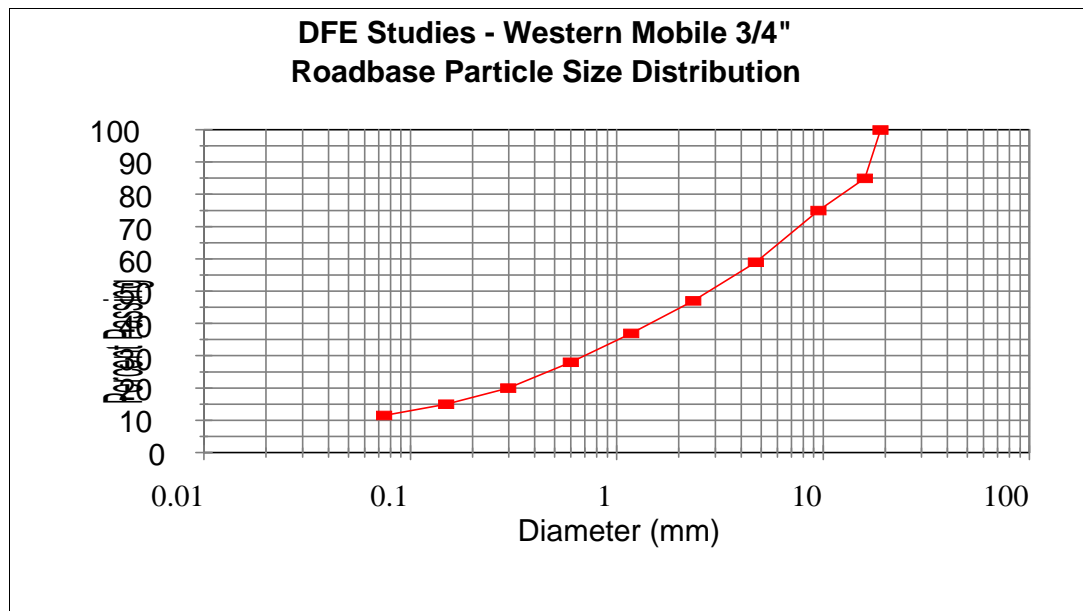


Figure F.1. Dam Foundation Erosion Studies - - Western Mobile 3/4 in. roadbase particle size distribution.

Table F.2. Particle size distribution of particles found in scour hole -- 07/16/97.

Tailwater Elevation (ft) 10.00
Ground Surface Elevation (ft) 7.20
Angle of Nozzle 35

Particle Size (mm)	% passing Before test-18'	% passing Before test-21'	% passing Before test-16'	% passing Bottom sc hole	% passing DS Slope	% passing US Slope	% passing Mound
25.4	100.00	100.00	100.00	100.00	100.00	100.00	100.00
19.05	100.00	99.38	100.00	100.00	95.00	100.00	100.00
16	95.69	93.48	95.00	89.96	70.16	96.35	91.81
9.52	78.95	74.84	73.81	39.95	9.58	83.43	57.45
4.75	61.27	56.85	54.92	9.32	0.84	67.45	34.78
2.36	46.20	43.90	42.20	1.14	0.74	51.77	22.62
1.18	31.07	30.17	29.22	0.63	0.66	33.74	12.71
0.6	17.61	17.19	18.14	0.45	0.50	17.60	4.38
0.3	8.73	8.83	8.66	0.33	0.32	6.21	0.79
0.125	3.68	3.63	3.56	0.21	0.16	2.38	0.16
0.075	2.55	2.54	2.32	0.15	0.13	1.55	0.11
d ₅₀ (mm)	2.96	3.49	3.83	10.83	13.84	2.24	7.96
d ₈₅ (mm)	11.86	13.05	12.94				

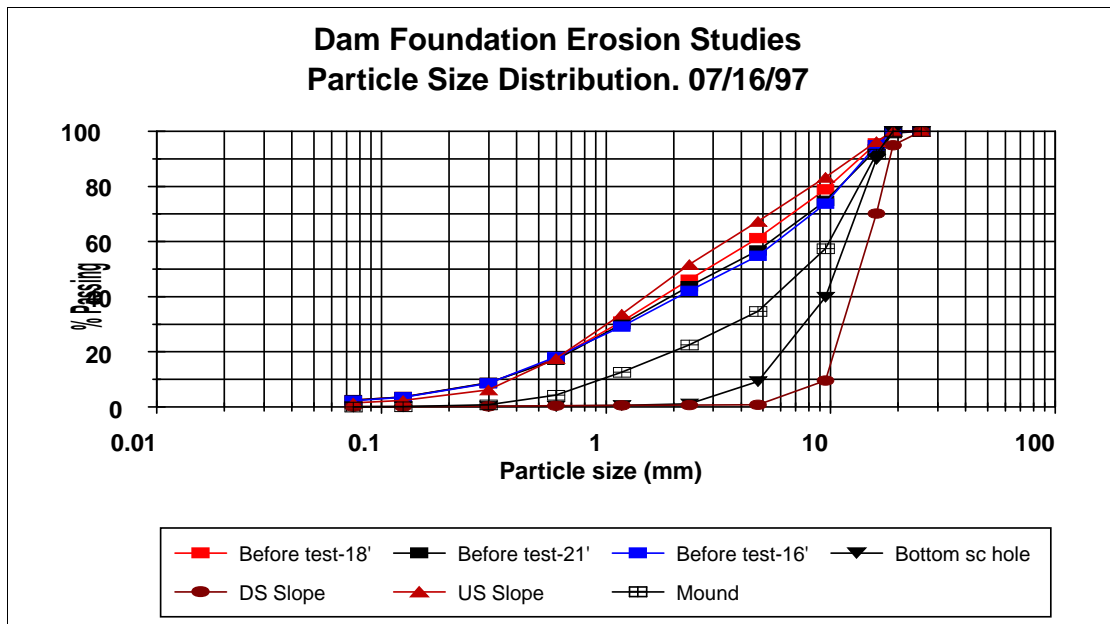


Figure F.2. Dam Foundation Erosion Studies -- particle size distribution 07/16/97.

Table F.3. Particle size distribution of particles found in scour hole -- 07/24/97.

Tailwater Elevation (ft) 8.50
Ground Surface Elevation (ft) 6.85
Angle of Nozzle 35

Particle Size (mm)	% passing Before run 1	% passing Before run 2	% passing After run-Bottom	% passing DS Slope	% passing US Slope	% passing Mound
25.4	100.00	100.00	100.00	100.00	100.00	100.00
19.05	99.24	100.00	98.45	96.97	96.97	98.83
16	94.26	94.58	84.61	60.48	82.39	90.01
9.52	74.96	70.08	42.88	8.91	48.51	59.15
4.75	57.97	55.00	21.13	2.37	29.66	43.62
2.36	45.95	43.80	10.88	1.66	20.99	33.52
1.18	30.22	25.81	5.60	1.48	13.02	23.14
0.6	15.82	14.55	2.50	1.04	5.34	11.33
0.3	8.65	8.63	0.86	0.44	1.64	2.95
0.125	3.75	4.23	0.30	0.18	0.59	0.41
0.075	2.80	3.09	0.20	0.11	0.38	0.24
0	0.00	0.00	0.00	0.00	-0.00	-0.00
d ₅₀ (mm)	3.16	3.68	10.62	14.68	9.81	6.71
d ₈₅ (mm)	12.89	13.47				

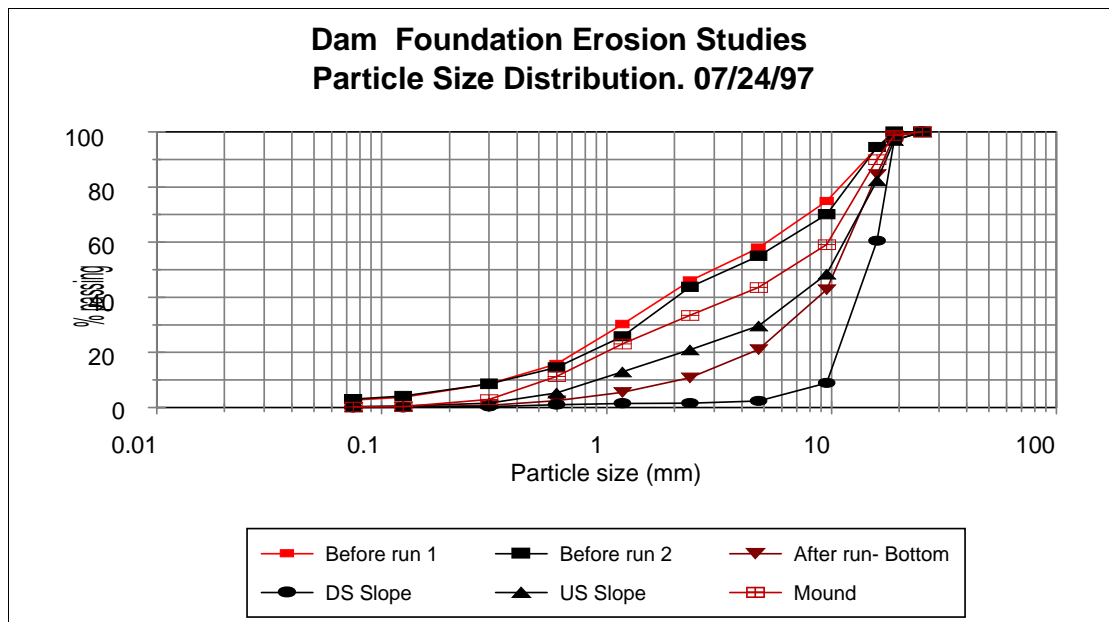


Figure F.3. Dam Foundation Erosion Studies -- particle size distribution, 07/24/97.

Table F.4. Particle size distribution of particles found in scour hole -- 09/02/97.

Tailwater Elevation (ft) 8.40
Ground Surface Elevation (ft) 7.07
Angle of Nozzle 25

Particle Size (mm)	% passing Before run 1	% passing Before run 2	% passing After run-Bottom	% passing DS Slope	% passing US Slope	% passing Mound
25.4	100.00	100.00	100.00	100.00	100.00	100.00
19.05	98.98	100.00	92.90	94.18	96.05	99.30
16	96.78	92.32	50.99	55.71	90.53	89.62
9.52	75.29	62.98	6.16	5.85	58.36	57.39
4.75	56.80	62.55	2.88	1.72	32.62	35.92
2.36	43.04	47.41	2.64	1.63	8.03	25.01
1.18	28.83	30.03	2.51	1.51	7.31	16.63
0.5	12.34	13.61	1.91	1.33	5.54	8.18
0.3	6.39	8.40	1.21	0.96	3.54	3.58
0.125	2.97	4.54	0.67	0.57	1.92	1.00
0	0.00	0.00	0.00	-0.00	-0.00	0.00
d ₅₀ (mm)	3.57	2.77	15.85	15.26	7.97	7.87
d ₈₅ (mm)	12.45	14.38				

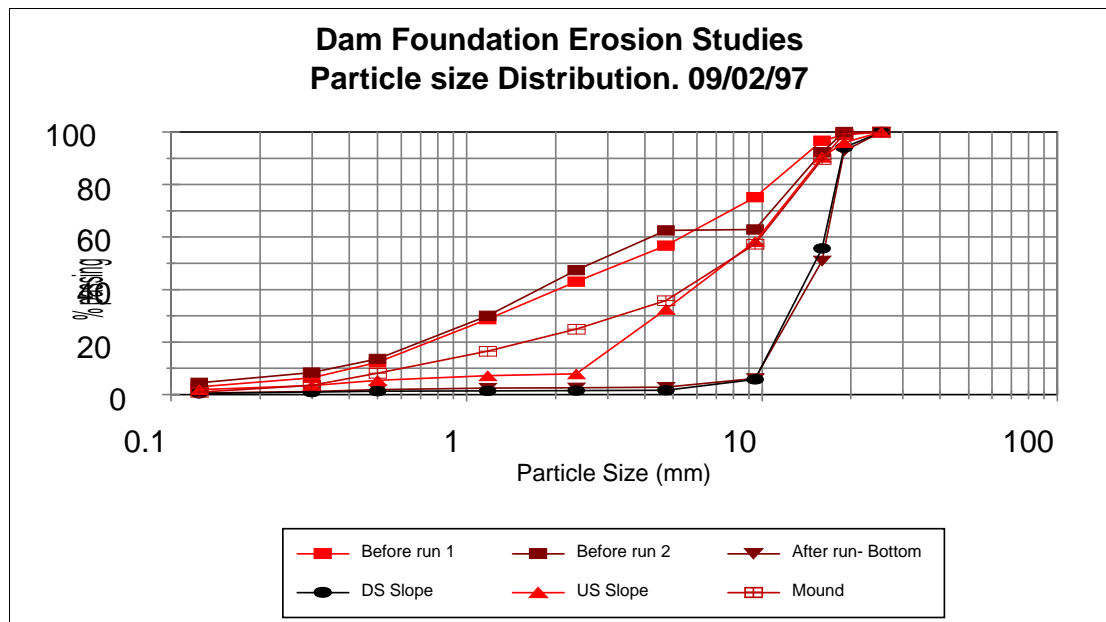


Figure F.4. Dam Foundation Erosion Studies -- particle size distribution, 09/02/97.

Table F.5. Particle size distribution of particles found in scour hole -- 09/11/97.

Tailwater Elevation (ft) 9.50
Ground Surface Elevation (ft) 6.96
Angle of Nozzle 25

Particle Size (mm)	% passing Before run 1	% passing Before run 2	% passing Before Run-3	% passing After run-Bottom	% passing DS Slope	% passing US Slope	% passing Mound
25.4	100.00	100.00	100.00	100.00	100.00	100.00	100.00
19.05	99.28	99.16	100.00	93.62	91.01	100.00	100.00
16	94.99	97.52	97.16	49.39	36.60	96.57	97.10
9.52	81.62	76.30	80.46	7.06	1.12	84.83	75.62
4.75	64.60	58.03	62.02	0.82	0.54	75.20	54.62
2.36	40.93	39.06	43.58	0.44	0.48	65.67	37.47
1.18	23.53	21.33	25.22	0.42	0.43	51.58	22.02
0.5	13.95	10.45	13.71	0.38	0.37	25.01	7.32
0.3	9.62	6.84	9.31	0.31	0.33	9.87	2.07
0.125	5.49	3.75	5.26	0.26	0.28	2.28	0.48
0	0.00	0.00	0.00	-0.00	-0.00	-0.00	-0.00
d ₅₀ (mm)	3.28	3.74	3.19	16.04	16.75	1.13	4.1
d ₈₅ (mm)	11.16	12.18	11.28				

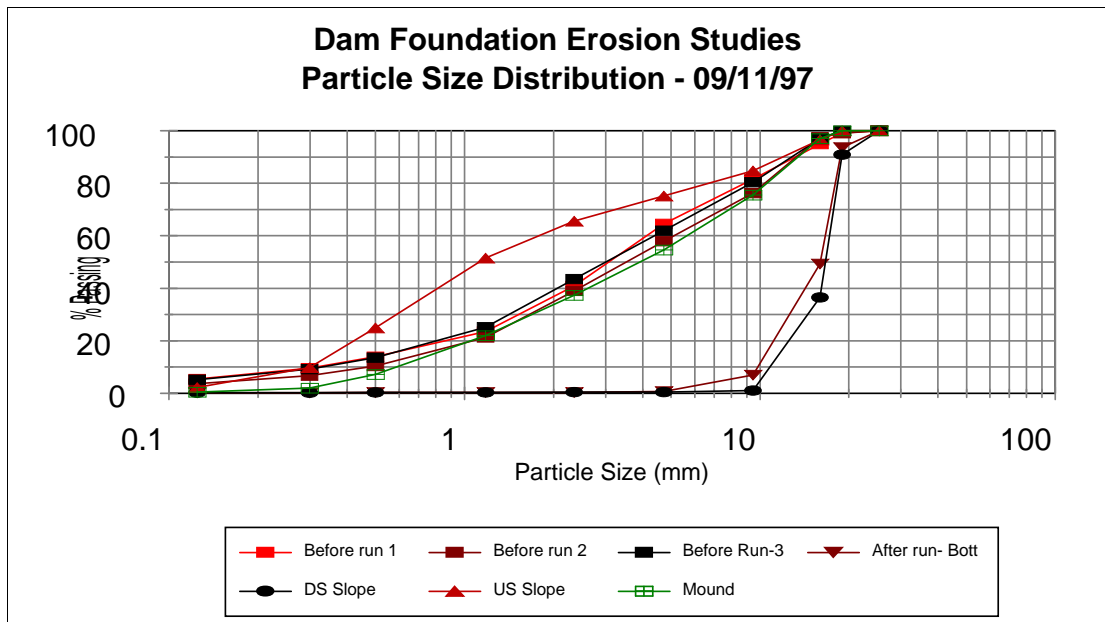


Figure F.5. Dam Foundation Erosion Studies -- particle size distribution, 09/11/97.

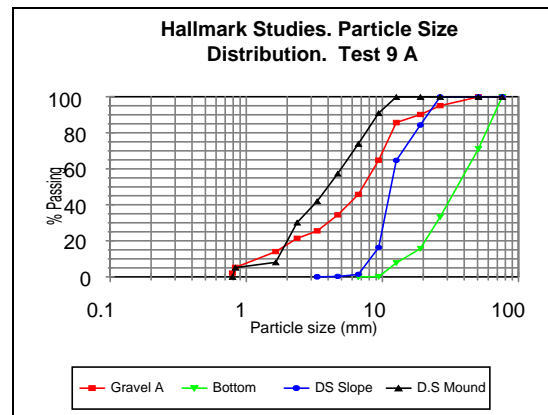
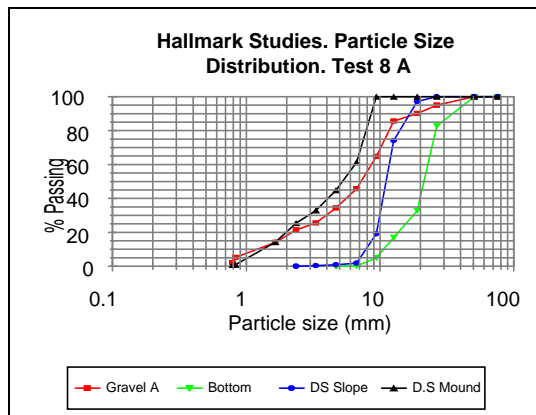
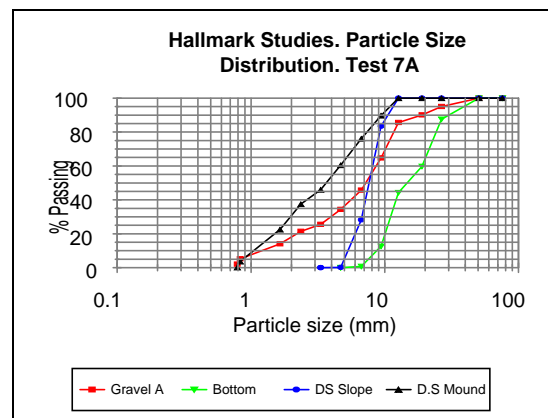
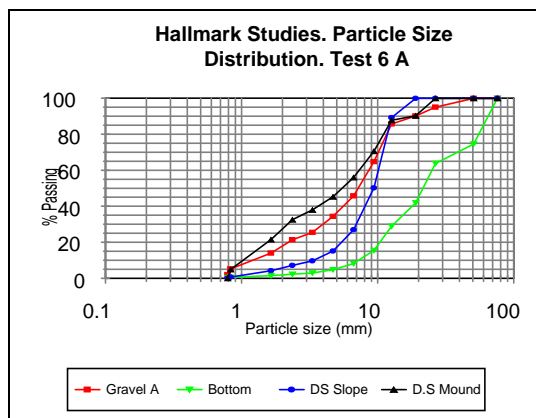
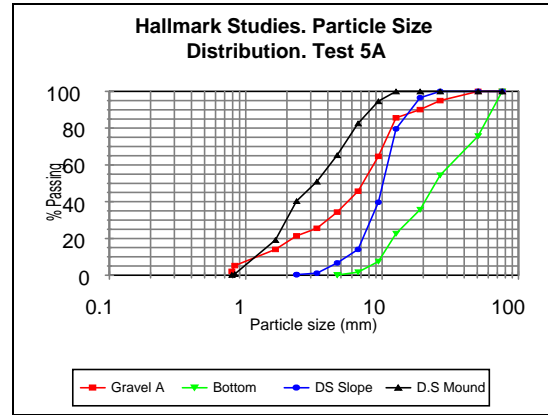
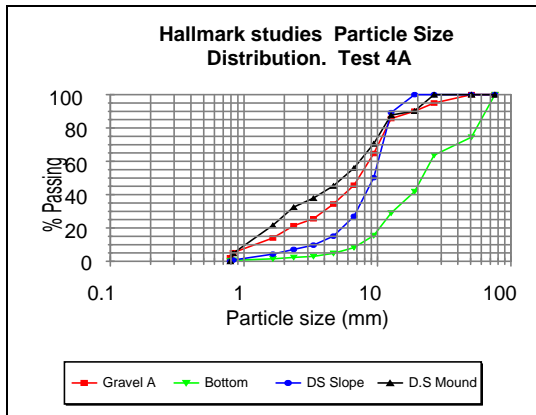


Figure F.6. Hallmark Series A Tests -- particle size distribution.

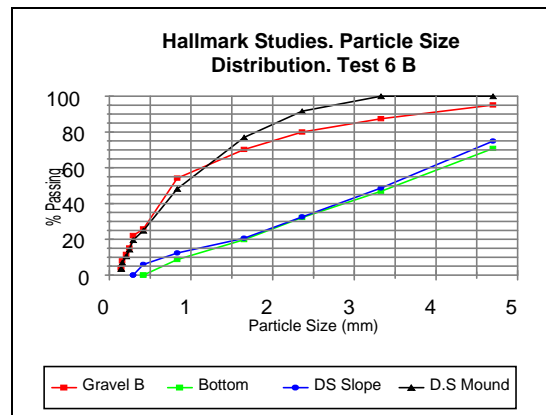
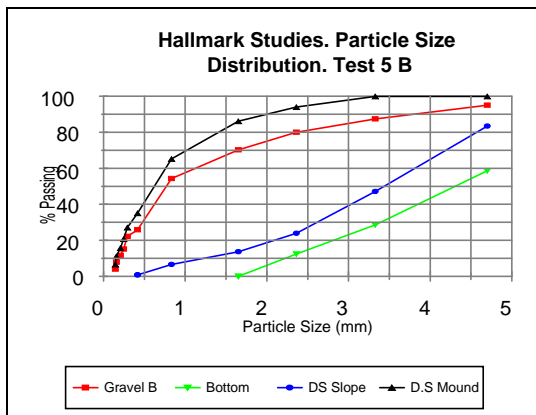
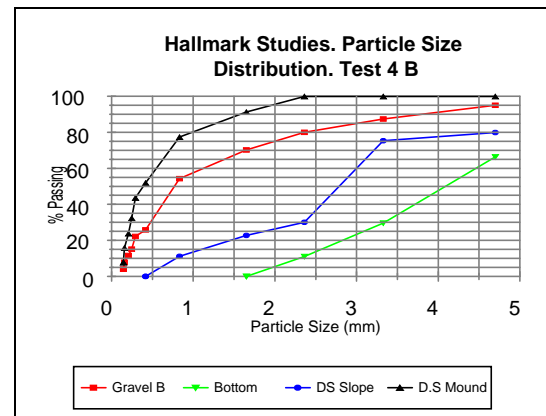
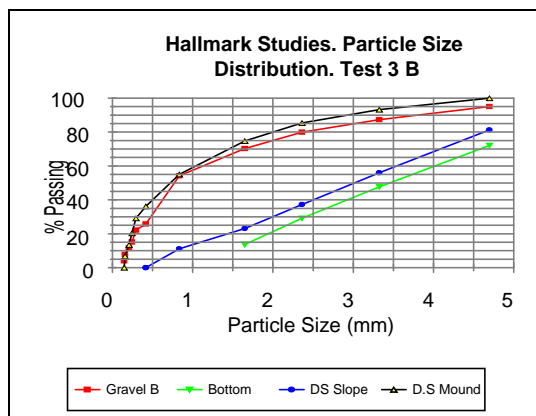
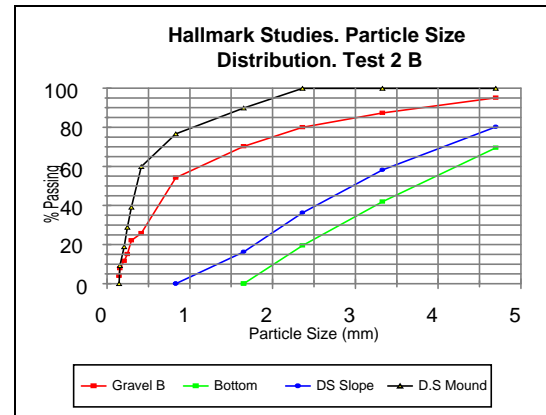
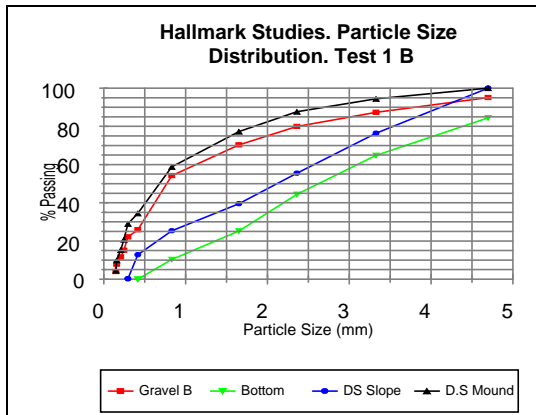


Figure F.7. Hallmark Series B Tests -- particle size distribution.

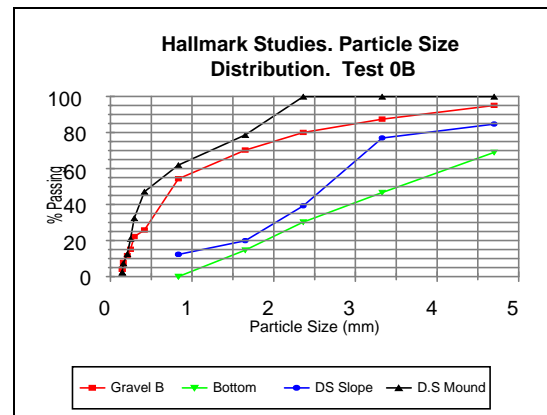
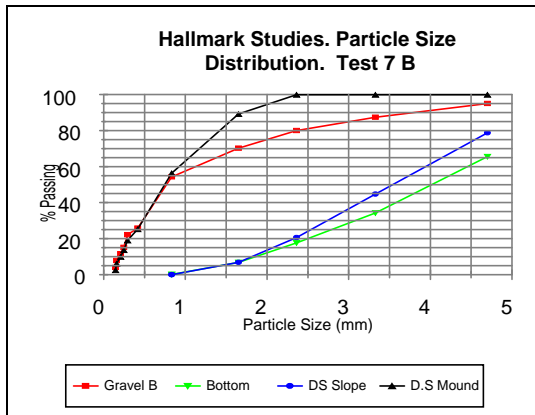


Figure F.7 (cont.). Hallmark Series B Tests -- particle size distribution.

APPENDIX G
SCOUR HOLE GEOMETRY

APPENDIX G

SCOUR HOLE GEOMETRY

G.1 Introduction

The geometry of the scour holes produced by the jets in the tests carried out at DFE is given in Appendix G. The dimensionless longitudinal profiles as described in Section 5.11 are given in Figures G.3 through G.5. Contour maps of the scour holes are given in Figures G.6 through G.17. Longitudinal profiles (passing through the deepest point) are included in Figures G.18 through G.29. Figures G.30 through G.41 include lateral profiles at the deepest point of the scour holes. Three dimensional views of scour holes are given in Figures G.42 through G.53.

G.2 Volumes Above and Below Initial Bed Level

Using Surfer[®], volumes of scour and deposition were calculated for each of the tests carried out at the DFE Facility. The initial bed elevation was used as the reference level. Table G.1 summarizes the results.

Table G.1. Volumes of scour and deposition.

Test	Date	Tailwater Depth - TW m (ft)	Deposition m ³ (ft ³)	Scour m ³ (ft ³)
96-1	08/26/96	0.57 (1.87)	15.55 (549.1)	34.88 (1231.7)
96-2	09/03/96	0.85 (2.59)	19.26 (680.3)	29.65 (1047.2)
96-3	09/09/96	0.27 (0.97)	0.02 (0.7)	50.20 (1772.8)
96-4	09/23/96	1.85 (5.96)	12.79 (451.6)	14.92 (526.9)
96-5	09/30/96	1.80 (5.87)	16.13 (569.7)	15.80 (558.0)
96-6	10/03/96	1.17 (3.87)	23.69 (836.6)	23.47 (828.8)
96-7	10/09/96	1.16 (3.80)	23.98 (847.0)	24.15 (852.9)
96-8	10/18/96	1.80 (5.93)	8.72 (308.0)	19.54 (308.7)
97-1	07/16/97	0.84 (2.75)	15.69 (553.9)	33.86 (1195.9)
97-2	07/23/97	0.50 (1.64)	5.07 (179.0)	43.79 (1546.3)
97-3	09/02/97	0.41 (1.33)	5.34 (188.6)	39.69 (1401.5)
97-4	09/11/97	0.77 (2.54)	17.93 (633.3)	28.02 (989.4)

Volume above the initial bed level corresponds mainly to the volume of the mound deposited downstream of the scour hole. Volume below the initial bed level corresponds mainly to the scour hole volume. Assuming the bed was perfectly leveled before the test, both volumes should be equal, unless material was swept over the end sill of the tailbox. Bed material was eroded away several times during the tests carried out at the DFE Facility, as can be seen in Table G.1. Part of the material eroded away was deposited at the end basin. The rest was carried away. When the tailwater depth was very low, large amounts of material were removed from the tailbox.

G.3 Width of the Scour Hole

The width of the scour hole is measured in the lateral section that contains the deepest point of the scour hole. The reference level was taken where a break in the slope occurred. In some cases the reference level coincided with the original bed material. For

scour holes that were scoured with low tailwater depths, the reference level was lower than the original bed material, where the limits of a scour hole were clear. Final widths of scour holes were plotted against tailwater depths and for calculated angles of impingement of 12 degrees with respect to the vertical (water was released at 15 degrees departure from vertical) and 19 degrees with respect to the vertical (water was released at 25 degrees departure from vertical), width decreased with an increase in tailwater depth. For angles of impingement of approximately 27 degrees (water was released at a 35 degrees departure with respect to the vertical) and low tailwater depths, the final widths of the scour hole probably exceeded the limits of the basin, but there was an increase in width for an increase in tailwater between 1.16 m (3.8 ft) and 1.81 m (5.93 ft). However, the width of the scour hole converges to approximately 6 m (20 ft) for a tailwater depth of approximately 1.80 m (6 ft) for the same discharge as can be seen in Figure G.1. Two points are missing when the angle of impingement was 27. In those two cases, the boundaries of the scour hole were unclear near the walls. Apparently, recirculation caused additional scour near the east and west walls.

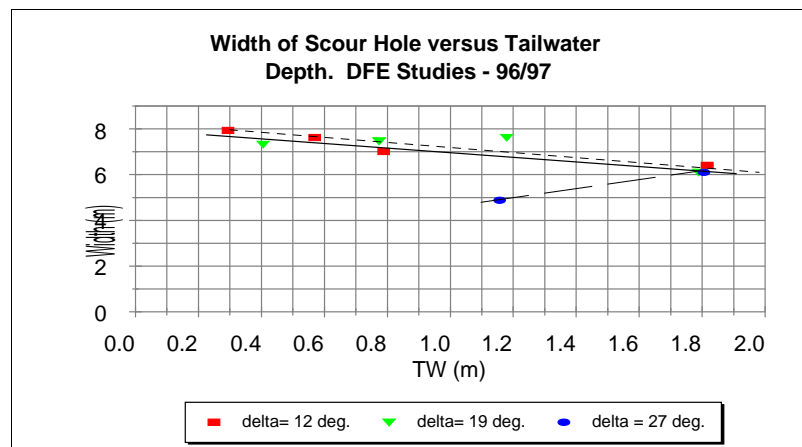


Figure G.1. Width of scour hole versus tailwater depth.

Table G.2.1. Dam Foundation Erosion Studies -- angle of downstream slope, θ , versus angle of impingement, δ .

Angle of Impingement δ (deg.)	θ (deg.)				
	DFE - Rectangular Jet	Doehring - Circular Jet	Hallmark A - Free Overfall	Hallmark B - Free Overfall	Doehring - DS Slope
11.636	26.565				
11.887	24.513				
11.438	24.560				
12.064	26.243				
19.875	23.557				
19.150	29.899				
26.360	20.907				
27.395	15.961				
25.869	18.624				
25.229	17.223				
18.346	24.891				
18.683	26.012				
37.010		27.022			0.510
48.430		26.473			0.498
56.370		18.983			0.344
62.140		17.693			0.319
30.270		24.655			0.459
41.120					
49.330		24.228			0.450
55.670		22.441			0.413
23.490		24.655			0.459
33.030		24.228			0.450
40.920		27.112			0.512
47.490		27.429			0.519
12.439			30		
8.999			30		
9.548			30		
8.124			30		
6.049			30		
6.460			30		
5.783			30		
9.536			30		
9.536			30		
7.895				30	
7.070				30	
6.460				30	
5.984				30	
6.460				30	
10.016				30	
10.016				30	
5.963				30	
6.365				30	

Table G.2.2. Dam Foundation Erosion Studies — DFE data.

Angle of Impingement δ (deg.)	DS Slope Angle θ (deg.)	$\cos \delta$	$\sin \theta$	$\cos \theta$
19.875	23.557	0.940	0.400	0.917
26.360	20.907	0.896	0.357	0.934
27.395	15.961	0.888	0.275	0.961
25.869	18.624	0.900	0.319	0.948
25.229	17.223	0.905	0.296	0.955
18.346	24.891	0.949	0.421	0.907
18.683	26.012	0.947	0.439	0.899
19.150	29.899	0.945	0.498	0.867

Regression ($\theta = C - C1 \delta$)

Regression Output:

Constant	46.576
Std Err of Y Est	2.430
R Squared	0.780
No. of Observations	8
Degrees of Freedom	6
X Coefficient(s)	-1.081
Std Err of Coef.	0.234

S_o : $\theta = 46.58 - 1.081 \delta$ if $\delta > 18$ deg. $\theta = 26$ deg. if $\delta < 18$ deg.

Table G.2.3. Dam Foundation Erosion Studies -- Doehring data.

Angle of Impingement δ (deg.)	DS Slope Angle θ (deg.)
48.430	26.473
56.370	18.983
62.140	17.693
49.330	24.228
55.670	22.441
47.490	27.429

Regression Output:

Constant	57.475
Std Err of Y Est	1.363
R Squared	0.904
No. of Observations	6.000
Degrees of Freedom	4.000
X Coefficient(s)	-0.650
Std Err of Coef.	0.106

S_0 : $\theta = 57.475 - 0.650 \delta$ if $\delta > 47$ deg. $\theta = 27.5$ deg. if $\delta < 47$ deg.

Table G.3. Dam Foundation Erosion Studies -- statistical properties of angle of downstream slope versus angle of impingement.

Angle of Impingement δ (deg.)	DFE - Rectangular Jet θ (deg.)
11.636	26.565
11.887	24.513
11.438	24.560
12.064	26.243
19.875	23.557
19.150	29.899
26.360	20.907
27.395	15.961
25.869	18.624
25.229	17.223
18.346	24.891
18.683	26.012

Values for DS Slope (deg.)	
Mean	23.246
SD	4.023
α	0.05
t _{0.05,11}	1.7959
-t _{0.05,11}	-1.7959

DS Slope θ (deg.)	t	Pass
26.565	2.857	NO
24.513	1.091	Yes
24.560	1.131	Yes
26.243	2.580	NO
23.557	0.268	Yes
29.899	5.728	NO
20.907	-2.014	NO
15.961	-6.273	NO
18.624	-3.980	NO
17.223	-5.186	NO
24.891	1.416	Yes
26.012	2.382	NO

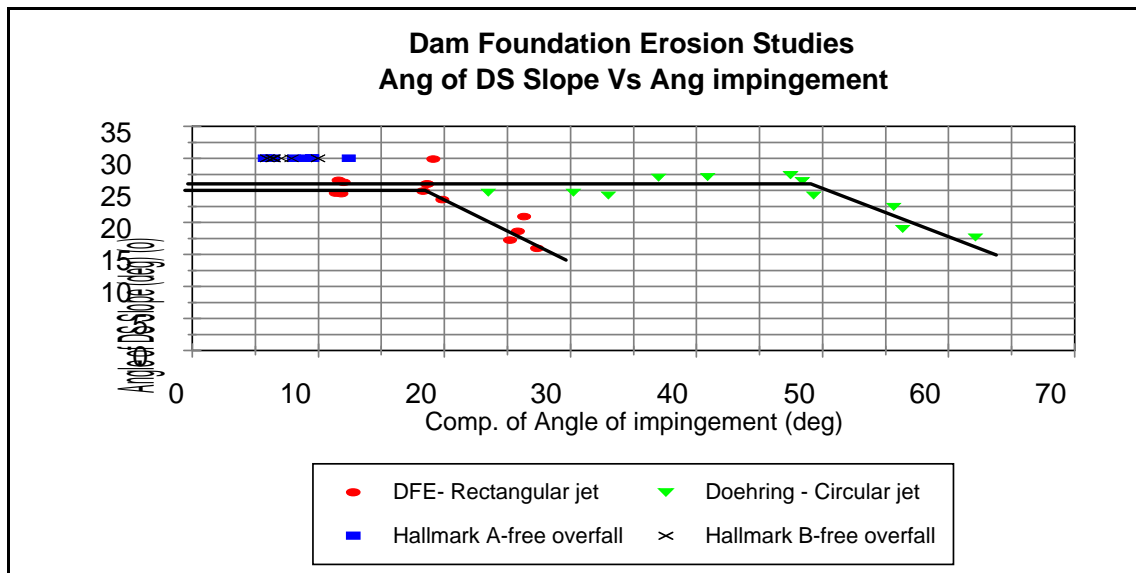


Figure G.2. Dam Foundation Erosion Studies -- angle of downstream slope versus angle of impingement plot.

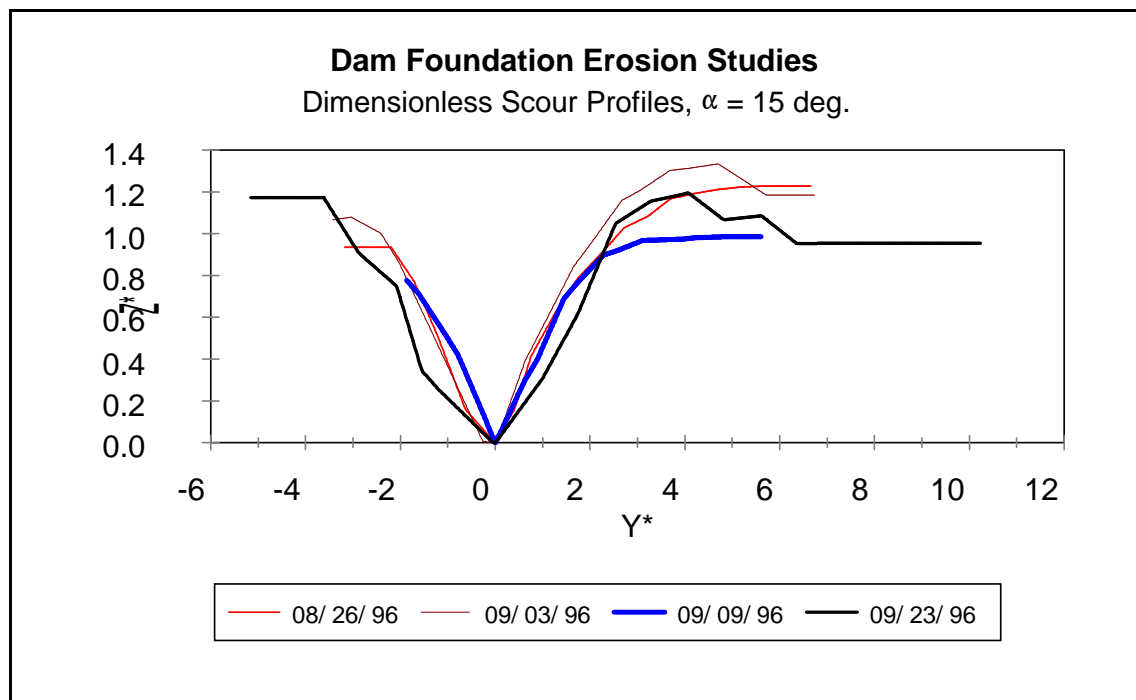


Figure G.3. Dam Foundation Erosion Studies - - dimensionless scour profiles, $\alpha = 15^\circ$.

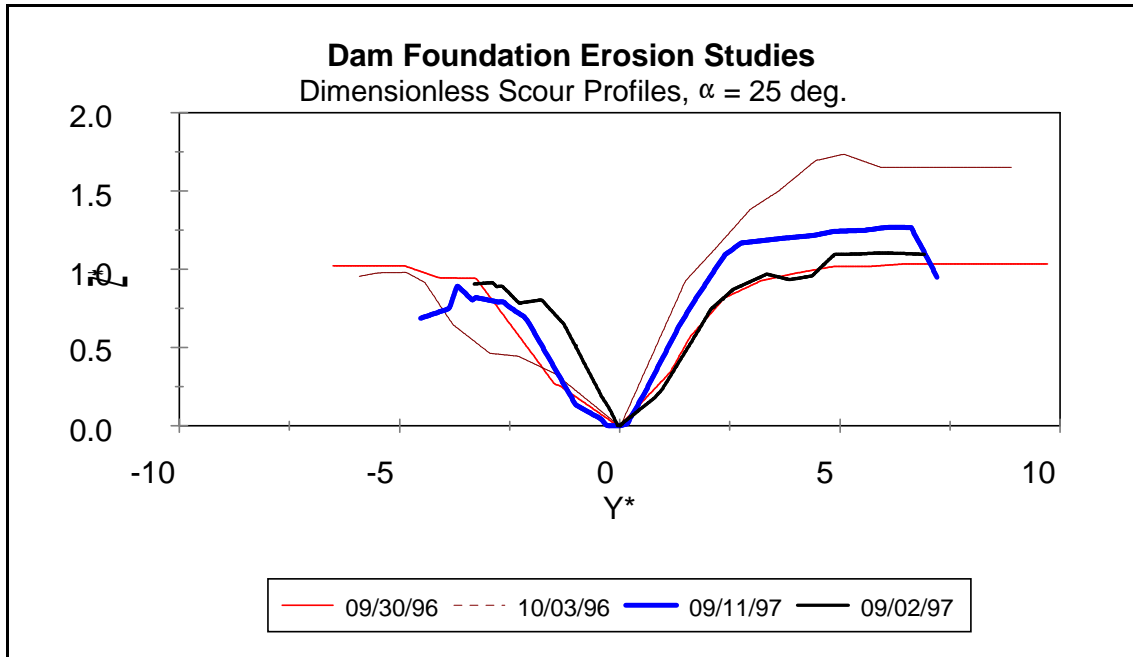


Figure G.4. Dam Foundation Erosion Studies - - dimensionless scour profiles, $\alpha = 25^\circ$.

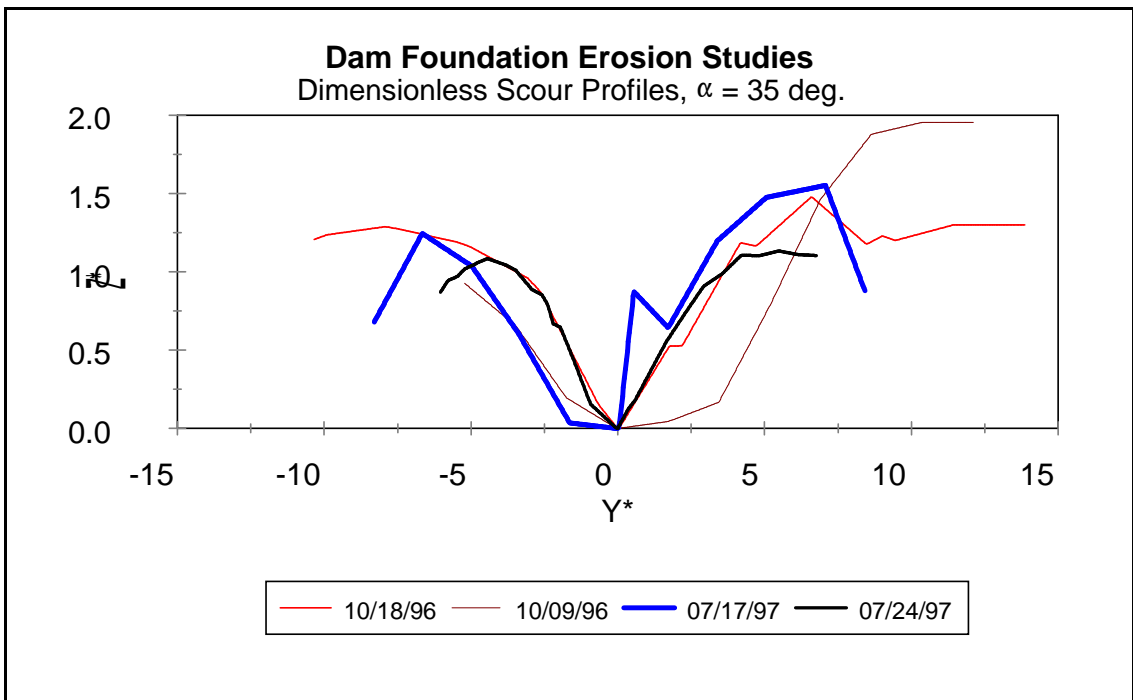


Figure G.5. Dam Foundation Erosion Studies - - dimensionless scour profiles, $\alpha = 35^\circ$.

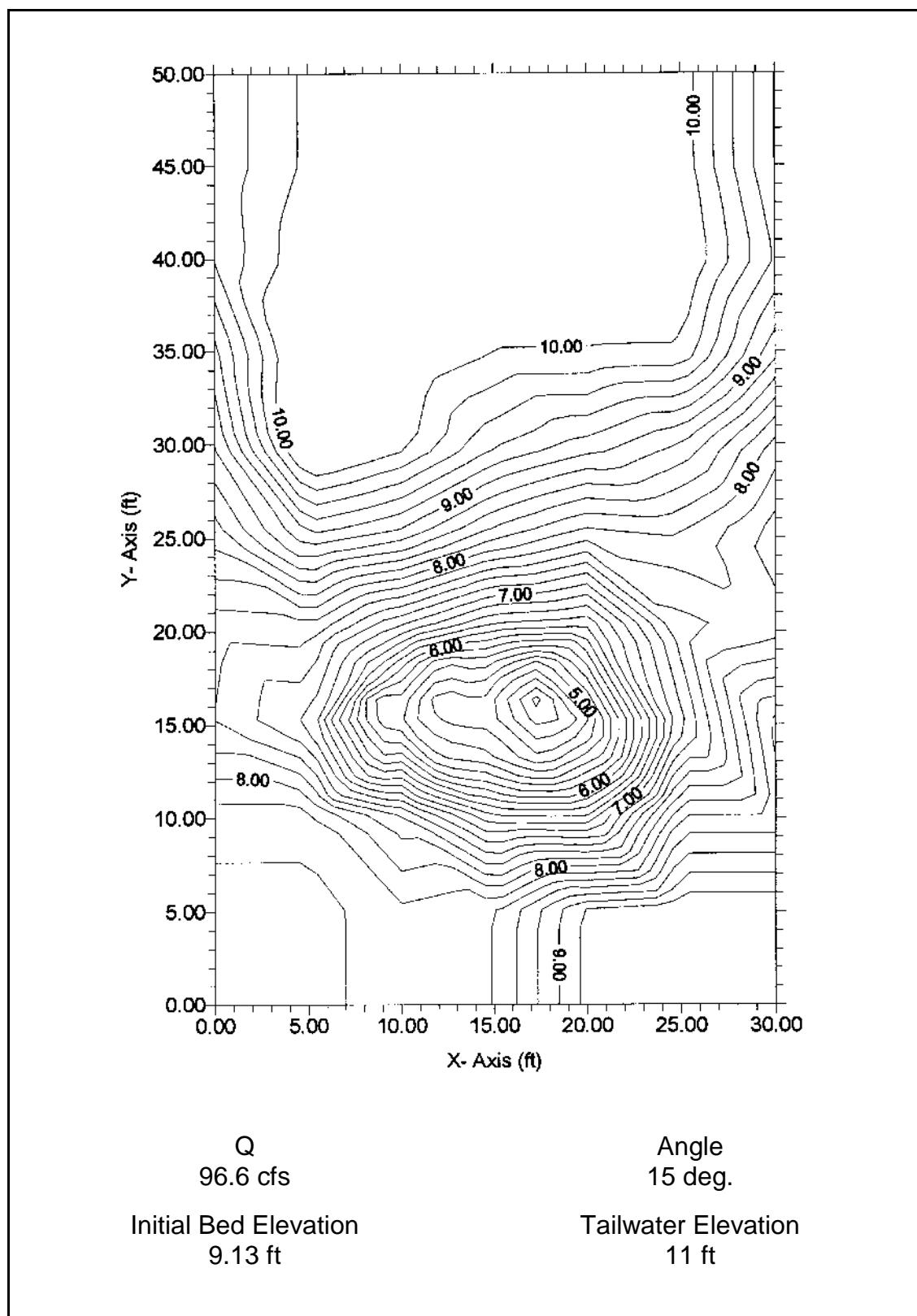


Figure G.6. Dam Foundation Erosion Studies -- contour map of scour hole for test conducted on August 26, 1996.

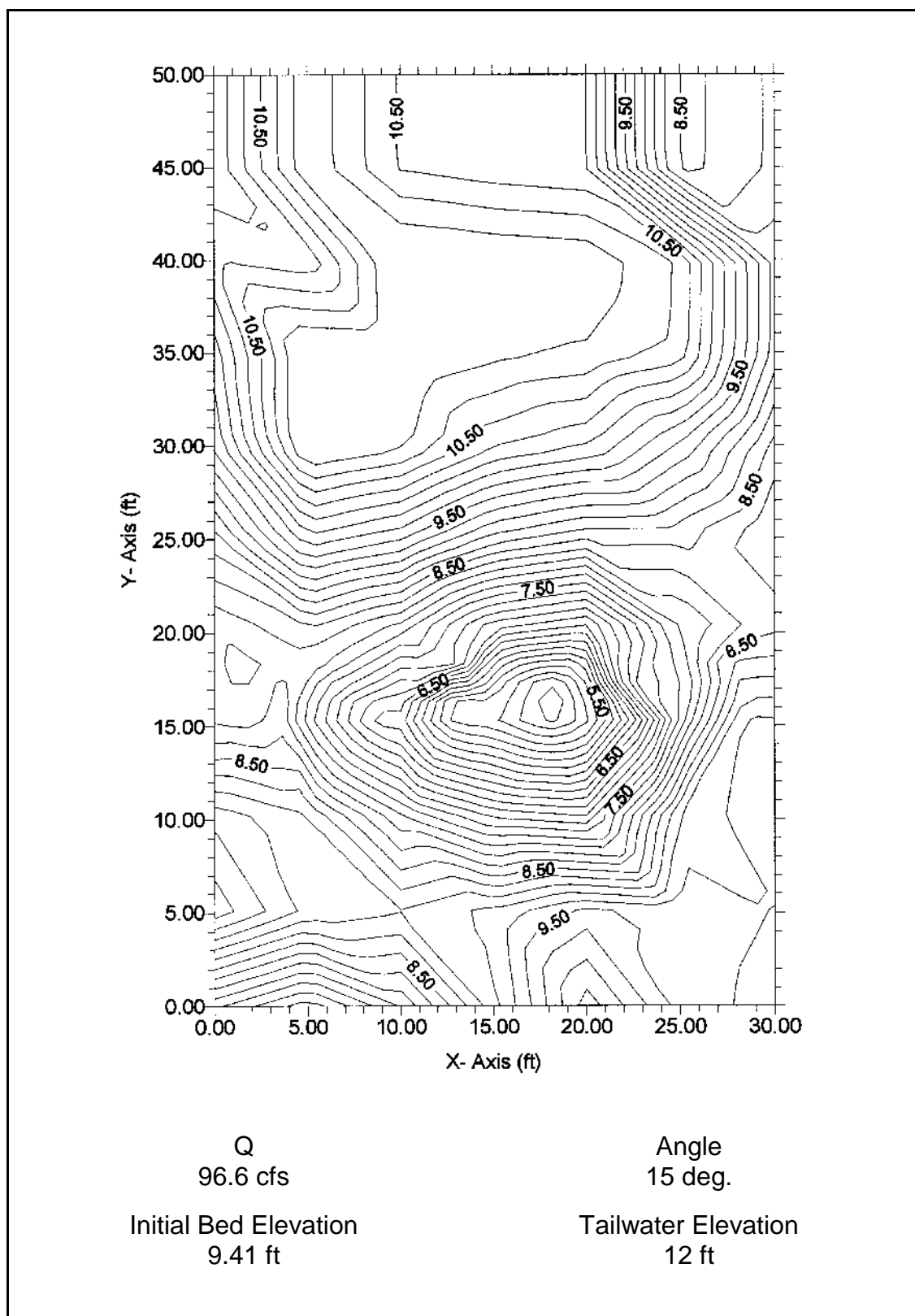


Figure G.7. Dam Foundation Erosion Studies -- contour map of scour hole for test conducted on September 3, 1996.

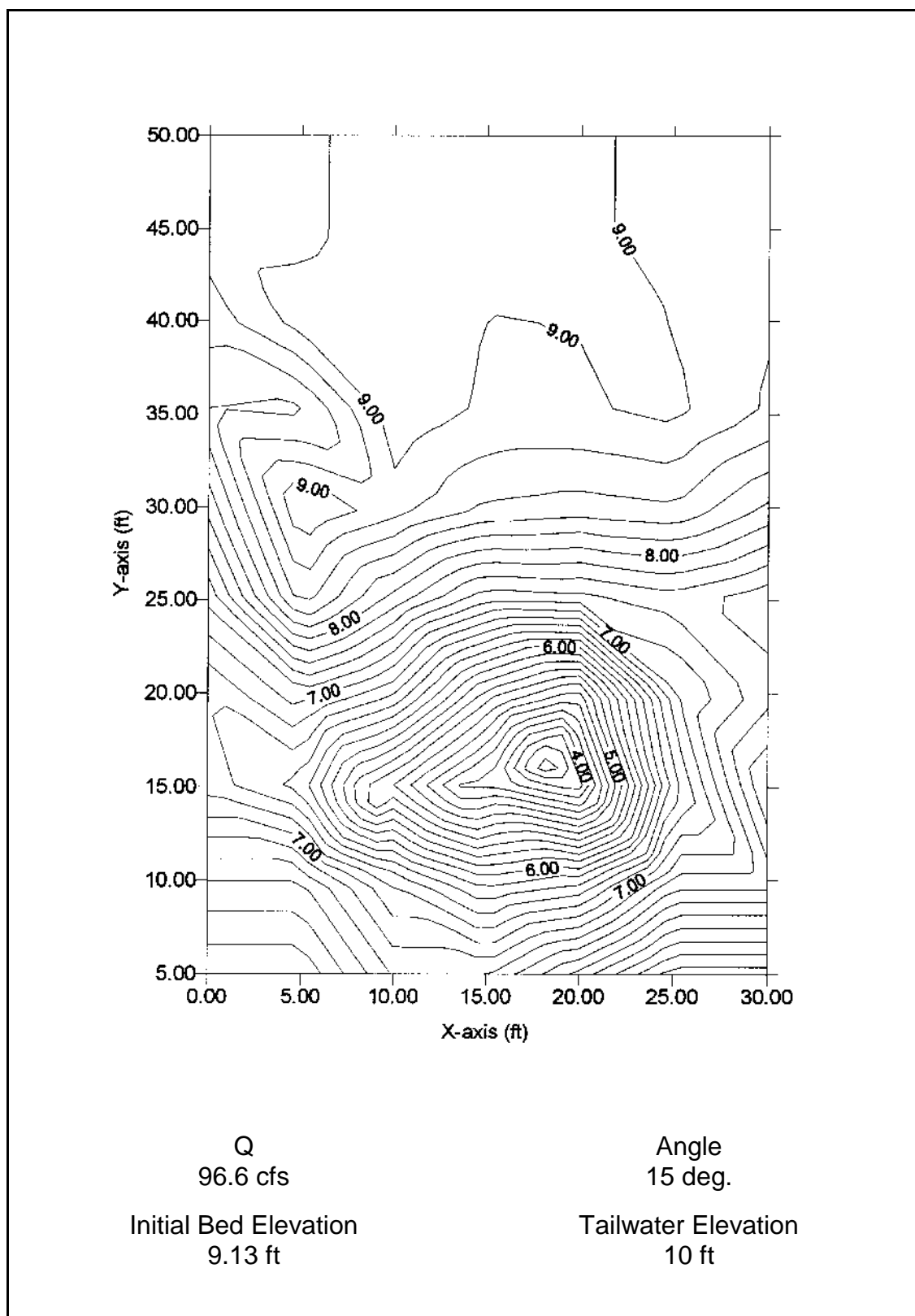


Figure G.8. Dam Foundation Erosion Studies -- contour map of scour hole for test conducted on September 9, 1996.

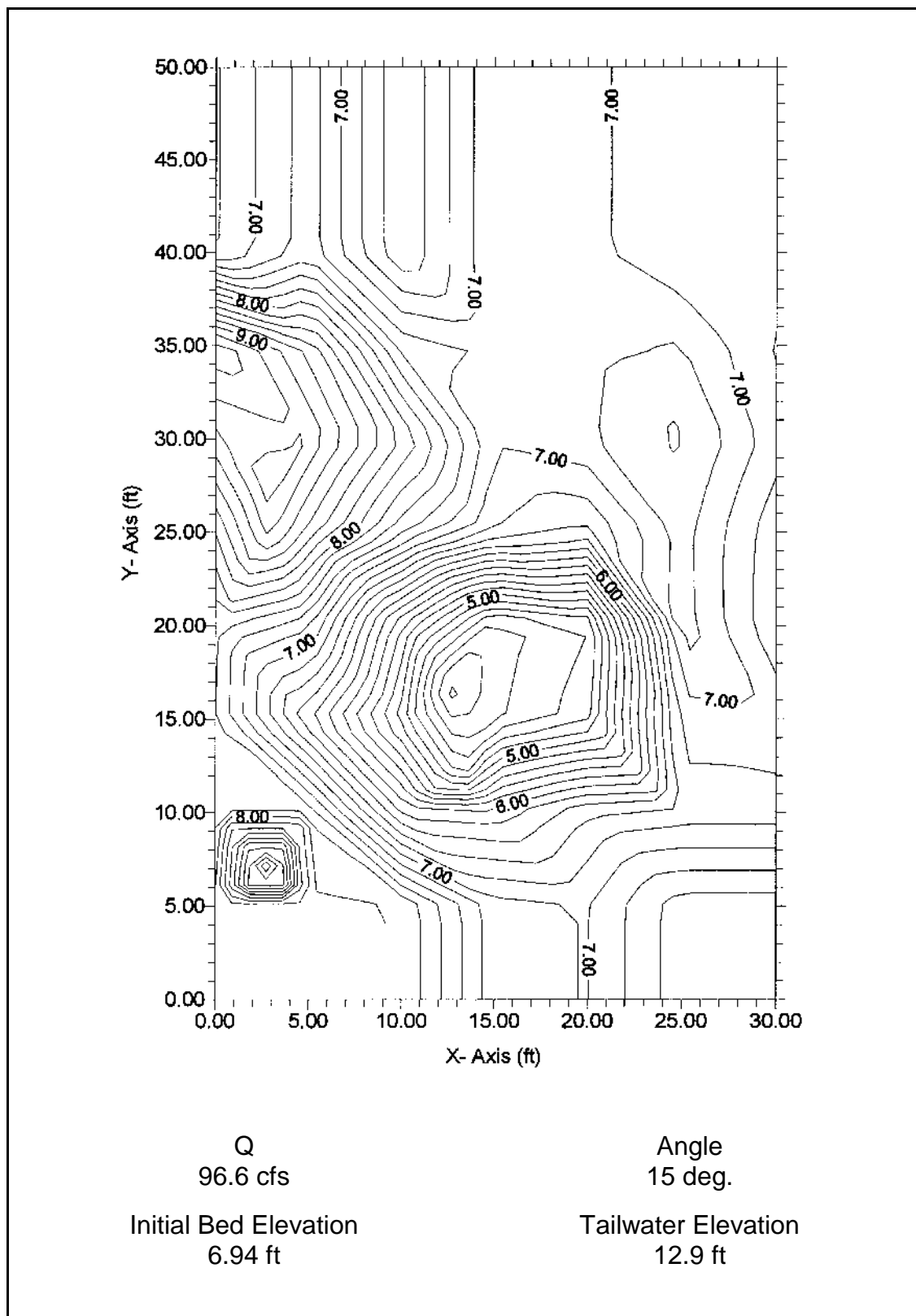


Figure G.9. Dam Foundation Erosion Studies -- contour map of scour hole for test conducted on September 23, 1996.

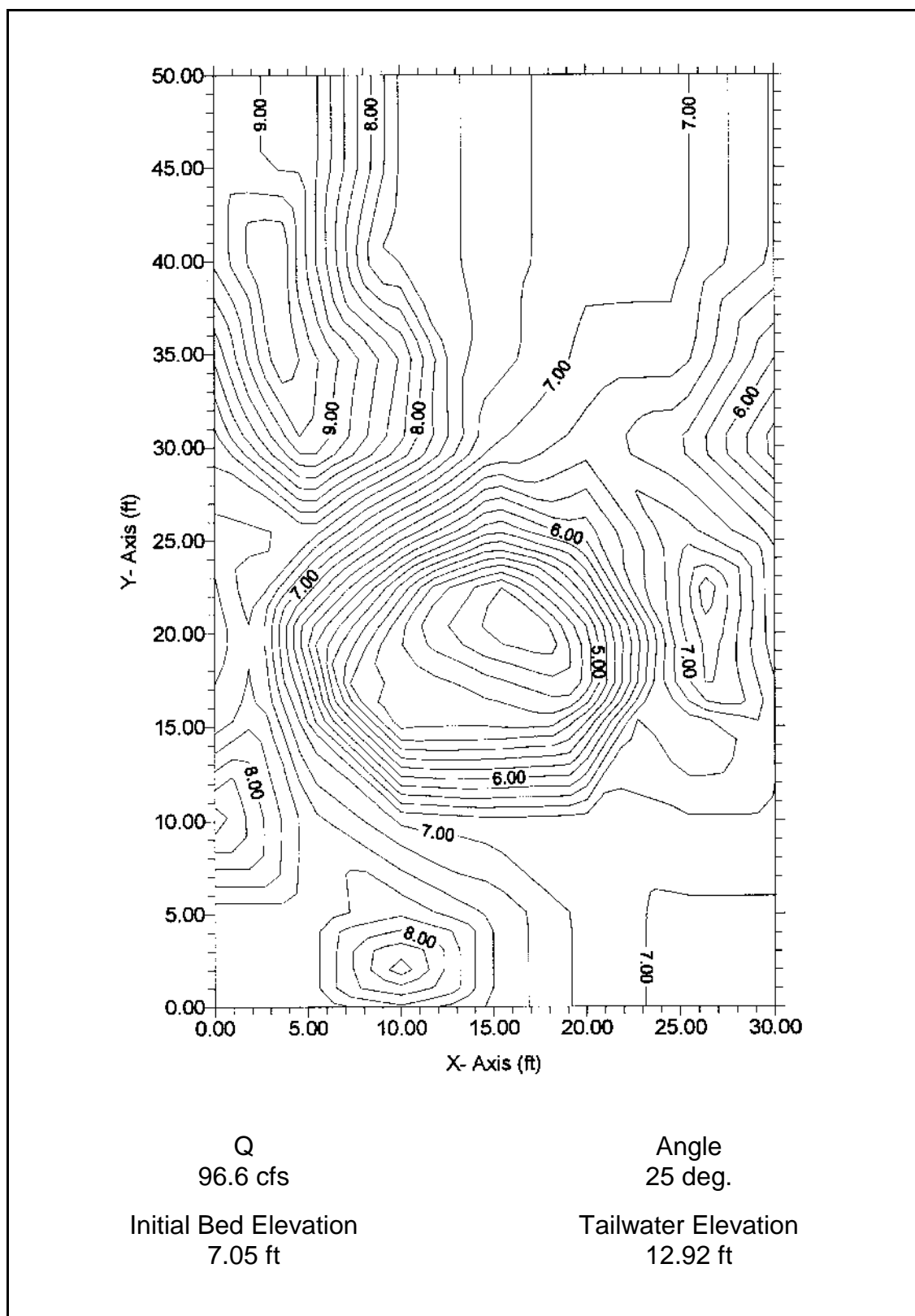


Figure G.10. Dam Foundation Erosion Studies -- contour map of scour hole for test conducted on September 30, 1996.

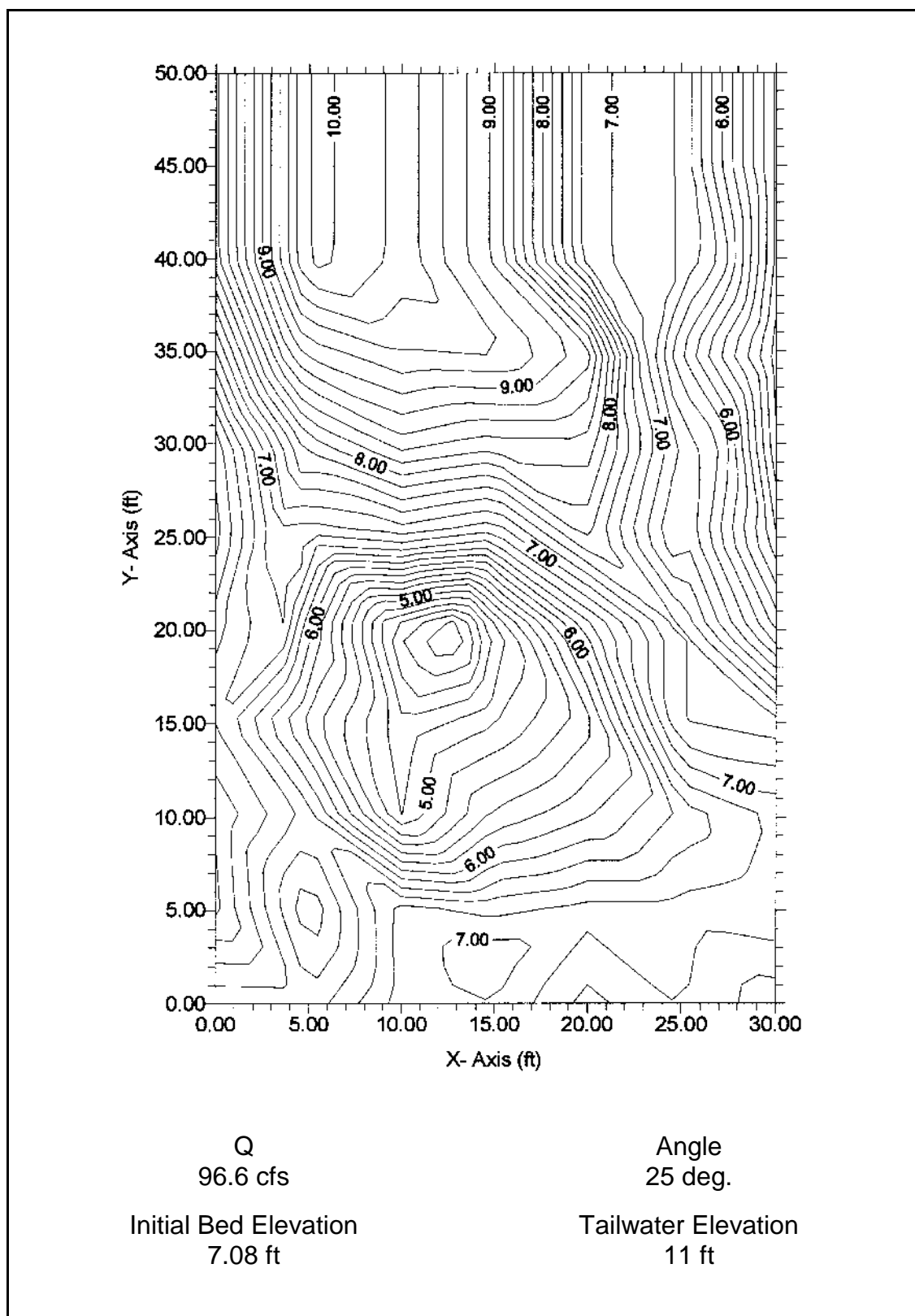


Figure G.11. Dam Foundation Erosion Studies -- contour map of scour hole for test conducted on October 3, 1996.

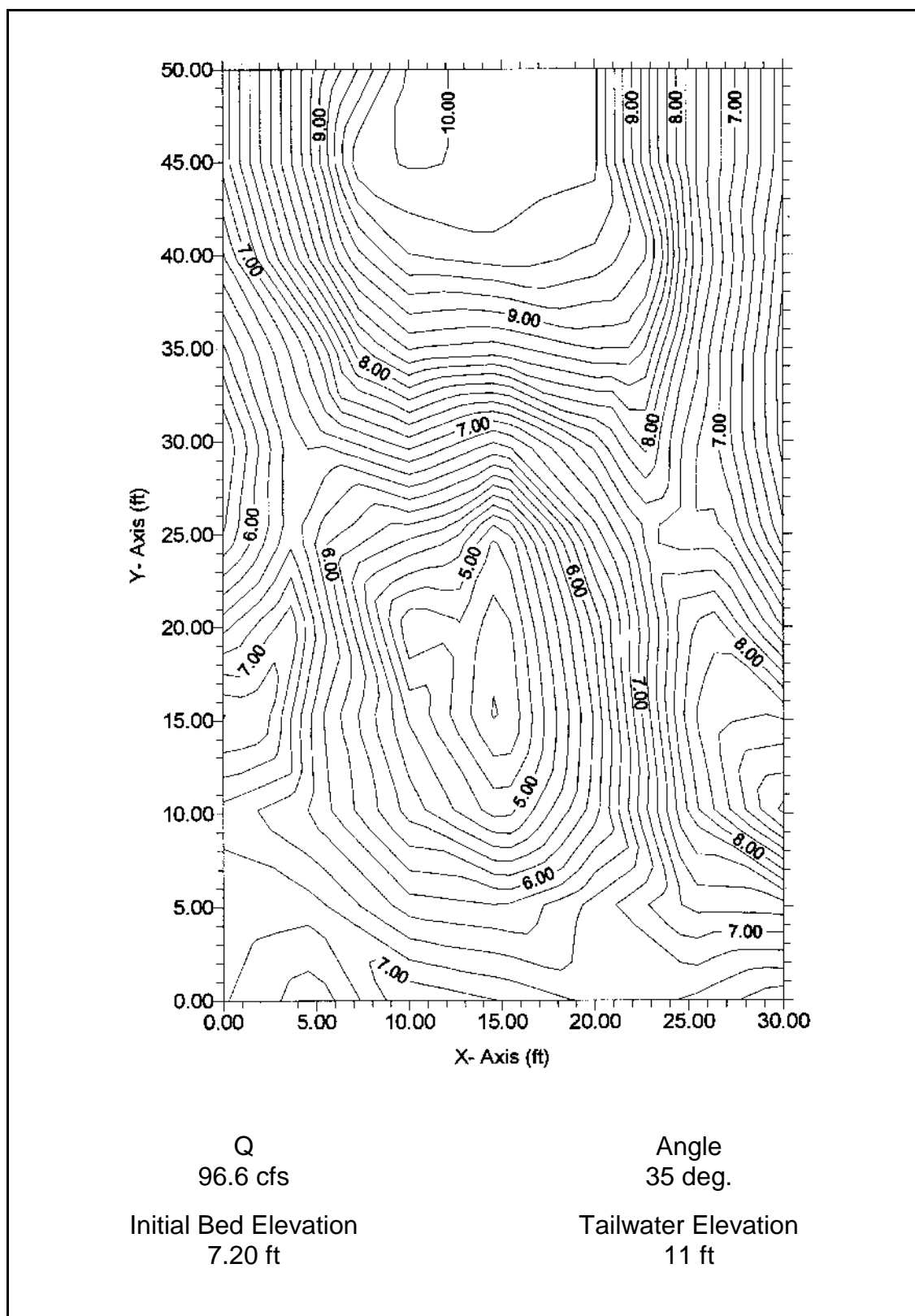


Figure G.12. Dam Foundation Erosion Studies -- contour map of scour hole for test conducted on October 9, 1996.

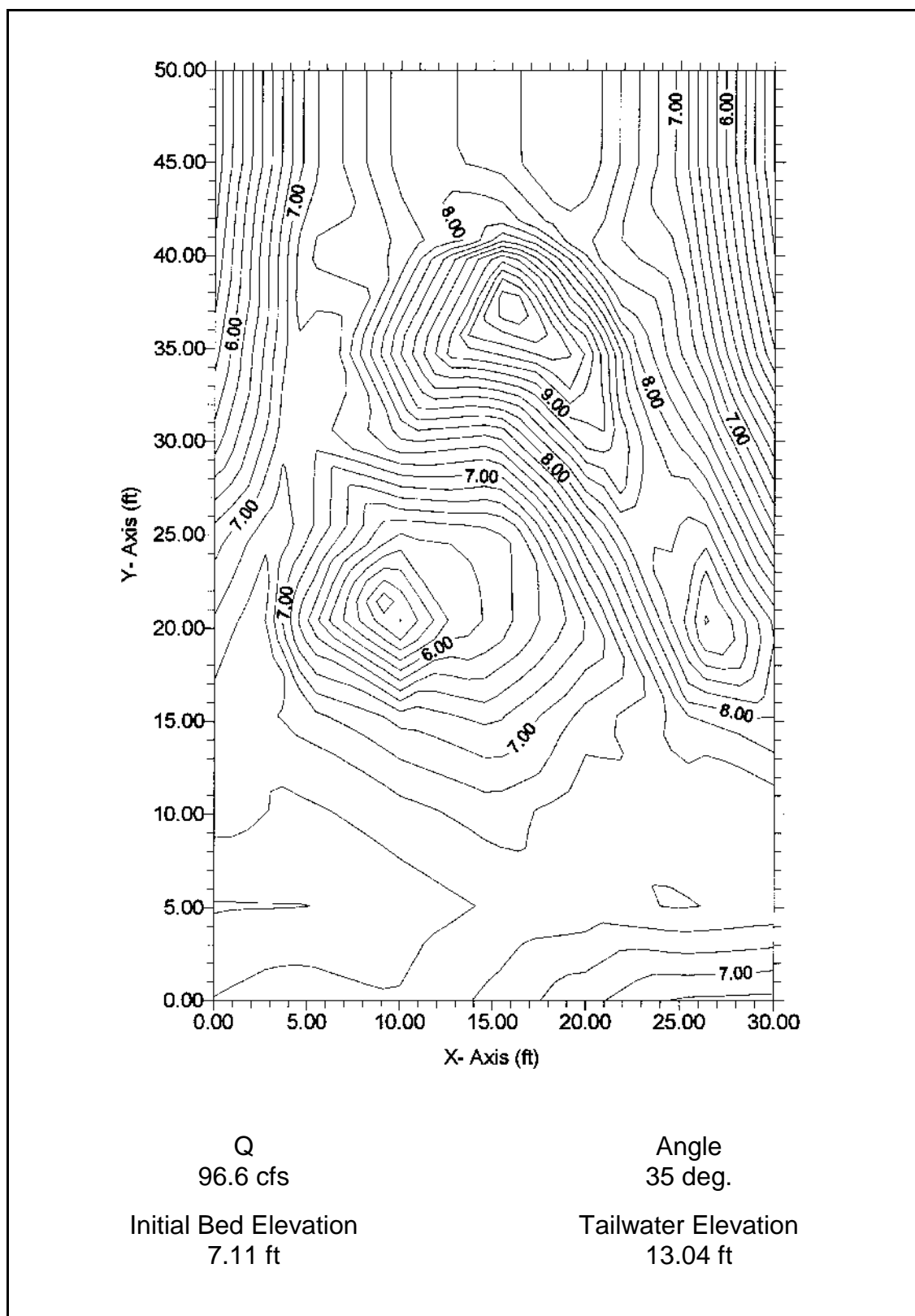


Figure G.13. Dam Foundation Erosion Studies -- contour map of scour hole for test conducted on October 18, 1996.

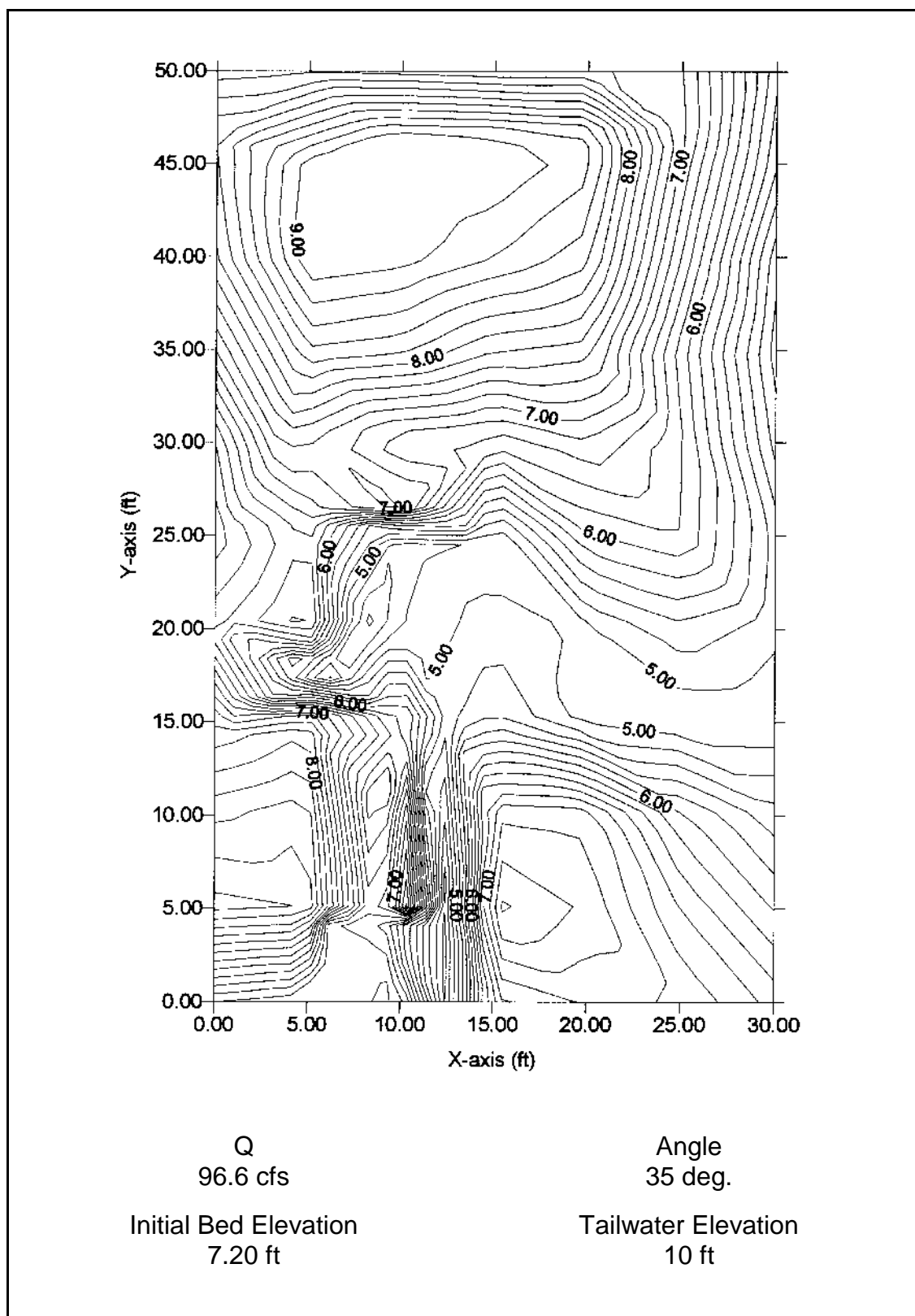


Figure G.14. Dam Foundation Erosion Studies -- contour map of scour hole for test conducted on July 16, 1997.

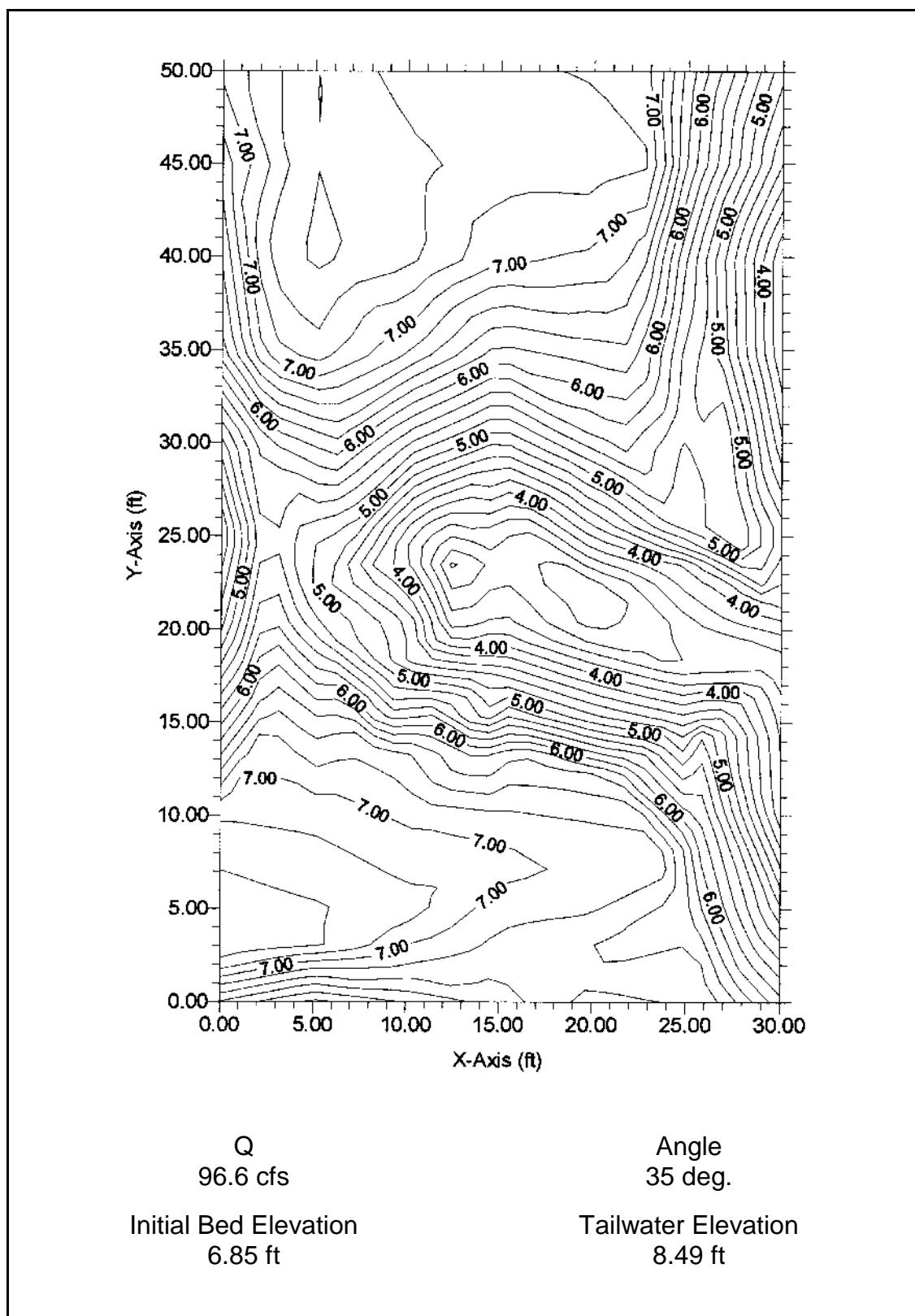


Figure G.15. Dam Foundation Erosion Studies -- contour map of scour hole for test conducted on July 23, 1997.

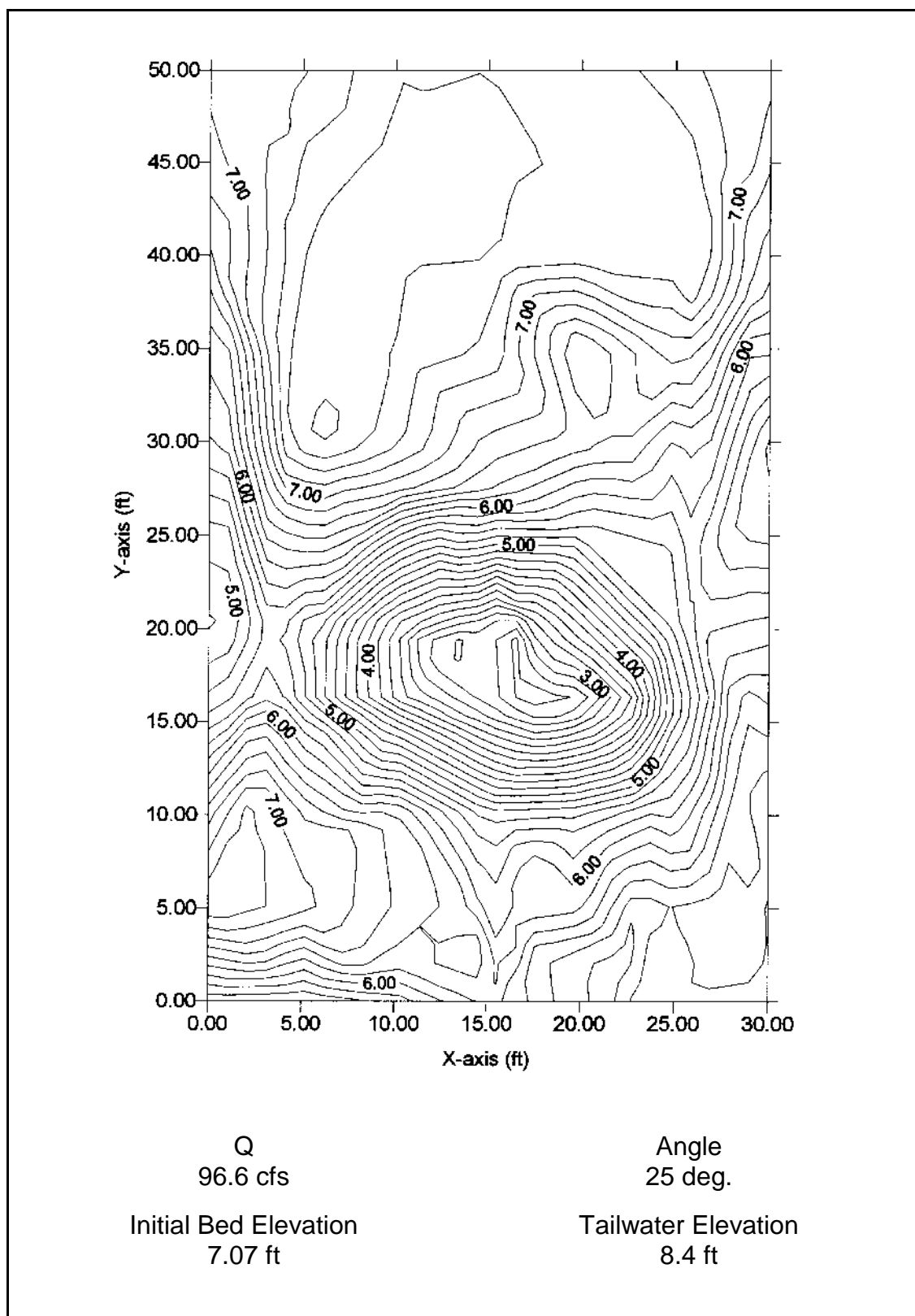


Figure G.16. Dam Foundation Erosion Studies -- contour map of scour hole for test conducted on September 2, 1997

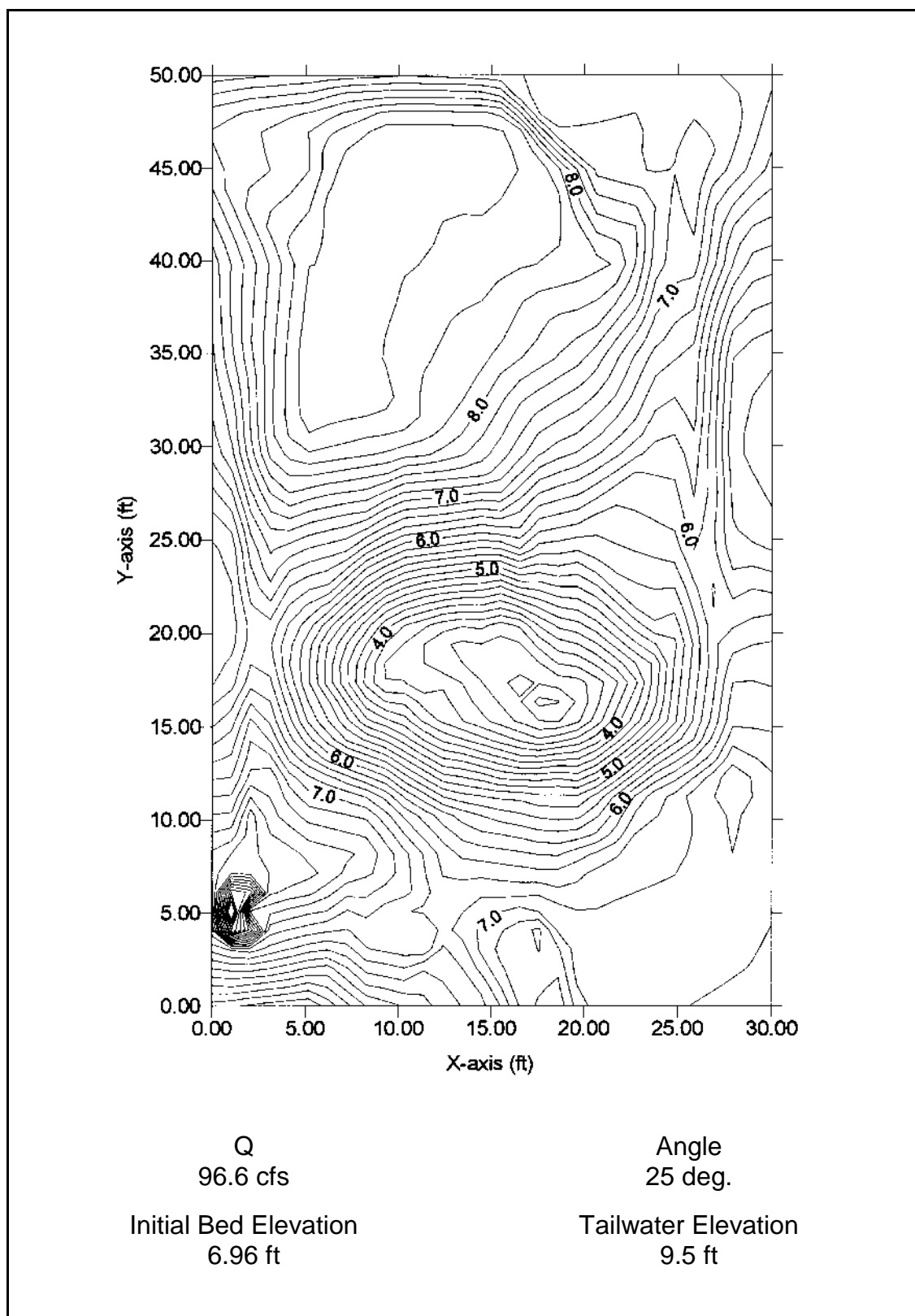


Figure G.17. Dam Foundation Erosion Studies -- contour map of scour hole for test conducted on September 11, 1997.

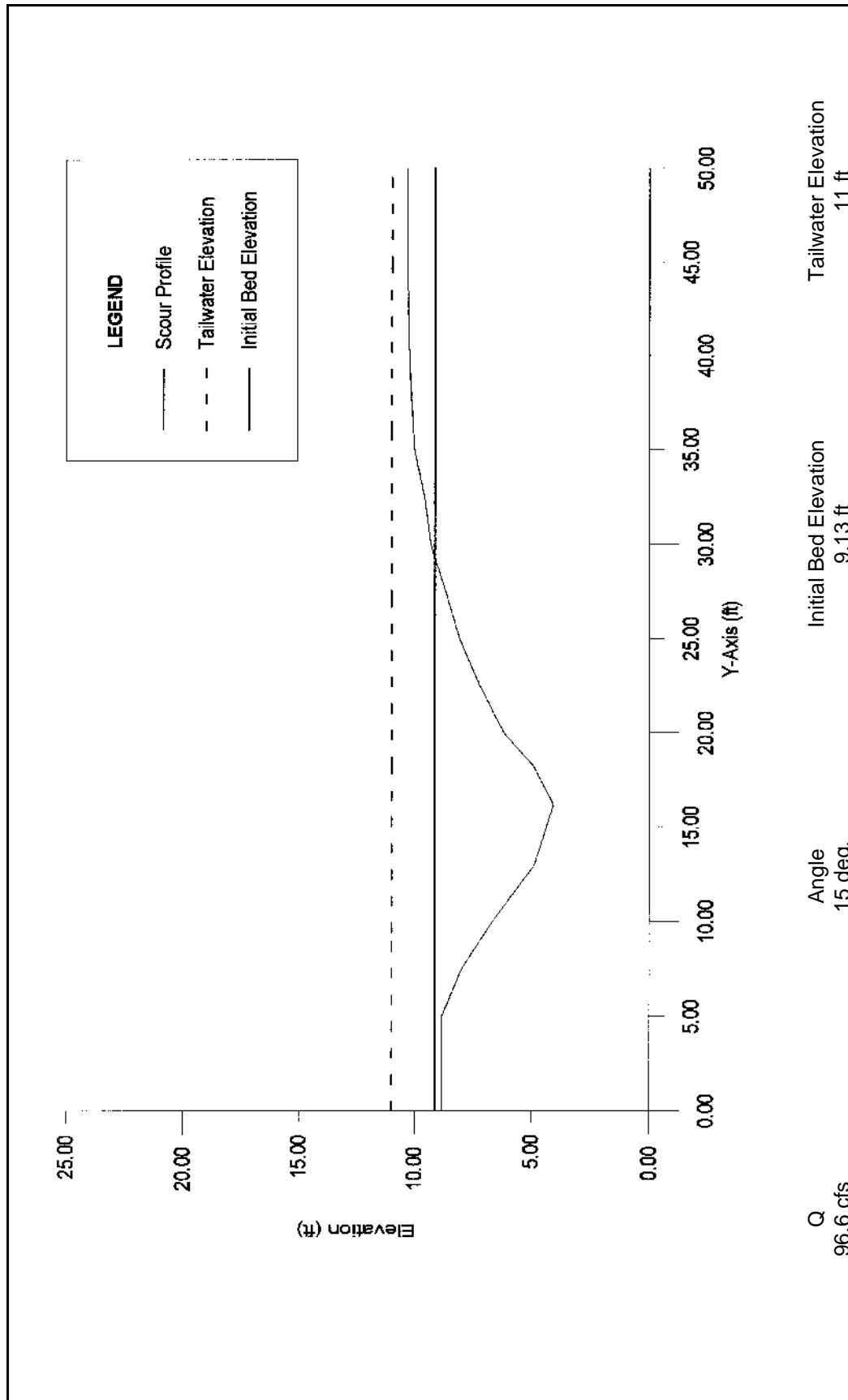


Figure G.18. Dam Foundation Erosion Studies -- longitudinal profile of scour hole for test conducted on August 26, 1996.

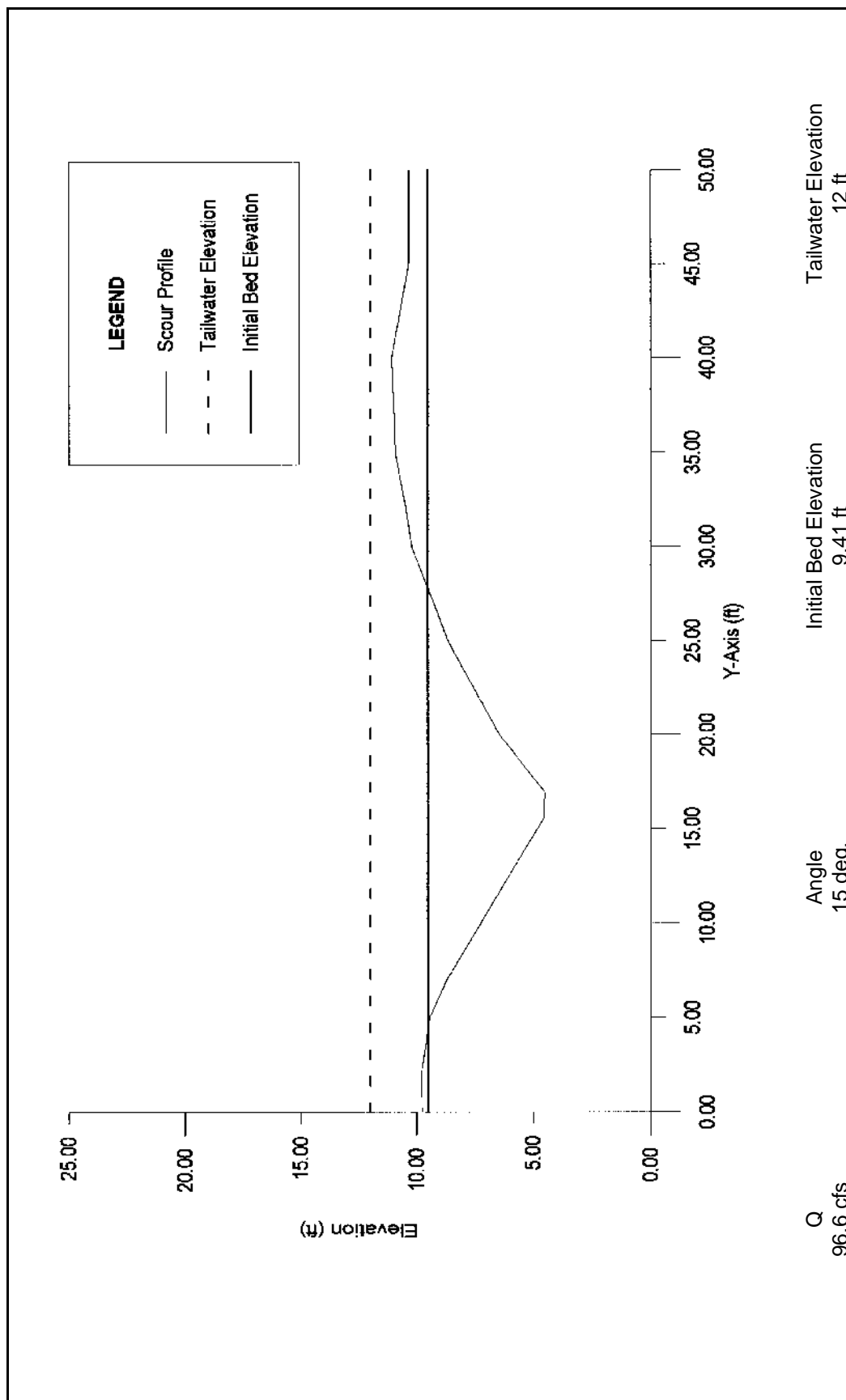


Figure G.19. Dam Foundation Erosion Studies -- longitudinal profile of scour hole for test conducted on September 3, 1996.

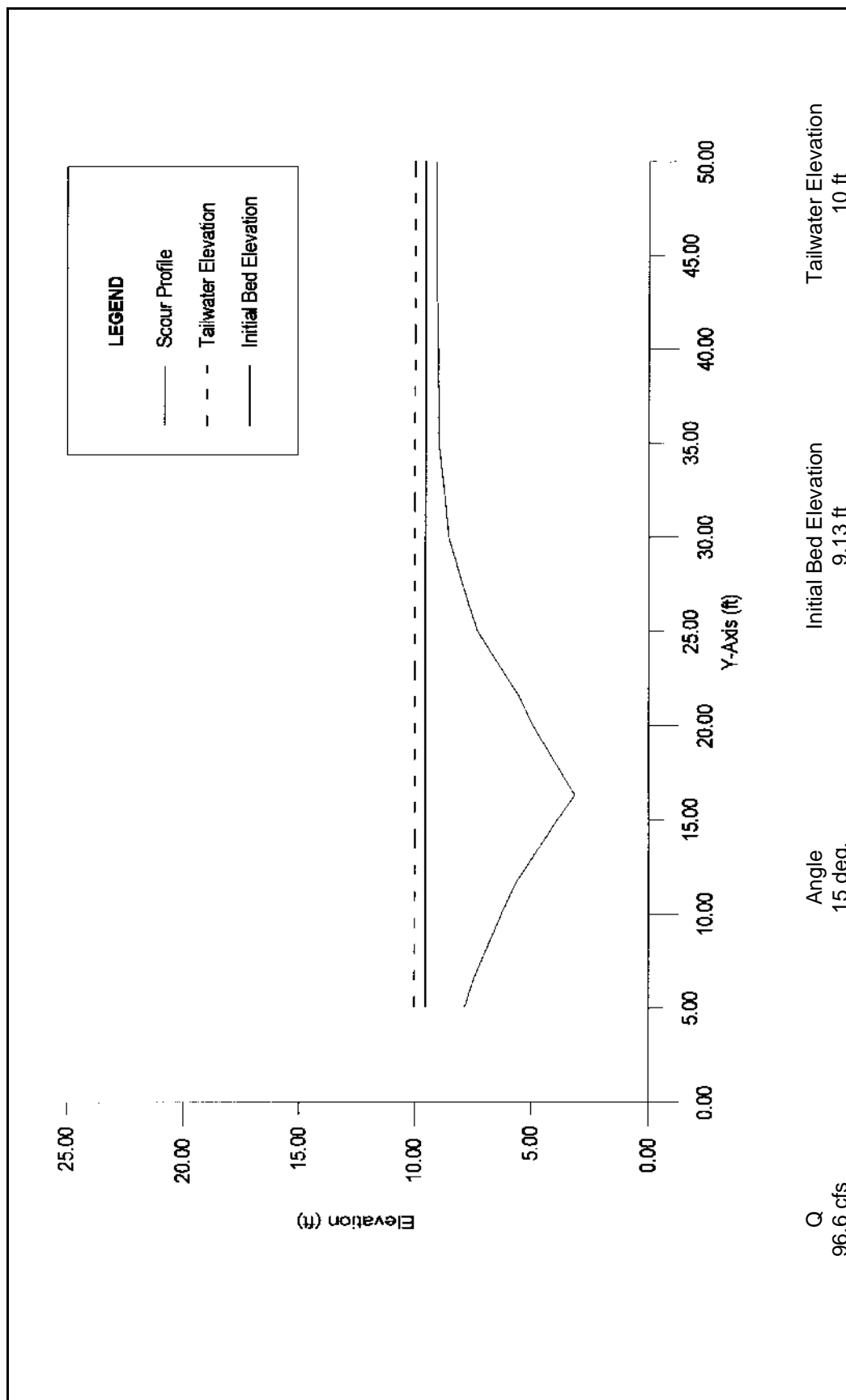


Figure G.20. Dam Foundation Erosion Studies -- longitudinal profile of scour hole for test conducted on September 9, 1996.

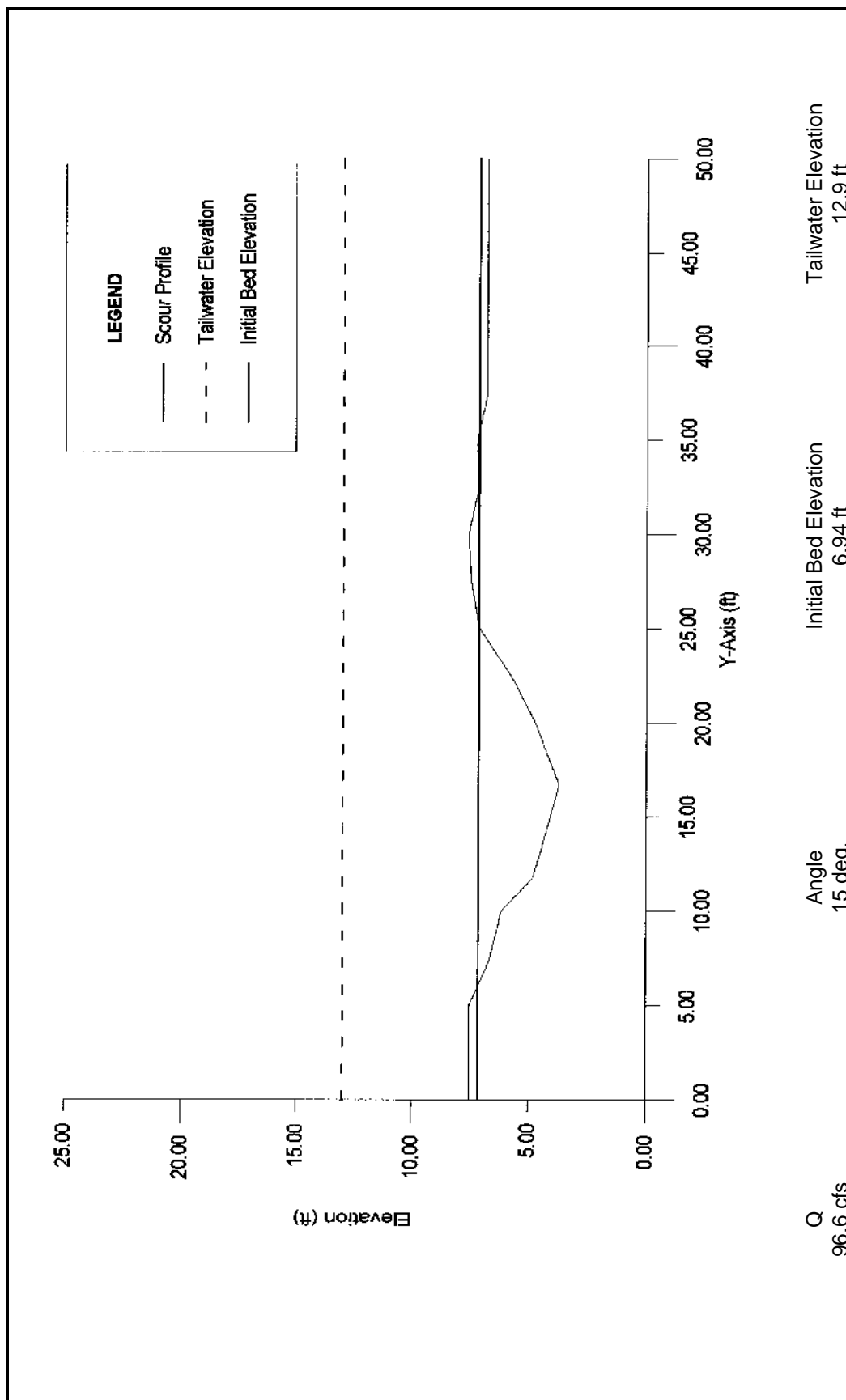


Figure G.21. Dam Foundation Erosion Studies -- longitudinal profile of scour hole for test conducted on September 23, 1996.

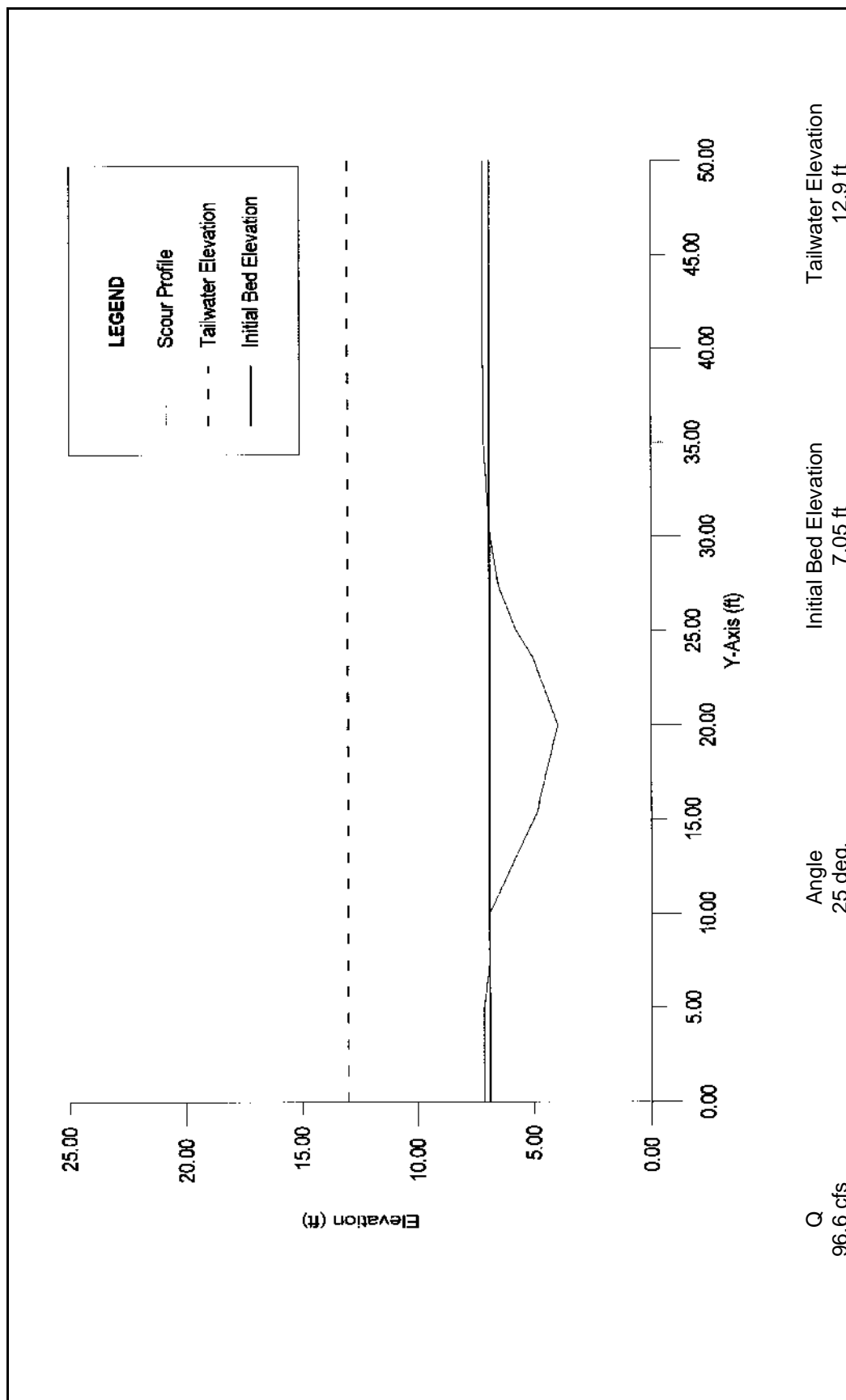


Figure G.22. Dam Foundation Erosion Studies -- Longitudinal profile of scour hole for test conducted on September 30, 1996.

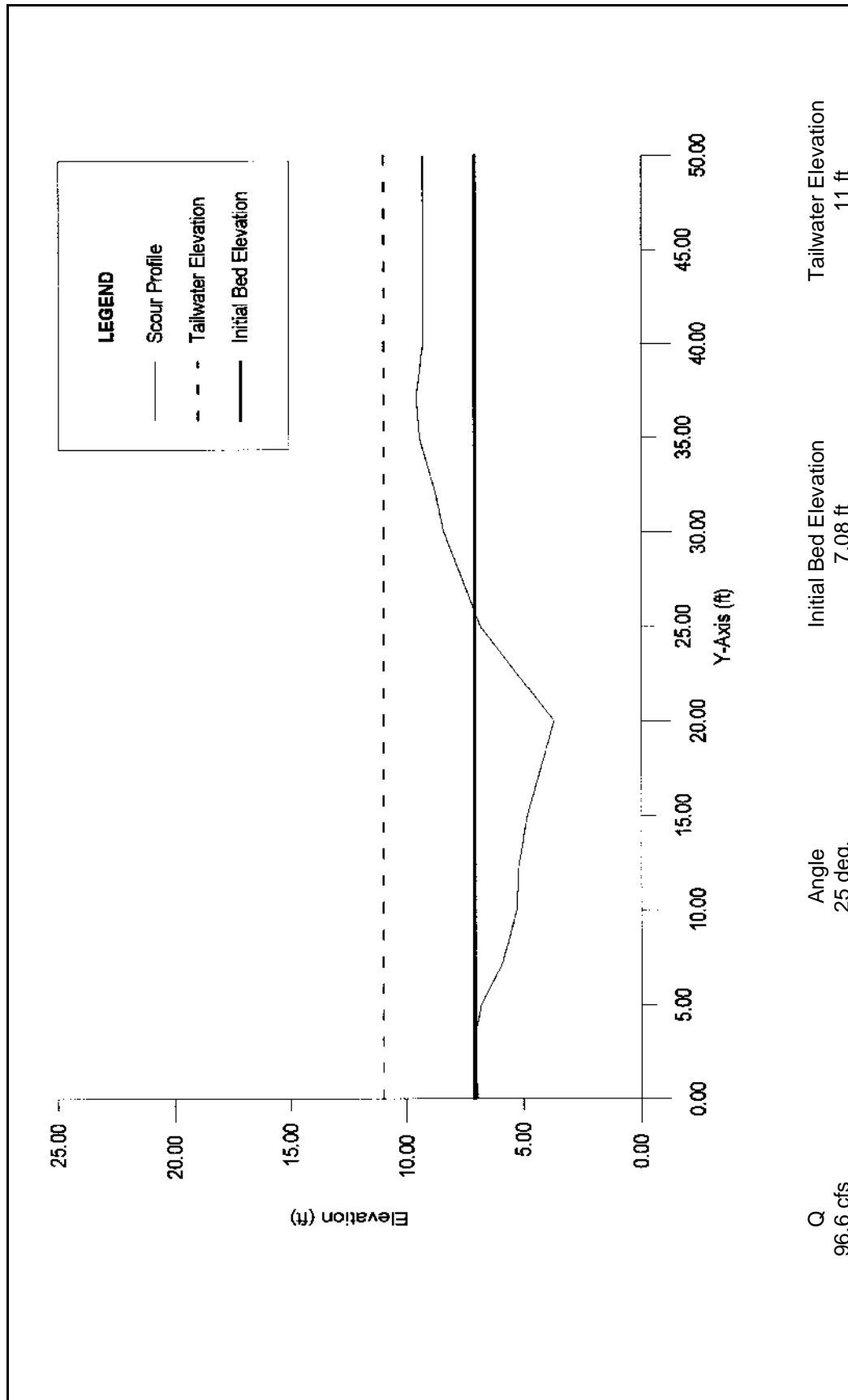


Figure G.23. Dam Foundation Erosion Studies -- longitudinal profile of scour hole for test conducted on October 3, 1996.

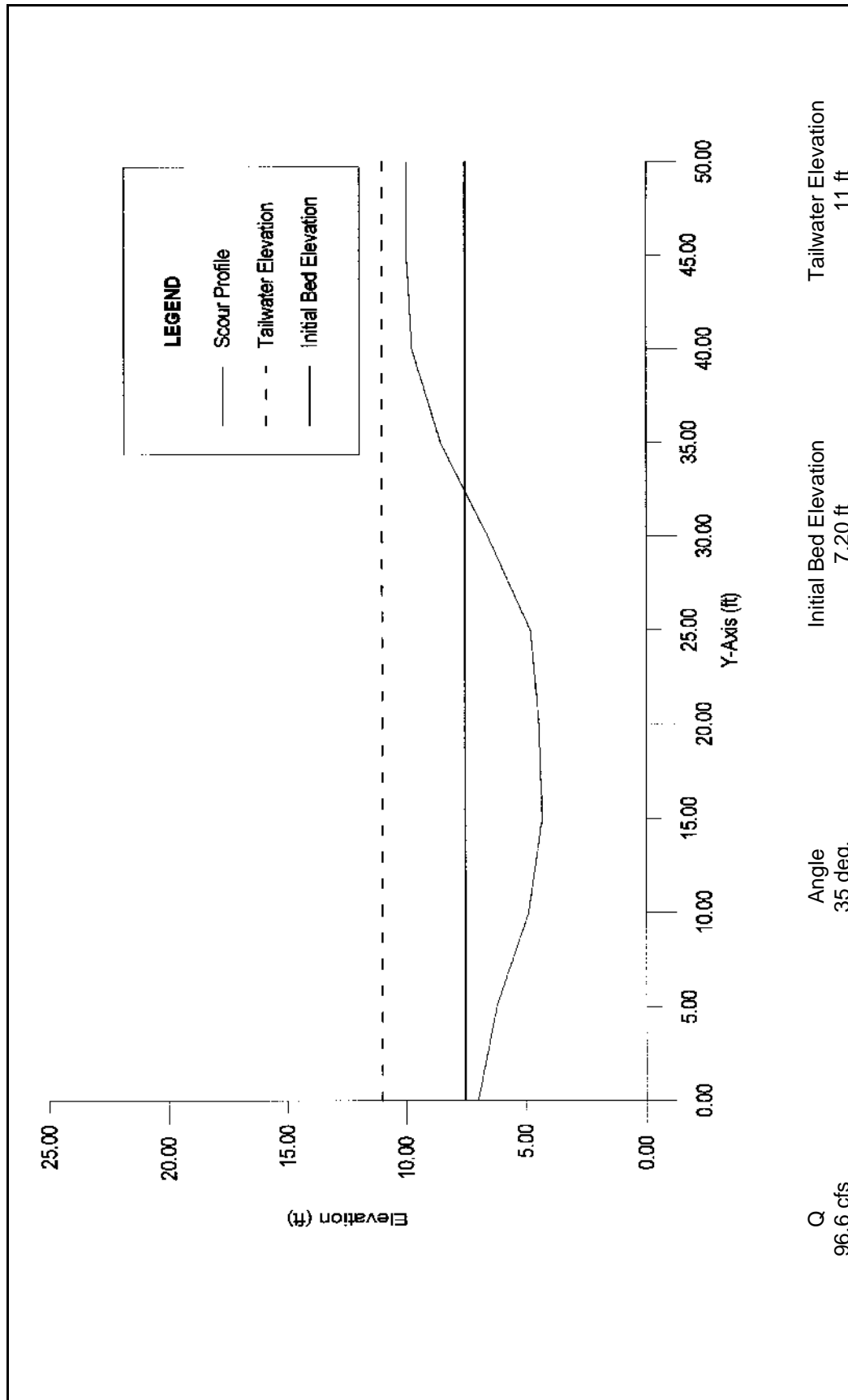


Figure G.24. Dam Foundation Erosion Studies -- longitudinal profile of scour hole for test conducted on October 9, 1996.

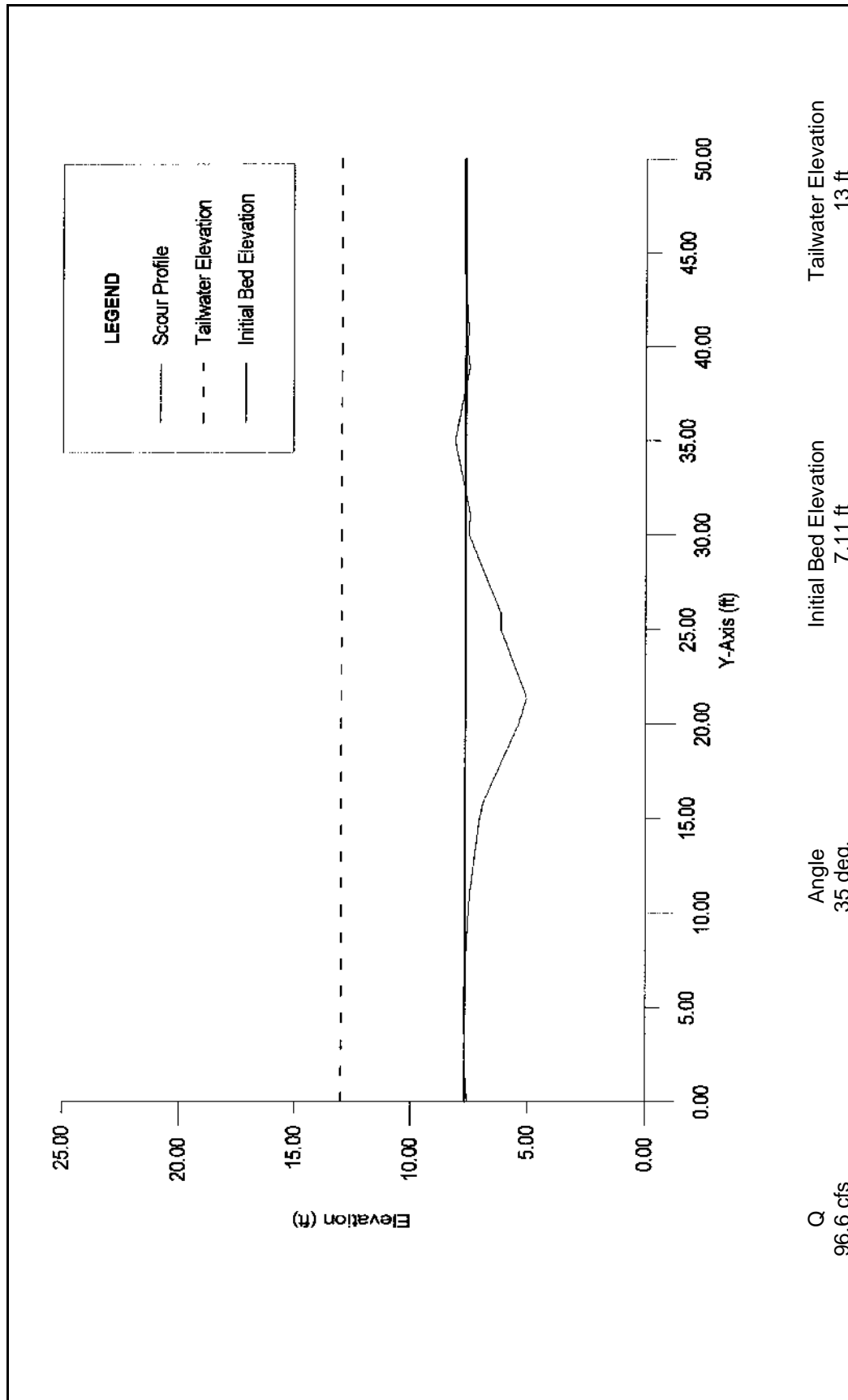


Figure G.25. Dam Foundation Erosion Studies -- longitudinal profile of scour hole for test conducted on October 18, 1996.

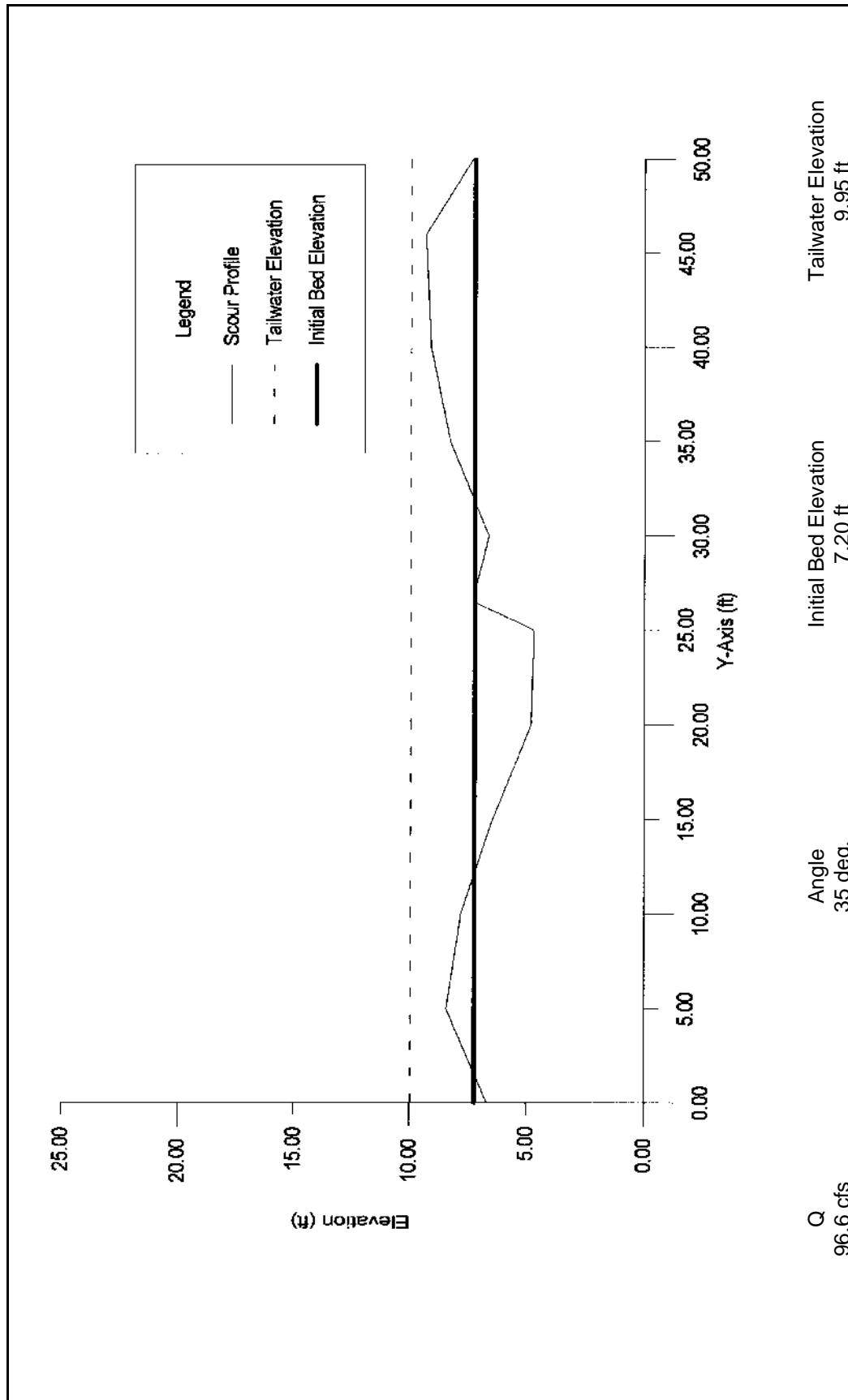


Figure G.26. Dam Foundation Erosion Studies -- longitudinal profile of scour hole for test conducted on July 16, 1997.

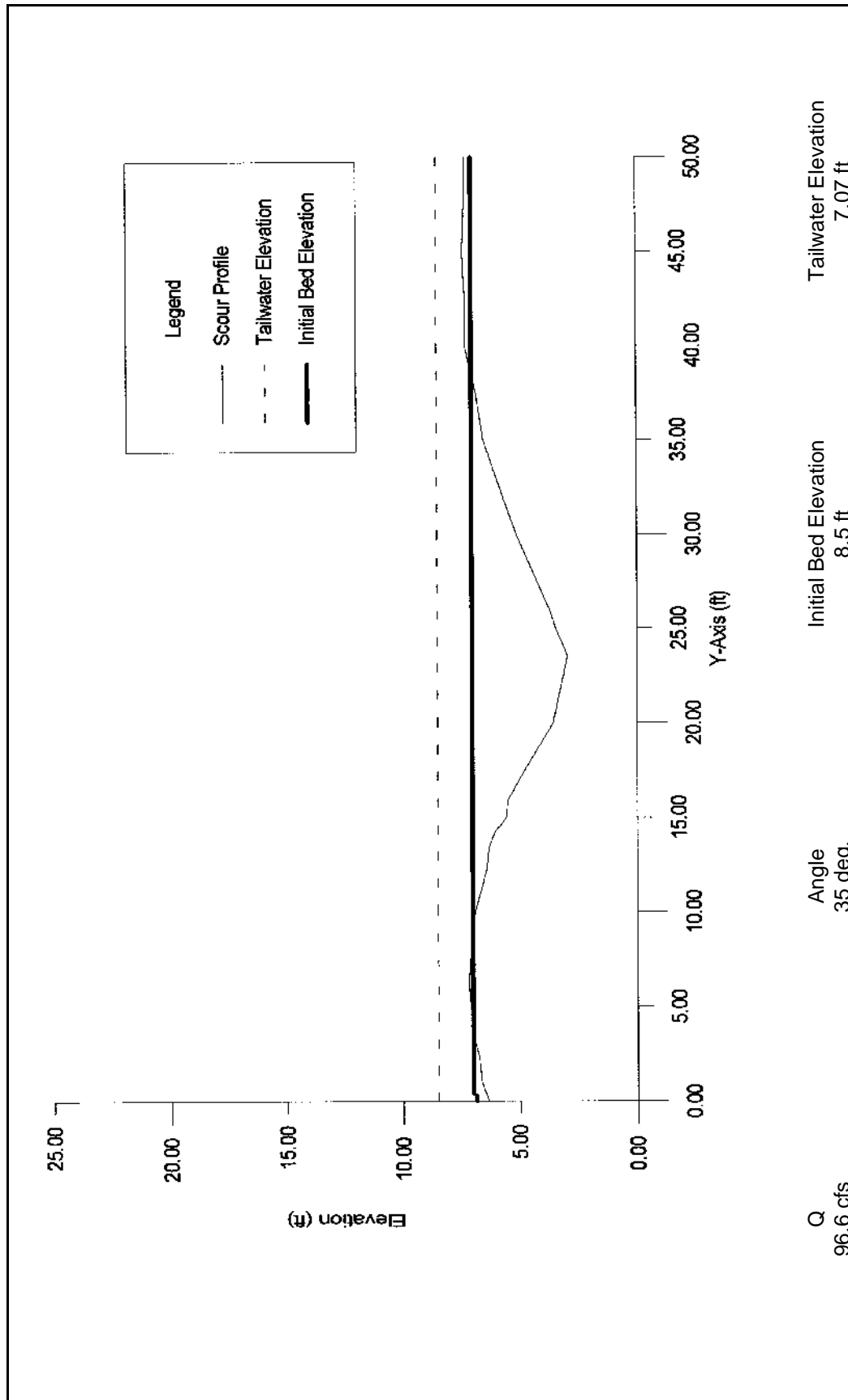


Figure G.27. Dam Foundation Erosion Studies -- longitudinal profile of scour hole for test conducted on July 23, 1997.

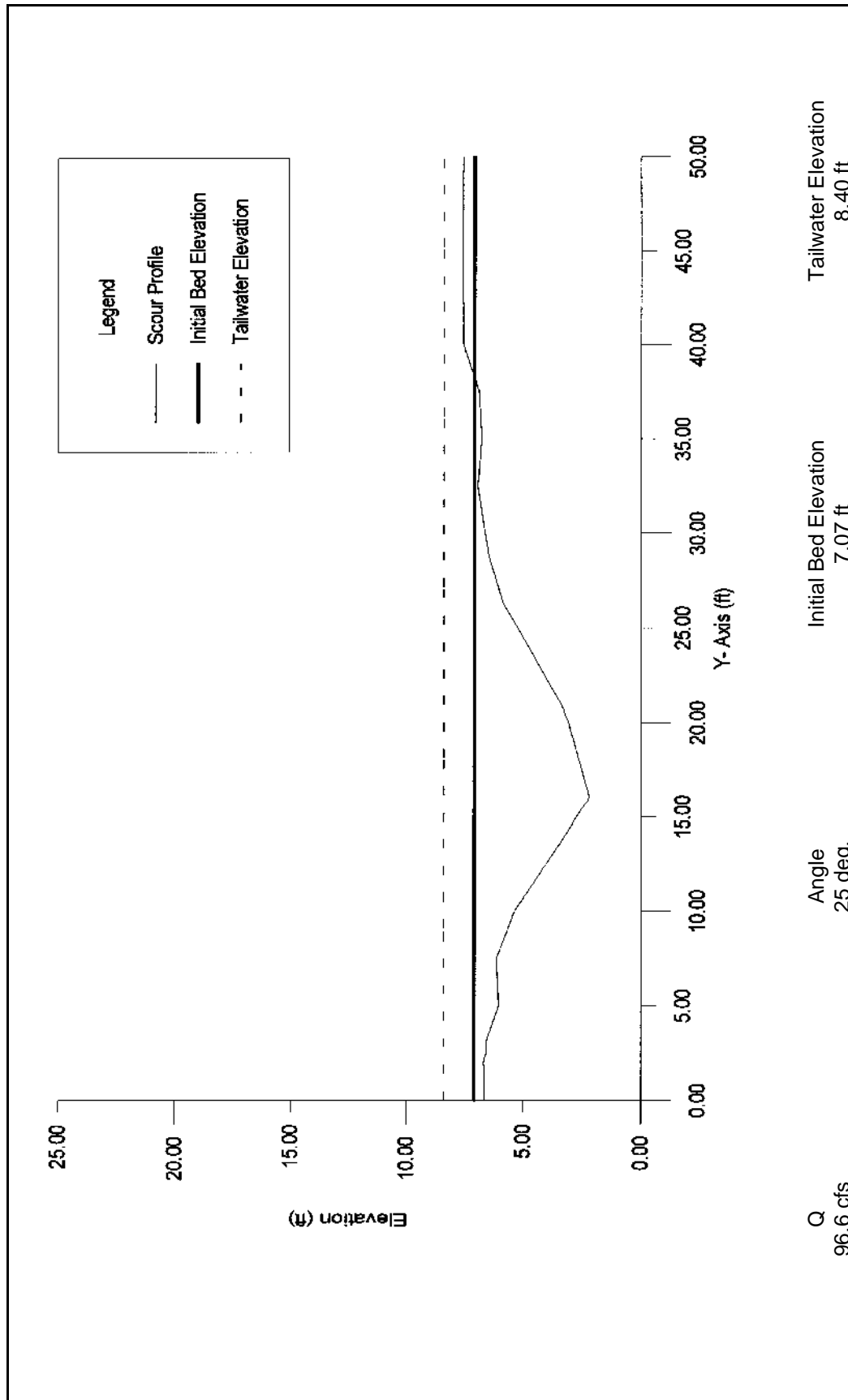


Figure G.28. Dam Foundation Erosion Studies -- longitudinal profile of scour hole for test conducted on September 2, 1997.

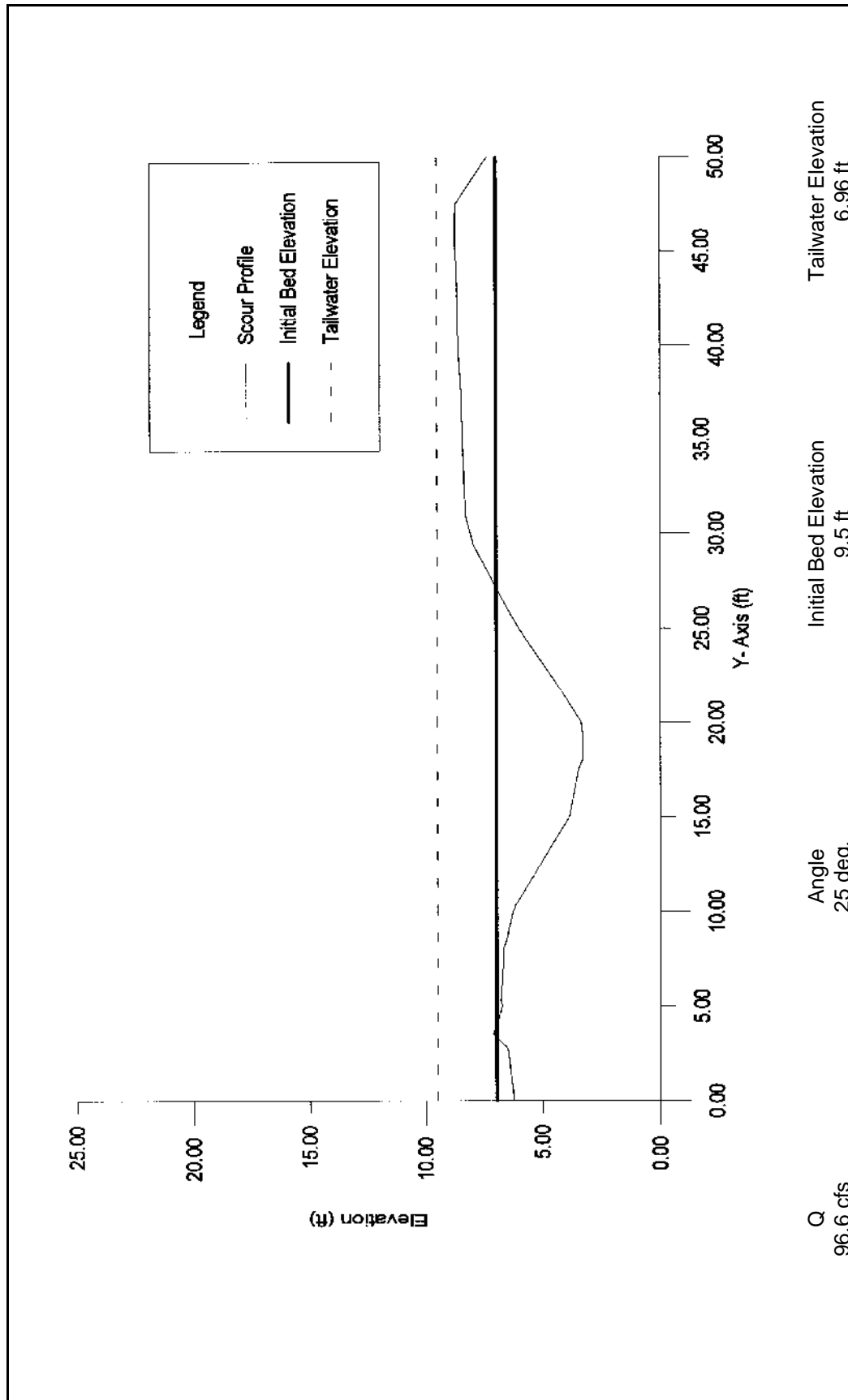


Figure G.29. Dam Foundation Erosion Studies -- longitudinal profile of scour hole for test conducted on September 11, 1997.

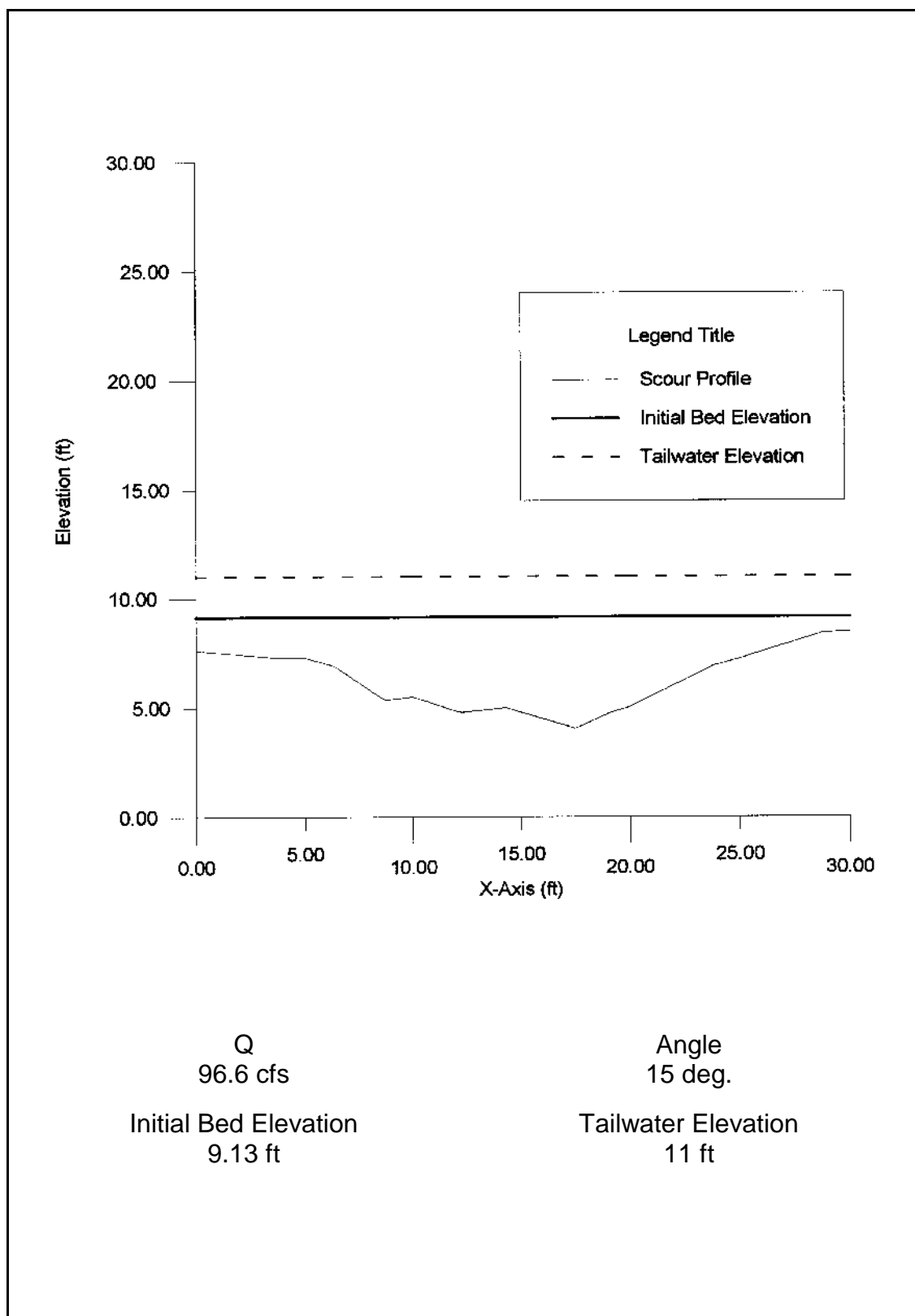


Figure G.30. Dam Foundation Erosion Studies -- lateral profile of scour hole for test conducted on August 26, 1996.

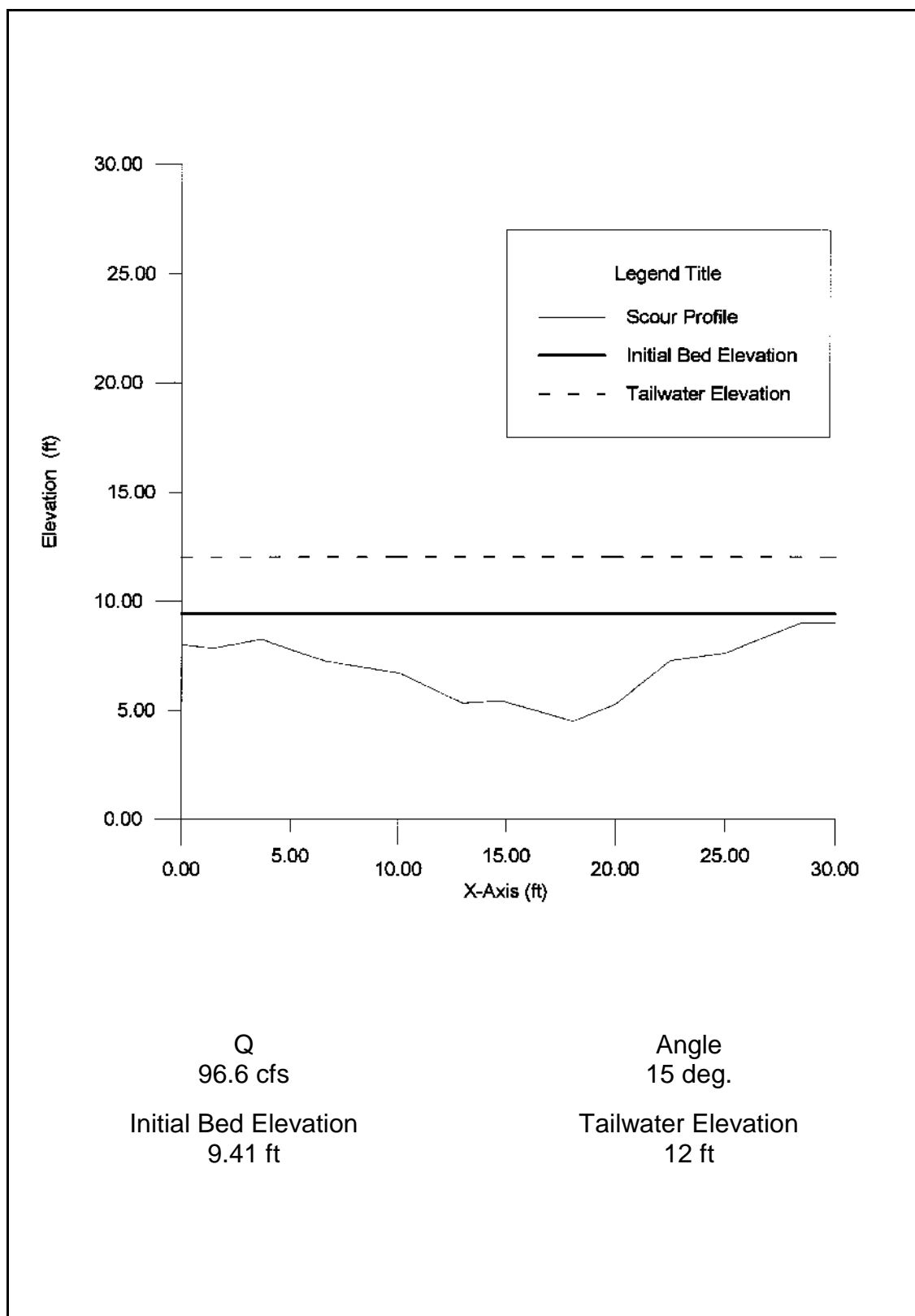


Figure G.31. Dam Foundation Erosion Studies -- lateral profile of scour hole for test conducted on September 3, 1996.

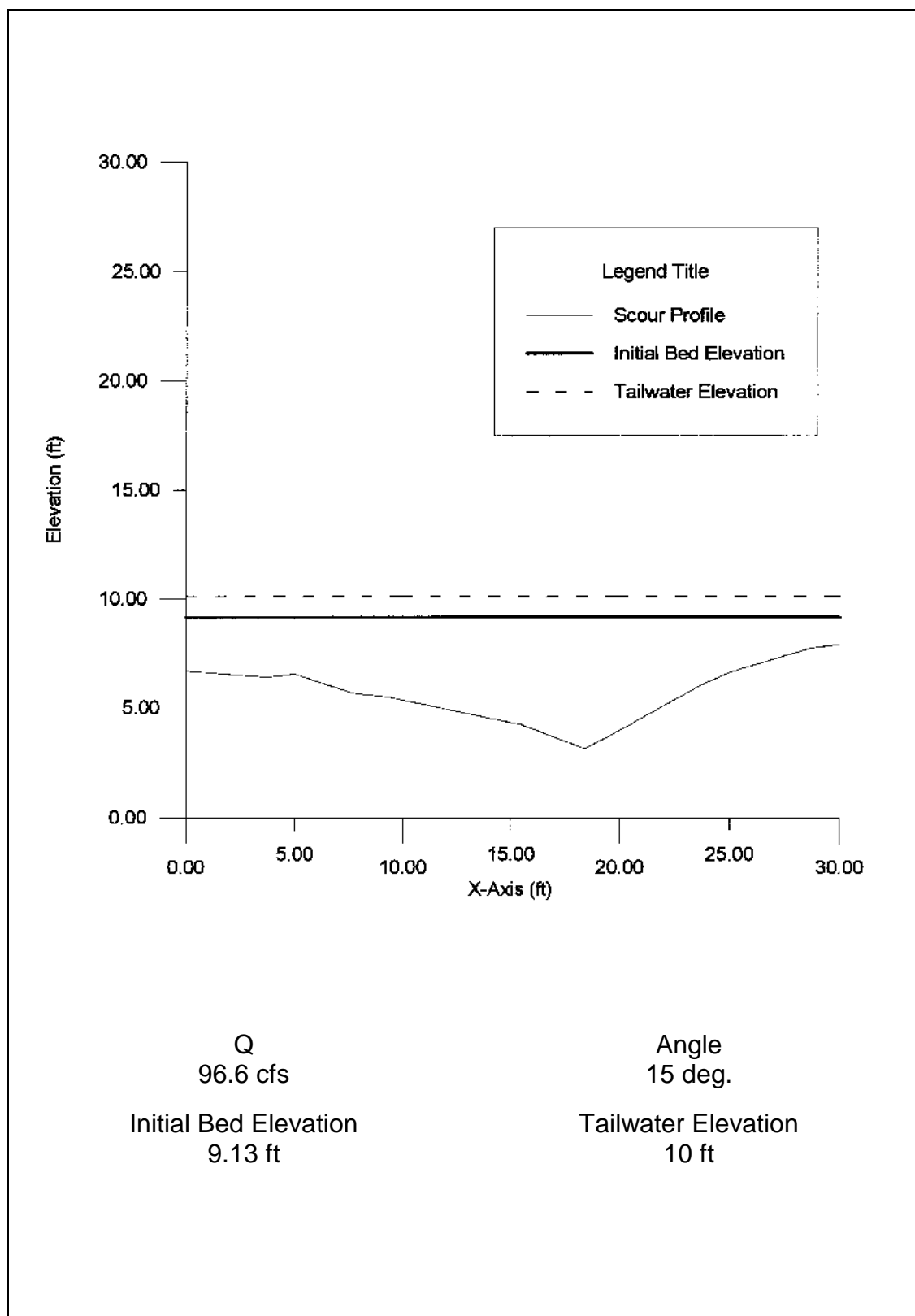


Figure G.32. Dam Foundation Erosion Studies -- lateral profile of scour hole for test conducted on September 9, 1996.

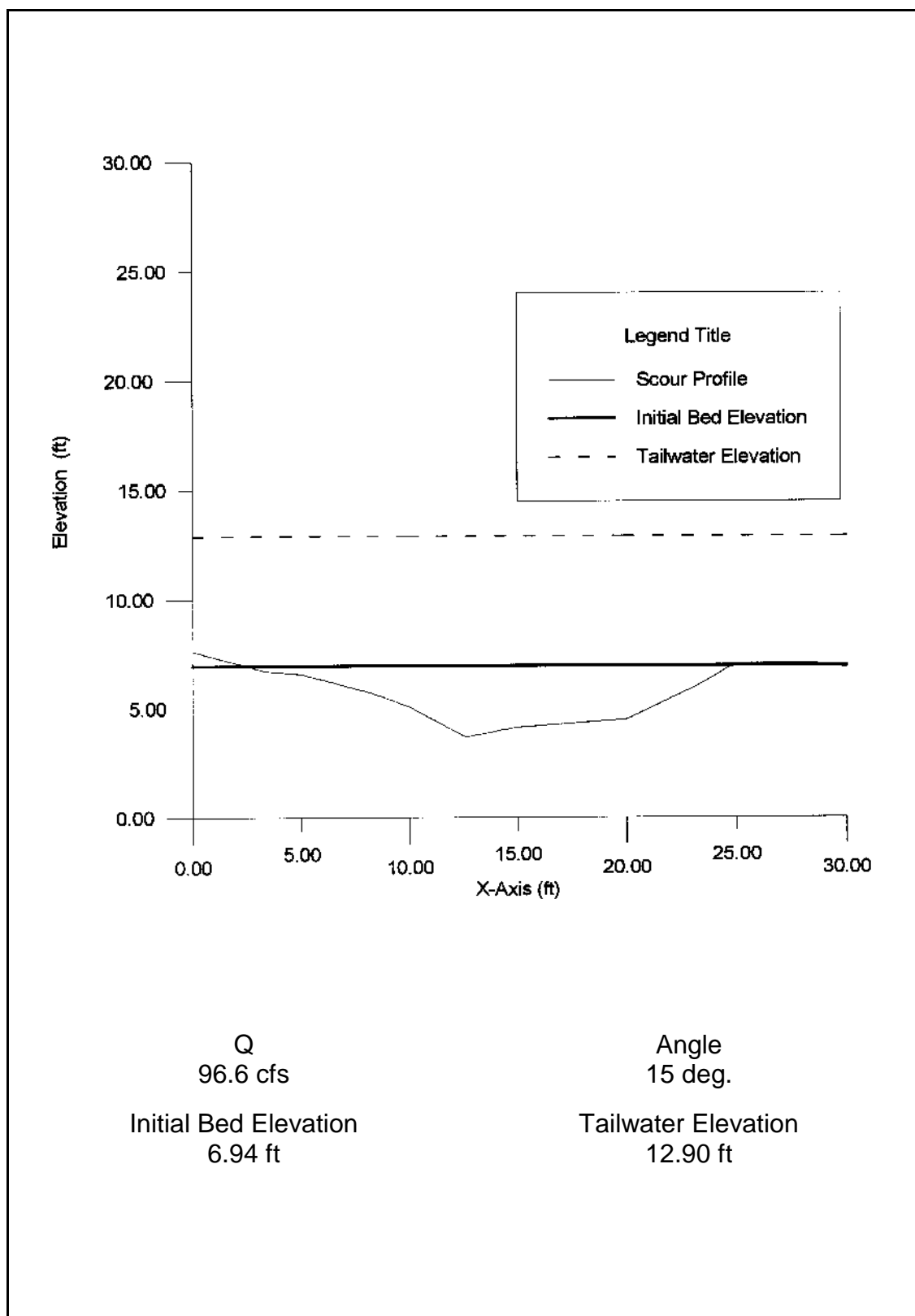


Figure G.33. Dam Foundation Erosion Studies -- lateral profile of scour hole for test conducted on September 23, 1996.

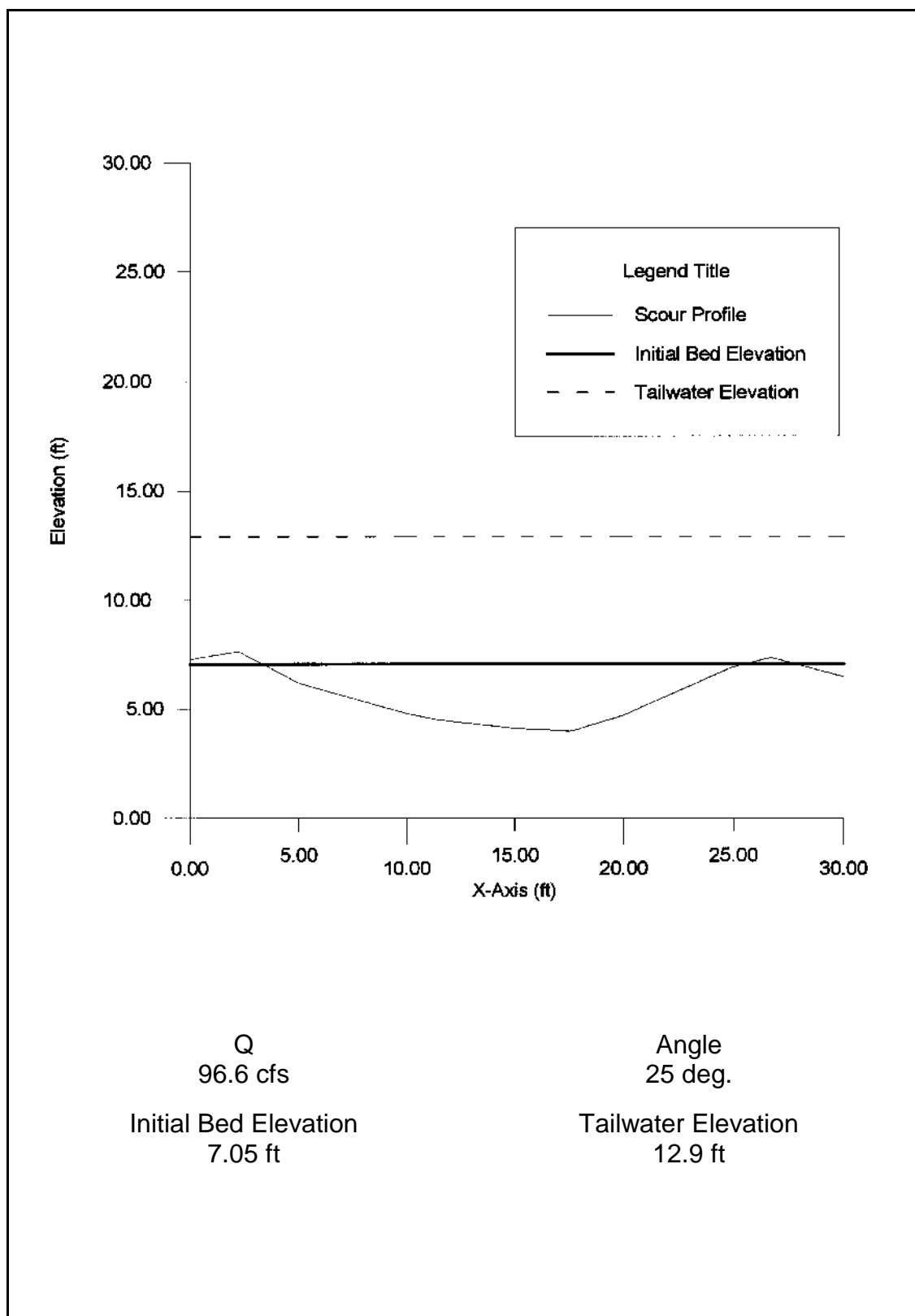


Figure G.34. Dam Foundation Erosion Studies -- lateral profile of scour hole for test conducted on September 30, 1996.

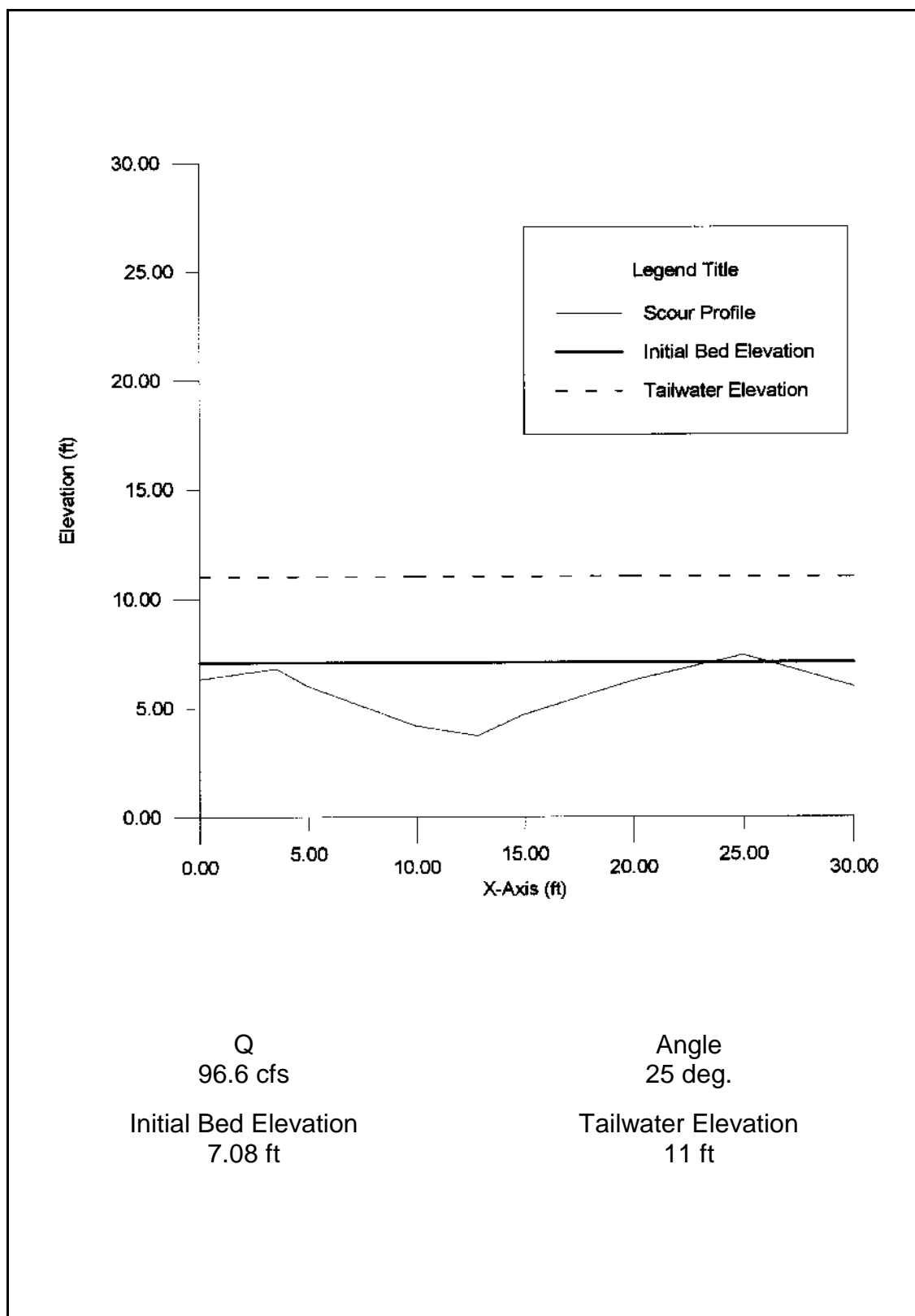


Figure G.35. Dam Foundation Erosion Studies -- lateral profile of scour hole for test conducted on October 3, 1996.

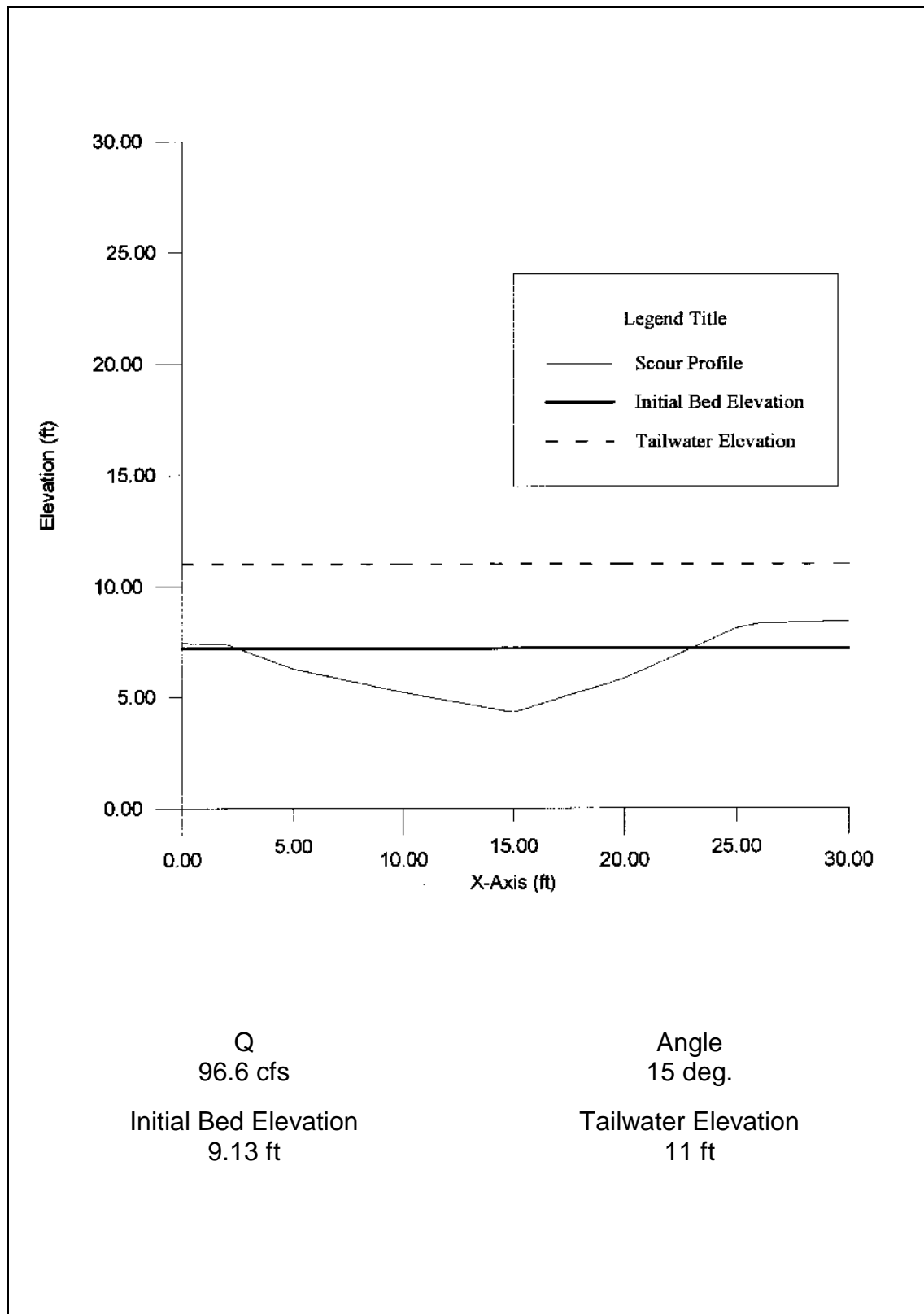


Figure G.36. Dam Foundation Erosion Studies -- lateral profile of scour hole for test conducted on October 9, 1996.

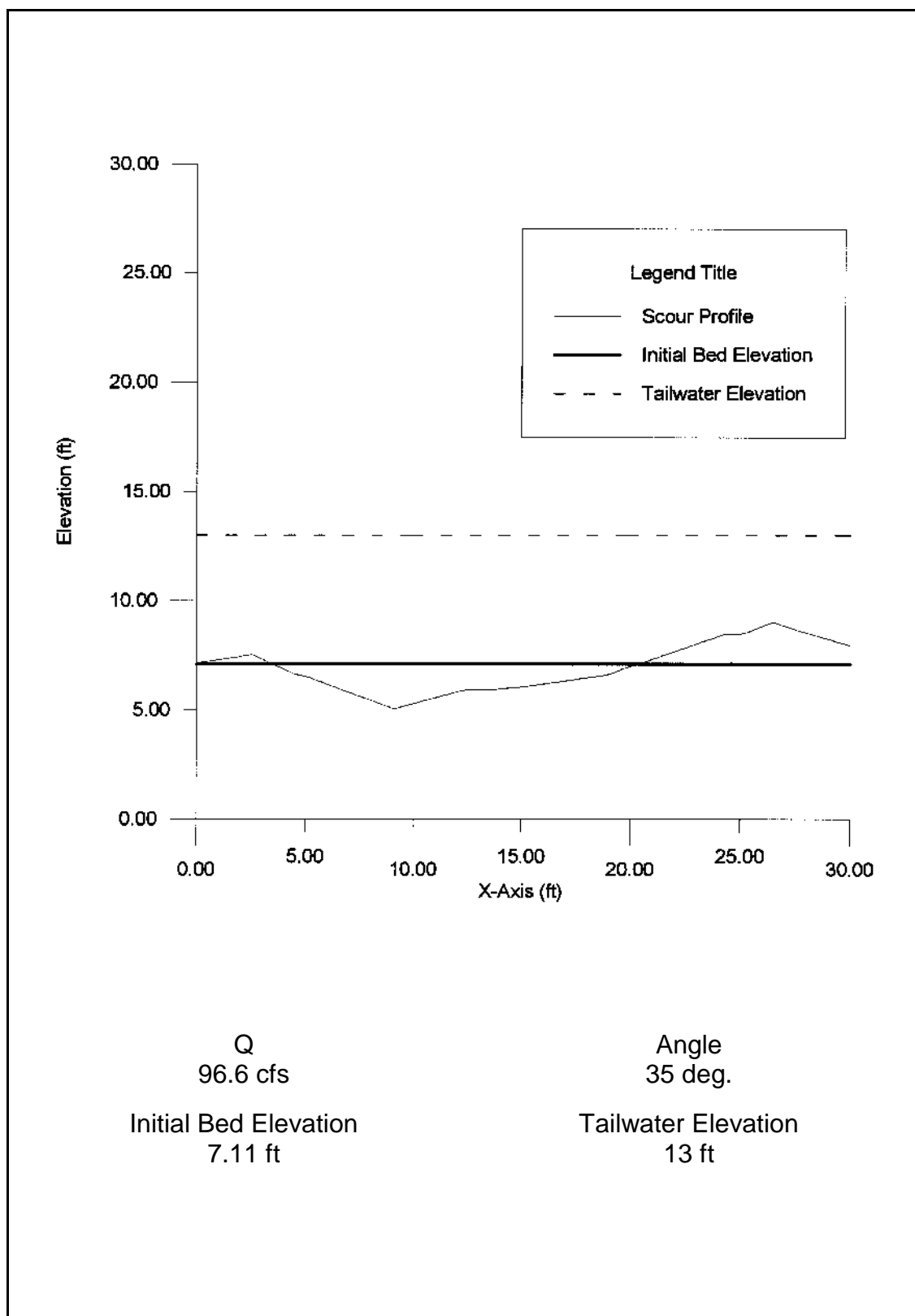


Figure G.37. Dam Foundation Erosion Studies -- lateral profile of scour hole for test conducted on October 18, 1996.

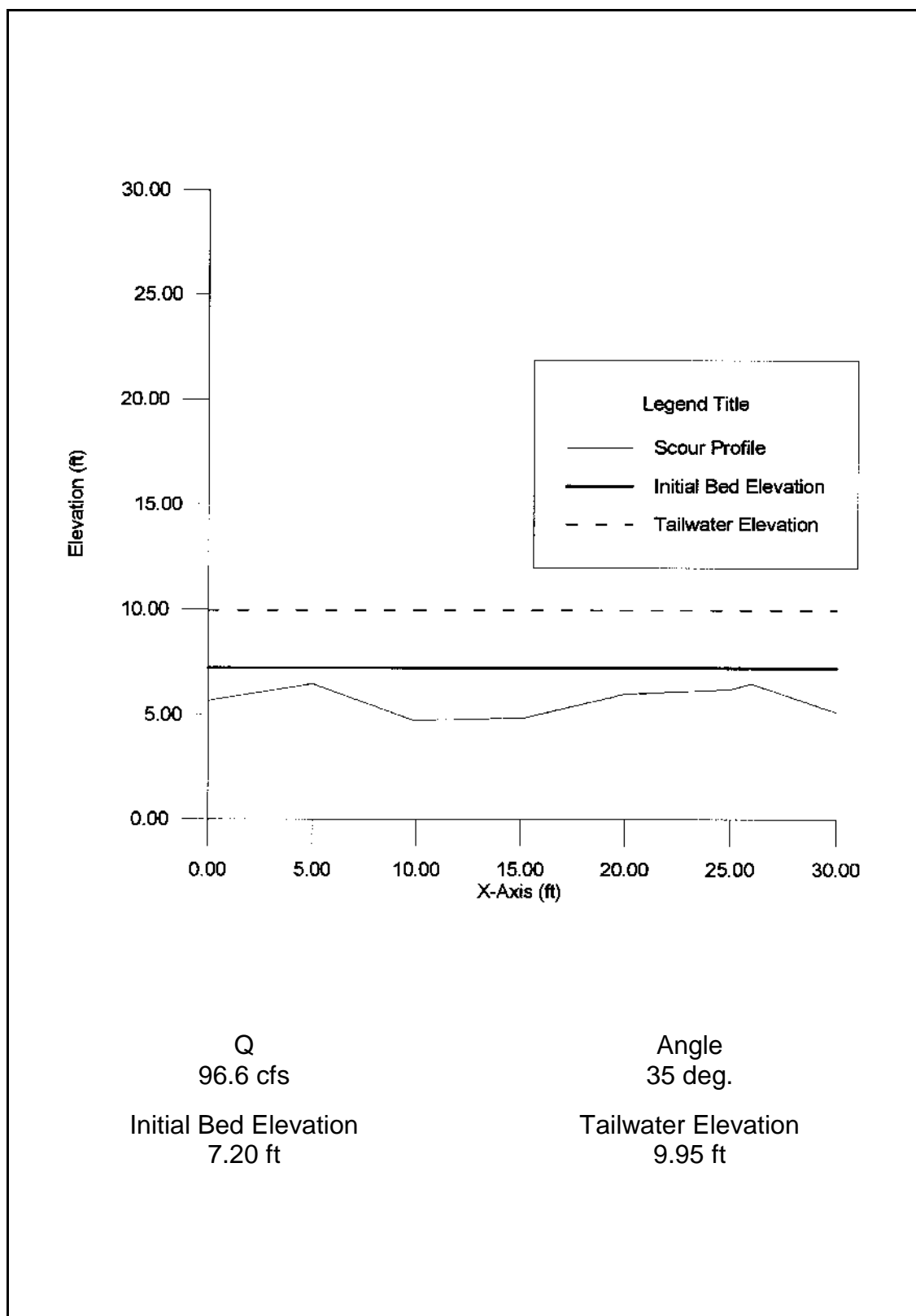


Figure G.38. Dam Foundation Erosion Studies -- lateral profile of scour hole for test conducted on July 16, 1997.

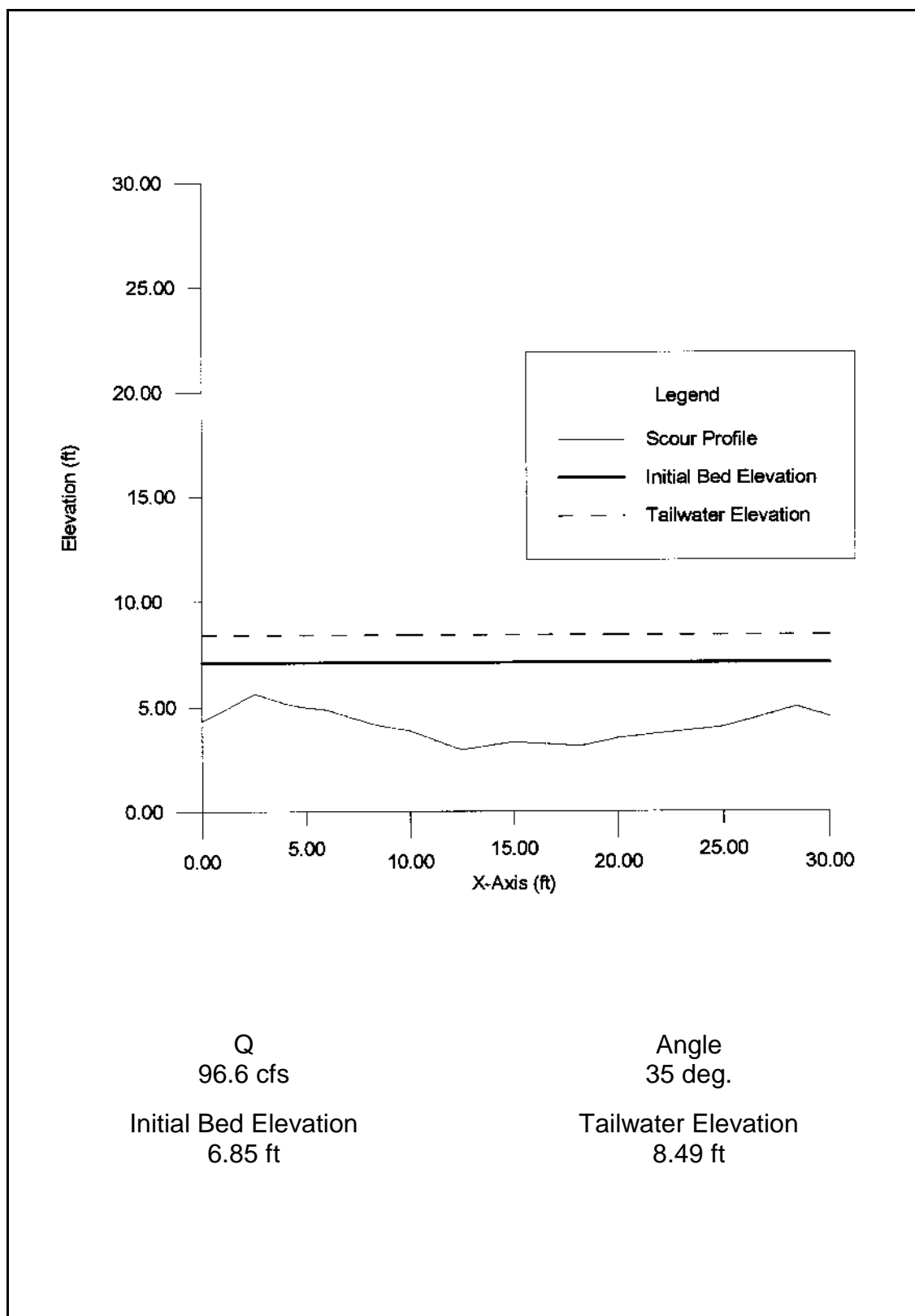


Figure G.39. Dam Foundation Erosion Studies -- lateral profile of scour hole for test conducted on July 23, 1997.

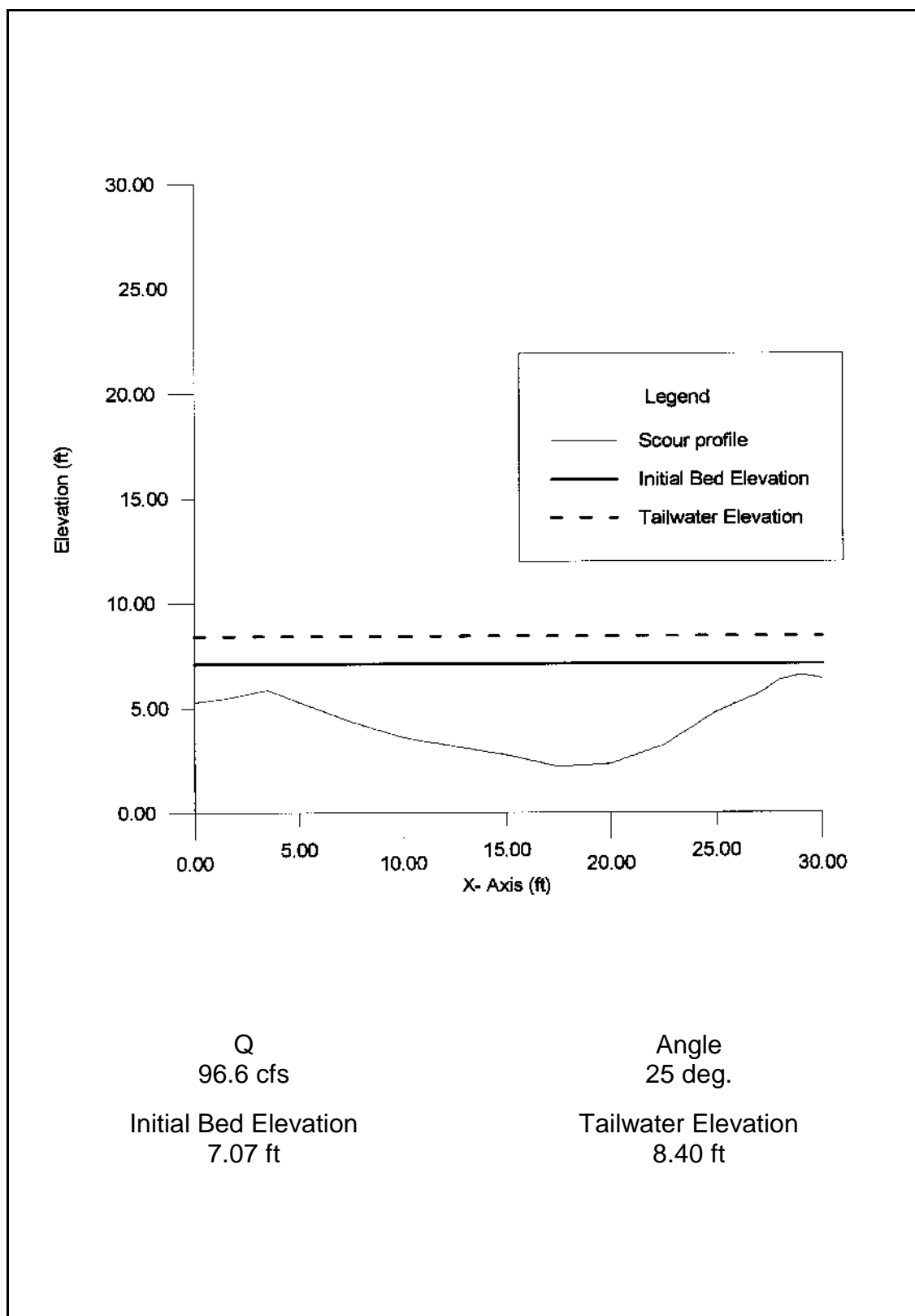


Figure G.40. Dam Foundation Erosion Studies -- lateral profile of scour hole for test conducted on September 2, 1997.

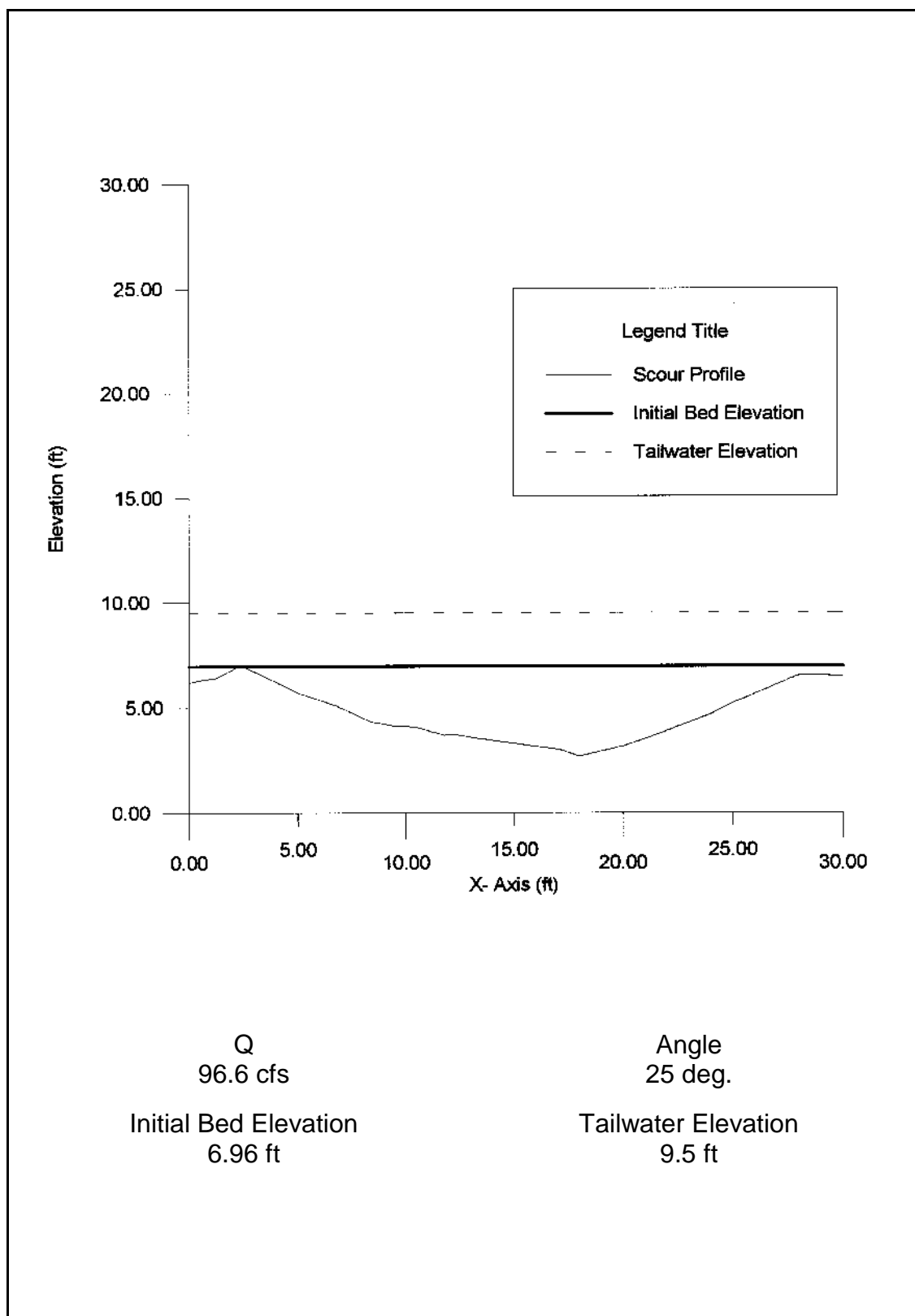


Figure G.41. Dam Foundation Erosion Studies -- lateral profile of scour hole for test conducted on September 11, 1997.

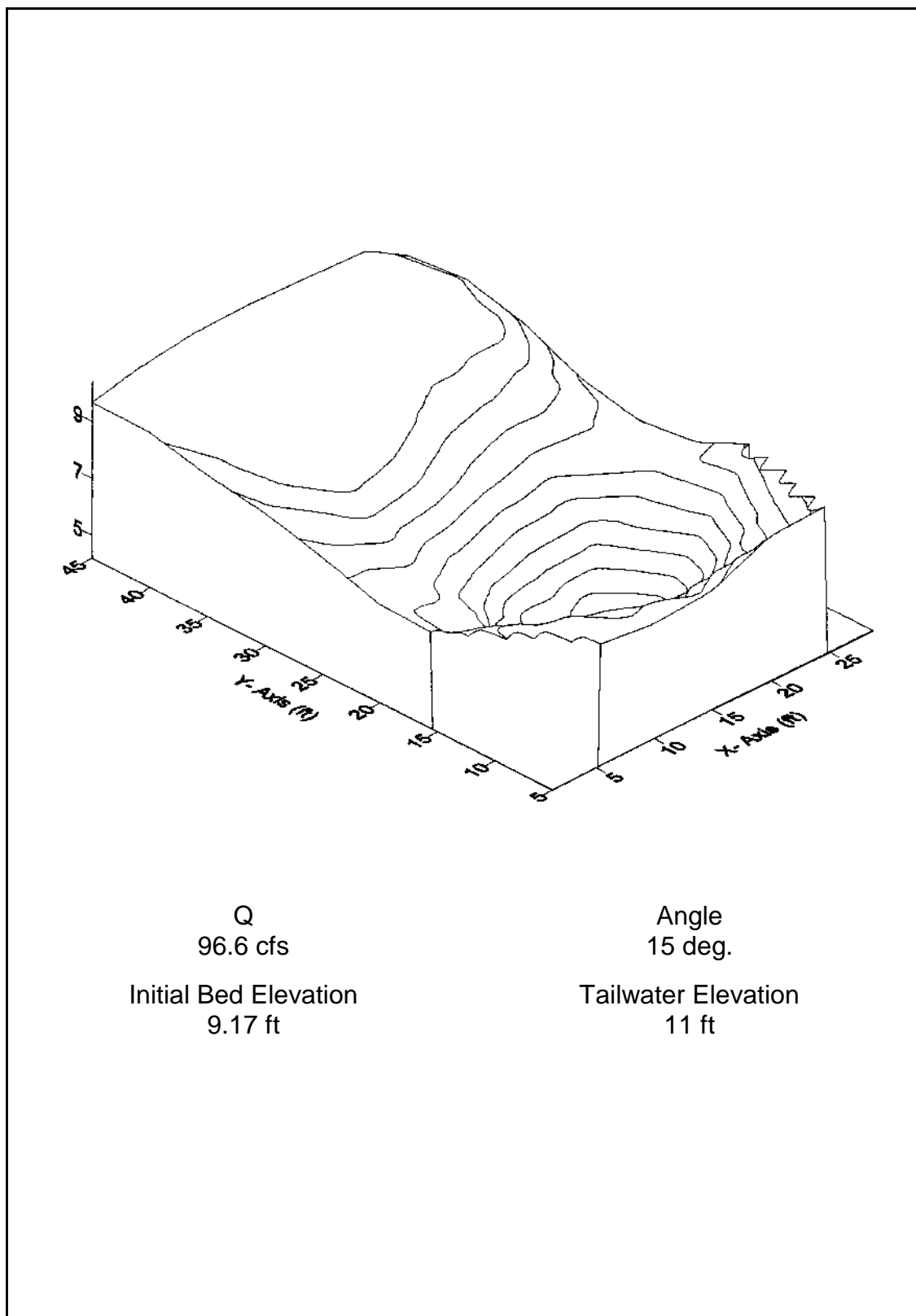


Figure G.42. Dam Foundation Erosion Studies -- three dimensional view of scour hole for test conducted on August 26, 1996.

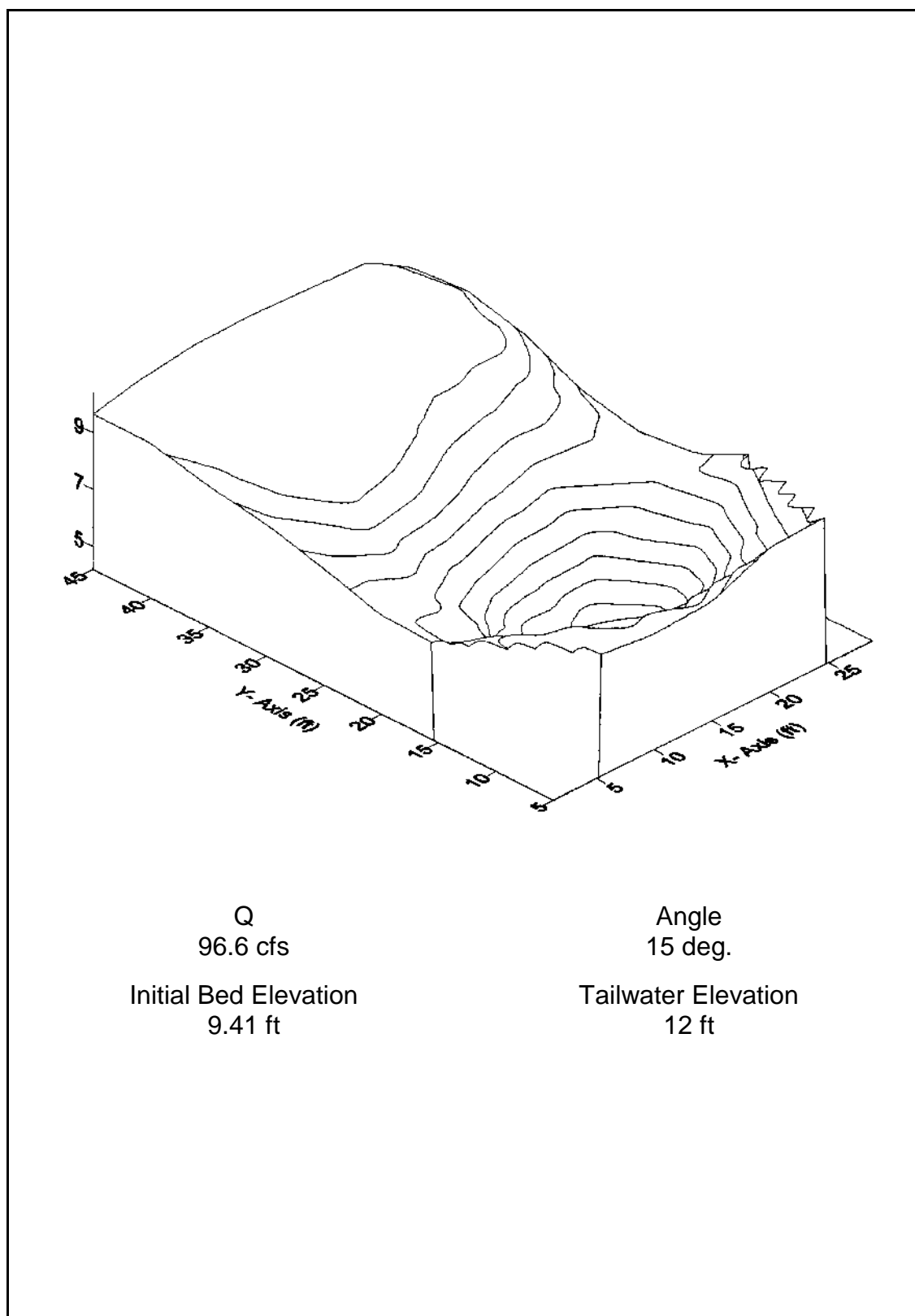


Figure G.43. Dam Foundation Erosion Studies -- three dimensional view of scour hole for test conducted on September 3, 1996.

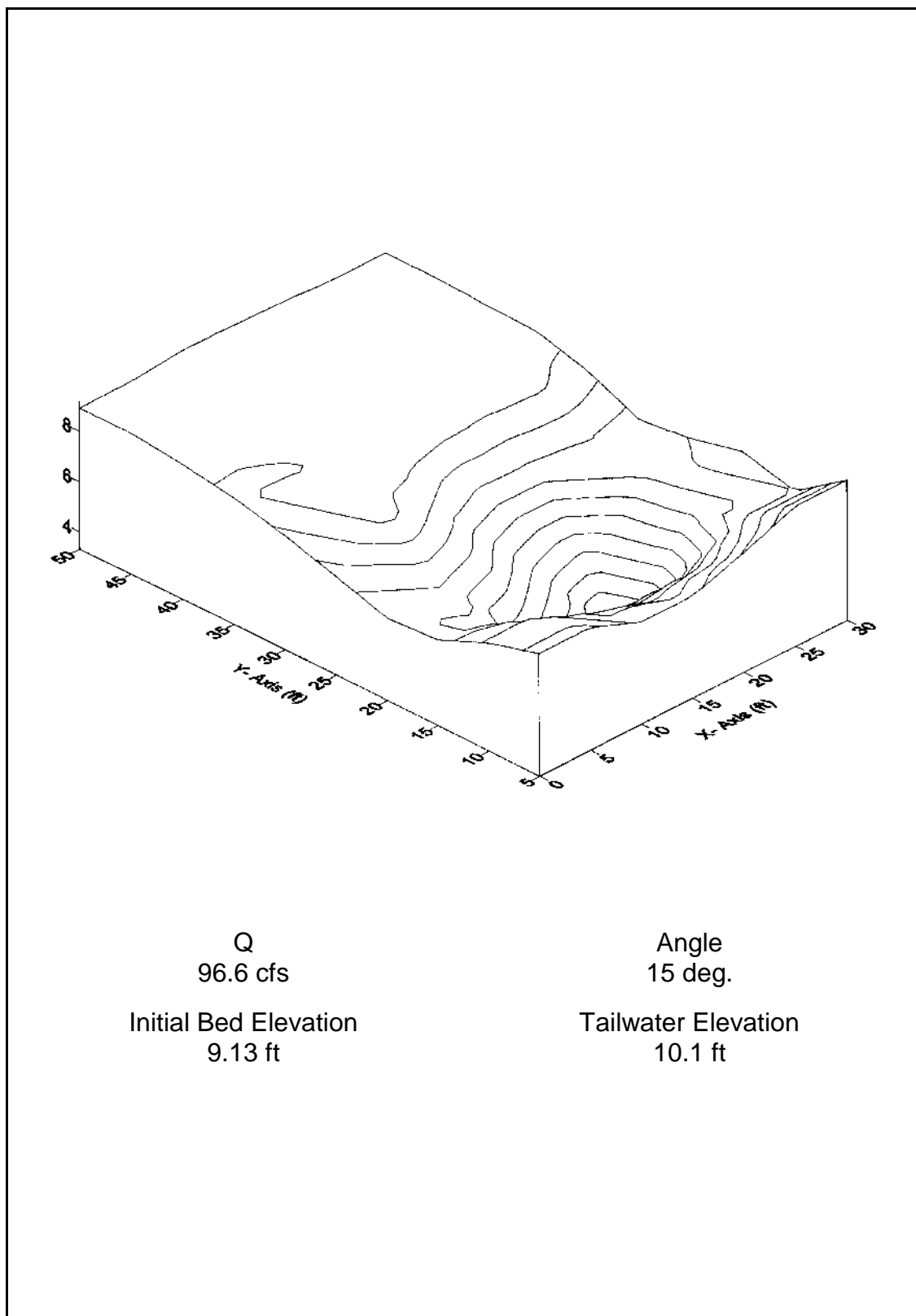


Figure G.44. Dam Foundation Erosion Studies -- three dimensional view of scour hole for test conducted on September 9, 1996.

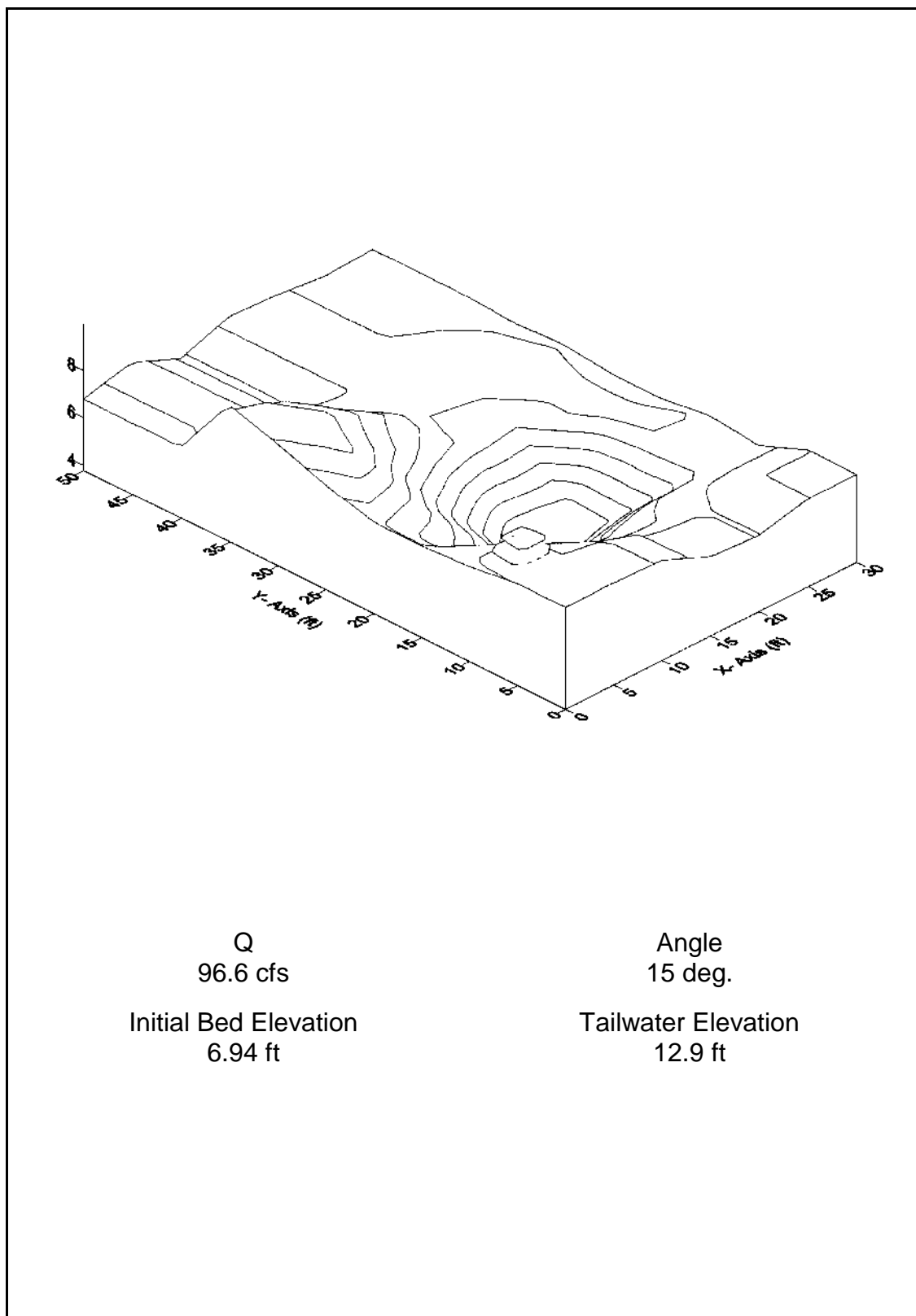


Figure G.45. Dam Foundation Erosion Studies -- three dimensional view of scour hole for test conducted on September 23, 1996.

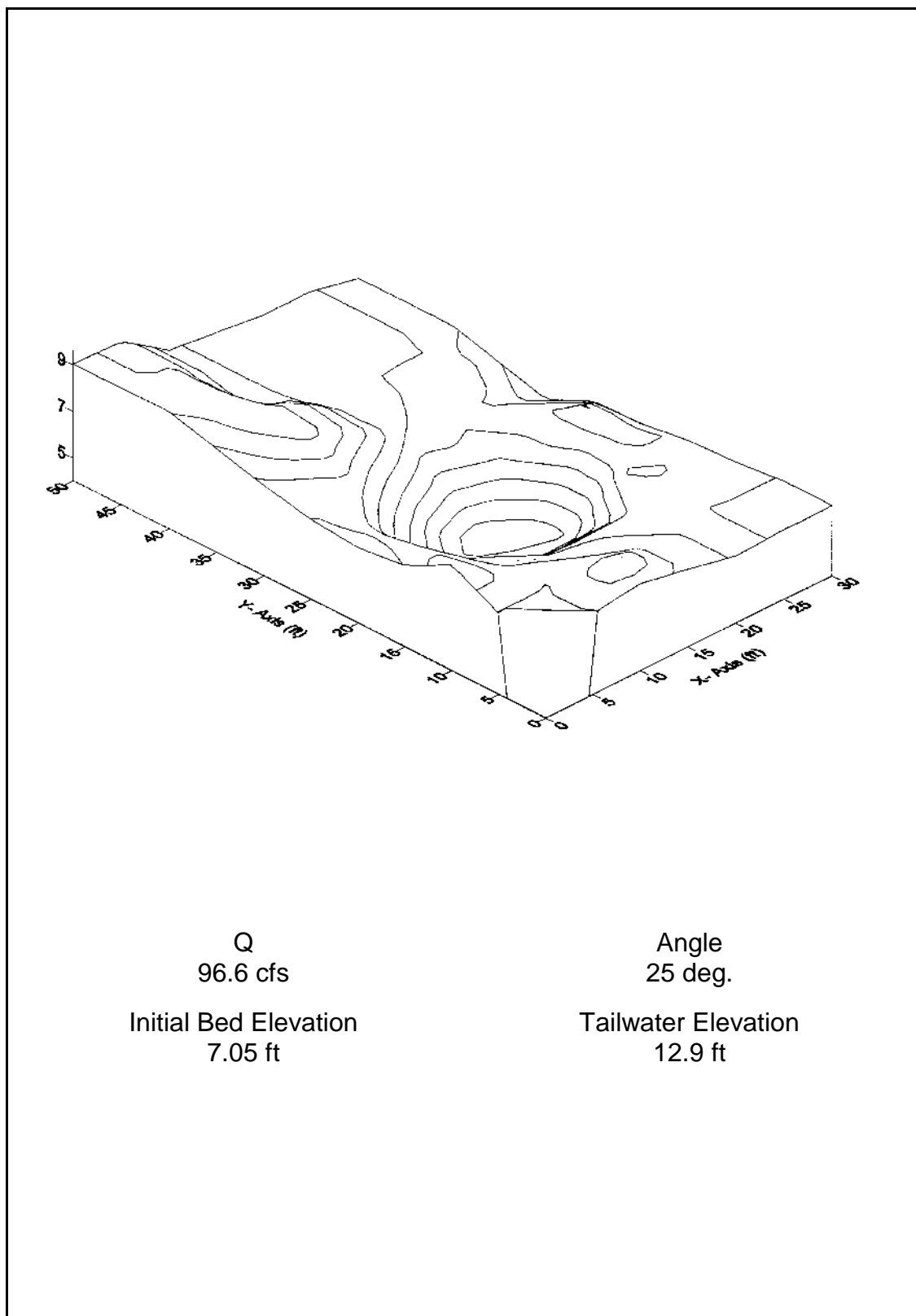


Figure G.46. Dam Foundation Erosion Studies -- three dimensional view of scour hole for test conducted on September 30, 1996.

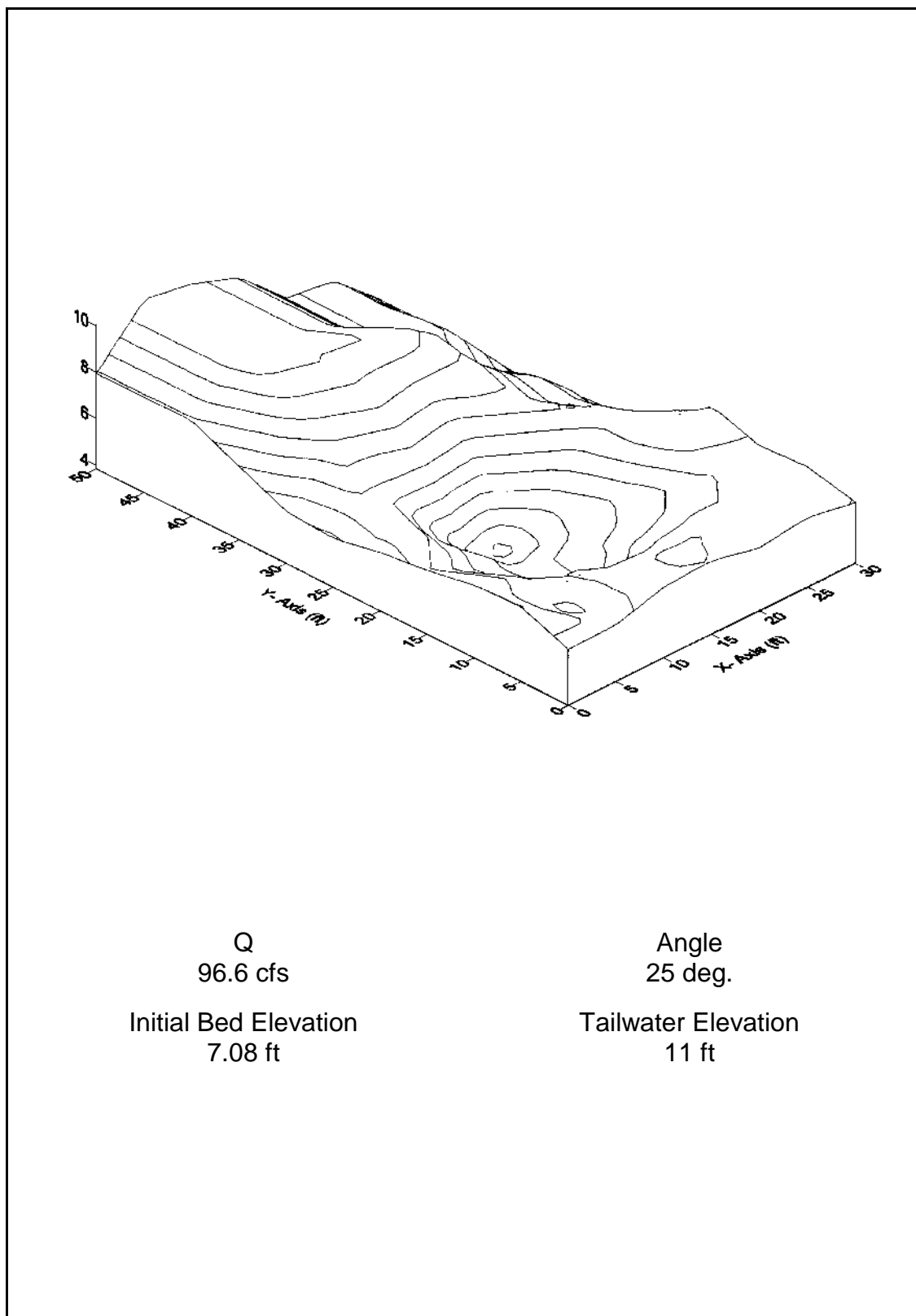


Figure G.47. Dam Foundation Erosion Studies -- three dimensional view of scour hole for test conducted on October 3, 1996.

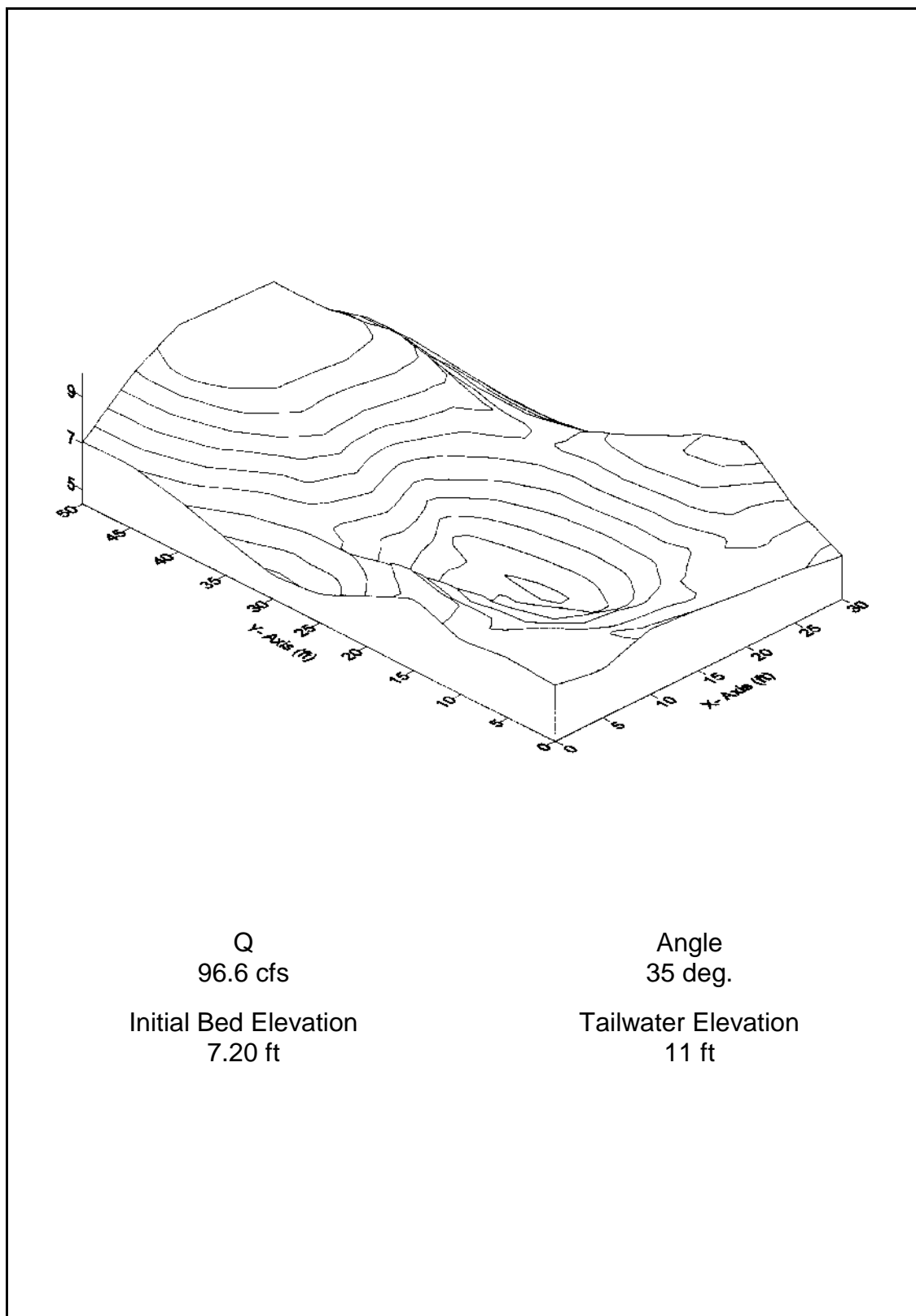


Figure G.48. Dam Foundation Erosion Studies -- three dimensional view of scour hole for test conducted on October 9, 1996.

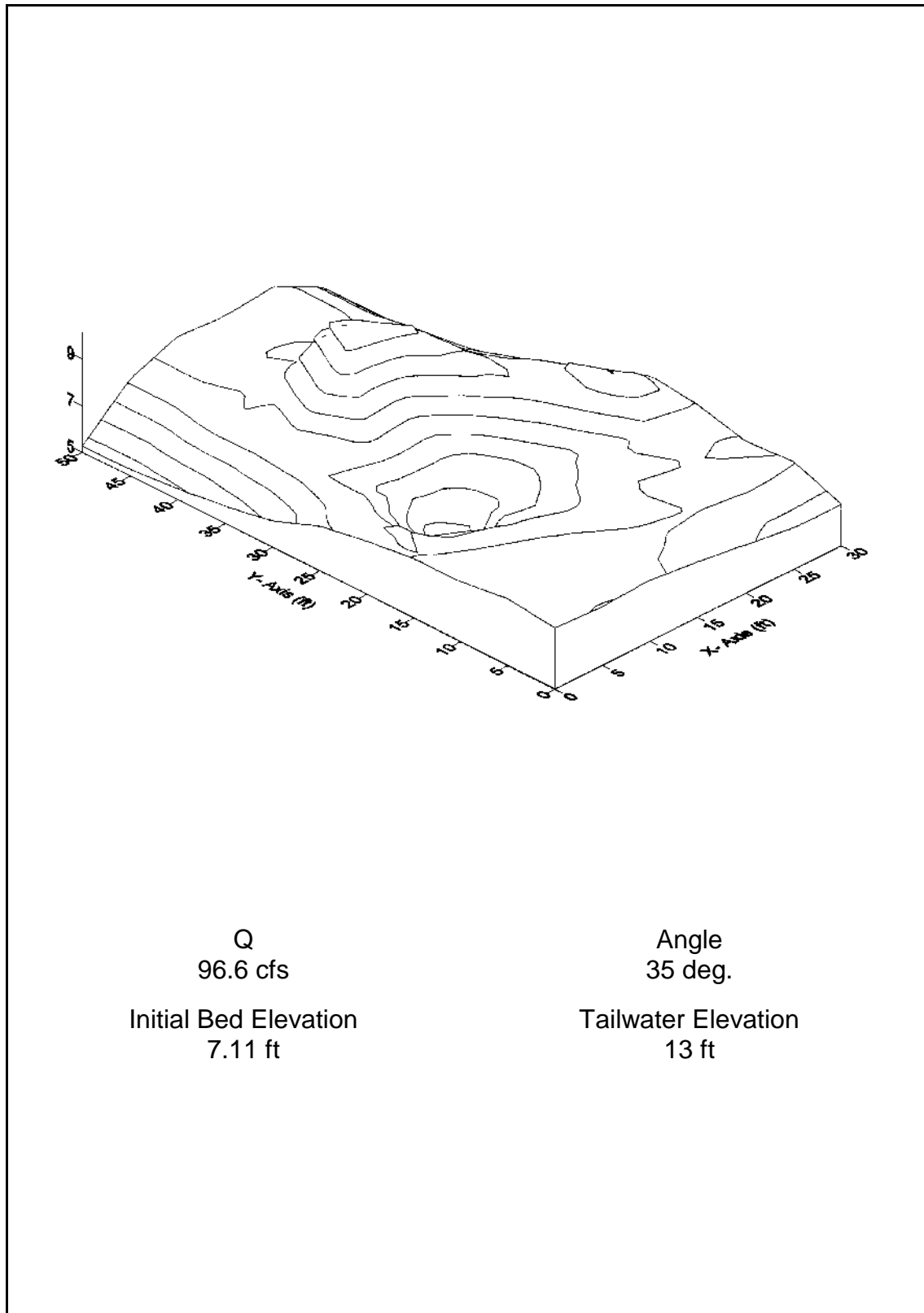


Figure G.49. Dam Foundation Erosion Studies -- three dimensional view of scour hole for test conducted on October 18, 1996.

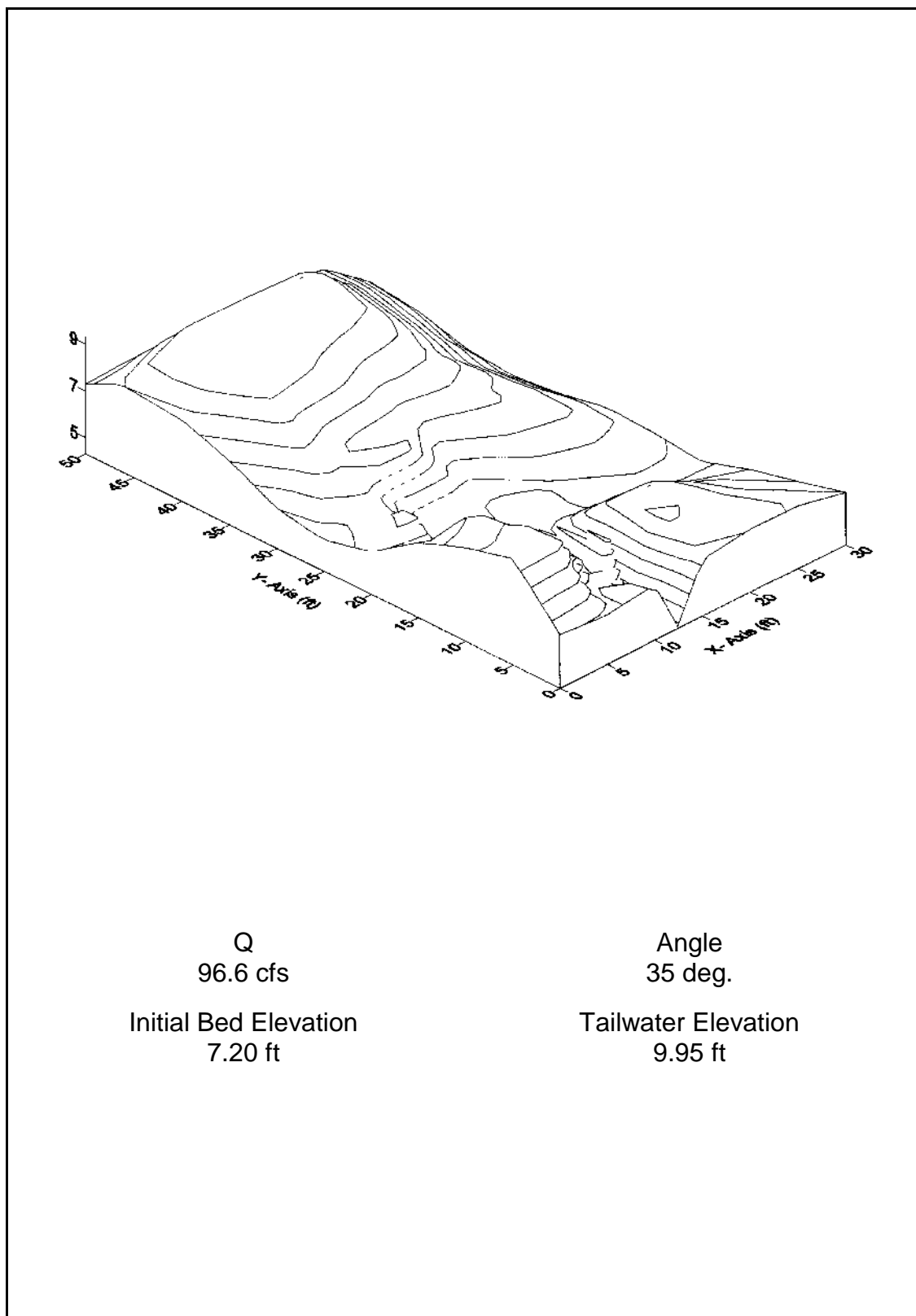


Figure G.50. Dam Foundation Erosion Studies -- three dimensional view of scour hole for test conducted on July 16, 1997.

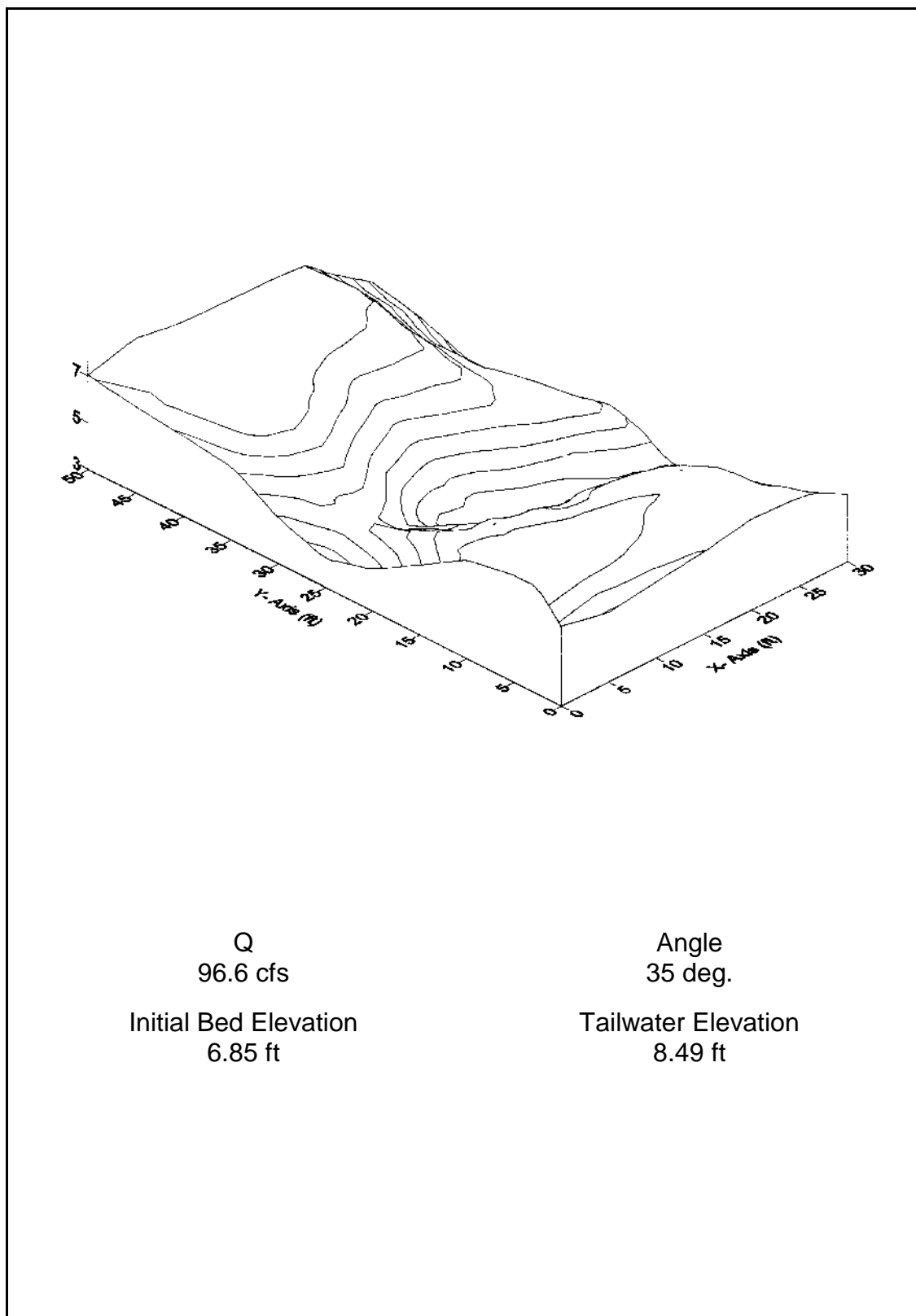


Figure G.51. Dam Foundation Erosion Studies -- three dimensional view of scour hole for test conducted on July 23, 1997.

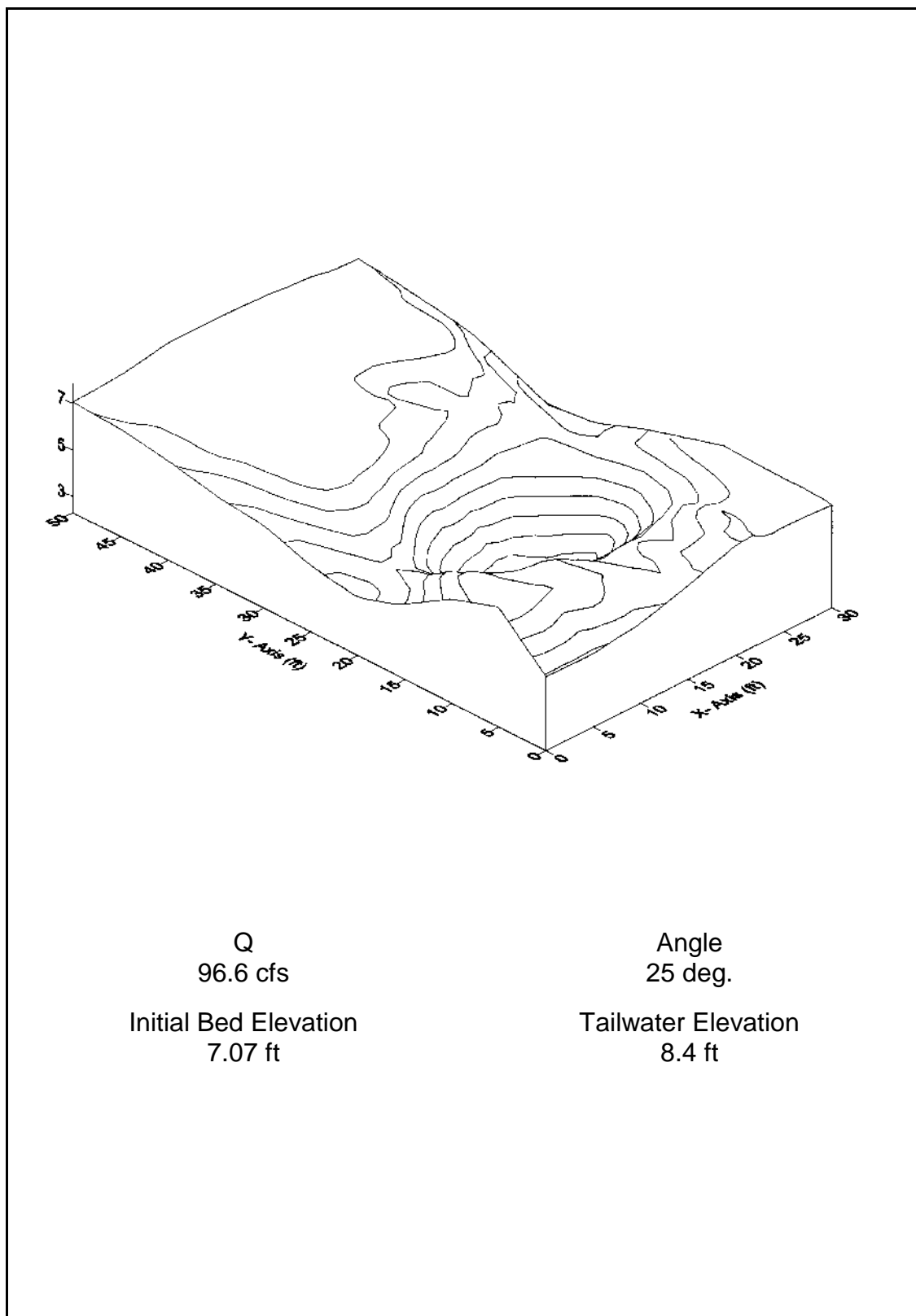


Figure G.52. Dam Foundation Erosion Studies -- three dimensional view of scour hole for test conducted on September 2, 1997.

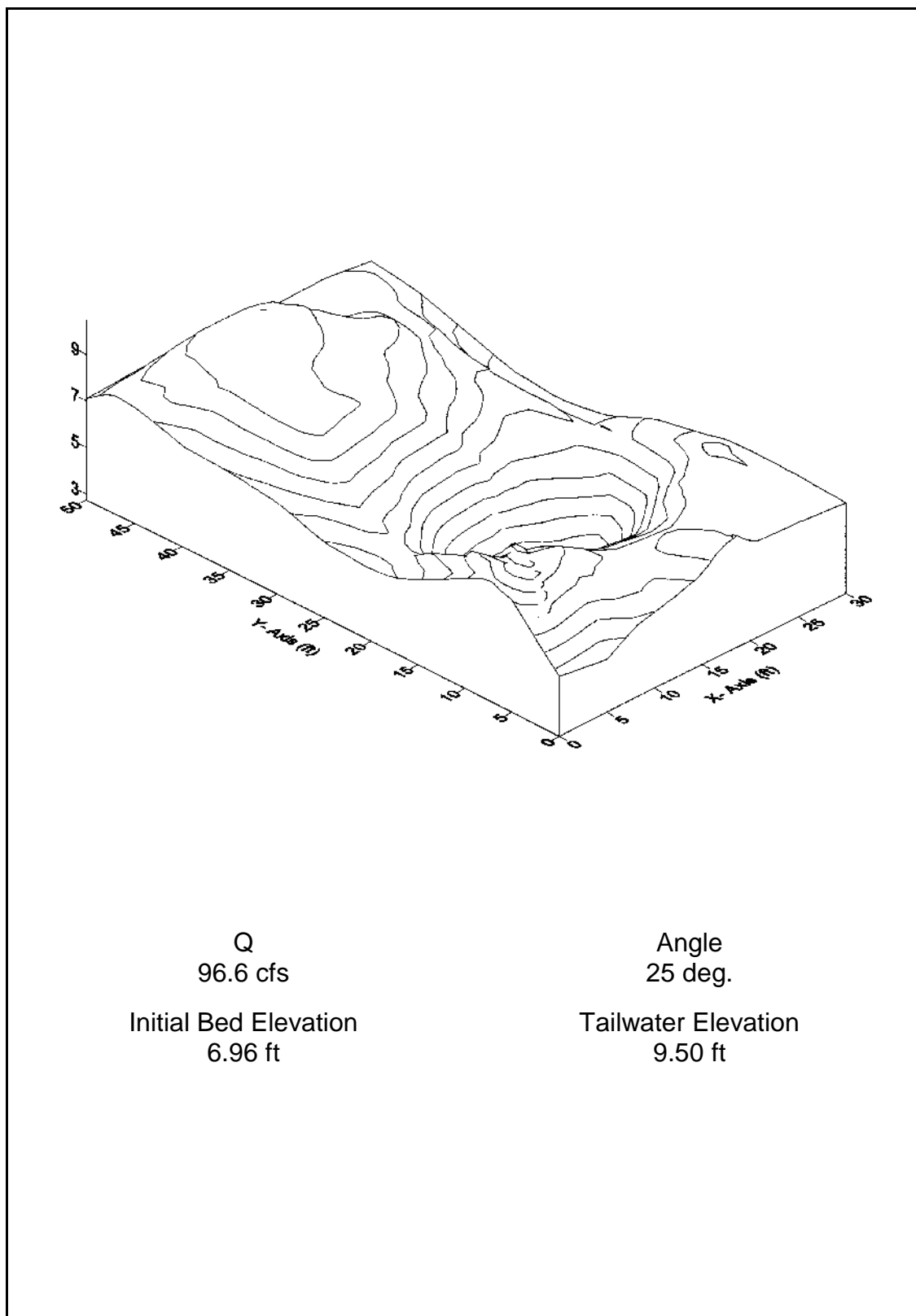


Figure G.53. Dam Foundation Erosion Studies -- three dimensional view of scour hole for test conducted on September 11, 1997.

Q (cfs)	96.6
d ₈₅ (ft)	0.0525
b (ft)	10
L1	Horizontal dist
L2	Horizontal dist
W	Width of scour

Test	Date	Angle of Nozzle	Angle of Impingement	Tailwater Elevation (ft)	Initial Bed Elevation (ft)	TW depth (ft)	Final GS Elevation (ft)	L1 @ Final GS (ft)	L2 @ Final GS (ft)	L @ Final GS (ft)	Width @ Final GS	L2/L1
96-1	08/26/96	15	11.64	11.0	9.13	1.87			8.7	7.8	16.5	25.0
96-2	09/03/96	15	11.89	12.0	9.41	2.59	8.2		8.4	7.6	16.0	23.0
96-3	09/09/96	15	11.44	10.1	9.13	0.97			7.7	7.8	15.5	26.0
96-4	09/23/96	15	12.06	12.9	6.94	5.96	6.8		9.7	8.3	18.0	21.0
96-5	09/30/96	25	19.87	12.9	7.05	5.87	6.6		9.5	9.0	18.5	20.0
96-6	10/03/96	25	19.15	11.0	7.08	3.87	6.5		13.5	5.0	18.5	25.0
96-7	10/09/96	35	26.36	11.0	7.20	3.80	6.2		10.0	14.0	24.0	16.0
96-8	10/18/96	35	27.40	13.0	7.11	5.93	7.3		11.4	9.6	21.0	20.0
97-1	07/16/97	35	25.87	10.0	7.20	2.75	7.2		8.5	14.0	22.5	n/a
97-2	07/29/97	35	25.23	8.5	6.85	1.64	6.9		14.0	15.5	29.5	n/a
97-3	09/02/97	25	18.35	8.4	7.07	1.33	5.8		12.0	11.0	23.0	24.0
97-4	09/11/97	25	18.68	9.5	6.96	2.54	6.9		10.5	11.5	21.0	24.5

Table G.4 (cont.). DFE Studies 1996/97 -- L2 versus Y (distance from the DFE Studies).

Width Versus Tailwater for Different Angles of Impingement				Metric			
TW	delta = 12 deg.	Width delta = 19 deg.	delta = 27 deg.	TW (m)	Width (m) delta = 12 deg.	delta = 19 deg.	delta = 27 deg.
1.87	25			0.57	7.62		
2.59	23			0.79	7.01		
0.97	26			0.30	7.92		
5.96	21			1.82	6.40		
5.87		20		1.79		6.10	
3.87		25		1.18		7.62	
1.33		24		0.41		7.32	
2.54		24.5		0.77		7.47	
3.80			16	1.16			4.88
5.93			20	1.81			6.10

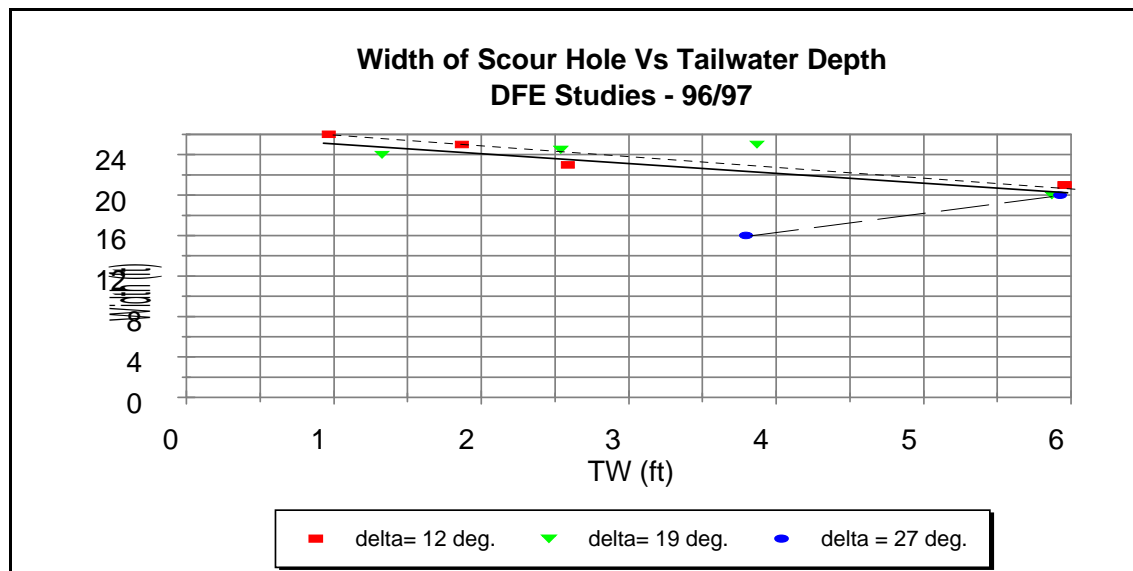


Figure G.54. Dam Foundation Erosion Studies -- width of scour hole versus tailwater depth, 96/97.

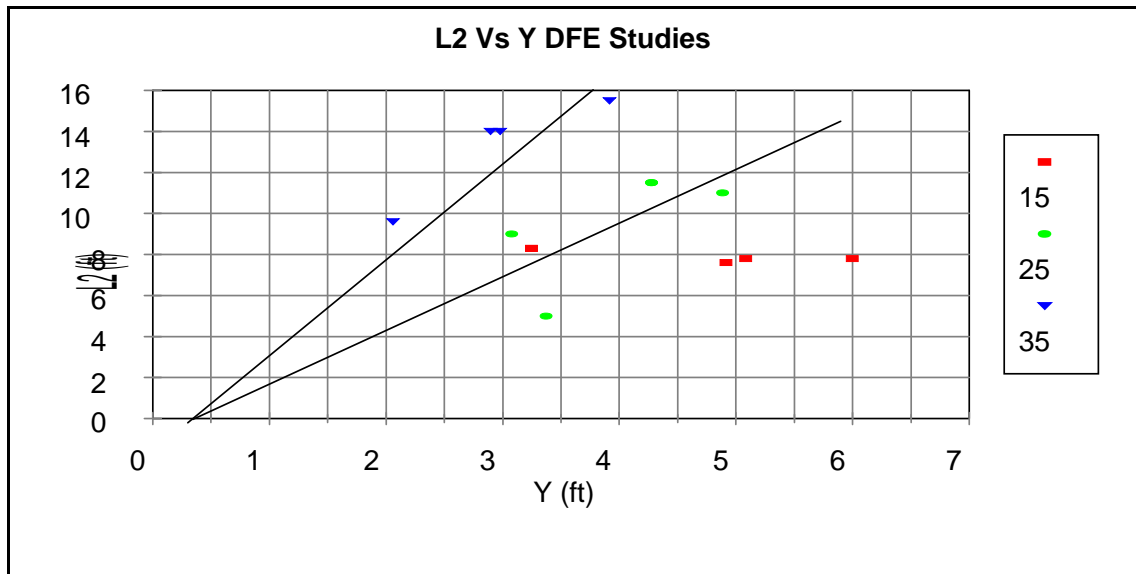


Figure G.55. L2 versus DFE Studies.

Table G.5. Calculated distance of impact at bottom of scour hole, X_i versus actual distance of impact, X_{max} (measured from the north wall).

Dam Foundation Erosion Studies

Summary of maximum scour depths

Q (cfs) = 96.6
 V_o (ft/s) = 31.9338842975207
 X_i (ft) = 10

Angle of Nozzle From Vertical (deg.)	Date of Test	Bed Elevation	Tailwater Elevation	Upstream Tailwater Elevation	Water Depth	Scour Hole Elevation--Deepest Pt. of Scour	Max Depth	Z	X_2	X_3	cos d	δ (deg.)	90-Measured	90-d	X_4	X_i	X_{max}	$X_{max} > X_i$
(ft)	(ft)	(ft)	(ft)	(ft)	(ft)	(ft)	(ft)	(ft)	(ft)	(ft)	(ft)	(deg.)	(deg.)	(ft)	(ft)	(ft)	(ft)	(ft)
15	08/26/96	9.13	11.00	N/A	1.87	4.04	5.09	13.99	0.686	3.130	0.982	10.87	79.13	75.00	0.359	14.17	16.20	YES
15	09/03/96	9.41	12.20	11.9	2.79	4.49	4.92	12.79	0.686	2.897	0.981	11.10	78.90	75.00	0.547	14.13	15.60	YES
15	09/09/96	9.13	10.00	9.83	0.87	3.13	6.00	14.99	0.686	3.320	0.983	10.69	79.31	75.00	0.164	14.17	16.30	YES
15	09/23/96	6.94	13.00	N/A	6.06	3.69	3.25	11.99	0.686	2.739	0.981	11.26	78.74	75.00	1.206	14.63	16.70	YES
25	09/30/96	7.05	12.95	12.8	5.90	3.97	3.08	12.04	1.120	4.703	0.948	18.57	71.43	64.00	1.983	17.81	20.00	YES
25	10/03/96	7.08	10.93	10.52	3.85	3.70	3.38	14.06	1.120	5.368	0.952	17.91	72.09	64.00	1.245	17.73	17.17	NO
35	10/09/96	7.20	11.00	10.37	3.80	4.30	2.90	13.99	1.520	7.768	0.908	24.70	65.30	68.00	1.748	21.04	15.00	NO
35	10/18/96	7.11	13.03	12.67	5.92	5.05	2.06	11.96	1.520	6.814	0.901	25.65	64.35	68.00	2.843	21.18	21.40	YES
35	07/16/97	7.20	9.95	9.47	2.75	4.22	2.98	15.04	1.520	8.246	0.912	24.25	65.75	68.00	1.239	21.01	18.00	NO
35	07/23/97	6.85	8.49	8.15	1.64	2.93	3.92	16.5	1.520	8.895	0.916	23.66	66.34	68.00	0.719	21.13	23.50	YES
25	09/02/97	7.07	8.4	8.05	1.33	2.18	4.89	16.59	1.120	6.168	0.955	17.18	72.82	64.00	0.411	17.70	16.00	NO
25	09/11/97	6.96	9.5	9.1	2.54	2.68	4.28	15.49	1.120	5.825	0.954	17.49	72.51	64.00	0.800	17.74	16.00	NO

Table G.6. Side slopes.

The following are the side slopes of the scour holes for the tests carried out in 1996 and 1997:

Date	Angle of Nozzle	TW Depth m - (ft)	East Slope	West Slope
08/26/96	15	0.57 (1.87)	0.258	0.377
09/03/96	15	0.85 (2.79)	0.260	0.436
09/09/96	15	0.27 (0.87)	0.253	0.449
09/23/96	15	1.85 (6.06)	0.310	0.270
09/30/96	25	1.80 (5.90)	0.174	0.371
10/03/96	25	1.18 (3.87)	0.331	0.304
10/09/96	35	1.17 (3.85)	0.237	0.365
10/18/96	35	1.80 (5.92)	0.375	0.227
07/16/97	35	0.84 (2.75)	0.352	0.233
07/23/97	35	0.50 (1.64)	0.269	0.204
09/02/97	25	0.41 (1.33)	0.182	0.470
07/24/97	25	0.77 (2.54)	0.445	0.430

APPENDIX H

AIR CONCENTRATION AND VELOCITY READINGS

APPENDIX H

AIR CONCENTRATION AND VELOCITY READINGS

The air concentration, and velocity readings and of tests conducted on July 29, 1997 and September 4, 1997 are included in this Appendix. Air concentrations and velocities have been plotted against depths and presented in Figures H.1, H.2, H.3 and H.4.

Table H.1. Dam Foundation Erosion Studies -- air concentration and velocity readings (SI units).

Test	Pitot Tube Elevation (m)	TW Elevation (m)	Depth Above Pitot Tube (m)	Air Concentration (%)	Velocity (m/s)
07/16/97				96	>18.29
07/29/97	2.59	2.59	0.00	96	>18.29
		2.59	0.00	96	>18.29
		2.74	0.15	96	>18.29
		2.90	0.30	96	>18.29
		2.90	0.30	96	>18.29
		3.05	0.46	90	15.24
		3.05	0.46	92	19.51
		3.05	0.46	65	7.32
		3.20	0.61	28	3.96
		3.35	0.76	10	<3.05
		3.35	0.76	20	3.05
		3.66	1.07	10	below range
		3.66	1.07	10	below range
07/30/97		3.05	0.46	90	40.00
09/02/97			N/A	96	
09/04/97	2.60	2.87	0.27	100	
		3.05	0.45	90	12.19
		3.17	0.57	65	4.57
		3.20	0.60	60	4.57
		3.05	0.45	85	8.38
		3.35	0.75	45	3.81
		3.35	0.75	40	4.57
		3.51	0.91	30	3.05
		3.66	1.06	25	3.05
		3.66	1.06	30	3.05
09/11/97	3.60	2.90	N/A	94	>18.29

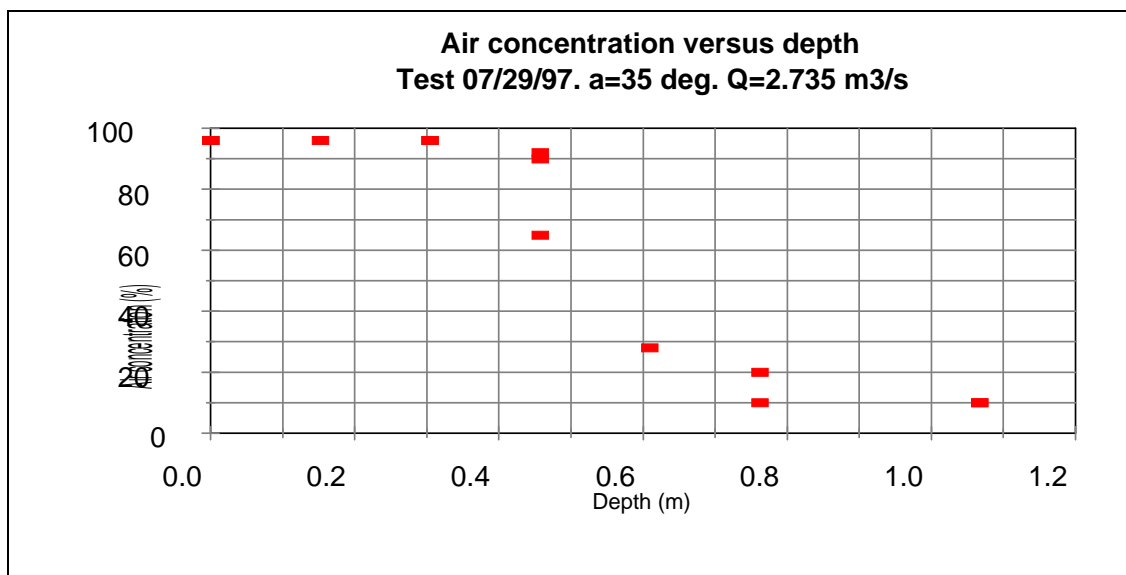


Figure H.1. Dam Foundation Erosion Studies -- air concentration versus depth, 07/29/97.

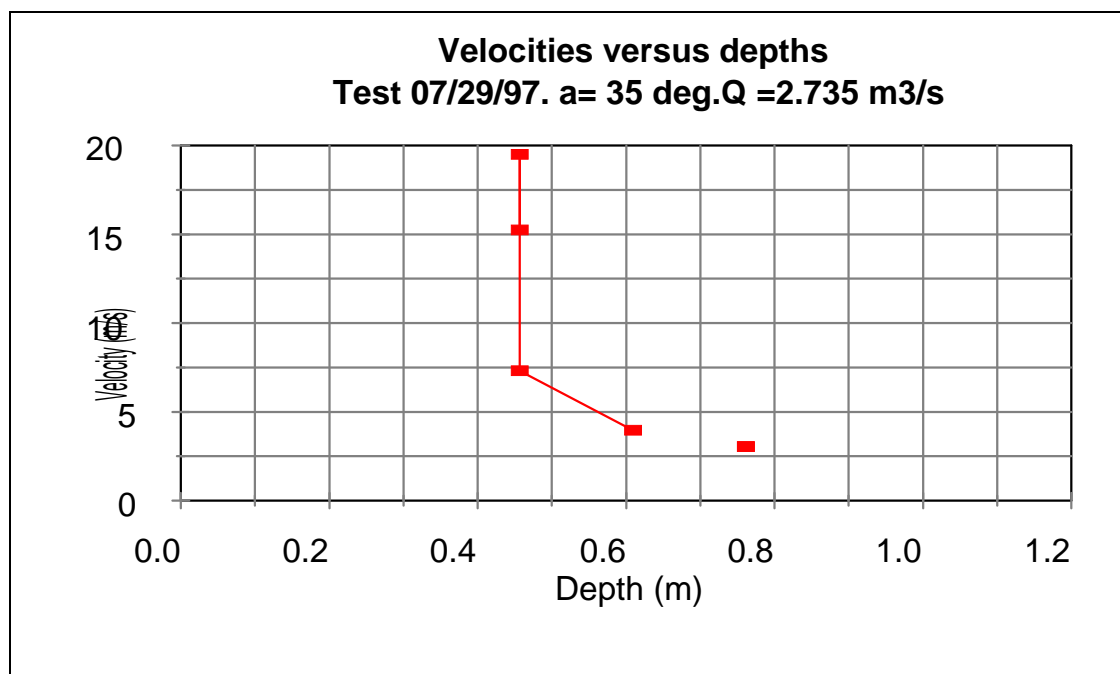


Figure H.2. Dam Foundation Erosion Studies -- velocities versus depth, 07/09/97.

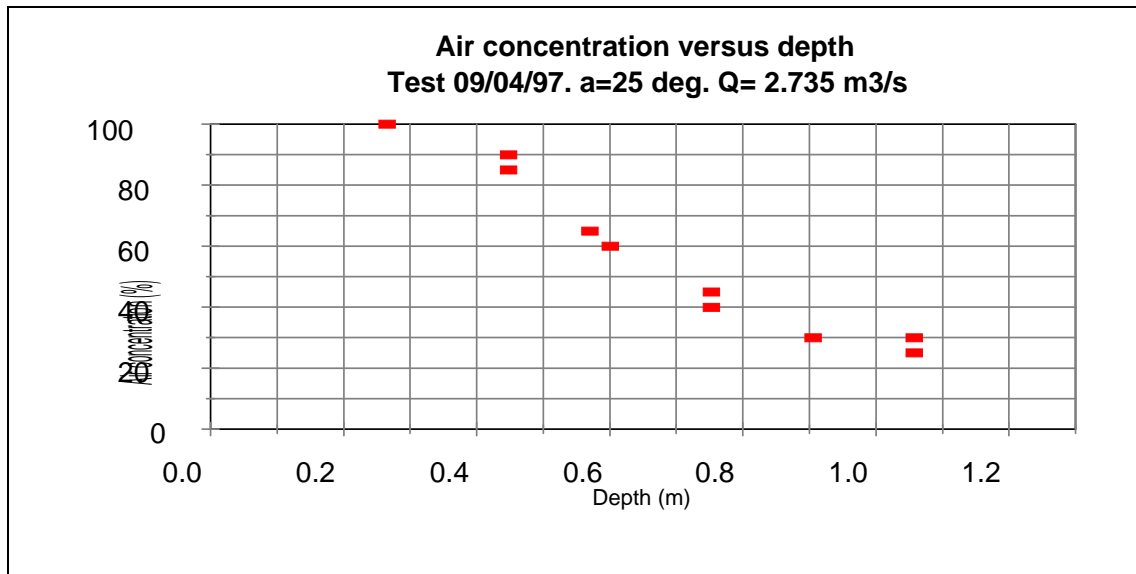


Figure H.3. Dam Foundation Erosion Studies -- air concentration versus depth, 09/04/97.

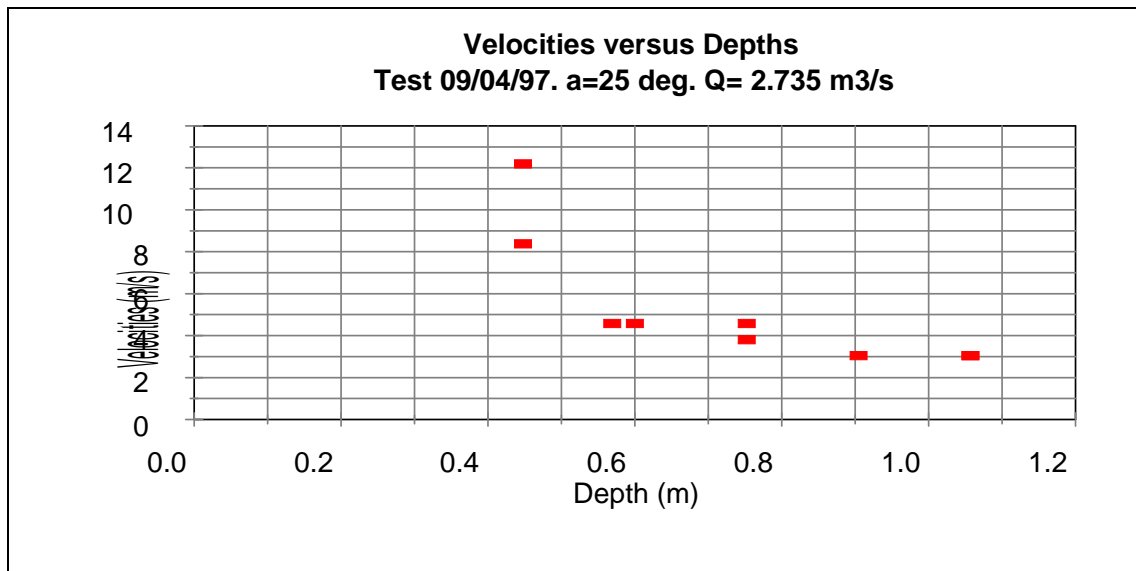


Figure H.4. Dam Foundation Erosion Studies -- velocities versus depths, 09/04/97.

APPENDIX I

FORCES AT THE BOTTOM OF A BLOCK,
 $Q = 1.13 \text{ m}^3/\text{s}$ (40 cfs), $1.27 \text{ m}^3/\text{s}$ (45 cfs), AND $1.42 \text{ m}^3/\text{s}$ (50 cfs)

APPENDIX I

FORCES AT THE BOTTOM OF A BLOCK, $Q = 1.13 \text{ m}^3/\text{s}$ (40 cfs), $1.27 \text{ m}^3/\text{s}$ (45 cfs), AND $1.42 \text{ m}^3/\text{s}$ (50 cfs)

Manometer readings of the piezometers installed along and across the simulated fractured rock testing surface are given in this appendix. Measurements were taken at $1.13 \text{ m}^3/\text{s}$ (40 cfs), $1.27 \text{ m}^3/\text{s}$ (45 cfs), and $1.42 \text{ m}^3/\text{s}$ (50 cfs). Average forces on the bottom of the blocks were calculated for the test conducted at $1.42 \text{ m}^3/\text{s}$ (50 cfs).

Table I.1. Dam Foundation Erosion Studies -- "fractured rock" test 1997, location of piezometer taps in bricks.

Tap Description							
tap #1 is at first groove from top on back side of brick							
tap #2 is at last groove from top on back side of brick							
C1 - center, tap #1							
C2 - center, tap #2							
NDP - North depth probe tap							
EDP - East depth probe tap							
WDP - West depth probe tap							
Tap Numbering: Direction from center_Distance from center_tap #							
example: N41 - four feet north of center, tap #1							
W82 - eight feet west of center, tap #2							
(x = 0, y = 0) = northwest inside corner of box							
x - North to South							
y - West to East							
Survey Data							
Tap	X (ft)	Y (ft)	Elevation (ft)	B.M. Reading (El. 9.89)	H.I.	Tap Reading	Tap Elevation
EDP	40.00	0.00	-				
WDP	40.00	30.00	-				
NDP	0.00	15.00	-				
S81	22.50	15.29	6.61	2.65	12.54	5.93	6.61
S82	23.17	15.29	5.91	2.65	12.54	6.63	5.91
S41	18.25	15.25	6.60	2.70	12.59	5.99	6.60
S42	18.92	15.25	5.93	2.70	12.59	6.66	5.93
C1	14.50	15.29	6.65	2.57	12.46	5.81	6.65
C2	15.17	15.29	5.91	2.57	12.46	6.55	5.91
N41	10.63	15.33	6.64	2.57	12.46	5.82	6.64
N42	11.33	15.33	5.91	2.57	12.46	6.55	5.91
N81	6.79	15.38	6.63	2.66	12.55	5.92	6.63
N82	7.50	15.38	5.91	2.66	12.55	6.64	5.91
E81	14.54	23.67	6.67	2.57	12.46	5.79	6.67
E82	15.21	23.67	5.95	2.57	12.46	6.51	5.95
E41	14.54	19.17	6.63	2.57	12.46	5.83	6.63
E42	15.21	19.17	5.90	2.57	12.46	6.56	5.90
W41	14.50	11.46	6.60	2.57	12.46	5.86	6.60
W42	15.17	11.46	5.92	2.57	12.46	6.54	5.92
W81	14.67	7.63	6.69	2.57	12.46	5.77	6.69
W82	15.33	7.63	5.92	2.57	12.46	6.54	5.92

Table I.2. Manometer readings.

DFE - "Fractured Rock" Test 1997
Manometer Readings

Tap	Elevation (ft)	Date 10/16/97 Discharge = 40 cfs			Date 10/16/97 Discharge = 45 cfs			Date 10/21/97 Discharge = 50 cfs		
		Manometer Reading (in.)	Manometer Elevation (ft)	Pressure Head (ft)	Manometer Reading (in.)	Manometer Elevation (ft)	Pressure Head (ft)	Manometer Reading (in.)	Manometer Elevation (ft)	Pressure Head (ft)
EDP	-	7.75	0.65	7.65	7.63	0.64	7.64	8.25	0.69	7.69
WDP	-	7.50	0.63	7.63	7.50	0.63	7.63	7.88	0.66	7.66
NDP	-	9.75	0.81	7.81	10.50	0.88	7.88	11.25	0.94	7.94
S81	6.61	8.50	0.71	7.71	8.00	0.67	7.67	9.19	0.77	7.77
S82	5.91	8.63	0.72	7.72	9.25	0.77	7.77	9.50	0.79	7.79
S41	6.60	8.13	0.68	7.68	8.63	0.72	7.72	8.63	0.72	7.72
S42	5.93	8.25	0.69	7.69	8.75	0.73	7.73	8.75	0.73	7.73
C1	6.65	8.41	0.70	7.70	11.50	0.96	7.96	6.75	0.56	7.56
C2	5.91	8.41	0.70	7.70	12.75	1.06	8.06	14.13	1.18	8.18
N41	6.64	7.13	0.59	7.59	10.00	0.83	7.83	10.13	0.84	7.84
N42	5.91	9.38	0.78	7.78	10.38	0.86	7.86	9.94	0.83	7.83
N81	6.63	9.06	0.76	7.76	9.88	0.82	7.82	10.63	0.89	7.89
N82	5.91	9.38	0.78	7.78	10.00	0.83	7.83	10.63	0.89	7.89
E81	6.67	8.25	0.69	7.69	9.13	0.76	7.76	9.50	0.79	7.79
E82	5.95	8.38	0.70	7.70	9.50	0.79	7.79	10.38	0.86	7.86
E41	6.63	8.50	0.71	7.71	10.13	0.84	7.84	9.63	0.80	7.80
E42	5.90	9.00	0.75	7.75	10.38	0.86	7.86	14.25	1.19	8.19
W41	6.60	8.00	0.67	7.67	11.25	0.94	7.94	12.00	1.00	8.00
W42	5.92	9.56	0.80	7.80	11.69	0.97	7.97	14.25	1.19	8.19
W81	6.69	8.00	0.67	7.67	8.63	0.72	7.72	9.50	0.79	7.79
W82	5.92	9.00	0.75	7.75	10.38	0.86	7.86	11.75	0.98	7.98

Tap	Date 10/21/97 Discharge = 40 cfs			Date 10/21/97 Discharge = 45 cfs		
	Manometer Reading (in.)	Manometer Elevation (ft)	Pressure Head (in.)	Manometer Reading (ft)	Manometer Elevation (ft)	Pressure Head (ft)
EDP	7.56	0.63	7.63	8.00	0.67	7.67

Table I.3. Summary of piezometer data -- USC units.

	X (ft)	Tap	Y (ft)	40 cfs		40 cfs		45 cfs		45 cfs		50 cfs	
				Manometer		Manometer		Manometer		Manometer		Manometer	
				Tap 1 (Upper) - Elevation (ft)	Tap 2 (Lower) - Elevation (ft)	Tap 1 (Upper) - Elevation (ft)	Tap 2 (Lower) - Elevation (ft)	Tap 1 (Upper) - Elevation (ft)	Tap 2 (Lower) - Elevation (ft)	Tap 1 (Upper) - Elevation (ft)	Tap 2 (Lower) - Elevation (ft)	Tap 1 (Upper) - Elevation (ft)	Tap 2 (Lower) - Elevation (ft)
N-S-1	0.00	NDP	15.00	7.81				7.88				7.94	
	6.79	N81	15.38	7.76				7.82				7.89	
	10.63	N41	15.33	7.59				7.83				7.84	
	14.50	C1	15.29	7.70				7.96				7.56	
	18.25	S41	15.25	7.68				7.72				7.72	
	22.50	S81	15.29	7.71				7.67				7.77	
	40.00	WDP	30.00	7.63				7.63				7.66	
N-S-2	0.00	NDP	15.00		7.81						7.88		7.94
	7.50	N82	15.38		7.78						7.83		7.89
	11.33	N42	15.33		7.78						7.86		7.83
	15.17	C2	15.29		7.70						8.06		8.18
	18.92	S42	15.25		7.69						7.73		7.73
	23.17	S82	15.29		7.72						7.77		7.79
	40.00	WDP	30.00		7.63						7.63		7.66
W-E-1	14.67	W81	7.63	7.67				7.72				7.79	
	14.50	W41	11.46	7.67				7.94				8.00	
	14.50	C1	15.29	7.70				7.96				7.56	
	14.54	E41	19.17	7.71				7.84				7.80	
	14.54	E81	23.67	7.69				7.76				7.79	
W-E-2	15.33	W82	7.63	7.75				7.86				7.98	
	15.17	W42	11.46	7.80				7.97				8.19	
	15.17	C2	15.29	7.70				8.06				8.18	
	15.21	E42	19.17	7.75				7.86				8.19	
	15.21	E82	23.67	7.70				7.79				7.86	

Table I.4. Summary of piezometer data -- metric.

	X (m)	Tap	Y (m)	1.13 m³/s		1.27 m³/s		1.42 m³/s	
				1.13 m³/s		1.27 m³/s		1.42 m³/s	
				Manometer Tap 1 (Upper) - Elevation (m)	Manometer Tap 2 (Lower) - Elevation (m)	Manometer Tap 1 (Upper) - Elevation (m)	Manometer Tap 2 (Lower) - Elevation (m)	Manometer Tap 1 (Upper) - Elevation (m)	Manometer Tap 2 (Lower) - Elevation (m)
N-S-1	0.00	NDP	4.57	2.38		2.40		2.42	
	2.07	N81	4.69	2.36		2.38		2.40	
	3.24	N41	4.67	2.31		2.39		2.39	
	4.42	C1	4.66	2.35		2.43		2.31	
	5.56	S41	4.65	2.34		2.35		2.35	
	6.86	S81	4.66	2.35		2.34		2.37	
	2.29	N82	4.69		2.37		2.39		2.40
	3.45	N42	4.67		2.37		2.40		2.39
	4.62	C2	4.66		2.35		2.46		2.49
	5.77	S42	4.65		2.34		2.36		2.36
W-E-1	7.06	S82	4.66		2.35		2.37		2.37
	0.00								2.33
	8.00								2.33
	4.47	W81	2.32	2.34		2.35		2.37	
	4.42	W41	3.49	2.34		2.42		2.44	
	4.42	C1	4.66	2.35		2.43		2.31	
	4.43	E41	5.84	2.35		2.39		2.38	
	4.43	E81	7.21	2.34		2.37		2.37	
W-E-2	0.00	W82	2.33		2.36		2.40		2.43
	4.67	W42	3.49		2.38		2.43		2.50
	4.62	C2	4.66		2.35		2.46		2.49
	4.62	E42	5.84		2.36		2.40		2.50
	4.64	E82	7.21		2.35		2.37		2.40

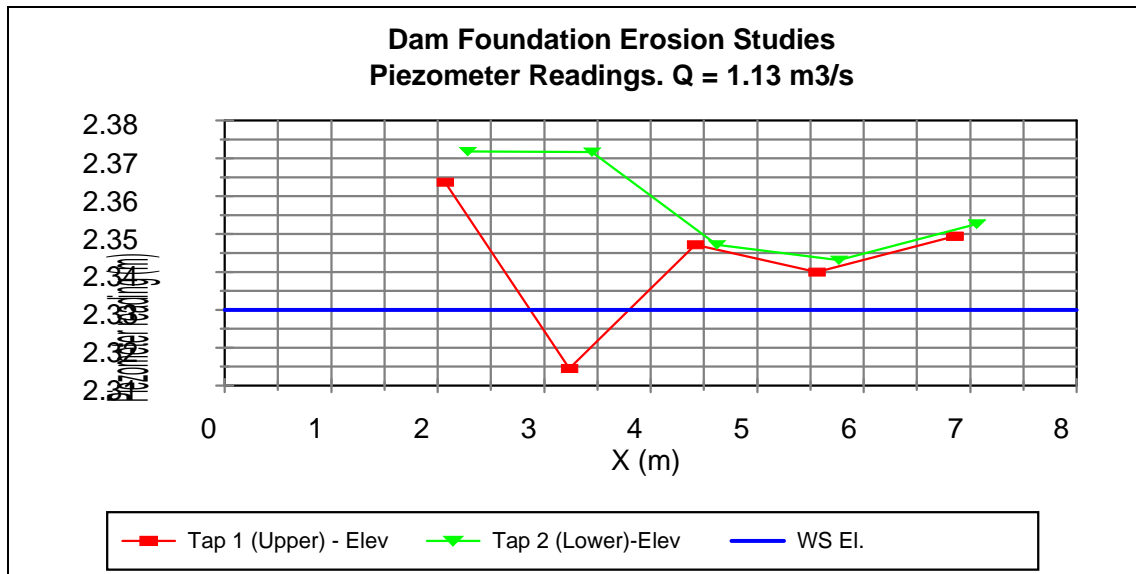


Figure I.1. Dam Foundation Erosion Studies -- piezometer readings, $Q = 1.13 \text{ m}^3/\text{s}$.

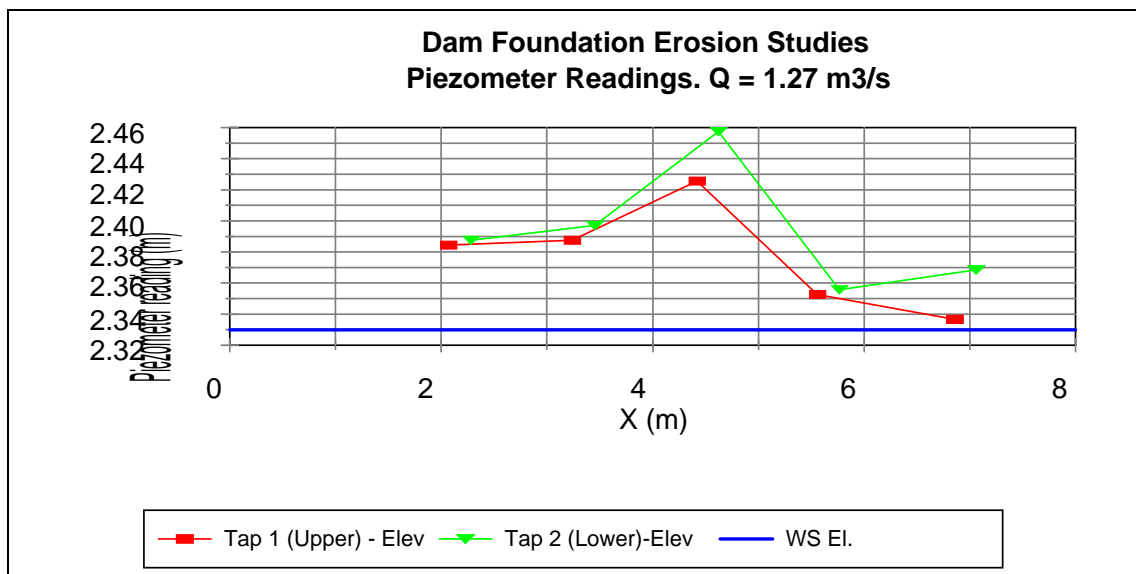


Figure I.2. Dam Foundation Erosion Studies -- piezometer readings, $Q = 1.27 \text{ m}^3/\text{s}$.

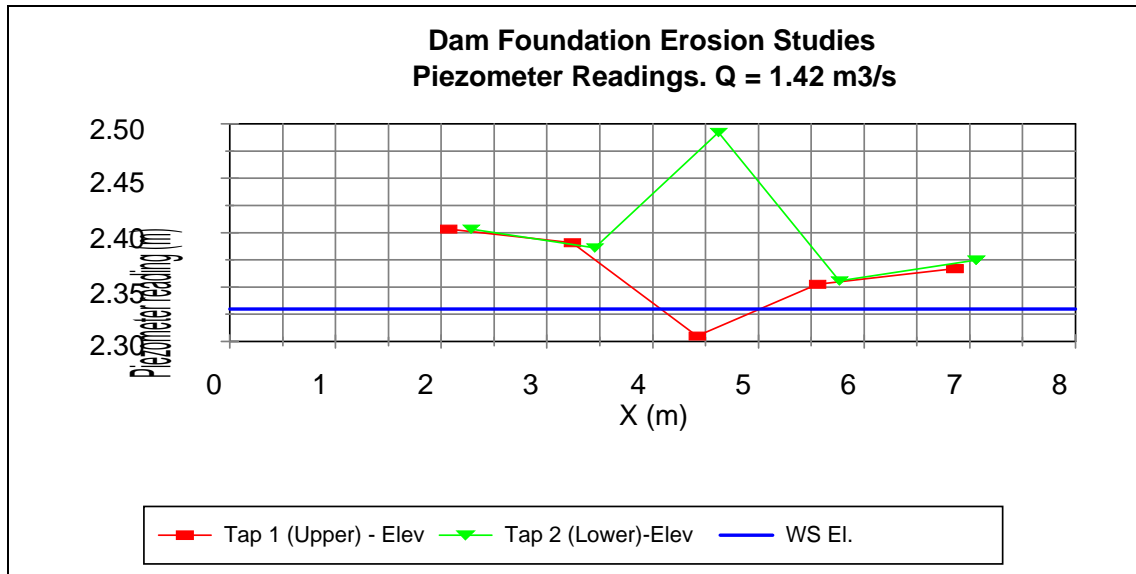


Figure I.3. Dam Foundation Erosion Studies -- piezometer readings, $Q = 1.42 \text{ m}^3/\text{s}$.

Table I.5. Heads in excess of static head close to the region of impingement.

Tap No 2					
Discharge (cfs)		40			
Water Surface Elevation:		7.64			
Four feet around the center					
	Reading	Head in Excess	Pressure	Calculated Force	
	(ft)	of Static	(lb/ft ²)	Bottom	
		(ft)		(lb)	
C2	7.70	0.06	3.74		0.52
N42	7.78	0.14	8.74		1.21
S42	7.69	0.05	3.12		0.43
W42	7.80	0.16	9.98		1.39
E42	7.75	0.11	6.86		0.95

Tap No 2					
Discharge (cfs)		45			
Water Surface Elevation:		7.64			
Four feet around the center					
	Reading	Head in Excess		Pressure	Calculated Force
	(ft)	of Static		(lb/ft ²)	Bottom
		(ft)			(lbs)
C2	8.06	0.42		26.21	3.64
N42	7.86	0.22		13.73	1.91
S42	7.73	0.09		5.62	0.78
W42	7.97	0.33		20.59	2.86
E42	7.86	0.22		13.73	1.91

Tap No 2					
Discharge (cfs)		50			
Water Surface Elevation:		7.68			
Four feet around the center					
	Reading	Head in Excess of Static		Pressure	Calculated Force Bottom
	(ft)	(ft)		(lb/ft ²)	(lbs)
C2	8.18	0.50		31.20	4.33
N42	7.83	0.15		9.36	1.30
S42	7.73	0.05		3.12	0.43
W42	8.19	0.51		31.82	4.42
E42	8.19	0.51		31.82	4.42

Block Characteristics	
Weight (lb)	17.00
Specific gravity	1.65
Specific weight (lb/ft ³)	102.96
Calculated volume (ft ³)	0.165
Calculated buoyancy (lb)	10.30
Calculated submerged weight (lb)	6.70

APPENDIX J

CALCULATIONS OF INTERLOCKING FACTOR

APPENDIX J

CALCULATIONS OF INTERLOCKING FACTOR

Values for the interlocking factor were found assuming the ratio of moment arms ranges from 0.5 to 1.5 and the lift coefficient to drag coefficient ranges from 0.1 to 0.4. The values of the downstream slope taken at the DFE facility were used. It was found that the interlocking factor does not vary significantly for the range of moment arms and lift coefficient ratios given above.

Table J.1. Values of the function $(\sin \theta + (K_1 a / K_2 c) \cos \theta) / (1 + K_3 (K_1 a / K_2 c))$ -- $K_3 = 0.1$.

Parameter	Value
$(K_1 a) / (K_2 c)$	0.50
K_3	0.10

θ (deg.)	$\sin \theta$	$\cos \theta$	$(\sin \theta + K_1 a / (K_2 c) \cos \theta) / (1 + K_3 (K_1 a / (K_2 c)))$
15.0	0.259	0.966	0.841
17.5	0.301	0.954	0.861
20.0	0.342	0.940	0.879
22.5	0.383	0.924	0.897
25.0	0.423	0.906	0.913
27.5	0.462	0.887	0.929
30.0	0.500	0.866	0.943
Mean			0.895
SD			0.034
CV			0.038

Parameter	Value
$(K_1 a) / (K_2 c)$	0.75
K_3	0.10

θ (deg.)	$\sin \theta$	$\cos \theta$	$(\sin \theta + K_1 a / (K_2 c) \cos \theta) / (1 + K_3 (K_1 a / (K_2 c)))$
15.0	0.259	0.966	0.956
17.5	0.301	0.954	0.972
20.0	0.342	0.940	0.987
22.5	0.383	0.924	1.000
25.0	0.423	0.906	1.013
27.5	0.462	0.887	1.024
30.0	0.500	0.866	1.034
Mean			0.998
SD			0.026
CV			0.026

Table J.1 (cont.). Values of the function $(\sin \theta + (K_1 a / K_2 c) \cos \theta) / (1 + K_3 (K_1 a / K_2 c))$ -- $K_3 = 0.1$.

Parameter	Value
$(K_1 a) / (K_2 c)$	1.00
K_3	0.10

θ (deg.)	$\sin \theta$	$\cos \theta$	$(\sin \theta + K_1 a / (K_2 c) \cos \theta) / (1 + K_3 (K_1 a / (K_2 c)))$
15.0	0.259	0.966	1.055
17.5	0.301	0.954	1.068
20.0	0.342	0.940	1.079
22.5	0.383	0.924	1.090
25.0	0.423	0.906	1.099
27.5	0.462	0.887	1.107
30.0	0.500	0.866	1.114
Mean			1.088
SD			0.020
CV			0.018

Parameter	Value
$(K_1 a) / (K_2 c)$	1.25
K_3	0.10

θ (deg.)	$\sin \theta$	$\cos \theta$	$(\sin \theta + K_1 a / (K_2 c) \cos \theta) / (1 + K_3 (K_1 a / (K_2 c)))$
15.0	0.259	0.966	1.142
17.5	0.301	0.954	1.152
20.0	0.342	0.940	1.161
22.5	0.383	0.924	1.169
25.0	0.423	0.906	1.176
27.5	0.462	0.887	1.182
30.0	0.500	0.866	1.186
Mean			1.167
SD			0.015
CV			0.013

Table J.1 (cont.). Values of the function $(\sin \theta + (K_1 a / K_2 c) \cos \theta) / (1 + K_3 (K_1 a / K_2 c))$ -- $K_3 = 0.1$.

Parameter	Value
$(K_1 a) / (K_2 c)$	1.50
K_3	0.10

θ (deg.)	$\sin \theta$	$\cos \theta$	$(\sin \theta + K_1 a / (K_2 c) \cos \theta) / (1 + K_3 (K_1 a / (K_2 c)))$
15.0	0.259	0.966	1.219
17.5	0.301	0.954	1.227
20.0	0.342	0.940	1.234
22.5	0.383	0.924	1.240
25.0	0.423	0.906	1.245
27.5	0.462	0.887	1.248
30.0	0.500	0.866	1.251
Mean			1.238
SD			0.011
CV			0.009

$(K_1 a) / (K_2 c)$	$(\sin \theta + K_1 a / (K_2 c) \cos \theta) / (1 + K_3 (K_1 a / (K_2 c)))$
0.500	0.895
0.750	0.998
1.000	1.088
1.250	1.167
1.500	1.238
Mean	1.077
SD	0.121
CV	0.113

Table J.2. Values of the function $(\sin \theta + (K_1 a / K_2 c) \cos \theta) / (1 + K_3 (K_1 a / K_2 c))$ — $K_3 = 0.2$.

Parameter	Value
$(K_1 a) / (K_2 c)$	0.50
K_3	0.20

θ (deg.)	$\sin \theta$	$\cos \theta$	$(\sin \theta + K_1 a / (K_2 c) \cos \theta) / (1 + K_3 (K_1 a / (K_2 c)))$
15.0	0.259	0.966	0.821
17.5	0.301	0.954	0.841
20.0	0.342	0.940	0.859
22.5	0.383	0.924	0.876
25.0	0.423	0.906	0.892
27.5	0.462	0.887	0.907
30.0	0.500	0.866	0.921
Mean			0.874
SD			0.033
CV			0.038

Parameter	Value
$(K_1 a) / (K_2 c)$	0.75
K_3	0.20

θ (deg.)	$\sin \theta$	$\cos \theta$	$(\sin \theta + K a / (K_2 c) \cos \theta) / (1 + K_3 (K_1 a / (K_2 c)))$
15.0	0.259	0.966	0.925
17.5	0.301	0.954	0.940
20.0	0.342	0.940	0.954
22.5	0.383	0.924	0.967
25.0	0.423	0.906	0.979
27.5	0.462	0.887	0.990
30.0	0.500	0.866	1.000
Mean			0.965
SD			0.025
CV			0.026

Table J.2 (cont.). Values of the function $(\sin \theta + (K_1 a/K_2 c) \cos \theta)/(1+K_3(K_1 a/K_2 c))$ — $K_3 = 0.2$.

Parameter	Value
$(K_1 a)/(K_2 c)$	1.00
K_3	0.20

θ (deg.)	$\sin \theta$	$\cos \theta$	$(\sin \theta + K_1 a/(K_2 c) \cos \theta)/(1 + K_3 (K_1 a/(K_2 c)))$
15.0	0.259	0.966	1.010
17.5	0.301	0.954	1.022
20.0	0.342	0.940	1.033
22.5	0.383	0.924	1.043
25.0	0.423	0.906	1.052
27.5	0.462	0.887	1.060
30.0	0.500	0.866	1.067
Mean			1.041
SD			0.019
CV			0.018

Parameter	Value
$(K_1 a)/(K_2 c)$	1.25
K_3	0.20

θ (deg.)	$\sin \theta$	$\cos \theta$	$(\sin \theta + K_1 a/(K_2 c) \cos \theta)/(1 + K_3 (K_1 a/(K_2 c)))$
15.0	0.259	0.966	1.083
17.5	0.301	0.954	1.093
20.0	0.342	0.940	1.102
22.5	0.383	0.924	1.109
25.0	0.423	0.906	1.116
27.5	0.462	0.887	1.121
30.0	0.500	0.866	1.125
Mean			1.107
SD			0.014
CV			0.013

Table J.2 (cont.). Values of the function $(\sin \theta + (K_1 a / K_2 c) \cos \theta) / (1 + K_3 (K_1 a / K_2 c))$ — $K_3 = 0.2$.

Parameter	Value
$(K_1 a) / (K_2 c)$	1.50
K_3	0.20

θ (deg.)	$\sin \theta$	$\cos \theta$	$(\sin \theta + K_1 a / (K_2 c) \cos \theta) / (1 + K_3 (K_1 a / (K_2 c)))$
15.0	0.259	0.966	1.146
17.5	0.301	0.954	1.154
20.0	0.342	0.940	1.161
22.5	0.383	0.924	1.166
25.0	0.423	0.906	1.171
27.5	0.462	0.887	1.174
30.0	0.500	0.866	1.176
Mean			1.164
SD			0.010
CV			0.009

$(K_1 a) / (K_2 c)$	$(\sin \theta + K_1 a / (K_2 c) \cos \theta) / (1 + K_3 (K_1 a / (K_2 c)))$
0.500	0.874
0.750	0.965
1.000	1.041
1.250	1.107
1.500	1.164
Mean	1.030
SD	0.103
CV	0.100

Table J.3. Values of the function $(\sin \theta + (K_1 a / K_2 c) \cos \theta) / (1 + K_3 (K_1 a / K_2 c))$ — $K_3 = 0.3$.

Parameter	Value
$(K_1 a) / (K_2 c)$	0.50
K_3	0.30

θ (deg.)	$\sin \theta$	$\cos \theta$	$(\sin \theta + K_1 a / (K_2 c) \cos \theta) / (1 + K_3 (K_1 a / (K_2 c)))$
15.0	0.259	0.966	0.803
17.5	0.301	0.954	0.822
20.0	0.342	0.940	0.840
22.5	0.383	0.924	0.857
25.0	0.423	0.906	0.873
27.5	0.462	0.887	0.887
30.0	0.500	0.866	0.901
Mean			0.855
SD			0.033
CV			0.038

Parameter	Value
$(K_1 a) / (K_2 c)$	0.75
K_3	0.30

θ (deg.)	$\sin \theta$	$\cos \theta$	$(\sin \theta + K_1 a / (K_2 c) \cos \theta) / (1 + K_3 (K_1 a / (K_2 c)))$
15.0	0.259	0.966	0.896
17.5	0.301	0.954	0.911
20.0	0.342	0.940	0.924
22.5	0.383	0.924	0.937
25.0	0.423	0.906	0.949
27.5	0.462	0.887	0.959
30.0	0.500	0.866	0.969
Mean			0.935
SD			0.024
CV			0.026

Table J.3 (cont.). Values of the function $(\sin \theta + (K_1 a / K_2 c) \cos \theta) / (1 + K_3 (K_1 a / K_2 c))$ — $K_3 = 0.3$.

Parameter	Value
$(K_1 a) / (K_2 c)$	1.00
K_3	0.30

θ (deg.)	$\sin \theta$	$\cos \theta$	$(\sin \theta + K_1 a / (K_2 c) \cos \theta) / (1 + K_3 (K_1 a / (K_2 c)))$
15.0	0.259	0.966	0.971
17.5	0.301	0.954	0.982
20.0	0.342	0.940	0.993
22.5	0.383	0.924	1.003
25.0	0.423	0.906	1.011
27.5	0.462	0.887	1.019
30.0	0.500	0.866	1.025
Mean			1.000
SD			0.018
CV			0.018

Parameter	Value
$(K_1 a) / (K_2 c)$	1.25
K_3	0.30

θ (deg.)	$\sin \theta$	$\cos \theta$	$(\sin \theta + K_1 a / (K_2 c) \cos \theta) / (1 + K_3 (K_1 a / (K_2 c)))$
15.0	0.259	0.966	1.033
17.5	0.301	0.954	1.042
20.0	0.342	0.940	1.050
22.5	0.383	0.924	1.057
25.0	0.423	0.906	1.064
27.5	0.462	0.887	1.069
30.0	0.500	0.866	1.073
Mean			1.055
SD			0.014
CV			0.013

Table J.3 (cont.). Values of the function $(\sin \theta + (K_1 a / K_2 c) \cos \theta) / (1 + K_3 (K_1 a / K_2 c))$ — $K_3 = 0.3$.

Parameter	Value
$(K_1 a) / (K_2 c)$	1.50
K_3	0.30

θ (deg.)	$\sin \theta$	$\cos \theta$	$(\sin \theta + K_1 a / (K_2 c) \cos \theta) / (1 + K_3 (K_1 a / (K_2 c)))$
15.0	0.259	0.966	1.085
17.5	0.301	0.954	1.093
20.0	0.342	0.940	1.099
22.5	0.383	0.924	1.104
25.0	0.423	0.906	1.109
27.5	0.462	0.887	1.112
30.0	0.500	0.866	1.114
Mean			1.102
SD			0.010
CV			0.009

$(K_1 a) / (K_2 c)$	$(\sin \theta + K_1 a / (K_2 c) \cos \theta) / (1 + K_3 (K_1 a / (K_2 c)))$
0.500	0.855
0.750	0.935
1.000	1.000
1.250	1.055
1.500	1.102
Mean	0.989
SD	0.087
CV	0.088

Table J.4. Values of the function $(\sin \theta + (K_1 a / K_2 c) \cos \theta) / (1 + K_3 (K_1 a / K_2 c))$ — $K_3 = 0.4$.

Parameter	Value
$(K_1 a) / (K_2 c)$	0.50
K_3	0.40

θ (deg.)	$\sin \theta$	$\cos \theta$	$(\sin \theta + K_1 a / (K_2 c) \cos \theta) / (1 + K_3 (K_1 a / (K_2 c)))$
15.0	0.259	0.966	0.786
17.5	0.301	0.954	0.805
20.0	0.342	0.940	0.823
22.5	0.383	0.924	0.839
25.0	0.423	0.906	0.854
27.5	0.462	0.887	0.869
30.0	0.500	0.866	0.882
Mean			0.837
SD			0.032
CV			0.038

Parameter	Value
$(K_1 a) / (K_2 c)$	0.75
K_3	0.40

θ (deg.)	$\sin \theta$	$\cos \theta$	$(\sin \theta + K_1 a / (K_2 c) \cos \theta) / (1 + K_3 (K_1 a / (K_2 c)))$
15.0	0.259	0.966	0.870
17.5	0.301	0.954	0.884
20.0	0.342	0.940	0.897
22.5	0.383	0.924	0.910
25.0	0.423	0.906	0.921
27.5	0.462	0.887	0.931
30.0	0.500	0.866	0.940
Mean			0.908
SD			0.024
CV			0.026

Table J.4 (cont.). Values of the function $(\sin \theta + (K_1 a / K_2 c) \cos \theta) / (1 + K_3 (K_1 a / K_2 c))$ — $K_3 = 0.4$.

Parameter	Value
$(K_1 a) / (K_2 c)$	1.00
K_3	0.40

θ (deg.)	$\sin \theta$	$\cos \theta$	$(\sin \theta + K_1 a / (K_2 c) \cos \theta) / (1 + K_3 (K_1 a / (K_2 c)))$
15.0	0.259	0.966	0.935
17.5	0.301	0.954	0.947
20.0	0.342	0.940	0.957
22.5	0.383	0.924	0.966
25.0	0.423	0.906	0.974
27.5	0.462	0.887	0.982
30.0	0.500	0.866	0.988
Mean			0.964
SD			0.018
CV			0.018

Parameter	Value
$(K_1 a) / (K_2 c)$	1.25
K_3	0.40

θ (deg.)	$\sin \theta$	$\cos \theta$	$(\sin \theta + K_1 a / (K_2 c) \cos \theta) / (1 + K_3 (K_1 a / (K_2 c)))$
15.0	0.259	0.966	0.989
17.5	0.301	0.954	0.998
20.0	0.342	0.940	1.006
22.5	0.383	0.924	1.012
25.0	0.423	0.906	1.018
27.5	0.462	0.887	1.023
30.0	0.500	0.866	1.027
Mean			1.010
SD			0.013
CV			0.013

Table J.4 (cont.). Values of the function $(\sin \theta + (K_1 a / K_2 c) \cos \theta) / (1 + K_3 (K_1 a / K_2 c))$ — $K_3 = 0.4$.

Parameter	Value
$(K_1 a) / (K_2 c)$	1.50
K_3	0.40

θ (deg.)	$\sin \theta$	$\cos \theta$	$(\sin \theta + K_1 a / (K_2 c) \cos \theta) / (1 + K_3 (K_1 a / (K_2 c)))$
15.0	0.259	0.966	1.033
17.5	0.301	0.954	1.040
20.0	0.342	0.940	1.046
22.5	0.383	0.924	1.051
25.0	0.423	0.906	1.055
27.5	0.462	0.887	1.058
30.0	0.500	0.866	1.060
Mean			1.049
SD			0.009
CV			0.009

$(K_1 a) / (K_2 c)$	$(\sin \theta + K_1 a / (K_2 c) \cos \theta) / (1 + K_3 (K_1 a / (K_2 c)))$
0.500	0.837
0.750	0.908
1.000	0.964
1.250	1.010
1.500	1.049
Mean	0.954
SD	0.075
CV	0.079

Table J.5. Summary of average values of interlocking factor.

$(K_1 a)/(K_2 c)$	$K_3 = 0.1$	$K_3 = 0.2$	$K_3 = 0.3$	$K_3 = 0.4$
0.500	0.895			
0.750	0.998			
1.000	1.088			
1.250	1.167			
1.500	1.238			
0.500		0.874		
0.750		0.965		
1.000		1.041		
1.250		1.107		
1.500		1.164		
0.500			0.855	
0.750			0.935	
1.000			1.000	
1.250			1.055	
1.500			1.102	
0.500				0.837
0.750				0.908
1.000				0.964
1.250				1.010
1.500				1.049

APPENDIX K

PREDICTION OF DRAWDOWN DEPTHS USING
ZAHOOR'S EQUATION

APPENDIX K

PREDICTION OF DRAWDOWN DEPTHS USING ZAHOOR'S EQUATION

Zahoor's equation was used to predict the drawdown depth. The drawdown depth is the difference in elevation of the upstream tailwater surface with respect to the downstream tailwater surface. The calculations and a graph of the predicted values versus the measured values of drawdown is given in this Appendix. Zahoor's equation is given below:

$$h_c = d_2 \sqrt{F_2^2 \left(1 - \frac{V_i \cos \delta}{V_2} \right) + \left(\frac{TW}{d_2} \right)^2} \quad (K.1)$$

where: TW = water depth in the basin, without drawdown;

h_c = upstream TW depth;

d_2 = water depth in exit channel;

V_2 = flow velocity in exit channel;

F_2 = Froude number in exit channel;

V_i = flow of incoming jet;

δ = entrance angle of jet into basin; and

h_o = drawdown depth = TW - h_c .

Table K.1. Calculation of drawdown depth using Zahoor's equation.

Study	q (m ² /s)	Y (m)	b _o (m)	z (m)	α (deg.)	V _o (m/s)	V _i (m/s)	b _i (m)	cos δ	TW (m)	D (m)	V ₂ (m/s)	Fr ₂	h _c (m)	H _o -pred. (m)	H _o -meas. (m)
DFE	0.897	1.55	0.087	3.48	15	10.28	13.19	0.077	0.980	0.57	2.12	1.57	0.345	1.99	0.14	N/A
DFE	0.897	1.50	0.087	3.12	15	10.28	12.92	0.078	0.979	0.85	2.35	1.06	0.220	2.18	0.17	0.09
DFE	0.897	1.83	0.087	3.79	15	10.28	13.41	0.076	0.981	0.27	2.09	3.38	0.747	2.04	0.05	0.05
DFE	0.897	0.99	0.087	2.87	15	10.28	12.73	0.078	0.979	1.85	2.84	0.49	0.092	2.57	0.26	N/A
DFE	0.897	0.94	0.087	2.94	25	10.28	12.78	0.078	0.947	1.80	2.74	0.50	0.096	2.47	0.27	0.05
DFE	0.897	1.03	0.087	3.55	25	10.28	13.24	0.077	0.950	1.17	2.20	0.76	0.165	1.92	0.28	0.12
DFE	0.897	0.88	0.087	3.60	35	10.28	13.28	0.077	0.914	1.16	2.04	0.77	0.173	1.73	0.31	0.19
DFE	0.897	0.63	0.087	2.98	35	10.28	12.81	0.078	0.908	1.80	2.43	0.50	0.102	2.10	0.33	0.11
DFE	0.897	0.91	0.087	3.92	35	10.28	13.51	0.076	0.917	0.84	1.75	1.07	0.259	1.43	0.31	0.14
DFE	0.897	1.19	0.087	4.37	35	10.28	13.83	0.075	0.920	0.50	1.69	1.80	0.440	1.51	0.18	0.11
DFE	0.897	1.49	0.087	4.32	25	10.28	13.80	0.075	0.954	0.41	1.90	2.21	0.513	1.78	0.12	0.11
DFE	0.897	1.30	0.087	3.99	25	10.28	13.56	0.076	0.952	0.77	2.08	1.16	0.257	1.88	0.20	0.13
DFE-Model	178	0.56	0.041	1.22	18	4.40	6.58	0.033	0.979	0.18	0.74	0.98	0.361	0.71	0.03	N/A
DFE-Rock	0.372	0.28	0.087	4.51	15	4.26	10.32	0.056	0.994	0.21	0.49	1.77	0.807	N/A	N/A	N/A
DFE-Rock	0.650	0.56	0.087	4.45	15	7.47	11.96	0.069	0.987	0.29	0.85	2.25	0.778	0.54	0.31	N/A

Table K.2. Summary.

Measured dH (m)	Predicted dH (m)	Identity (m)
N/A	0.14	
0.09	0.17	
0.05	0.05	
N/A	0.26	
0.05	0.27	
0.12	0.28	
0.19	0.31	
0.11	0.33	
0.14	0.31	
0.11	0.18	
0.11	0.12	
0.13	0.20	
0.00		0.00
0.40		0.40

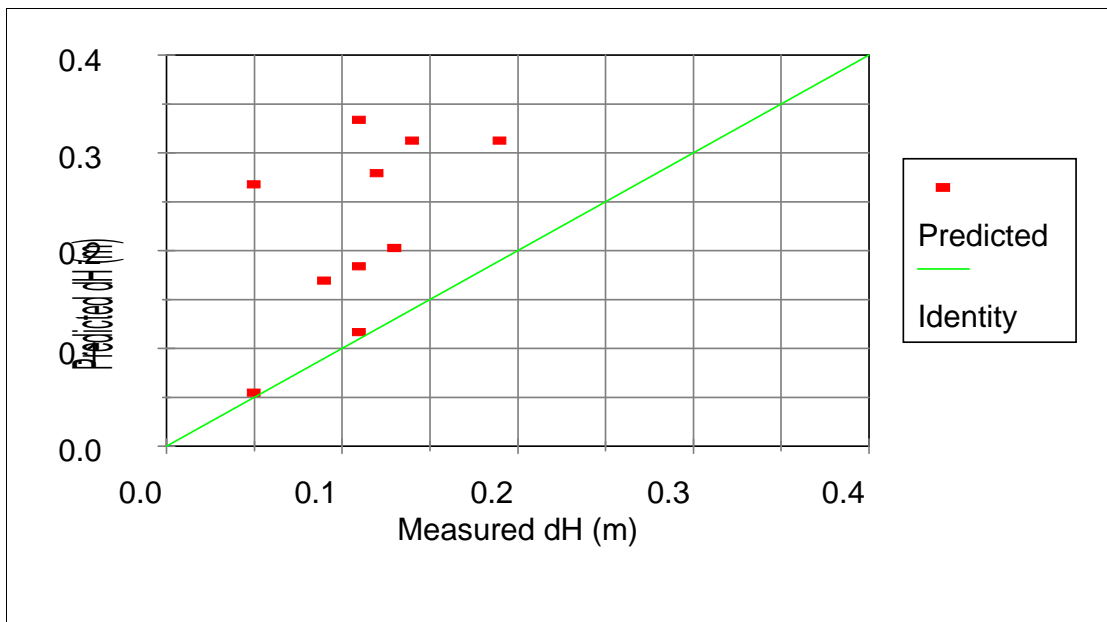


Figure K.1. Predicted values of drawdown depth using Zahoor's equation versus measured values of drawdown depth.

APPENDIX L

PREDICTION OF DEPTHS OF SCOUR USING HOFFMAN, MACHADO, AND MIRTSKHULAVA ET AL. EQUATIONS

APPENDIX L

PREDICTION OF DEPTHS OF SCOUR USING HOFFMAN,
MACHADO, AND MIRSTSKHULAVA ET AL.
EQUATIONS

The Dam Foundation Erosion data were compared to the predicted values of the depth of scour using the equations proposed by Hoffman (1998), Machado (1980), and Mirstkhulala et al. (1967). The predicted values were plotted against the measured values of scour. In all cases, the depth of scour was largely overestimated.

Table L.1. Hoffman's equation (1998).

Y-Measured (m)	TW (m)	d ₉₀ (m)	G	T °C	n (m ² /s)	d ₉₀	C _{2v}	q (m ² /s)	V _i (m/s)	cos δ	Y+TW (m)	Y-Predicted (m)
1.55	0.57	0.017	2.65	10	1.308E-06	359.93	2.9	0.897	13.50	0.980	3.19	2.62
1.50	0.85	0.017	2.65	10	1.308E-06	359.93	2.9	0.897	13.24	0.979	3.16	2.31
1.83	0.27	0.017	2.65	10	1.308E-06	359.93	2.9	0.897	13.72	0.980	3.22	2.95
0.99	1.85	0.017	2.65	10	1.308E-06	359.93	2.9	0.897	13.05	0.978	3.14	1.29
0.94	1.80	0.017	2.65	10	1.308E-06	359.93	2.9	0.897	13.10	0.945	3.09	1.29
1.03	1.17	0.017	2.65	10	1.308E-06	359.93	2.9	0.897	13.56	0.949	3.15	1.97
0.88	1.16	0.017	2.65	10	1.308E-06	359.93	2.9	0.897	13.59	0.912	3.09	1.93
0.63	1.80	0.017	2.65	10	1.308E-06	359.93	2.9	0.897	13.14	0.906	3.03	1.22
0.91	0.84	0.017	2.65	10	1.308E-06	359.93	2.9	0.897	13.82	0.914	3.12	2.28
1.19	0.50	0.017	2.65	10	1.308E-06	359.93	2.9	0.897	14.13	0.918	3.16	2.66
1.49	0.41	0.017	2.65	10	1.308E-06	359.93	2.9	0.897	14.10	0.952	3.22	2.81
1.30	0.77	0.017	2.65	10	1.308E-06	359.93	2.9	0.897	13.87	0.951	3.19	2.41
0.56	0.18	0.006	2.65	10	1.308E-06	126.88	2.9	0.178	6.58	0.979	0.99	0.81
0.28	0.21	0.213	2.65	10	1.308E-06	4506.47	2.9	0.372	10.32	0.994	1.81	1.60
0.56	0.29	0.213	2.65	10	1.308E-06	4506.47	2.9	0.650	11.96	0.987	2.57	2.28

Summary

Y-Measured (m)	Y-Predicted (m)	Identity
1.55	2.62	
1.50	2.31	
1.83	2.95	
0.99	1.29	
0.94	1.29	
1.03	1.97	
0.88	1.93	
0.63	1.22	
0.91	2.28	
1.19	2.66	
1.49	2.81	
1.30	2.41	
0.56	0.81	
0.28	1.60	
0.56	2.28	
0.00		0.00
0.50		0.50
1.00		1.00
1.50		1.50
2.00		2.00
2.50		2.50

Table L.2. Predicted depths of scour using Machado's formula.

TW (m)	Y-Measured (m)	C_v	q (m ² /s)	H_o (m)	d_{90} (m)	Y+TW (m)	Y-Predicted (m)
0.57	1.55	0.92	0.897	9.30	0.017	3.22	2.65
0.85	1.50	0.92	0.897	8.93	0.017	3.18	2.33
0.27	1.83	0.92	0.897	9.60	0.017	3.25	2.98
1.85	0.99	0.92	0.897	8.69	0.017	3.15	1.30
1.80	0.94	0.92	0.897	8.75	0.017	3.16	1.36
1.17	1.03	0.92	0.897	9.37	0.017	3.22	2.05
1.16	0.88	0.92	0.897	9.42	0.017	3.23	2.07
1.80	0.63	0.92	0.897	8.80	0.017	3.16	1.36
0.84	0.91	0.92	0.897	9.74	0.017	3.26	2.43
0.50	1.19	0.92	0.897	10.18	0.017	3.31	2.81
0.41	1.49	0.92	0.897	10.14	0.017	3.31	2.90
0.77	1.30	0.92	0.897	9.80	0.017	3.27	2.50
0.18	0.56	0.92	0.178	2.21	0.006	0.98	0.79
0.21	0.28	0.92	0.372	5.43	0.213	1.49	1.28
0.29	0.56	0.92	0.650	7.30	0.213	2.16	1.87

Summary		
Y-Measured (m)	Y-Predicted (m)	Identity (m)
1.55	2.65	
1.50	2.33	
1.83	2.98	
0.99	1.30	
0.94	1.36	
1.03	2.05	
0.88	2.07	
0.63	1.36	
0.91	2.43	
1.19	2.81	
1.49	2.90	
1.30	2.50	
0.56	0.79	
0.28	1.28	
0.56	1.87	
0.00		0.00
0.50		0.50
1.00		1.00
1.50		1.50
2.00		2.00
2.50		2.50
3.00		3.00

Table L.3. Predicted depths of scour using Machado's general equation (Equation (2.59)).

TW (m)	Y-Measured (m)	C_v	q (m ² /s)	H_o (m)	d_{90} (m)	Y+TW (m)	Y-Predicted (m)
0.57	1.55	0.92	0.897	9.30	0.017	4.54	3.97
0.85	1.50	0.92	0.897	8.93	0.017	4.49	3.64
0.27	1.83	0.92	0.897	9.60	0.017	4.57	4.31
1.85	0.99	0.92	0.897	8.69	0.017	4.46	2.61
1.80	0.94	0.92	0.897	8.75	0.017	4.47	2.67
1.17	1.03	0.92	0.897	9.37	0.017	4.54	3.37
1.16	0.88	0.92	0.897	9.42	0.017	4.55	3.39
1.80	0.63	0.92	0.897	8.80	0.017	4.47	2.67
0.84	0.91	0.92	0.897	9.74	0.017	4.59	3.75
0.50	1.19	0.92	0.897	10.18	0.017	4.64	4.14
0.41	1.49	0.92	0.897	10.14	0.017	4.63	4.23
0.77	1.30	0.92	0.897	9.80	0.017	4.60	3.82
0.18	0.56	0.92	0.178	2.21	0.006	1.41	1.23
0.21	0.28	0.92	0.372	5.43	0.213	2.55	2.34
0.29	0.56	0.92	0.650	7.30	0.213	3.63	3.34

Y-Measured (m)	Y-Predicted (m)	Identity (m)
1.55	3.97	
1.50	3.64	
1.83	4.31	
0.99	2.61	
0.94	2.67	
1.03	3.37	
0.88	3.39	
0.63	2.67	
0.91	3.75	
1.19	4.14	
1.49	4.23	
1.30	3.82	
0.56	1.23	
0.28	2.34	
0.56	3.34	
0.00		0.00
0.50		0.50
1.00		1.00
1.50		1.50
2.00		2.00
2.50		2.50
3.00		3.00

Table L.4. Mirtskhulava et al. equation (1967).

Y-Measured (m)	TW (m)	d_{90} (m)	G	w (m/s)	n	cos δ	δ (deg.)	B = 90 - δ	$\sin \beta / (1 - 0.175 \cot \beta)$	b_i (m)	V_i (m/s)	Y-Predicted (m)
1.55	0.57	0.017	2.65	0.561	1.5	0.980	11.57	78.432	1.016	0.077	13.50	8.04
1.50	0.85	0.017	2.65	0.561	1.5	0.979	11.80	78.204	1.016	0.078	13.24	8.02
1.83	0.27	0.017	2.65	0.561	1.5	0.980	11.39	78.612	1.016	0.076	13.72	8.03
0.99	1.85	0.017	2.65	0.561	1.5	0.978	11.96	78.044	1.016	0.078	13.05	8.21
0.94	1.80	0.017	2.65	0.561	1.5	0.945	19.01	70.991	1.006	0.078	13.10	8.14
1.03	1.17	0.017	2.65	0.561	1.5	0.949	18.42	71.582	1.007	0.077	13.56	8.14
0.88	1.16	0.017	2.65	0.561	1.5	0.912	24.26	65.736	0.990	0.077	13.59	8.01
0.63	1.80	0.017	2.65	0.561	1.5	0.906	25.00	64.998	0.987	0.078	13.14	8.00
0.91	0.84	0.017	2.65	0.561	1.5	0.914	23.91	66.093	0.991	0.076	13.82	8.01
1.19	0.50	0.017	2.65	0.561	1.5	0.918	23.44	66.563	0.993	0.075	14.13	8.04
1.49	0.41	0.017	2.65	0.561	1.5	0.952	17.75	72.251	1.009	0.075	14.10	8.13
1.30	0.77	0.017	2.65	0.561	1.5	0.951	18.03	71.969	1.008	0.076	13.87	8.14
0.56	0.18	0.006	2.65	0.333	1.5	0.979	11.68	78.321	1.016	0.033	6.58	2.79
0.28	0.21	0.213	1.65	1.246	1.5	0.994	6.09	83.909	1.013	0.056	10.32	1.74
0.56	0.29	0.213	1.65	1.246	1.5	0.987	9.19	80.814	1.016	0.069	11.96	2.57

Summary		
Y-Measured (m)	Y-Predicted (m)	Identity
1.55	8.04	
1.50	8.02	
1.83	8.03	
0.99	8.21	
0.94	8.14	
1.03	8.14	
0.88	8.01	
0.63	8.00	
0.91	8.01	
1.19	8.04	
1.49	8.13	
1.30	8.14	
0.56	2.79	
0.28	1.74	
0.56	2.57	